The Application of Magnetic Resonance Elastography to Atherosclerosis

Lauren Elizabeth Jane Thomas-Seale

Doctor of Philosophy

The University of Edinburgh

2015

Declaration

I hereby declare that the research recorded in this thesis and the thesis itself, was composed entirely by myself and originated from my own work, except where explicitly stated in the text. The research was conducted in the Medical Physics Group and the Centre for Cardiovascular Science at The University of Edinburgh and has not been submitted for any other degree or professional qualification.

Lauren Elizabeth Jane Thomas-Seale

Submitted: December 2014

Final Revision: April 2015

Abstract

Atherosclerosis is the root cause of a wide range of cardiovascular diseases. Although it is a global arterial disease, some of the most severe consequences, heart attack and stroke, are caused by ischemia due to local plaque rupture. The risk of rupture is related to the mechanical properties of the plaque. Magnetic resonance elastography (MRE) images tissue elasticity by inverting, externally excited, harmonic wave displacement into a stiffness map, known as an elastogram. The aim of this thesis is to computationally and experimentally investigate the application of MRE to image the mechanical properties of atherosclerotic plaques.

The cardiac cycle, lumen boundary, size and inhomogeneous nature of atherosclerotic plaques pose additional complications compared to more well-established MRE applications. Computational modelling allowed these complications to be assessed in a controlled and simplified environment, prior to experimental studies. Computational simulation of MRE was proposed by combining steady state shear waves, yielded by finite element analysis, with the 2D Helmholtz inversion algorithm. The accuracy and robustness of this technique was ascertained through models of homogeneous tissue.

A computational sensitivity study was conducted through idealised atherosclerotic plaques, incorporating the effects of disease variables and mechanical, imaging and inversion parameters on the wave images and elastograms. Subject to parameter optimisation, a change in local plaque shear modulus with composition was established. Amongst other variables, an increase of the lipid pool volume in $10mm^3$ increments was shown to decrease the predicted shear modulus for stenosis sizes between 50% and 80%. The limitations of the Helmholtz inversion algorithm were demonstrated.

A series of arterial phantoms containing plaques of various size and stiffness were developed to test the experimental feasibility of the technique. The lumen was identifiable in the wave images and elastograms. However the experimental wave propagation, noise and resolution left the vessel wall and plaque unresolvable. A computational replica of the phantoms yielded clearer wave images and elastograms, indicating that changes to the experimental procedure could lead to more successful results. The comparison also highlighted certain areas for improvement in the computational work. Imaging protocol for *in vivo* MRE through the peripheral arteries of healthy volunteers and peripheral artery disease patients was developed. The presence of physiological motion and low signal to noise ratios made the vessel anatomy unidentifiable.

The application of MRE to atherosclerotic plaques through simulations, arterial phantoms, healthy volunteers and patients has shown that although there is the potential to identify a change in shear modulus with composition, the addition of realistic experimental complications are severely limiting to the technique. The gradual addition of complications throughout the thesis has allowed their impact to be assessed and in turn has highlighted areas for future research.

Acknowledgements

This thesis was made possible by the unwavering support of so many people.

I would like to thank my supervisors Peter Hoskins, Pankaj Pankaj and Neil Roberts for your help and guidance. Thank you for encouraging me to find the edge of science. Particular thanks go to my primary supervisor Pete.

The encouragement and support from my parents, through my many years of studying, have been unconditional. Thank you for everything you have given me and everything that you have helped me to achieve. To my brother and grandparents, thank you for believing in me. To my parents in law, thank you for all your support, especially in the final year.

I have had the privilege of working with so many fantastic people in Medical Physics, CVS and the CRIC. Thank you to Carmel and Irene for all your help and advice. Thank you to Dave, Barry and Noel for sharing your FE knowledge. Thank you to Stan and Tom for helping me to design and manufacture my arterial phantom moulds. Thank you to Adele and Mairead for being great friends along the way.

Thank you to Paul, Scott, Saeed and Annette for scanning my phantoms, volunteers and patients. Particular thanks go to Paul for all your advice with regards to MRE and MRI. Thank you to Lyam for the MRE brainstorms. Thank you to the Berlin MRE Group, especially to Dieter, for sharing your inversion algorithm code and helping to set up MRE at the CRIC. Thank you to Steven for creating the mechanical side of the MRE technique. Last, but not least, thank you to all my proof readers.

I would like to acknowledge the financial support of the Engineering and Physical Sciences Research Council for funding my PhD and The Edinburgh Fund and Chest, Heart and Stroke Scotland for enabling my research to go that little bit further.

To five very special friends of mine Zoë, Becky, Kate, Hayley and Beth, thank you for always being there for me.

To my little Emmeline, you have given me the invaluable gift of self-belief. Thank you for being my ray of sunshine, thank you for just being you.

Matthew, the words ‘thank you’ do not even come close to expressing the gratitude I feel towards you. You have tirelessly and selflessly, encouraged and supported me in countless ways, you are my rock and without you I could not have achieved this.

Thank you God for giving me the strength, patience and faith.

Matthew,

I dedicate my thesis to you.

What truly is logic? Who decides reason? My quest has taken me to the physical, the metaphysical, the delusional, and back. I have made the most important discovery of my career, the most important discovery of my life. It is only in the mysterious equations of love that any logic or reasons can be found. I am only here tonight because of you.

You are the only reason I am. You are all my reasons. Thank you.

- A Beautiful Mind

Contents

List of Figures

List of Tables

Abbreviations

ARFI	Acoustic radiation force imaging
CFD	Computational fluid dynamics
CT	Computed tomography
DSA	Digital subtraction angiography
ESCT	European Carotid Surgery Trial
FEA	Finite element analysis
FEM	Finite element model
FoV	Field of view
FSI	Fluid solid interaction
ICA	Interal carotid artery
IVE	Intravascular ultrasound elastography
IVUS	Intravascular ultrasound
LDL	Low density lipoproteins
LSME	Lagrangian speckle model estimator
MEG	Motion encoding gradient
MIP	Maximum intensity projection
MR	Magnetic resonance
MRA	Magnetic resonance angiography
MRE	Magnetic resonance elastography
MRI	Magnetic resonance imaging
NASCET	North American Symptomatic Carotid Endarterectomy Trial
NIVE	Non-invasive vascular elastography
PAD	Peripheral artery disease
PC	Phase contrast
PC-MRI	Phase contrast magnetic resonance imaging
PE	Phase endocing
PVA	Polyvinyl alcohol
PVA-C	Polyvinyl alcohol cryogel
PWV	Pulse wave velocity
RF	Radiofrequency
RO	Read out
SNR	Signal to noise ratio
SS	Slice select
TE	Echo time
TMM	Tissue mimicking material
ToF	Time of flight
HV1	Healthy volunteer 1
HV2	Healthy volunteer 2
P1	Patient 1
P2	Patient 2

P3	Patient 3
TR	Repetition time
VMM	Vessel mimicking material
1D	One dimensional
2D	Two dimensional
3D	Three dimensional

Nomenclature

A	Wave amplitude	t	Time
A_G	gain	u	Displacement (time domain)
$\overline{A_s}$	Average amplitude of the wave signal	U	Displacement (frequency domain)
c	Wave speed	W	Width
D	Depth	X, Y, Z	Axes directions
e	Offset	z	Distance
E	Young’s modulus	H	High Pass (subscript)
E_c	Eccentricity	I	Inner (subscript)
E_P	Pressure strain elastic modulus	L	Low Pass (subscript)
f	Frequency	O	Outer (subscript)
f_i	Body forces	T	Tissue (subscript)
G	Dynamic shear modulus	V	Vessel (subscript)
h	Vessel wall thickness	i, j, k	Axes (subscripts)
H	Frequency response	x, y, z	Axes (subscripts)
i	Imaginary	∞	Longterm (subscript)
K	Bulk modulus	‘	Storage (superscript)
K_0	Motion encoding gradient frequency	‘‘	Loss (superscript)
L	Length	α	Angle
n	Order of filter	γ	Gyromagnetic ratio
p	Pressure	δ	Loss Angle
q	Number of motion encoding gradient cycles	δ_{ij}	Kronecker delta
R	Radius	ε	Strain
S	Stenosis	η	Shear viscosity

λ	First (longitudinal) Lamé parameter
μ	Second (shear) Lamé parameter or shear modulus
υ	Poisson’s ratio
ρ	Density
σ	Stress
σ_n	Standard deviation of noise
ϕ	Diameter
Φ	Wave phase
ω	Circular frequency
ω_0	Cut-off frequency

Chapter 1

Introduction

1.1) Cardiovascular Disease

Cardiovascular diseases are the leading causes of death in the world; responsible for 31% of global mortalities in 2011 (Mendis *et al.* 2011). This generates a huge burden on the global economy. Current statistics estimate this to be $315 billion in the United States and £19 billion in the United Kingdom (Townsend *et al.* 2012, Go *et al.* 2014).

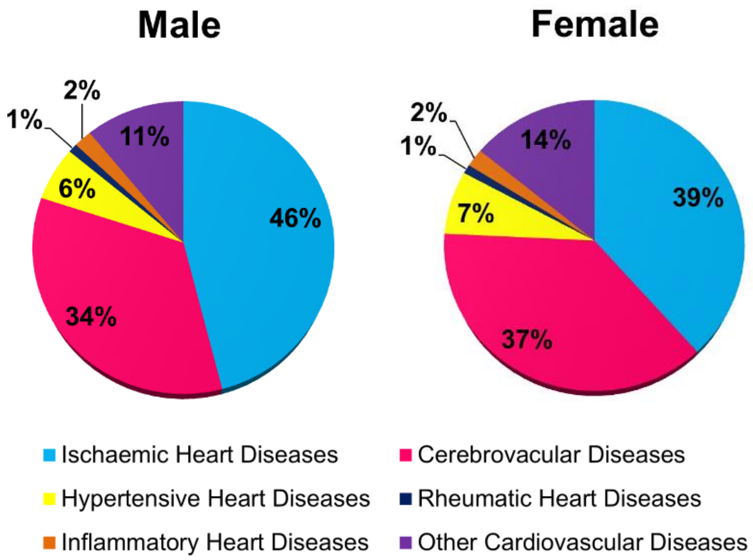

Figure 1.1: *The distribution of mortalities due to cardiovascular diseases, 2011. Replicated and adapted from the World Health Organisation, Global Atlas on Cardiovascular Disease Prevention and Control (Mendis et al. 2011).*

Cardiovascular diseases are conditions which affect the heart and blood vessels; encompassing a wide range of afflictions including hypertension, cardiomyopathies, cardiac arrhythmias, peripheral arterial disease (PAD), stroke and heart attack. Figure 1.1 shows the distribution of male and female deaths due to different types of cardiovascular diseases in

2011 (Mendis *et al.* 2011). Of all deaths from cardiovascular disease, atherosclerosis is the root cause of the majority (Go *et al.* 2014).

The development of atherosclerosis is a complex process and described in detail in section 1.2. It is a disease affecting the wall of the artery; the accumulation of low density lipoproteins (LDL) leads to the growth of a plaque, the narrowing of the lumen and eventually the risk of rupture. The consequences of atherosclerosis are strongly dependent on the severity of the disease and the artery in which it develops. Severe symptoms of plaque rupture include ischemia in the coronary arteries leading to a heart attack and ischemia in the carotid artery causing stroke. The effects of PAD in the lower extremities can range from asymptomatic, to various levels of claudication and in severe cases gangrene (Hirsch *et al.* 2006).

1.2) Atherosclerosis: Disease Development

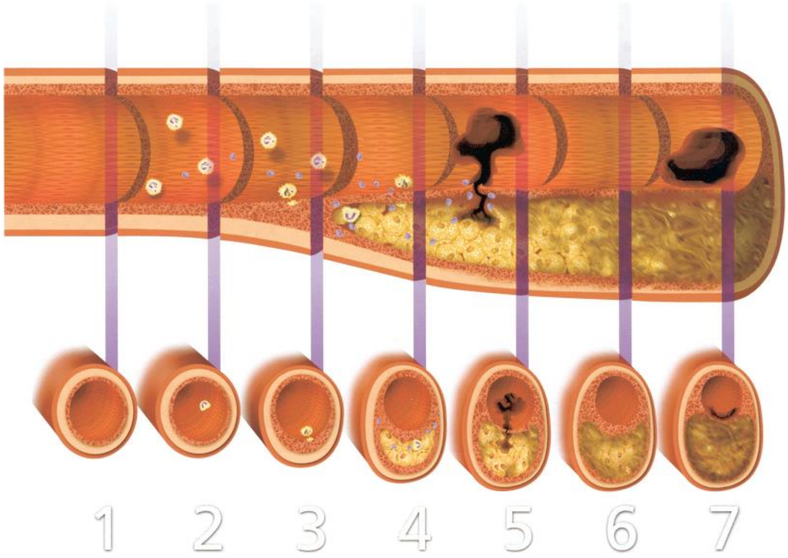

Figure 1.2: *Atherosclerosis disease development. (1) Healthy artery wall. (2) Expression of adhesion molecules and attraction of inflammatory leukocytes. (3) Fatty streak develops. (4) Atheroma with fibrous cap, type IV lesion. (5) Rupture and thrombosis. (6) Advanced plaque with significant fibrotic tissue, type V lesion. (7) Complicated plaque with thrombi generated by superficial erosion, type VI lesion. Reused with permission from Wolters Kluwer Publishers (Libby 2001).*

Figure 1.2, shows the visual propagation of atherosclerosis from a healthy artery wall to a ruptured plaque. The pathogenesis of atherosclerosis is a complicated biological and biomechanical process. An in-depth review of the mechanopathobiology can be found in (VanEpps and Vorp 2007). An overview of the disease development will be given in this section.

1.2.1) Healthy Arterial Structure

The artery wall is composed of three layers; the intima, media and adventitia, Figure 1.2 (1). Within the intima there are two structures. The innermost is a layer of endothelial cells interfacing with the blood. This structure has a depth of only one cell, fissures between these create permeability to various substances and under normal conditions these cells are elongated in the direction of the flow (Vito and Dixon 2003). Supporting the endothelial cells is the basement membrane, the second structure within the intima, composed of collagen, fibronectin and laminin (Vito and Dixon 2003).

The media surrounds the intima and contributes largely to the overall mechanical properties of the artery by controlling the contraction and expansion of the diameter; its primary components are circumferential smooth muscle cells, elastin and collagen (Vito and Dixon 2003). The smooth muscle cells allow vasodilation, an increase of the diameter under blood pressure, by relaxing (Waite and Fine 2007). Elastic fibres are passive tissues, they do not contain living cells; they support the blood vessel and allow recoil, vasoconstriction, upon removal of the internal pressure (Waite and Fine 2007). The outermost layer of the artery is the adventitia; composed of passive elastic and collagen fibres (Waite and Fine 2007) and in some arteries, a vascular network called the vasa vasorum (Vito and Dixon 2003). The main function of the adventitia, is to structurally secure the artery to the surrounding tissue (Vito and Dixon 2003).

1.2.2) Disease Initiation

The well-established risk factors of atherosclerosis include smoking, a high cholesterol diet, physical inactivity and hypertension (Go *et al.* 2014). These are known as global risk factors i.e. their influence is present throughout the entire arterial system, however atherosclerosis is essentially a focal disease (Stanton 1999). It is generally accepted that biomechanical forces either facilitate or protect against atherosclerosis, thus leading to its anatomical location specific nature (VanEpps and Vorp 2007). The correlation between arterial geometry and the locations of atherosclerotic plaques has been widely attributed to low wall shear stress (Caro *et al.* 1971, Hoskins and Hardman 2009).

The precipitation of the atherosclerotic process is said to be a ‘response to injury’ (Ross 1993). Chronic low level damage to the endothelium results in endothelial dysfunction (Ross 1993, VanEpps and Vorp 2007). Multiple studies have investigated the effect of shear stress on endothelial cells. Barbee et al. (1994) demonstrated, *in vitro*, that endothelial cells exposed to steady shear stress become elongated and aligned in the flow direction, in comparison to the unorientated and polygonal shape of unsheared cells. Himburg et al. (2004) showed that endothelial cells display increased permeability to macromolecules in areas of low and cyclic shear stress. In areas of reduced shear stress activated leukocytes show pseudopodium extensions and express surface adhesion molecules which promote adherence and migration through the endothelium (Stanton 1999). The proliferation and apoptosis rate of endothelial cells is also altered by shear stress (VanEpps and Vorp 2007), indicating that low shear stress can increase cell turnover (Lin *et al.* 2000).

Fatty streaks are an increase of LDL within the intima of the artery wall, Figure 1.2 (3). They have been found in the aorta and coronary arteries of children as young as two (Berenson *et al.* 1998). Although they are asymptomatic, some may go on to develop into an atherosclerotic lesion (Packard and Libby 2008). Van Epps and Vorp (2007) hypothesise that lipid accumulation occurs by three means; 1) Endothelial dysfunction, leading to the loss of a selective barrier and 2) altered expression of lipoprotein receptors and 3) the consequent ingestion and retention of LDL by smooth muscle cells and macrophages. The accumulation of LDL is increased when the circulating levels in the blood are raised (Lusis 2000).

1.2.3) Disease Development

Once LDL has migrated from the blood stream into the artery wall, it undergoes modification; oxidation, lipolysis, proteolysis and aggregation (Lusis 2000). Oxidised LDL has been identified as a pathogen which triggers and sustains an inflammatory response (Miller *et al.* 2003). Conversely, high density lipoproteins are atheroprotective; inhibiting lipoprotein oxidation and aiding in the removal of excess cholesterol from peripheral tissue (Lusis 2000).

The risk factors associated with atherosclerosis, are also known as pro-inflammatory stimuli; they trigger the expression of surface adhesion molecules by the endothelium, encouraging the attachment of inflammatory leukocytes such as monocytes and lymphocytes, Figure 1.2 (2), (Packard and Libby 2008). Once the monocytes have migrated across the endothelium, they mature into macrophages, via a macrophage colony stimulating factor, expressed by the inflamed intima (Packard and Libby 2008). Scavenger receptors expressed from the macrophages mediate the ingestion of oxidised LDL, which convert the macrophages into foam cells (Libby *et al.* 2002). These macrophages also amplify the inflammatory response by secreting growth factors and cytokines (Packard and Libby 2008). In turn, the inflammatory response stimulates migration and proliferation of smooth muscle cells (Ross 1999).

Continual accumulation of monocytes and the migration and proliferation of smooth muscle cells leads to growth and restructure of the lesion; a fibrous cap covering a core of lipid and necrotic tissue, Figure 1.2, (4), (Ross 1999). As the plaque grows in size, the artery becomes occluded; the measurement of this occlusion is known as a stenosis. A stenosis alters the flow through the artery and thus the hemodynamic forces acting upon the plaque. Relating back to the initiation of the disease which occurs in areas of low shear stress; at the outlet of the stenosis the flow is often oscillatory, therefore the downstream shoulders of the plaque are exposed to low levels of shear stress, which encourages the progression of atherosclerosis (Slager *et al.* 2005).

1.2.4) Rupture

Histologically, an atherosclerotic lesion is defined as advanced when associated with structural disorganisation, repair, thickening of the intima and deformity of the arterial wall (Stary *et al.* 1994). The American Heart Association classifies advanced lesions into three types, IV, V, and VI (Stary *et al.* 1995); where type I, II and III refer to the initial, fatty streak and intermediate lesion respectively (Stary *et al.* 1994). Type IV lesions are known as atheromas; a dense accumulation of extracellular lipid occupying an extensive but well-defined region of the intima, Figure 1.2 (4), (Stary *et al.* 1995). Type V lesions have significant growth of fibrous tissue, although this may be subdivided to include lesions with multiple layers and lipid cores (Va), calcified lesions (Vb) and fibrotic lesions with minimal lipids (Vc), Figure 1.2 (6), (Stary *et al.* 1995). Type VI or complicated lesions include surface disruption (VIa), hematoma or hemorrhage (VIb), and thrombosis (VIc) or all three (VIabc), Figure 1.2 (7), (Stary *et al.* 1995).

Thrombosis, exposure of the thrombogenic plaque core to the blood, may be caused by plaque rupture or endothelial erosion, Figure 1.2 (5) and (7) respectively, (Hansson 2005). Whether a plaque will rupture or not is determined by the properties of the plaque and the hemodynamics forces acting upon it (Falk *et al.* 1995). The vulnerability of a plaque to rupture depends upon the size and consistency of the lipid core, the thickness and stiffness of the fibrous cap, inflammation within the cap and cap fatigue (Falk *et al.* 1995).

Identifying plaques that are vulnerable to rupture is a very active area of research with various methods of approaching the problem. Examples include imaging the plaque composition (Sanz and Fayad 2008, Corti and Fuster 2011), molecular imaging (Sanz and Fayad 2008, Mulder *et al.* 2014) including inflammation tracking using ultra small super-paramagnetic iron oxide particle enhanced magnetic resonance imaging, image guided modelling the hemodynamics (Hoskins and Hardman 2009, Seneviratne *et al.* 2013) or imaging the biomechanics. The biomechanics of the artery wall in itself is a large area of research. How to measure and model them, with an emphasis on elastography is discussed in sections 1.5 to 1.7.

1.3 Atherosclerosis: Clinical Management

In reality everyone is susceptible to some degree of atherosclerosis. Fatty streaks can develop in childhood (Berenson *et al.* 1998) and in the Western population it is assumed that in the majority of the population aged over 50, have coronary and carotid atherosclerosis in a presymptomatic state (Ricotta *et al.* 2008). Whether a person will develop atherosclerosis to the point where medical intervention is required largely is dependent on their exposure to the risk factors, some preventable and some non-preventable; examples include cholesterol levels, hypertension, diabetes, physical inactivity, family history and obesity.

1.3.1) Diagnosis

Cardiovascular risk factors affect the whole arterial system; they give an indication of the global risk. However clinical assessment of the severity of atherosclerosis in a particular artery is based upon patient symptoms or imaging the extent of lumen occlusion. The symptoms of atherosclerosis depend upon the location. Carotid atherosclerosis gives rise to focal neurological symptoms (Golledge and Siew 2008), the ischemia caused by coronary artery disease can be detected using electrocardiography, echocardiography and cardiac nuclear perfusion (Ricotta *et al.* 2008) and PAD causes claudication (Hirsch *et al.* 2006). However the exact location and the size of the plaque can only be diagnosed via imaging.

The severity of an atherosclerotic plaque may be defined by its percent stenosis; the ratio of the minimum diameter of the stenosed artery compared to an equivalent healthy section. There can be slight variations of this method, as displayed between the American and European methods of carotid plaque diagnosis. The North American Symptomatic Carotid Endarterectomy Trial (NASCET) compared the minimum diameter to the distal internal carotid artery (ICA), Figure 1.3 (B), (Barnett *et al.* 1998, Rothwell *et al.* 2003b). The European Carotid Surgery Trial (ECST) compared the minimum diameter to an estimate of the original width of the artery, Figure 1.3 (A), (Farrell *et al.* 1998, Rothwell *et al.* 2003b). The ECST method shall be used to define stenosis size for the duration of this thesis.

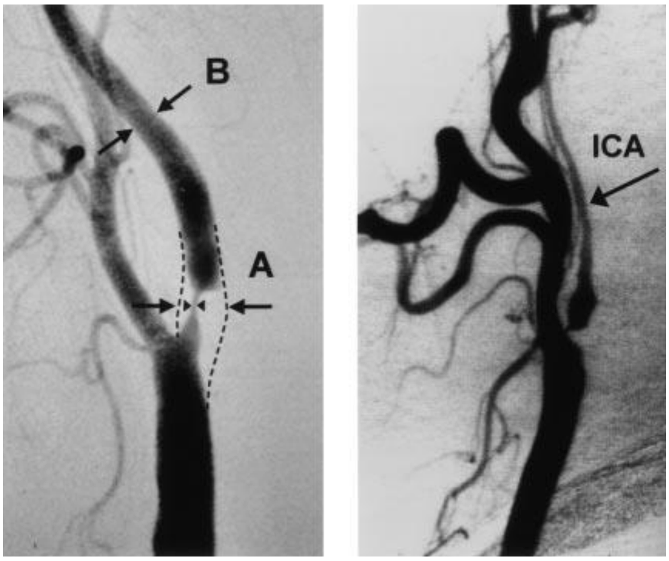

Figure 1.3: *The ECST and NASCET method of quantifying stenosis size in the internal carotid artery (ICA). ECST: the minimum diameter of the occlusion divided by the estimated original diameter (A). NASCET: the minimum diameter of the occlusion, divided by the diameter of the distal ICA (B). Reused with permission from Wolters Kluwer Publishers (Rothwell et al. 2003b).*

The exact location and size of the stenosis is determined using imaging. Traditionally, digital subtraction angiography (DSA) is used to image diseased arterial geometry, for example in the carotid endarterectomy trials NASCET and ECST. In recent years there has been a drive towards using non-invasive methods; removing the 1-2% risk of neurological complications (U-King-Im *et al.* 2004). Non-invasive methods of imaging diseased arteries include non-invasive ultrasound, magnetic resonance angiography (MRA) without contrast agents and spiral computed tomography (CT) scanning. Details of some of the methods used to image arteries shall be expanded upon in section 1.4.

1.3.2) Treatment

The prevention of cardiovascular disease is preferable to the treatment, with various health organisations placing a large emphasis on the preventable risk factors; physical activity, weight, cholesterol level, alcohol intake and smoking (Mendis *et al.* 2011, Townsend *et al.* 2012, Go *et al.* 2014). Lifestyle changes affect the global risk of atherosclerosis, if they fail or the patient is identified as high risk, other global therapies can be administered such as anticoagulants and LDL-lowering drugs (Townsend *et al.* 2012).

Surgical intervention differs, depending on the location of the symptomatic plaque. A carotid stenosis is treated by either an endarterectomy or angioplasty (Ricotta *et al.* 2008). An endarterectomy surgically removes the plaque from the artery wall. An angioplasty involves inserting a catheter into the obstructed vessel, widening it by the inflation of a small balloon and retaining the lumen with a stent. Carotid angioplasty is a less invasive alternative to endarterectomy, especially for patients with a high perioperative risk (Murad *et al.* 2008).

The main surgical options for coronary stenosis are percutaneous coronary intervention, primarily angioplasty and stenting, and coronary artery bypass graft surgery (Anderson *et al.* 2007). Coronary artery bypass surgery, involves grafting a vessel taken from another part of the patient’s body, to improve blood flow to the heart muscle. In the event of a myocardial infarction the decision to perform revascularization is based not only upon the degree of stenosis and number of effected vessels but life expectancy, comorbidity, severity of symptoms and functional capacity (Anderson *et al.* 2007).

Limb ischemic symptoms can vary largely and thus patients are selected for revascularization based upon the severity of symptoms, failure of medical therapies, lack of comorbid conditions and favourable risk/benefit ratio (Hirsch *et al.* 2006). The decision of how to treat lesions in the iliac, femoral or popliteal arteries depends upon the frequency and extent of the disease. Endovascular techniques include several percutaneous transluminal angioplasty treatments; balloon angioplasty, stenting, atherectomy, fibrinolysis/fibrinectomy, laser and thrombolysis and thrombectony (Hirsch *et al.* 2006). Surgical intervention i.e. bypass grafts, are only used where endovascular procedures are not favourable (Hirsch *et al.* 2006).

The stenosis threshold for surgery in the presence or lack of symptoms is a well-discussed topic, particularly in the carotid artery. The two well-known trials to research the outcomes of carotid endarterectomies have already been mentioned; the NASCET and ECST. Over the two studies it was concluded that in symptomatic patients surgical intervention was effective in stenosis greater than 70% (Barnett *et al.* 1998) and 80% (Farrell *et al.* 1998); where 80% in the ECST is equivalent to 60% in the NASCET (Barnett *et al.* 1998). Due to the discrepancies in stenosis calculation between the studies, Rothwell et al. conducted an analysis of complied data, unifying the measurements of the ECST, NASCET (2003b) and the Veterans Affairs Trial 309 (2003a). Rothwell et al. concluded that the NASCET and ECST give a comparable absolute risk reduction of stroke or operative death from surgery compared to medical treatment (2003b) and after 5 years this value was shown to be 15.3% for the 70-99% stenoses (2003a). Even though this does show that endarterectomies have long term benefits to patients with larger occlusions, it also translates to almost 7 operations required to prevent one stroke or death. The statistics for asymptomatic carotid artery stenoses are even lower, with the risk reduction of any stroke or death falling from 11% to 5% with surgical treatment (Toole *et al.* 1995). Considering the economic impact of cardiovascular disease on the world, discussed in section 1.1, it is easy to see that improved diagnostics could reduce the economic burden.

1.4) Imaging Modalities

Imaging the artery wall, to determine stenosis size, can be done using several different imaging modalities. These imaging modalities are applicable to clinical diagnosis. They are also employed to image wall motion and composition to inform the analysis techniques discussed sections 1.5, 1.6 and 1.7.

1.4.1) X-Ray

Digital subtraction angiography is an x-ray based method of imaging the lumen of the artery. X-rays are an electromagnetic wave, consisting of relatively high energy protons, when compared to visible light (Suetens 2009). The absorption of x-rays is dependent on the linear attenuation coefficient of the medium (Suetens 2009). Digital subtraction angiography is an invasive procedure; an injection of an iodinated contrast agent is given to the patient and an image of the vessel is taken pre and post injection (Webb 1988). By subtracting the original x-ray from the post injection x-ray, an image just containing the contrast agent passing through the region of interest (ROI) is generated (Webb 1988). This removes any anatomy that may interfere with the clarity, leaving only the vessels (Farr and Allisy-Roberts 1997).

A limitation of DSA is that the two dimensional (2D) image, through only one plane, may not capture the maximum stenosis size (Hyde *et al.* 2004). This may be overcome by using three dimensional (3D) rotational angiography, which utilizes CT (Hyde *et al.* 2004). Both DSA and 3D CT angiography have risks associated with the invasive nature of the procedure and radiation dose from the imaging method.

1.4.2) Ultrasound

Ultrasound utilizes high frequency sound waves; the most common mode of ultrasound, B-mode, appears as a cross-sectional image through the body (Martin 2010). When an ultrasound beam hits a boundary between two tissues some of the wave is reflected back and some is transmitted (Farr and Allisy-Roberts 1997); an image is constructed from these wave reflections, known as echoes (Martin 2010). Ultrasound is used extensively in the clinical diagnosis of arterial disease; it is a relatively inexpensive, portable, time efficient and risk free imaging technique.

The main limitation of ultrasound is penetration depth. Attenuation, described as the exponential decrease of a plane wave with distance, increases with frequency in tissue (Webb 1988). In bone and air, attenuation is very high; air creates a total reflection meaning that gas-filled organs cast shadows (Farr and Allisy-Roberts 1997). Intravascular ultrasound (IVUS) involves inserting a catheter containing an ultrasound transducer into an artery or vein (De Jong *et al.* 2007). This can overcome the penetration problems of conventional ultrasound, allowing high resolution imaging of arteries located deeper in the body. However intravascular ultrasound introduces the risks and complications of an invasive procedure.

1.4.3) Magnetic Resonance Imaging

Magnetic resonance imaging (MRI) is based upon a property of the nucleus of an atom; nuclear magnetic resonance (Farr and Allisy-Roberts 1997). The theory behind MRI may be expressed in terms of classical or quantum mechanics; ideally a little bit of both. For simplicity, consider a hydrogen nucleus, which contains one proton and is an abundant element within the body (McRobbie 2007). This proton spins about it owns axis and since it is positively charged, creates its own tiny magnetic field (McRobbie 2007).

The static magnetic field of the MRI machine compels these previously randomly arranged charges, with a zero magnetic effect, to orientate themselves with the axis of the bore (Farr and Allisy-Roberts 1997). The protons do not align rigidly along this axis, instead they exhibit behaviour analogous to a gyroscope, known as precession (Farr and Allisy-Roberts 1997). The frequency of the rotation of the proton axis tilted about an axis is known as the Larmor frequency and it depends on the strength of the external magnetic field (Farr and Allisy-Roberts 1997). A proton may align itself in two stable directions along the axis of the bore, either with the main field (parallel) or opposed to it (anti-parallel); the parallel state is slightly favoured as the anti-parallel state requires slightly more energy (McRobbie 2007). The energy required to swap a proton between these two alignments, takes the form of a photon of electromagnetic radiation and is again expressed in the Larmor frequency (McRobbie 2007). On a macroscopic level, the overall effect of a group of protons may be considered. Therefore the summation of their magnetic fields may be represented by an average magnetic moment, which is measurable in the order of microtesla (McRobbie 2007).

Surrounding the area of interest are coils, through which passes a radiofrequency (RF) current, creating an alternating magnetic field perpendicular to the main field, at the Larmor frequency (Farr and Allisy-Roberts 1997). In the presence of the RF pulse the average magnetic moment of the group of protons moves away from the bore axis; the strength or duration of the pulse determines the alignment (McRobbie 2007). A 180 degree RF pulse, imparts enough energy to reverse the magnetic moment (Farr and Allisy-Roberts 1997). A 90 degree pulse imparts half that energy so the average magnetic moment lies in the transverse plane (McRobbie 2007). The receiver coil is sensitive to magnetization in the perpendicular plane; so the RF pulse induces a detectable voltage (McRobbie 2007). As the protons relax back towards the bores axis, the signal in the transverse plane can be measured. By manipulating the behaviour of the protons using single or multiple RF pulses, known as pulse sequences, tissue specific relaxation parameters can be measured.

Magnetic resonance angiography (MRA) is used to highlight blood flow and in tandem the lumen of the artery, it can be conducted in two ways; a time-of-flight (ToF) or a phase contrast (PC) sequence (McRobbie 2007), both of which take advantage of the inherent motion of blood flow within the artery. ToF MRA is conducted in tandem with a gradient echo sequence; the surrounding tissue is saturated by repetitive excitation, the new unsaturated blood flowing into the slice can be excited and the consequent large signal intensity is highlighted against the stationary background (Alger and Frew 2007).

Phase contrast magnetic resonance imaging (PC-MRI) is a well-used technique, both diagnostically in MRA and in research to measure other types of motion, for example, physiological blood flow velocities to calculate wall shear stresses (Marshall *et al.* 2004), or externally excited waves such as that seen in magnetic resonance elastography, discussed in section 1.7.2. As mentioned earlier, protons exhibit precession; as they move along a magnetic field gradient, compared to the stationary protons, their phase shifts proportionally to their velocity (Fraser 2007). Gradients, which may be applied in only one or all three directions, establish a linear relationship between the motion velocity and phase of the signal (McRobbie 2007). A maximum velocity encoding value is set, corresponding to a phase shift of 180°. The 360° constraints of phase, means that when the phase shift exceeds 180° or the velocity exceeds the maximum, the phase becomes ‘wrapped’ back around to between the -180° and 0 ° range (McRobbie 2007). Both ToF and PC MRA can be conducted with or without contrast agent enhancement, the most common of which are gadolinium based.

MRI has also shown success in terms of imaging atherosclerotic plaque compositions using multi-parametric techniques. The combination of MRI images generated using a selection of different parameters can detect and quantify lipid, fibro-cellular, calcium, intraplaque haemorrhage and thrombus (Saam *et al.* 2007, Sanz and Fayad 2008). The composition images yielded by these techniques have shown good correlations between histology, patient symptoms and other imaging techniques (Fayad *et al.* 2000, Yuan *et al.* 2002, Cai *et al.* 2005, Takaya *et al.* 2006).

The advantages of MRI; high resolution at any depth and the absence of any harmful radiation, are offset by a few limitations. The magnetic nature of the MRI technique means that patients with any embedded metallic items cannot be imaged. MRI is a fairly expensive technique and may induce feelings of claustrophobia in patients.

1.5) The Biomechanics of the Arterial Wall

1.5.1) The Characteristics of the Arterial Wall

The artery wall contains cells and the fibrous constituents, elastin and collagen (Vito and Dixon 2003) and, as described in section 1.2.1 the composition of each layer of the artery wall is different. In tandem the distribution of the cells elastin and collagen, vary throughout the arterial system (Vito and Dixon 2003). The percentage volume of the components within each layer allows correlation between the mechanical properties and tissue structure (Fung 1993). Generally, proximal arteries tend to be more elastic and distal arteries more muscular (Holzapfel *et al.* 2002a). As described in section 1.2.4, the composition of the artery wall becomes increasingly complex with the development of atherosclerotic disease. Considering the above points, there is a huge variation in the mechanical properties through the healthy artery wall, throughout the global arterial system as well as through the local areas of disease.

The artery wall has a complex structure and composition; it has both heterogeneous and anisotropic properties (Vito and Dixon 2003). Anisotropy and heterogeneity describe mediums whose material properties vary with direction and location respectively. Arteries also display a complicated constitutive relationship; how the tissue deforms under an applied load. Arteries are nonlinearly viscoelastic (Waite and Fine 2007). A nonlinear material does not display a linear relationship between stress and strain; smooth muscle cells contract to resist strain (Waite and Fine 2007). In addition the viscoelastic property of arteries means that the stress is dependent on both the strain and the rate of strain (Waite and Fine 2007). Arteries are also subject to residual stresses; when all loads have been removed a stress still exists within the structure (Sumpio 1993). Biological tissue has a high water content, consequently it displays incompressible behaviour at physiologic pressures (Vito and Dixon 2003).

The stiffness of an artery may be expressed in terms of only the inherent material properties or in tandem with the structural properties, including geometric factors (Hayashi 1993). Material stiffness is a property of the medium, independent of the artery diameter or wall thickness (Claridge *et al.* 2009). Whereas, structural stiffness describes the overall behaviour of the whole arterial wall (Claridge *et al.* 2009).

The modelling of the artery wall is discussed in section 1.6. The different characteristics of the artery wall, heterogeneity, anisotropy and nonlinear viscoelasticity, add levels of complexity to constitutive models used in computational modelling. The following sections overview some of the methods used to quantify the stiffness of the arterial wall.

1.5.2) Measuring Arterial Stiffness

Measuring arterial stiffness is long-standing and well-developed area of research (Parker 2009a). However the term ‘stiffness’ can be used very generally in this branch of research, rather than being associated with a measure of a specific quantity, it is sometimes used as an overhead to describe various measureable characteristics that change with the arterial system in response to ageing and cardiovascular disease (Hamilton *et al.* 2007). In addition the measures in this section represent the structural stiffness of the artery, which does not isolate the material properties of the wall or the components within it.

As the arterial wall stiffens, its distensibility decreases and the speed of the pressure wave created by the heart flows faster through the vessel. This concept is reflected in the Moens-Korteweg equation 1.1; where the wave speed c, is calculated from the Young’s modulus E, wall thickness h, vessel diameter ϕ and fluid density ρ (Hamilton *et al.* 2007). The Moens-Korteweg equation is a thin-walled model, equation 1.2 allows for increased wall thickness and compressibility, where υ is the Poisson’s ratio (Bergel 1961b, Hoskins and Bradbury 2012).

$$c = \sqrt{\frac{Eh}{\phi\rho}} \tag{1.1}$$

$$c = \sqrt{\frac{Eh}{\phi\rho\left(1-\nu^{2}\right)}} \tag{1.2}$$

Equations 1.1 and 1.2 can be informed by pulse wave velocity (PWV) measurements, in order to describe the stiffness of a section of the arterial system. The PWV is calculated via equation 1.3 incorporating z, the distance between the analysis points and Δt, the time delay between defined points on the pressure waveform. The limitations of the PWV method include differences in body shape, changes of the pressure pulse waveform as it propagates and dependence on blood pressure (Hamilton *et al.* 2007, Wang *et al.* 2008). The theory of PWV has been extended to pulse wave imaging, where the Moens-Korteweg equation is informed by PWV on a more localised section of the arterial wall (Li *et al.* 2013, Shahmirzadi *et al.* 2013).

$$PWV = \frac{z}{\Delta t} \tag{1.3}$$

There are several methods of measuring arterial stiffness by analysis of the pressure waveform. Pulse pressure, taken as the difference between the systolic and diastolic blood pressure, is a simple measure with a complex relationship to vascular pathology (Dart and Kingwell 2001). Further insight can be gained by considering wave reflections generated where there is an impedance mismatch; bifurcations and tapers where changes of diameter and/or stiffness occurs (Hamilton *et al.* 2007, Wang *et al.* 2008). The Augmentation Index, the difference between the first and second systolic peaks, is defined as the percentage of the central pulse pressure, generated by impedance mismatches, and is considered a measure of increased arterial stiffness (Laurent *et al.* 2006). The Ambulatory Arterial Stiffness Index is derived from analysis of the dynamic interaction between diastolic and systolic blood pressure over 24 hours (Wang *et al.* 2008). More complex wave intensity analysis, can solve the summation of successive wave fronts propagating forward and backwards along the vessel via the conservation of mass and momentum, yielding the local wave speed (Parker 2009b).

Whilst predominantly each of the above techniques yield a simple non-invasive measure of arterial stiffness, they are also spatially invariant, providing either a global measure or one along a specific segment of the arterial tree. The pressure strain elastic modulus E_P offers a local value of structural arterial wall stiffness, from measures of the vessel diameter and change in pressure Δp, equation 1.4 (Hayashi 1993). The Young's modulus and pressure strain elastic modulus are related by equation 1.5 (Hoskins and Bradbury 2012).

$$E_P = \frac{\Delta p \phi}{\Delta \phi} \tag{1.4}$$

$$E = \frac{\phi}{2h} E_p \tag{1.5}$$

1.5.3) Measuring the Biomechanical Properties of the Arterial Wall

The material properties of a section or component of the arterial wall can be extracted from *ex vivo* samples of the tissue. The parameters of the chosen constitutive model are then fitted to the behaviour of the tissue under mechanical testing; this can be done by using simple deformation curve fitting or finite element analysis (Loree *et al.* 1994a, Barrett *et al.* 2009). However the conditions upon the artery wall *in vivo* are completely different to those during *ex vivo* mechanical testing, so the extracted properties can only have a limited accuracy.

Assessing the biomechanical properties of the arterial wall *in vivo*, specifically the material properties as opposed to the structural stiffness, requires accurate measurement of the tissue deformation under a known applied load. Elastography is the broad term used to describe various modalities of imaging tissue deformation subject to an applied load in order to determine tissue stiffness; these techniques are discussed further in section 1.7, of which a number have arterial applications. Elastography is often combined with finite element analysis, section 1.7.4. Computational modelling of the artery wall shall be overviewed first in section 1.6.

There are a few studies which bridge the gap between assessing local arterial stiffness and the biomechanical properties of the wall. These studies define the viscoelastic properties of the artery by fitting the pressure-displacement behaviour of the wall to a rheological model (Balocco *et al.* 2010, Valdez-Jasso *et al.* 2011).

1.6) Computational Modelling of the Arterial Wall

Finite element analysis (FEA) is a numerical method of modelling the response of a solid system to an applied load. The appropriate differential equations are solved over the geometry, broken down into series of finite elements, to give an approximate solution to the problem assembled over the entire model (Pepper and Heinrich 1992). Finite element models

(FEMs) require the system to be specified in terms of geometry, material properties, boundary conditions and loads. Although FEA is a widely used technique, the accuracy of the results are highly dependent on the assumptions and simplifications made in the model (Migliavacca *et al.* 2002).

FEA is used in the arena of arterial biomechanics for a wide range of purposes; the response of atherosclerotic plaques to loads, the change in plaque stress with altered compositions, to investigate placement of stents (Holzapfel *et al.* 2002b, Lally *et al.* 2005, Early and Kelly 2010), to identify rupture sites in abdominal aortic aneurysms (Doyle *et al.* 2010) and the phenomena of residual stresses (Raghavan *et al.* 2004). Fluid structure interaction (FSI) models extend structural FEA to incorporate computational fluid dynamics (CFD) to model the behaviour of fluids. They demonstrate the effect of wall motion on the blood flow and associated hemodynamic forces on the wall. This type of modelling is beyond the scope of this research. However, some FSI studies will be discussed in this section, in terms of how they model the arterial wall.

1.6.1) Geometry

Arterial wall geometry may be modelled as idealised or patient specific in two or three dimensions, where the elements used to mesh the model are varied accordingly. Idealised geometry is often used to investigate the effect of changing a model parameter on the system response, simply because the geometry can be closely controlled and varied linearly. A multitude of 2D FEMs have been used to investigate the deformation, peak stress, crack propagation or fatigue in plaques of various compositions (Loree *et al.* 1992, Li *et al.* 2005, Versluis *et al.* 2006). Three dimensional idealised geometries have been utilised in FSI models to examine the wall stress distribution through plaques with a variation in stenosis size (Li 2007) and composition (Tang *et al.* 2004a).

Patient specific geometries offer a more realistic model of the arterial wall behaviour. They can be informed by histology or imaging. Histology is the gold standard for determining plaque geometry and composition, however histology processing can in itself cause geometric distortions (Chau *et al.* 2004). Chau et al. (2004) compared the mechanical analysis of excised coronary arteries based upon geometry from optical coherence tomography and histology. The segmentation and characterisation of the image data was based upon the signal properties matched to histology in a previous study (Yabushita *et al.*

2002). The results displayed a close correspondence but not an identical geometry and stress distribution (Chau *et al.* 2004).

The combination of imaging and FEA is known as image guided modelling. A series of studies combining MRI and FEA have been conducted by Gillard et al. (Li *et al.* 2005, Li *et al.* 2007, Tang *et al.* 2008). The MRI image data was manually traced using segmentation software, distinguishing between vessel wall, lumen, lipid core and fibrous cap, depending on signal characteristics (Li *et al.* 2007). This technique was validated against the histological gold standard; Trivedi et al. (2004) conducted a comparison between the percentage areas occupied by each component of the total plaque area within the MRI slice against *ex vivo* stained histological sections. Some FSI models also incorporate image guided modelling to create patient specific geometries (Tang *et al.* 2004b, Gao *et al.* 2009).

1.6.2) Material Properties

The material properties of the artery wall are represented by a constitutive model and can be modelled to varying degrees of complexity. As discussed in section 1.5.1, the artery wall has heterogeneous, anisotropic, nonlinear, viscoelastic, incompressible properties and is also subject to residual stresses. With the exception of incompressibility, which actually simplifies matters, the inclusion or neglect of the remaining properties from constitutive models makes them more or less complex and more or less applicable. When choosing the appropriate constitutive model, it is often a trade-off between the complexity of the model, which effects computational memory and time requirements, and the accuracy of the results.

Unfortunately when dealing with the arterial wall, particularly ones containing atherosclerosis, simplifying the heterogeneous property whilst retaining any detail about the system, is not possible. Anisotropy, however, may be simplified to either transverse isotropy, or fully isotropic. Full isotropy assumes that the mechanical properties do not vary with direction. When a material is linearly elastic it is described as a Hookean Elastic Solid and when combined with isotropy, it may be defined by the Lamé shear and longitudinal parameters μ and λ (Fung 1993). Transverse isotropy, the assumption of symmetric isotropy, assumes that the mechanical properties in the axial and circumferential direction are the same, but vary in the radial direction (Loree *et al.* 1992, Cheng *et al.* 1993). Anisotropy, is clearly a very complex property to include, nevertheless Holzapfel et al. (2004a, 2004b, Gasser *et al.* 2006) have explored the characterisation and modelling of arterial anisotropy.

Arteries are hyperelastic (Holzapfel *et al.* 2000); they exhibit nonlinear behaviour at large strains (Bower 2010). However, although the stress-strain relationship of arterial tissue displays both nonlinearity and hysteresis, under preconditioned cyclic loading, it displays some pseudoelastic behaviours; approximately linear elastic behaviours through small cycle strains and small variation with strain rate (Fung *et al.* 1979, Fung 1993). These properties allow arteries to be defined by a function of the strain state, known as strain-energy density functions, a few of which are reviewed in (Holzapfel *et al.* 2000).

Relatively few papers in the area of arterial mechanics incorporate viscoelasticity; Holzapfel et al. (2001, 2004a) incorporate the effects in their advanced constitutive models. There are also only a few papers, characterising the viscoelastic properties of arterial walls and plaques (Bergel 1961a, Lee *et al.* 1991, Loree *et al.* 1994b, Valdez-Jasso *et al.* 2011) which is where the innovative technique of elastography, outlined in section 1.7, has the potential to expand this knowledge base.

1.6.3) Loads and Boundary Conditions

The loads used in FEA are often based upon simplifications of the pressures seen in the cardiac cycle, for example Cheng et al. (1993) who applied a very simple intraluminal pressure load of 110mmHg. More realistic loading utilises waveforms based on measurements of arterial pressure waves, combined with a mean, systolic or diastolic pressure (Zhao *et al.* 2002, Versluis *et al.* 2006). Of course the most sophisticated application of the waveform comes from the interactions within an FSI model where the pressure is applied on the fluid at the inlet of the artery (Gao *et al.* 2009).

The boundary conditions applied in FEA models of arteries are less exact. Some studies employ a selection of constrained nodes around the circumference of the plaque (Chau *et al.* 2004), or in 3D the inlet and outlet of the artery (Tang *et al.* 2004a).

1.7) Elastography

Changes in tissue elasticity are strongly associated with pathology; for example cancer, liver cirrhosis, normal pressure hydrocephalus and osteoporosis (Ophir *et al.* 1991, Li and Snedeker 2011, Streitberger *et al.* 2011). Where possible, palpation has been the standard method of assessing tissue elasticity for centuries; it is used both non-invasively and during surgery (Greenleaf *et al.* 2003).

Elastography is the term given to the quantitative imaging of strain or elastic modulus through tissue (Ophir *et al.* 1991). It is a relatively recent innovation and has seen a large amount of progress in the last two decades. The basic theory behind elastography is that the tissue response to an applied load will vary with the mechanical properties of the tissue. The mechanical properties can be solved for, if the load and response can be quantified. The methods of exciting the tissue can be divided into approximately into three types; static, dynamic and transient, although there are areas of overlap.

Current elastography research is hugely varied, encompassing different imaging modalities, load applications and post-processing techniques; researching the mechanical properties of a wide range of tissue types and organs. This section is going to discuss ultrasound and MRI techniques, with a focus on the applications of elastography to arteries and the combination of elastography and FEA.

1.7.1) Ultrasound Elastography

Ultrasound was the first modality to utilise elastography (Ophir *et al.* 1991). Out of all the modalities to incorporate the technique, ultrasound has the biggest literature base in arterial applications, of which there are several different methodologies. Ultrasound elastography techniques which utilise FEA as an inversion technique are discussed in section 1.7.4.

Initial applications of ultrasound to elastography utilised intravascular methods to obtain the higher levels of imaging accuracy afforded by proximity. To image arterial wall motion in response to a force, Intravascular Ultrasound Elastography (IVE) more often than not exploits the inherent dilation in response to the cardiac cycle however inducing strain using an intravascular balloon has been proposed (Choi *et al.* 2002). Mechanically the transducer is placed at the tip of the catheter and a cross-sectional image of the vessel is generated by sequentially sweeping the ultrasound beam over a 360^0 angle (Maurice *et al.* 2004a). The most common method of creating an intravascular elastogram is using a one dimensional (1D) cross-correlation technique to create a strain image from the displacement derivative (Maurice *et al.* 2008).

De Korte et al. used this methodology in a series of studies ranging from arterial phantoms (1997) to diseased coronary and femoral arteries *in vitro* (2000, Schaar *et al.* 2003) and coronary *in vivo* (2002). Maurice et al. suggested that using correlation techniques to assess tissue motion may not be optimal to investigate such complex strain patterns and they proposed the application of the Lagrangian speckle model estimator (LSME) (1999) offering 2D strain information (2008).

Non-invasive vascular elastography (NIVE) has some similarities to the image processing methods applied to IVE. Since IVE will always be limited to a certain extent by its invasive nature (De Korte *et al.* 2011), research in NIVE often follows on from work already conducted using IVE. The inherent difficulty with NIVE is that instead of imaging along the same axis as the strain, i.e. radially, the ultrasound beam propagates axially and thus is only parallel to the motion at angles 0^0 and 180^0 (Maurice *et al.* 2005). The effect of this is the presence of hardening and softening artefacts (Maurice *et al.* 2004b).

Kanai et al. (2003) proposed the phase tracking method, to image the elasticity of carotid atheroma, albeit only through a longitudinal section of the artery. De Korte et al. continued their work using the cross-correlation method to obtain phantom and *in vivo* carotid artery noninvasive strain elastograms, using interpolation (Ribbers *et al.* 2005) and beam steering (Hansen *et al.* 2009). Maurice et al. combined the LSME with NIVE and proposed the use of the Von Mises coefficient (2004b); applied to healthy and diseased carotid arteries in rats (2005).

Fatemi and Greenleaf (1998) presented the methodology of vibroacoustography in 1998, imaging excised iliac arteries. Vibroacoustography utilizes the oscillatory force created from the interference of intersecting continuous wave ultrasound beams (Fatemi and Greenleaf 1998). The resulting harmonic displacement is a function of the material properties and corresponding acoustic emission may be detected by a hydrophone (Greenleaf 2003). The distinct advantage that this methodology has over most other forms of elastography is that the interrogation is localised and thus the effect of boundary conditions are reduced. Fatemi and Greenleaf et al. have applied this technique to several more arterial applications; the femoral artery of a pig *in vivo* (1998), excised carotid arteries (2000), calcified arteries in breast tissue (Alizad *et al.* 2003) and PAD in porcine femoral arteries (Pislaru *et al.* 2008).

There is a transfer of momentum associated with an acoustic wave travelling through a medium; this arises from the absorption or reflection of the wave (Torr 1984). Acoustic radiation force imaging (ARFI) utilizes this transfer of momentum as a body force (Nightingale *et al.* 2002); where a short duration of acoustic radiation force otherwise known as a pushing pulse creates a displacement in the tissue which may be tracked spatially and temporally using ultrasonic correlation methods (Nightingale *et al.* 2002).

Trahey et al. have contributed a significant amount of research into the clinical feasibility of ARFI. Initial work focussed on the differentiation of breast tissue (Nightingale *et al.* 2001, Nightingale *et al.* 2002) however subsequent studies have included applications to arteries; diseased *ex vivo* femoral and popliteal arteries (Pinton *et al.* 2003) and *in vivo* carotid and femoral arteries (Trahey *et al.* 2003). Further validation work was conducted on *in vivo* and *ex vivo* diseased porcine arteries (Behler *et al.* 2006, Dumont *et al.* 2006, Behler *et al.* 2009) and *in vivo* feasibility was tested on the carotid atherosclerotic plaques and PAD (Dahl *et al.* 2009, Dumont *et al.* 2009).

1.7.2) Magnetic Resonance Elastography

Magnetic resonance elastography (MRE) has been combined with static, quasi-static and transient loads. However the most common form is dynamic MRE (Glaser *et al.* 2012) upon which this section shall focus. Low frequency mechanical shear waves, in the region of 10-1000Hz, are imaged as they propagate through the tissue (Manduca *et al.* 2001). Longitudinal waves are unsuitable for MRE since, through the almost incompressible medium of tissue, they are based upon the very high bulk modulus and thus propagate very quickly with an extremely long wavelength (Manduca *et al.* 2001). The temporal wave behaviour is imaged using PC-MRI at increasing time offsets from the beginning of the steady state wave cycle, coordinated by a trigger between the wave generator and operating station. MRE studies vary in terms of the method of wave excitation, the imaging methodology utilised, the algorithm used to invert the wave images into an image of stiffness, and the organ under analysis.

Magnetic resonance elastography has a much smaller body of literature in arterial applications than ultrasound elastography. Traditionally MRE has focussed on organs such as the liver (Klatt *et al.* 2006), brain (Sack *et al.* 2008) and breast (Sinkus *et al.* 2005). Although in recent years there has been a drive towards organs with added complexities such as motion, smaller size and boundaries; examples include the heart (Sack *et al.* 2009), lungs (Mariappan *et al.* 2011), prostate (Sahebjavaher *et al.* 2014) and arteries (Kolipaka *et al.*

2012). The technique of MRE shall be discussed in terms of its broader applications, with a focus on arterial research in section 1.7.3.

The MR Elastography Group, Charité Univesitätsmedizin Berlin, (Diagnostic and Interventional Radiology and Nuclear Medicine, Charitéplatz 1, 10117 Berlin), whose collaboration aided the set-up of the MRE facility at The University of Edinburgh, Clinical Research Imaging Centre, favour the mechanical method. Vibrations are generated in the MRI scanning room and transmitted via a piston and actuator attached around the organ of interest. The apparatus used at The University of Edinburgh can be seen in Figure 1.4. A diverse range of other wave excitation methods exist including pneumatic, electromagnetic and piezoelectric. Pneumatically, an active driver controls the wave generation remote to the MRI scanner and a passive driver distributes the waves to the organ of interest (Kolipaka *et al.* 2012). Electromagnetic actuators take advantage of the fixed magnetic field by passing an alternating current through a coil aligned with the bore, creating a torque that can be used to generate waves (Sinkus *et al.* 2000, Braun *et al.* 2003). Piezoelectric actuators create motion as the piezoelectric crystals expand under an applied electric voltage (Uffmann *et al.* 2002, Hirsch *et al.* 2014).

Figure 1.4: *Mechanical method of MRE wave excitation at The University of Edinburgh, Clinical Research Imaging Centre: sub-woofer, piston and MRI scanner.*

The detail behind MRE pulse sequences is complex and beyond the scope of this thesis; a good overview can be found in (Mariappan *et al.* 2010). Pulse sequences can be 1D, 2D or 3D and include a range of MRI techniques; gradient-echo, spin-echo, echo-planar and balanced steady-state free precession (Glaser *et al.* 2012). Conventional PC-MRI was overviewed in section 1.4.3 and MRE uses a similar technique. The excitation wave is synchronised with a motion encoding gradient (MEG) of the same frequency, creating a measurable phase shift proportional to the displacement (Manduca *et al.* 2001). The MEG can be through one, two or three dimensions simultaneously (Glaser *et al.* 2012) and the excitation frequency can be applied singularly or as a multi-frequency study (Klatt *et al.* 2007). The phase images of waves propagating through the ROI are inverted into an image of stiffness, known as an elastogram; examples through the aorta can be seen in Figure 1.5 in section 1.7.3.

Inversion algorithms are concerned with inverting the equations of motion, subject to various assumptions, and extracting the stiffness parameters. A few studies have compared the mechanical properties yielded by MRE and associated inversion alogorithms to mechanical testing (Hamhaber *et al.* 2003, Ringleb *et al.* 2005). The Helmholtz inversion algorithm is utilised in this thesis and the full derivation can be found in section 2.2.6.

The majority of inversion algorithms are based upon the equation of harmonic motion in an isotropic, linear, elastic solid equation 1.6; allowing a medium to be expressed in terms of the Lamé shear and longitudinal parameters μ and λ (Manduca *et al.* 2001). Where u is the displacement, ρ is the density and ω is the circular frequency. These equations may be solved using the variational method or finite element analysis (Romano *et al.* 1998, Van Houten *et al.* 1999).

$$\left[\lambda u_{j,j}\right]_{,i} + \left[\mu(u_{i,j} + u_{j,i})\right]_{,j} = -\rho\omega^2 u_i \tag{1.6}$$

Assuming homogeneity, removes the dependence on position and allows the Lamé parameters to be solved for locally (Manduca *et al.* 2001), by algebraic inversion of the differential equation, equation 1.7, (Oliphant *et al.* 2001).

$$\mu\nabla^2 \bar{u} + (\lambda + \mu)\nabla(\nabla \cdot \bar{u}) = -\rho\omega^2 \bar{u} \tag{1.7}$$

Equation 1.5 can be simplified further, in two ways. Either, under the assumption that λ is orders of magnitude larger than μ, allowing the compression wave to be removed via the curl operator (Sinkus *et al.* 2005). Or under the assumption that soft tissue is predominantly water based and therefore incompressible (Fung 1993); equation 1.7 may be simplified to the Helmholtz inversion algorithm 1.8 (Manduca *et al.* 2001). Application of this inversion algorithm requires the compressional wave component to be filtered out of the MRE data using bandpass filtering and the shear modulus and viscosity to be extracted using a viscoelastic model (Klatt *et al.* 2007).

$$\mu\nabla^2\bar{u} = -\rho\omega^2\bar{u} \tag{1.8}$$

The Local Frequency Estimation method introduces the assumptions of no attenuation and $\rho \approx 1000kgm^{-3}$ for soft tissues, simplifying the Helmholtz equation further to 1.9 (Braun *et al.* 2001, Manduca *et al.* 2001).

$$\mu = \frac{f^2_{mechanical}}{f^2_{spatial}} \tag{1.9}$$

1.7.3) Arterial Magnetic Resonance Elastography

Although arteries are natural wave guides and they could be described as well suited to analysis by dynamic elastography (Romano *et al.* 2005, Woodrum *et al.* 2006), the literature in the area of arterial MRE is sparse. Other inherent characteristics of arteries make the application of MRE challenging; imaging resolution and the thickness of the wall, the boundary with the lumen and the motion of the cardiac cycle in terms of interference with the excitation wave and imaging flow artefacts.

A few studies have broached imaging the mechanics of the artery wall using static MRE to image strain. Although not termed elastography, PC-MRI has been used to image strain in porcine and human aortas (Wedding *et al.* 2002, Draney *et al.* 2004) and using a black blood sequence to increase signal in the carotid wall (Nederveen *et al.* 2014). Franquet et al. (2013a) applied PC-MRI strain imaging in combination with FEA inversion to atherosclerosis in the carotid artery. Kates (2011) used FEA and arterial phantoms to demonstrate the application of static MRE in chronic total occlusions.

The first application of dynamic MRE, using external stimulation, to vessels was conducted by Woodrum et al. (2006); PC-MRI was used to visualize propagating mechanical waves along the longitudinal axis of arterial phantoms, *ex vivo* porcine aorta's and *in vivo* femoral arteries. The wavelengths were isolated by directional filtering (Manduca *et al.* 2003) and inverted using the Moens-Korteweg equation 1.1 (Woodrum *et al.* 2006). Phantoms containing stenoses were assessed using windowed spatial Fourier transforms to separate the displacements into incident and reflected waves (Woodrum *et al.* 2006). This work was continued in porcine aortas to investigate the *ex vivo* changes of stiffness induced by hypertension and formalin fixation (Woodrum *et al.* 2009, Xu *et al.* 2012) and recently progressed onto the stiffness of the *in vivo* abdominal aorta (Kolipaka *et al.* 2012, Xu *et al.* 2013). Figure 1.5 shows an example of the normotensive results, yielded by Kolipaka et al. (2012). Another dynamic approach to imaging arterial stiffness was proposed by Zheng et al. (2007) who employed twin drivers to create an interference shear wave pattern around the femoral artery.

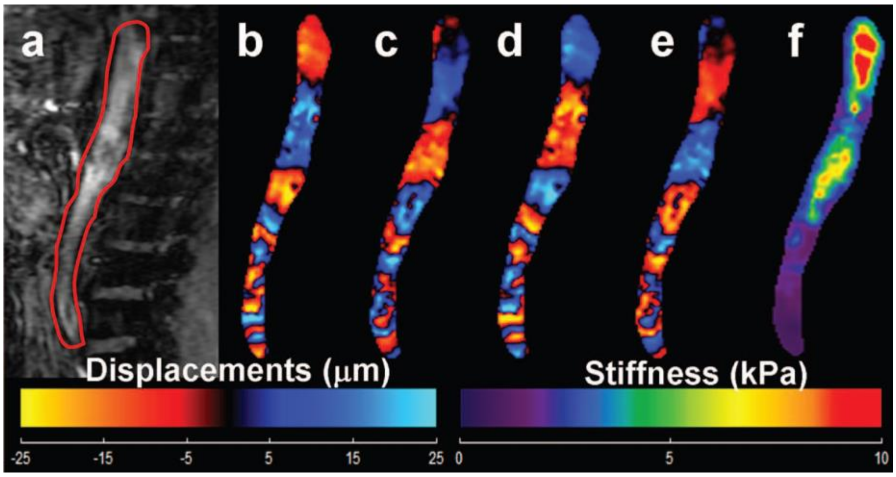

Figure 1.5: *Arterial MRE through the aorta of a normotensive volunteer. a) Sagittal slice of the aortic anatomy. b-e) Phase images of the in-plane wave component. f) Weighted stiffness map from three motion encoding directions. Reused with permission from John Wiley and Sons Ltd. (Kolipaka et al. 2012).*

1.7.4) Computational Modelling and Elastography

In this section the key studies will be overviewed, focussing on arterial applications, however the in depth details of the FEMs shall be omitted; as discussed in section 1.5, the number of variables in a computational model are extensive. FEA and elastography are combined over a range of imaging modalities for various purposes, primarily inversion of the displacement data.

Baldewsing et al. (2002, 2004a) initially used FEA to compare 2D IVUS strain elastograms through arterial phantoms and diseased coronary arteries with replicated ones from FEMs. Baldewsing et al. (2005, 2006, 2008) developed this research into an inversion tool for converting strain elastograms into an image of the Young's modulus, using a minimization algorithm between the IVUS strain image and a parameter based FEM. Vonesh et al. (1997) proposed a similar optimisation method to obtain a regional solution of the inverse problem on 3D IVUS data. This methodology was applied to porcine carotid atheromas (Chandran *et al.* 2003, Hamilton *et al.* 2005, Nagaraj *et al.* 2005). The IVE and NIVE work described in section 1.7.1 was also extended to include FEA inversions (Hansen *et al.* 2013, Bouvier *et al.* 2014).

Finite element analysis can also be used as an inversion algorithm in tandem with dynamic MRE, albeit to date technique has not been applied to arteries. Van Houten et al. (1999) proposed the subzone technique; a minimization algorithm was applied to a ROI divided into small overlapping subzones. This algorithm was tested on simulated and *in vivo* breast tissue (Van Houten *et al.* 2001, Van Houten *et al.* 2003). More recently this algorithm has been combined with a Rayleigh damped material model and applied to phantom and *in vivo* brain imaging (Petrov *et al.* 2012). Franquet et al. (2013a, 2013b) combined PC-MRI strain imaging with a FEA minimizing algorithm to calculate a local elastic modulus of the carotid artery wall, with and without atherosclerosis. Although not under the heading of elastography, the work of Bertoglio et al. (2014) proposed the combination of non-invasive 3D arterial image acquisition via MRI or CT with an FSI model subjected to physiological loads in order to solve the inverse problem.

Essentially studies using FEA to invert elastography data have similar methodologies, they are all concerned with solving the inverse problem based upon displacement data; several more studies have proposed FEA inversion techniques independent of an imaging method (Guo *et al.* 2010, Eskandari *et al.* 2011). FEA can also be combined with elastography for other purposes; to assess MRE inversion algorithms (Romano *et al.* 1998, Van Houten *et al.* 2001) sensitivity studies (Baldewsing *et al.* 2004b, Franquet *et al.* 2012, Doherty *et al.* 2013) and comparison with experimental work (Chen *et al.* 2006).

1.8) Thesis Outline

1.8.1) Critical Analysis and Projected Contribution

Reviewing the mechanics of plaque rupture, 1.2.4, and the current clinical diagnosis methods and surgical treatment thresholds, 1.3.1 and 1.3.2; it becomes apparent that there is a need for a more definitive diagnosis technique. The potential to contribute to this area of research has been identified; using MRE to image the mechanical properties of atherosclerotic plaques.

The application of MRE to arteries is currently extremely under-researched. Several studies have investigated MRE wave behaviour through the arterial wall (Woodrum *et al.* 2006, Zheng *et al.* 2007). This research field has recently progressed onto imaging the elasticity of the arterial wall both *ex vivo* (Woodrum *et al.* 2009, Xu *et al.* 2012) and *in vivo* (Kolipaka *et al.* 2012, Xu *et al.* 2013). The concept of applying MRE to atherosclerotic plaques has only been raised in terms of assessing stenosis size in arterial phantoms (Woodrum *et al.* 2006). Therefore computational simulations and the experimental application of MRE to atherosclerosis in phantoms and patients are all novel contributions to this area of research.

This proposal also introduces some significant complications over current MRE applications; the lumen boundary, inhomogeneities, the small size of the plaque and the motion from the cardiac cycle. Some of these difficulties are tackled in recent areas of MRE research (Sack *et al.* 2009, Kolipaka *et al.* 2012, Klein *et al.* 2014) but not simultaneously. Computational modelling offers a powerful tool to approach some of these problems and assess their impact. A method of simulating MRE using a steady state analysis through a 3D linear, viscoelastic tissue is presented. The accompanying parameter assessment is a novel contribution to the field of computational MRE. Only a few other studies have investigated the impact of computational parameters on simulated MRE, using implicit and transient analyses through linear elastic mediums (Chen *et al.* 2005, Chen *et al.* 2006, Leclerc *et al.* 2013).

The MRE simulation technique is then applied to assess changes in the wave images, elastograms and local average predicted shear modulus with atherosclerotic disease development. In addition a sensitivity study on the technique parameters is conducted, prior to time consuming and expensive experimental studies.

Moving into an experimental environment, arterial phantoms give the opportunity to develop this work, whilst neglecting some of the inherent complications of imaging arteries *in vivo*.

A method of creating vessels containing 3D plaques of various size and stiffness is outlined, followed by MRE imaging of atherosclerotic plaque phantoms. These phantoms are replicated in an MRE simulation to compare the experimental and computational results; offering insight into the realism of the computational work and the potential for improving the experimental methodology.

Finally to assess the feasibility of progressing this research clinically, healthy volunteers and preliminary patient studies were imaged. Whilst using MRE to image the walls of the aorta in healthy volunteers and hypertensive patients has been conducted (Kolipaka *et al.* 2012, Xu *et al.* 2013), the application of MRE atherosclerotic plaques in peripheral artery disease patients is unique.

1.8.2) Aim and Objectives

The aim of this thesis is to investigate the application of magnetic resonance elastography to image the mechanical properties of atherosclerotic plaques.

The aim shall be undertaken using the following series of objectives:

1) Develop a method of computationally simulating MRE using 3D FEA.
2) Conduct a computational sensitivity study on the geometric, mechanical, imaging and inversion parameters of MRE applied to idealised atherosclerotic plaques.
3) Design a series of arterial phantoms with variable plaque size and stiffness, to aid experimental validation of the technique.
4) Test the experimental feasibility of the technique on arterial phantoms; gain insight on both the experimental and computational work by comparison with replicated simulations.
5) Conduct an *in vivo* feasibility study on healthy volunteers and PAD patients.

1.8.3) Thesis Structure

Chapter 1 gave an overview of cardiovascular disease, focussing on atherosclerosis; how the disease develops, the clinical diagnosis and treatment methods. Imaging methods, relevant to clinical and research based imaging of the artery wall, were discussed. The methodologies used to measure and model the biomechanical properties of the artery wall were outlined, with an emphasis on elastography. The potential to contribute within the area of MRE research was identified; a computational and experimental feasibility study of the applicability of using this technique to image atherosclerotic plaques. Finally the thesis aims and objectives were discussed, followed by a breakdown of the thesis structure.

The purpose of Chapter 2 is to assess the purely computational variables in a very simple simulation of MRE; the simulation type, material properties, the element length and in tandem the imaging pixel size. This chapter will create a firm foundation for the computational sections of the thesis, ensuring that the proposed technique can give accurate results.

Chapters 3 and 4 will address the sensitivity of the geometric, mechanical, selected imaging and inversion parameters in a simulation of MRE through idealised atherosclerotic plaques. The purposes of these chapters are to assess the proposed hypothesis in an idealised environment and to ascertain what the ideal parameters of the technique are in advance of moving into the experimental field. Chapter 3 focusses on the wave response of the simulation, omitting the inversion algorithm. The parameters under observation are predominantly the geometric plaque and mechanical variables. Chapter 4 extends this work to incorporate the inversion algorithm and the additional imaging, inversion and plaque composition variables.

Chapter 5 describes the manufacture of a range of arterial phantoms containing plaques of various stenosis sizes and stiffnesses. These phantoms were imaged using MRE as a intermediate step between the computational and *in vivo* work; allowing the technique to be assessed in a more realistic manner without the additional complications of physiological motion. Chapter 6 is a computational replica of Chapter 5, comparison of the results from both chapters will give insight into the realism of the simulations and how the experimental results could be improved under idealised conditions.

The technique is developed and assessed through healthy volunteers and peripheral artery disease patients in Chapter 7. This chapter will allow the complications of *in vivo* arterial MRE imaging to be fully assessed.

Chapter 8 provides a summary of the thesis; allowing the results to be discussed as a whole and the impact of this research on the field to be assessed.

Chapter 2

Simulating Magnetic Resonance Elastography

2.1) Introduction

The concept of simulating MRE is based around replacing MRI with FEA. Using FEA to simulate MRE is fairly common practise in the literature, to assess excitation type (Sinkus *et al.* 2000), frequency (Chen *et al.* 2005) and to test inversion algorithms (McGarry and Van Houten 2008, Kolipaka *et al.* 2009, McGee *et al.* 2011, Clayton *et al.* 2013).

Computational modelling introduces a range of parameters that are not present in experimental MRE, outlined in Table 2.1. The accuracy of the technique can vary depending on the chosen computational parameters. Whilst a precise representation of a realistic system is desired, the technique needs to maintain reasonable simulation run times and memory usage. It is important to investigate the impact of any simplifications in the simulation and the sensitivity of the results to variations in the computational parameters in order to assess the validity of using FEA to simulate MRE. Before progressing on to simulating MRE through atherosclerotic plaques, a sensitivity study shall be conducted on a simple homogeneous block of tissue, to remove any additional complications created by physiological geometries.

There are relatively few papers evaluating the sensitivity of the computational parameters in MRE simulations. Leclerc et al. (2013) compared the wave displacement through phantoms and simulated replicas with variations in mesh density, poisons ratio and density using a 3D linear elastic, dynamic implicit analysis. Chen et al. (2005, 2006) studied the change in wavelength, through a 2D axisymmetric, linear elastic, transient simulation with material properties, element type, excitation frequency, boundary conditions, and pre-tension.

This chapter outlines an implicit and steady state analysis through a 3D linear, viscoelastic homogeneous block of tissue. The aim is to assess the effect of varying the analysis type, material properties, element and pixel size on the predicted shear modulus and viscosity in simulated MRE and in tandem identify the limitations of this technique.

2.2) Method

2.2.1) Overview

The most efficient way of demonstrating the differences and similarities between experimental MRE and a simulated procedure is to compare the methodology in a flow chart, Figure 2.1. In a computational simulation the displacement data, describing the propagation of harmonic waves through the tissue, is provided by FEA as opposed to MRI. Figure 2.1 shows that at a certain point, marked with a dashed line, both the experimental and computational techniques have the same methodology.

The parameters which affect experimental and simulated MRE are outlined in Table 2.1. These include variables with respect to FEA, the mechanical waves, MRI, the wave inversion algorithm and the region of interest. The parameters have been grouped into purely computational, which are unique to a simulation of MRE, and those which would affect both a computational and experimental MRE study. This chapter shall assess the accuracy of some of the variables chosen to create a FEA; primarily the ones involved in a purely computational simulation of MRE. The sensitivity of the results to the analysis type, material properties and element and pixel size shall be investigated.

The raw data from experimental MRE and the input into the inversion algorithm is in the form of phase with units of radians. The raw data from simulations and the input into the inversion algorithm of the computational methodology is in the form of displacement. The phase of the complex wave image Φ and the wave amplitude A are proportional via equation 2.1, (Klatt 2010). ω, γ, K_0 and q refer to the excitation frequency, gyromagnetic ratio, motion encoding gradient frequency and number of motion encoding gradient cycles, respectively.

$$A = \Phi \frac{\omega}{2\pi\gamma K_0 q} \tag{2.1}$$

The stiffness of the medium changes the wavelength and speed. The amplitude of the wave does not affect the predicted stiffness yielded by the inversion algorithm. The experimental complex wave image, displayed in radians and the computational complex wave image, displayed in microns will be compared directly in this thesis.

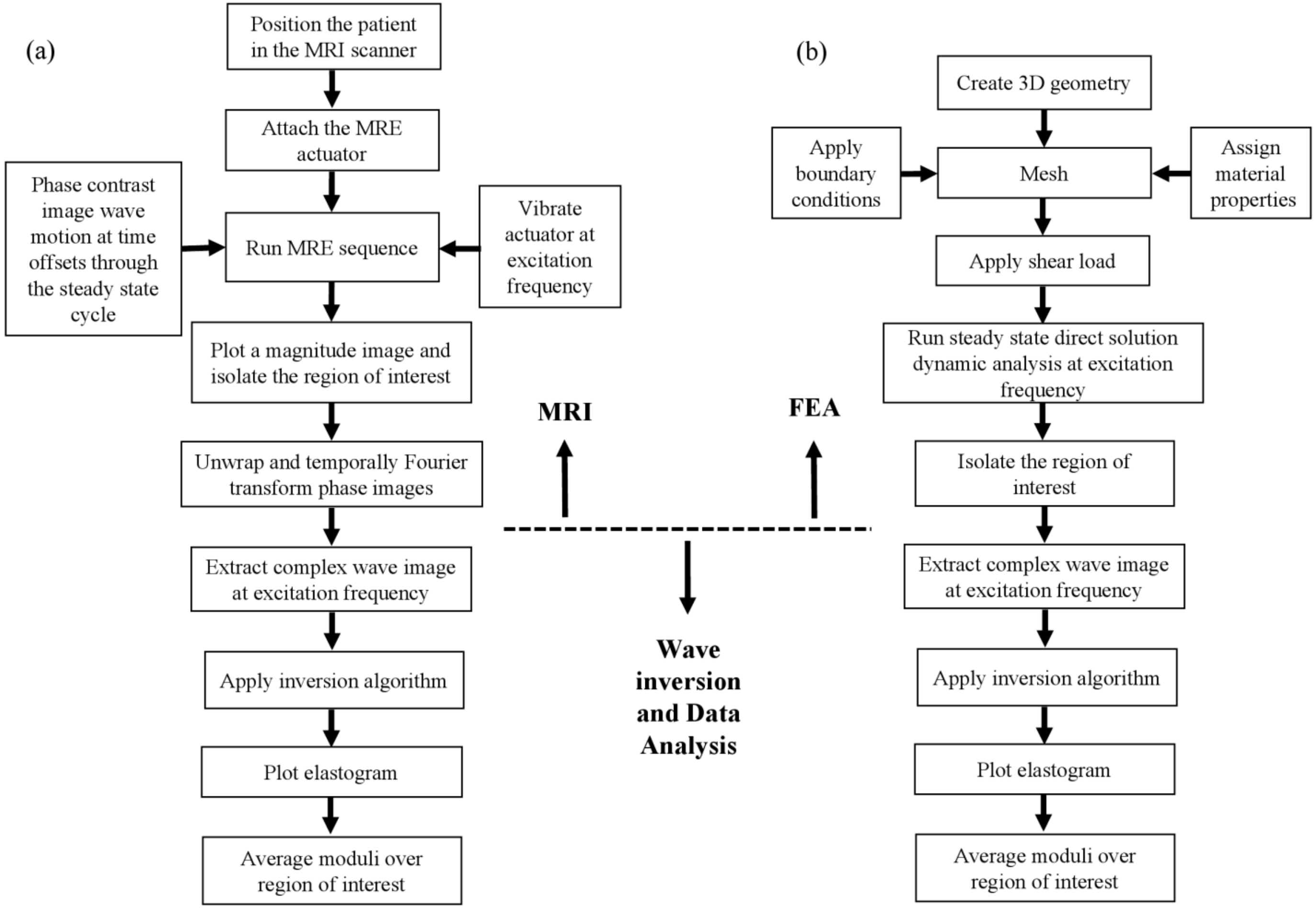

Figure 2.1: *MRE flow chart (a) experimental methodology and (b) computational methodology.*

Computational	**Experimental and Computational**			
FEA	**Mechanical Waves**	**MRI**	**Wave Inversion**	**ROI**
Analysis type	Frequency	Imaging plane	Algorithm	Geometry
Mesh density	Load amplitude	Pixel resolution	Filter type and thresholds	Tissue type
Element type	Load direction	Imaging/ Artificial noise		Physiological loads
Material properties				Surrounding tissue geometry and type
Boundary conditions				

Table 2.1: *Experimental and computational MRE parameters.*

For the purpose of this chapter, each parameter shall be assessed in isolation and all other parameters will be fixed. The material properties, display a dependence on the choice of rheological model, discussed in section 2.2.4. In this chapter, the Voigt model was employed to synchronise with its use in the inversion algorithm. The discretization of the wave depends upon the mesh element length and pixel size, thus both are investigated simultaneously. Artificial noise shall be omitted in this chapter and assessed in Chapter 4, where the filters in the inversion algorithm will be adjusted to compensate.

The model geometry was created and the finite element analysis was conducted using the software Abaqus/CAE version 6.10-1 (Dassault Systèmes, Simulia Corp., Providence, Rhode Island, USA). The code for the wave inversion algorithm was supplied by collaborators at the MR Elastography Group, Charité Univesitätsmedizin Berlin (Diagnostic and Interventional Radiology and Nuclear Medicine, Charitéplatz 1, 10117 Berlin). The data was formatted using Excel, (Microsoft Office, Microsoft Corporation, Microsoft UK Headquarters, Reading, UK) and the inversion algorithm was run on the programming software MATLAB R2011a, (MathWorks, Natick, Massachusetts, USA).

2.2.2) Fixed Simulation Parameters

All the geometry used in the following models was meshed using hybrid, linear, hexahedra elements; the advised element when dealing with incompressible or almost incompressible material properties (Dassault Systèmes Simulia Corp. 2010c). A tissue density of 1047kgm^{-3} was assigned; approximately average for soft tissue (Hoskins 2010).

To avoid the complications of wave interference caused by reflections at the edge of the model, boundary conditions were chosen to simulate the continued propagation of the waves beyond the model. Simple non-reflecting constraints were achieved by applying symmetric boundary conditions, with reference to the perpendicular axis, on all the outer faces of the surrounding tissue except the one to which the external load was applied.

2.2.3) Simulation Type

In experimental MRE the complex wave image, required as the input to the inversion algorithm, is generated by temporally Fourier transforming phase contrast images, taken at different time offsets through the steady state cycle (Klatt *et al.* 2007). The experimental technique is described in more detail in section 5.2.7. Simulating a steady state response in FEA is relatively simple; it yields the required complex wave image at the excitation frequency. A direct solution steady state dynamic analysis has the potential to provide a time efficient method of simulating the displacement data required for input into the wave inversion algorithm. To ensure that this simplification is applicable and does not limit the accuracy of the technique, two analysis types were compared; an implicit dynamic analysis and the steady state dynamic analysis.

The implicit dynamic analysis was used to simulate the propagation of waves through the tissue with time. The implicit Hilber-Hughes-Taylor operator was used to iteratively integrate the equations of motion over each time step (Dassault Systèmes Simulia Corp. 2010b). This operator is unconditionally stable for linear systems (Dassault Systèmes Simulia Corp. 2010b). Extracting the wave motion at a series of equally spaced time steps is analogous to imaging the propagation of waves through the tissue in experimental MRE. The analysis was run for a total time of 0.5 seconds, with displacement images extracted at 8 time offsets through each wave cycle. The analysis was run using a fixed time increment of

$3.125e^{-4}$ seconds. Through repeated simulations, this time step was found to be sufficiently small to give accurate results, whilst also analysing at the required time points.

The second simulation employed the direct solution steady state dynamic analysis; providing the amplitude and phase of the linear response of a structure under harmonic excitation (Dassault Systèmes Simulia Corp. 2010b). This simulation is a perturbation procedure, where the steady state response is calculated from the systems physical degrees of freedom using the mass, damping and stiffness matrices (Dassault Systèmes Simulia Corp. 2010b). The real and imaginary components of the complex wave image were extracted at the excitation frequency. The other computational parameters varied within the chapter remained fixed and are summarised in Table 2.2.

	Variable Parameters				
Parameter of Interest	**Simulation Type**	**Shear Modulus (kPa)**	**Shear Viscosity (Pas)**	**Element Size (mm^3)**	**Pixel Size (mm^2)**
Simulation Type	Implicit	3	1	1	1
	Steady State	3	1	1	1
Material Properties	Steady State	0.5 – 3.5	0.5 - 3.5	1	1
Element and Pixel Size	Steady State	3	1	0.5 - 2	0.5 - 2

Table 2.2: *Variable computational parameters: homogeneous tissue.*

The model geometry was a block with the following dimensions; 80mm height, by 80mm width by 50mm depth. The mesh was constructed from $1mm^3$ elements. This element size was applied because the implicit analysis was too computationally heavy to process at finer mesh density.

A simple isotropic, linear viscoelastic medium was employed with a shear modulus of 3kPa and shear viscosity of 1Pas. The dynamic shear modulus was modelled using the Voigt rheological model, equations 2.15 and 2.18, as per the rheological model used in the inversion algorithm, section 2.2.6. For the purpose of assessing the accuracy of the simulation type the tissue was modelled as almost incompressible with a Poisson's ratio of

0.49. This was done to avoid the complication of volumetric locking in the implicit analysis (Dassault Systèmes Simulia Corp. 2010c). The details of the material models will be expanded upon in section 2.2.4.

A cyclic, sinusoidal load of amplitude 3×10^{-4}N was applied to a selection of nodes on the upper surface of the model to mimic the load applied by an MRE actuator. The load was applied in the Z direction, to create a shear wave, at a frequency of 100Hz. The model axes, geometry, mesh and highlighted load nodes can be seen in Figure 2.2.

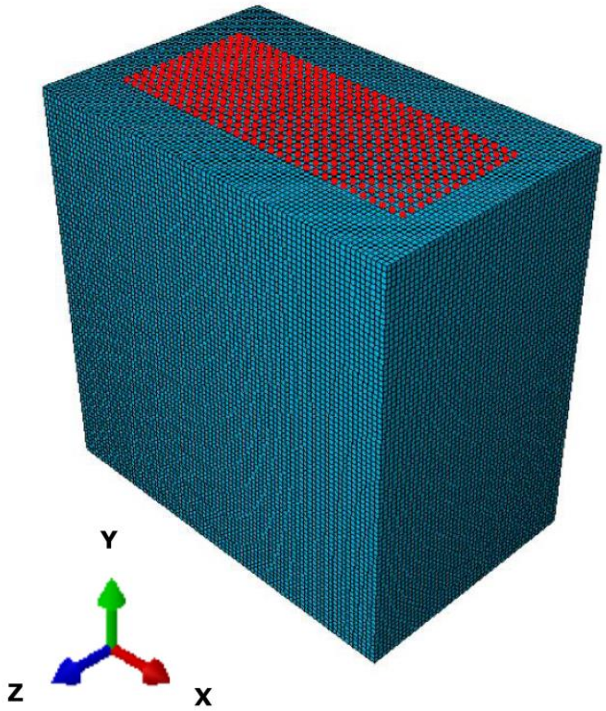

Figure 2.2: *Homogeneous tissue model (80mm x 80mm x 50mm) axes, geometry, mesh and load nodes.*

Results were extracted through a 64 by 64 matrix, in an X-Y plane through the centre of the block corresponding to the region of interest. A pixel size of 1mm^2 was chosen to give an element to pixel ratio of 1. In the implicit analysis, displacement images were taken at 8 time offsets through the wave cycle. These wave images were Fourier transformed with respect to time, yielding a series of complex wave images. The image corresponding to the excitation frequency was taken as the input to the inversion algorithm. To ensure that the images were obtained at steady state, a set of results were taken on the following wave cycles; 8th, 16th, 24th, 32nd, 40th and 48th. In the steady state dynamic analysis, the complex displacement results were taken from the analysis conducted at the excitation frequency.

The inversion algorithm, to be discussed in section 2.2.6, was applied to the complex wave image. Since any difference in the results from these simulations would be visible in the displacement results, the two analysis types were compared using the complex wave images, shear modulus and viscosity images, known as elastograms, as well the averaged moduli values.

2.2.4) Material Properties

In the simulations comparing the implicit and steady state analysis types, the Poisson's ratio was set at 0.49, to model an almost incompressible tissue without creating volumetric locking (Dassault Systèmes Simulia Corp. 2010c). The tissues in all other steady state simulations were modelled as incompressible; an assumption which is made applicable by the high water content of soft tissue (Fung 1993) and one that is also used again in the inversion algorithm (Manduca *et al.* 2001). The Poisson's ratio for these simulations was therefore set as 0.5.

Both the inversion algorithm and the material properties in the FEM were based upon the constitutive relationship of an isotropic Hookean Elastic Solid (Fung 1993, Manduca *et al.* 2001). Where the stress tensor, σ_{ij}, and strain tensor, ε_{ij}, are linearly proportional via equation 2.2 (Fung 1993).

$$\sigma_{ij} = \lambda\varepsilon_{\alpha\alpha}\delta_{ij} + 2\mu\varepsilon_{ij} \tag{2.2}$$

$$\delta_{ij} = \begin{cases} 1 & if \quad i = j \\ 0 & if \quad i \neq j \end{cases} \tag{2.3}$$

δ_{ij} is the Kronecker delta, defined by equation 2.3. λ is known as the first Lamé parameter, the second Lamé parameter is often called the shear modulus and denoted as μ. Expanding equation 2.2, into x, y, z, Cartesian coordinates yields equations 2.4 to 2.9 (Fung 1993).

$$\sigma_{xx} = \lambda(\varepsilon_{xx} + \varepsilon_{yy} + \varepsilon_{zz}) + 2\mu\varepsilon_{xx} \tag{2.4}$$

$$\sigma_{yy} = \lambda(\varepsilon_{xx} + \varepsilon_{yy} + \varepsilon_{zz}) + 2\mu\varepsilon_{yy} \tag{2.5}$$

$$\sigma_{zz} = \lambda(\varepsilon_{xx} + \varepsilon_{yy} + \varepsilon_{zz}) + 2\mu\varepsilon_{zz} \tag{2.6}$$

$$\sigma_{xy} = 2\mu\varepsilon_{xy} \tag{2.7}$$

$$\sigma_{yz} = 2\mu\varepsilon_{yz} \tag{2.8}$$

$$\sigma_{yz} = 2\mu\varepsilon_{yz} \tag{2.9}$$

The Lamé parameters are related to the Young's Modulus, E, Bulk Modulus, K, and Poisson's Ratio, υ, by equations 2.10 and 2.14 (Fung 1993).

$$\lambda = \frac{E\upsilon}{(1+\upsilon)(1-2\upsilon)} \tag{2.10}$$

$$\mu = \frac{E}{2(1+\upsilon)} \tag{2.11}$$

$$\upsilon = \frac{E}{2\mu} - 1 \tag{2.12}$$

$$E = 2\mu(1+\upsilon) \tag{2.13}$$

$$K = \frac{E}{3(1-2\upsilon)} \tag{2.14}$$

All biological tissues are viscoelastic (Fung 1993); the existence of elastic and viscous properties in a material (Barnes *et al.* 1989). Deformation in viscoelastic materials show a dependence on the rate of strain, leading to properties such as stress relaxation, creep and hysteresis (Fung 1993). Under an oscillatory load the viscoelasticity of a material may be expressed in terms of the dynamic shear modulus, G; incorporating the effect of both the elastic shear modulus, μ, and the viscosity, η, of the tissue. The dynamic shear modulus is composed of the real storage modulus, G', and imaginary loss modulus, G'', equation 2.15 (Sack *et al.* 2008), where these moduli are related to amplitude of the complex modulus, $|G|$, and phase by which the strain lags the stress, δ, by equations 2.16 and 2.17 (Fung 1993). δ is known as the loss angle.

$$G = G' + iG'' \tag{2.15}$$

$$G' = |G|\cos\delta \tag{2.16}$$

$$G'' = |G|\sin\delta \tag{2.17}$$

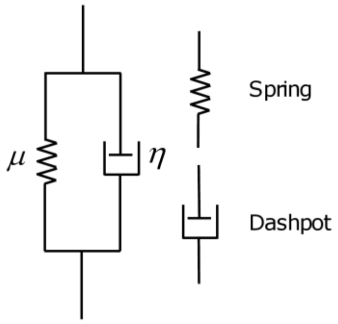

Figure 2.3: *Voigt viscoelastic model.*

The Voigt model, equation 2.18 was used to model the shear modulus and viscosity in the computational model and then again to extract them during the inversion algorithm (Klatt *et al.* 2007). The Voigt model is composed of a spring and dashpot in parallel, Figure 2.3; where the shear modulus is acting directly on the displacement and the viscosity on the velocity (Fung 1993). The applicability of rheological models shall be discussed in section 3.2.3.

$$G(\omega) = \mu + i\omega\eta \tag{2.18}$$

The shear modulus and viscosity were varied through the ranges outlined in Table 2.3, based approximately on values reported by previous MRE literature in healthy liver, breast and brain and liver tissue (Sinkus *et al.* 2005, Klatt *et al.* 2007, Sack *et al.* 2008).

Shear Modulus (kPa)	Shear Viscosity (Pas)	Load (N)
0.5 – 3.5	1.0	$1x10^{-4}$ – $3x10^{-4}$
3.0	0.5 – 3.5	$2.25x10^{-4}$ – $6.75x10^{-4}$

Table 2.3: *Material properties and load variables: homogeneous tissue.*

The ratio of shear modulus to shear viscosity and consequently the ratio of storage to loss modulus ratio, for a viscoelastic material can vary between the extremes of an elastic solid and viscous liquid (Barnes *et al.* 1989). Under a small-amplitude oscillatory shear load, the phase of the stress is in advance of the strain by the loss angle δ; dependent on the ratio of the loss modulus to storage modulus, equation 2.19, (Barnes *et al.* 1989). When the phase, δ, is 0º the response is purely elastic, and when the phase is 90º the response in purely viscous (Barnes *et al.* 1989). The ratio of the viscoelastic properties discussed in this chapter generally falls towards the elastic solid end of this range. However as the shear viscosity increases with respect to the shear modulus, δ increases and the properties of the material tend towards the viscous liquid end of the range. This results in increased attenuation.

$$\tan\delta = \frac{G''(\omega)}{G'(\omega)} = \frac{\eta\omega}{\mu} \tag{2.19}$$

The viscoelastic properties were programmed into the simulation using ratios of the shear storage and loss moduli, to the long-term shear modulus. Since the storage modulus has no dependence on frequency in the Voigt model, the long-term moduli are equal to the storage moduli, G_∞ = G’ and K_∞ = K’, with the bulk moduli approaching infinity due to the incompressible nature of the tissue.

The model geometry was the same as section 2.2.3; 80mm height, by 80mm width by 50mm depth with a 1mm^3 mesh. A sinusoidal load was applied at 100Hz however the magnitude, applied at the nodes highlighted in Figure 2.2, was adjusted slightly to compensate for the variation in stiffness and to induce similar deformations in each simulation, Table 2.3. The material properties validation was conducted using the steady state dynamic analysis.

The results were extracted on a 2D 64 x 64 matrix, in the X-Y plane centred on the origin, with a pixel size of 1mm^2. The inversion algorithm, to be discussed in section 2.2.6, was applied and the accuracy of the material model was assessed through wave images and elastograms and by comparing the predicted versus actual shear modulus and shear viscosity through a range of values.

2.2.5) Element and Pixel Size

The mesh has to be sufficiently fine so that the predicted stiffness will be independent of small changes in the mesh that will occur naturally with changes in the geometry in the more complicated arterial simulations. However in the proposed arterial application both the element and pixel size are relatively constrained. The plaque geometry is intricate and by default requires quite a fine mesh in order to resolve it. Yet a fine density can only be applied where necessary otherwise the simulations will require overly large computational resources.

The computational MRE technique intrinsically links the element size and pixel size; the meshing procedure and wave image extraction discretise the continuous waveform. The pixelated extraction of the results from the FEM is synonymous with resolution of MRI. The resolution of MRE is one of the parameters which make the applicability of the imaging technique to arteries, very difficult. Whilst computational simulations allow the technique to be idealised and remove the complication of imaging resolution, the chosen pixel size needs to remain within a realistic range.

To accommodate the smaller mesh densities and keep the simulation memory requirements reasonable, the model geometry had to be changed; 40mm height, by 40mm width by 40mm depth. The element size was varied between 0.5mm^3 and 2mm^3 and where the element size could not be fitted exactly within the model geometry, for example 0.75mm^3, a slightly larger model was created.

Simple isotropic, linear viscoelastic material properties were applied; a shear modulus of 3kPa and shear viscosity of 1Pas. The tissue was modelled as incompressible with a Poisson's ratio of 0.5. Similar to the model shown in Figure 2.2, the cyclic, sinusoidal load with a magnitude of $3\text{x}10^{-4}$N was applied to the upper surface nodes in the Z direction, at a frequency of 100Hz.

Results were extracted through a 32mm by 32mm ROI through the centre of the model in the X-Y plane. The pixel size was varied through 0.5mm^2 and 2mm^2, and where the pixel size could not correspond exactly with the ROI, for example for the 1.5mm^2 pixels, a fractionally larger region of interest was used. Similarly the load nodes could not be matched exactly between all simulations, due to the variation in meshes, however the same number across the same approximate surface area were utilised.

The element and pixel size study was conducted using the steady state analysis. The wave images, elastograms and averaged shear moduli for a range of element-pixel ratios were compared.

2.2.6) Image Processing

A variety of methods used to invert wave images into elastograms were discussed in section 1.7.2. The inversion algorithm utilised in this thesis is based upon the Helmholtz equation. A flow chart of the technique, applicable to experimental and computational wave images, is displayed in Figure 2.4. The full Matlab code for the inversion can be seen in Appendix A.

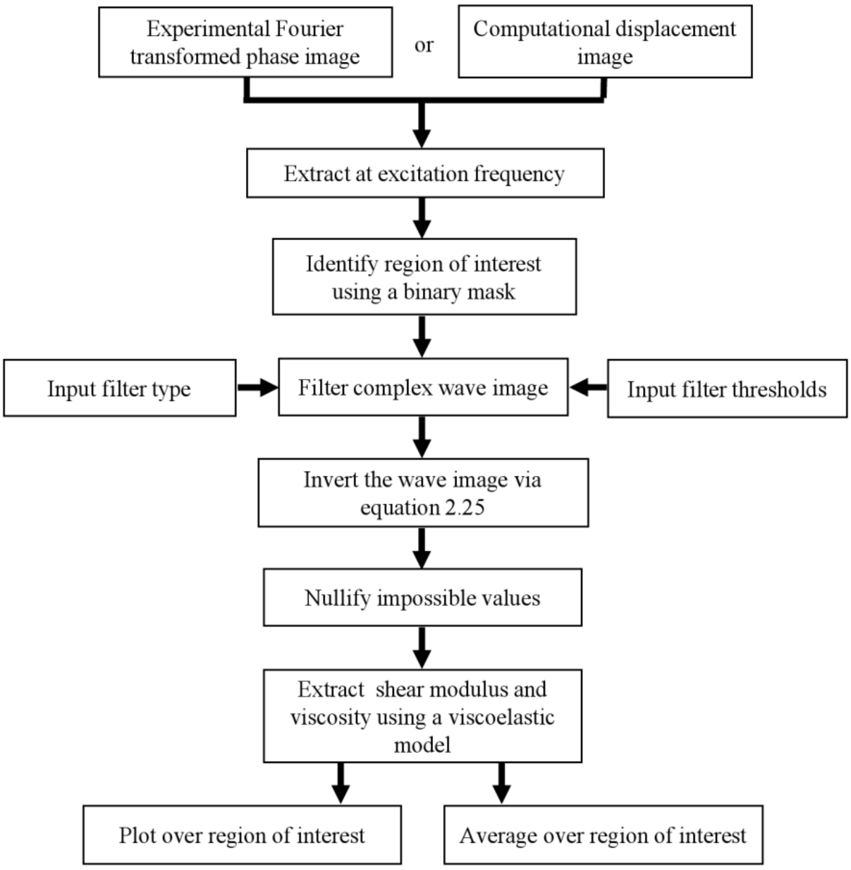

Figure 2.4: *Flow chart of the inversion methodology.*

The input to the algorithm is in the form of a complex wave image corresponding to the excitation frequency, either experimentally in units of phase or computationally in units of displacement. As described in section 2.2.3 in a computational simulation of MRE this complex wave image can be extracted directly from a steady state dynamic analysis. This data is imported into and formatted in Excel before being imported again into Matlab. Normally a binary mask is used to isolate the region of interest, however the complex wave images analysed in this chapter do not require segmentation, since the image data is taken from a simple square ROI within a block of homogeneous tissue. Prior to the inversion, the algorithm normally uses a highpass filter to remove compression wave components and a low pass filter to remove noise from the complex wave image (Klatt *et al.* 2007). However these filter thresholds may be highly tailored to the application and this can result in over idealised wave images; this phenomena is investigated in Chapter 4. Since the waves images in this chapter are simple, idealised and noise free, and the excitation method is primarily shear, allowing the effect of the compressional Lamé parameter to be neglected (Mariappan et al., 2010), the filtering step of the inversion algorithm was omitted.

The derivation of the inversion algorithm, adapted from (Manduca et al., 2001), begins with the constitutive relationship of an isotropic Hookean Elastic Solid, equation 2.2 (Fung 1993, Manduca *et al.* 2001), previously described in section 2.2.4. Where δ_{ij} is the Kronecker delta, defined by equation 2.3, and the Lamé parameters λ and μ have a complex form, where the imaginary part is related to the attenuation of tissue (Manduca *et al.* 2001). The complex form of μ shall be referred to as G. Inserting equation 2.2 into the equation of motion 2.20 (Skovoroda *et al.* 1994), with the strain tensor expressed in terms of displacement, $u_{i,j}$, equation 2.21, and neglecting body forces, f_i, yields equation 2.22; for harmonic motion in a linearly elastic medium (Manduca *et al.* 2001). The tissue density is denoted by ρ and the angular frequency of the excitation wave by ω.

$$\sigma_{ij,j} + f_i = \rho \frac{\partial^2 u_i}{\partial t^2} \tag{2.20}$$

$$\varepsilon_{ij} = \frac{(u_{i,j} + u_{j,i})}{2} \tag{2.21}$$

$$\left[\lambda u_{j,j}\right]_{,i} + \left[G(u_{i,j} + u_{j,i})\right]_{,j} = -\rho\omega^2 u_i \tag{2.22}$$

The components of equation 2.22 are coupled and therefore require the full 3D displacement field to solve (Manduca *et al.* 2001). Assuming local homogeneity simplifies the Lamé parameters from functions of position to single unknowns, which in turn simplifies equation 2.22 to equation 2.23 (Manduca *et al.* 2001), where ∇^2 is the Laplacian operator.

$$G\nabla^2 \bar{u} + (\lambda + G)\nabla(\nabla \cdot \bar{u}) = -\rho\omega^2 \bar{u} \tag{2.23}$$

Soft tissue has a very high water content, therefore can be assumed to be incompressible (Fung 1993). The assumption of incompressibility $(\nabla \cdot \bar{u} = 0)$ simplifies equation 2.23 to the Hemholtz equation 2.24, where the orthogonal directions have been decoupled effectively allowing the second Lamé parameter or dynamic shear modulus, G, to be solved for using one direction (Manduca *et al.* 2001). The use of the incompressibility assumption requires either the compression wave components to be filtered out of the wave image or purely shear wave excitation.

$$G\nabla^2 u = -\rho\omega^2 u \tag{2.24}$$

In summary, the equation of motion for harmonic waves, under the assumptions of isotropy, homogeneity, incompressibility, linear elasticity and in the absence of body forces is called the Helmholtz equation (Manduca et al. 2001). Temporally Fourier transforming a 2D scalar wave field u(x, y, t) to U(x, y, ω) and inverting the Helmholtz equation yields the 2D Helmholtz Inversion equation 2.25, used in this research (Klatt et al. 2007).

$$G(\omega) = \frac{-\rho\omega^2 U}{\nabla^2 U} \tag{2.25}$$

$$\nabla^2 U = \frac{\partial^2 u}{\partial x^2} + \frac{\partial^2 u}{\partial y^2} \tag{2.26}$$

Within equation 2.25 the density, ρ, and excitation frequency, ω, are scalar quantities. The Fourier transformed displacement, U, and the Laplacian, $\nabla^2 U$, are 2D matrices. The Laplacian, which can be expressed by equation 2.26, is a second order spatial derivative calculated from the displacement gradients surrounding the pixel of interest; equations 2.27 to 2.30.

$$\frac{\partial u}{\partial x} = \frac{u_{i+1} - u_{i-1}}{2dx} \tag{2.27}$$

$$\frac{\partial^2 u}{\partial x^2} = \frac{\left(\frac{\partial u}{\partial x}\right)_{i+1} - \left(\frac{\partial u}{\partial x}\right)_{i-1}}{2dx} \tag{2.28}$$

$$\frac{\partial u}{\partial y} = \frac{u_{j+1} - u_{j-1}}{2dy} \tag{2.29}$$

$$\frac{\partial^2 u}{\partial y^2} = \frac{\left(\frac{\partial u}{\partial y}\right)_{j+1} - \left(\frac{\partial u}{\partial y}\right)_{j-1}}{2dy} \tag{2.30}$$

Using generic tensor notation, Figure 2.5(a) shows how these are calculated in 1D and Figure 2.5(b) expands this to a 2D analysis. Figure 2.5 demonstrates how the Laplacian and hence the dynamic shear modulus at each pixel can be affected by displacement values within a two pixels.

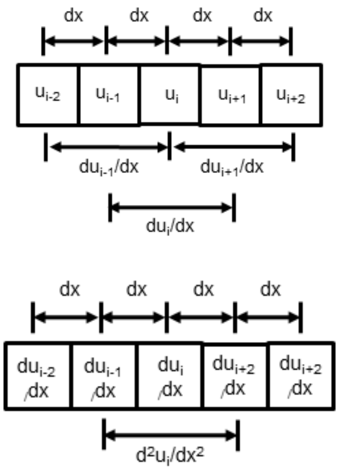

a) Derivatives in the x direction

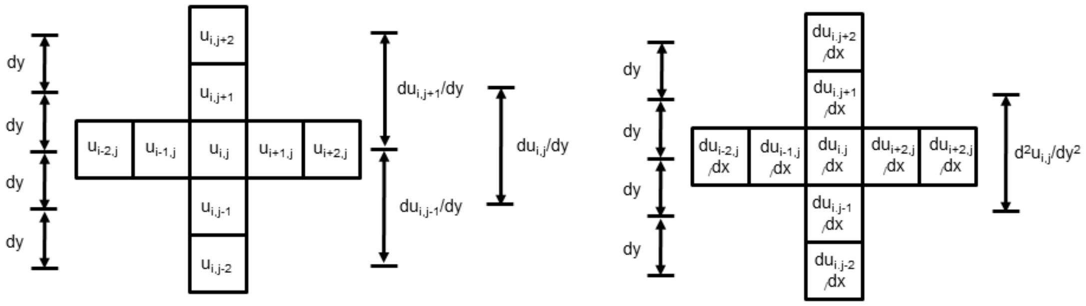

b) Derivatives in the y direction

Figure 2.5: *Calculation of the Laplacian operator in the inversion algorithm.*

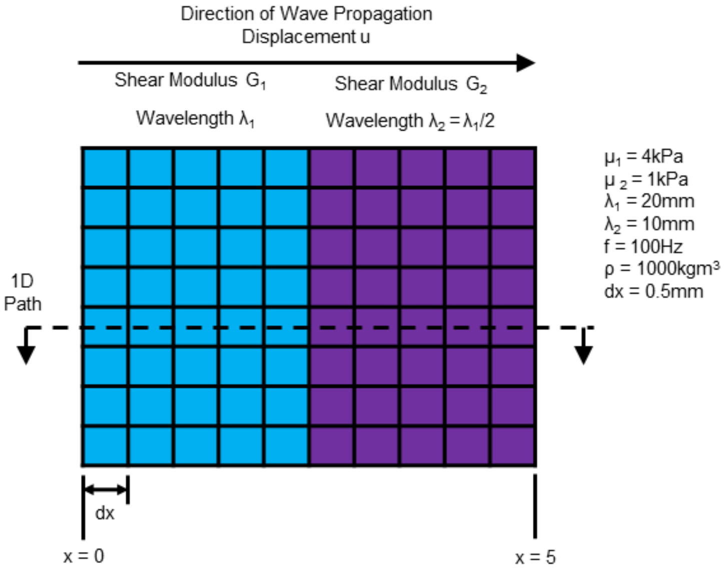

a) Geometry and material properties

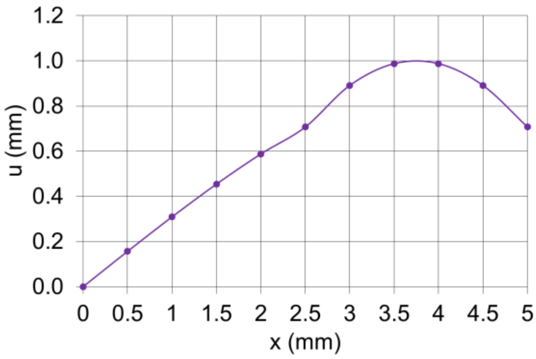

b) Wave displacement

Figure 2.6: *The geometry, material properties and 1D wave displacement through an interface of two semi-infinite media with different shear moduli.*

The consequence of a second order spatial derivative is that the inversion algorithm is extremely sensitive to inhomogeneities. Figure 2.6(a) displays an interface between two semi-infinite pixelated media of different shear moduli. The wave displacement is taken through a 1D path and is shown in Figure 2.6(b). It based upon a generic sine curve and the 1D equations for wavelength and wave speed, equations 2.31 and 2.32. As the wave passes from the region of higher shear modulus to lower shear modulus the wavelength is halved and there is a step change in the gradient of the wave.

$$c_s = \sqrt{\frac{G}{\rho}} \tag{2.31}$$

$$\lambda = \frac{c_s}{f} \tag{2.32}$$

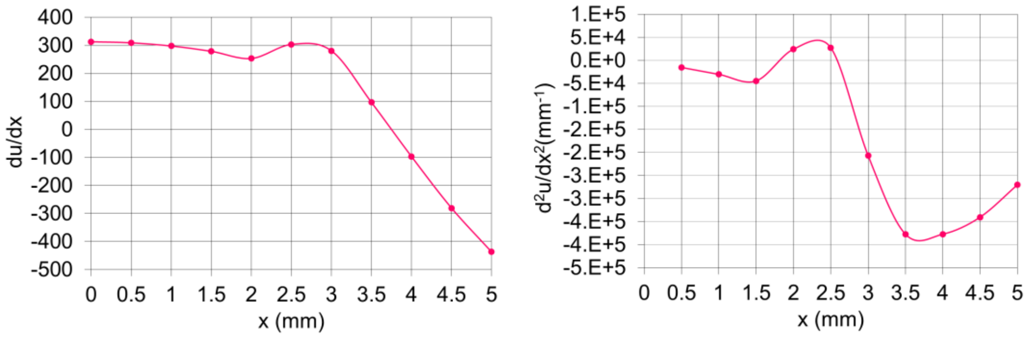

a) $\frac{\partial u}{\partial x}$ b) $\frac{\partial^2 u}{\partial x^2}$

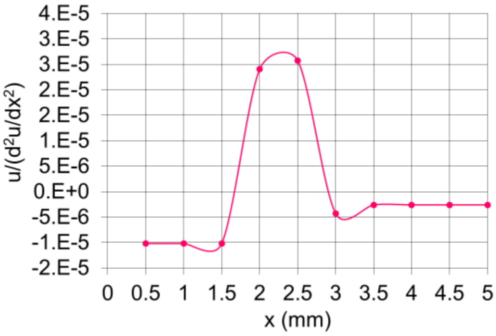

c) $\frac{u}{\frac{\partial^2 u}{\partial x^2}}$

Figure 2.7: *The spatial derivatives of the Helmholtz inversion algorithm of the semi-infinite system described in Figure 2.6.*

Since the system is semi-infinite, the 1D path can neglect displacement gradients in the y direction and the spatial derivatives are calculated purely in the x direction. The gradient change of the wave displacement in Figure 2.6(b) follows through to the displacement derivatives in Figure 2.7(a) and (b), most obviously between $2 \le x \ge 3$. The combined displacement term of equation 2.25 is shown in Figure 2.7(c) and the values in the range

$2 \leq x \geq 3$ are noticeably inflated. Figure 2.8 shows the shear modulus, calculated from equation 2.25 using the material properties in Figure 2.6(a), the wave displacement in 2.6(b) and the Laplacian in 2.7(b) and extracted using the rheological Voigt model. The final consequence of the boundary can be seen in the shear moduli of pixels $x = 2$ and $x = 2.5$; an incorrect positive Laplacian, shown in Figure 2.7(b) in the denominator of equation 2.25 combined with a positive displacement in Figure 2.6(b) leads to an impossible negative shear modulus. At $x = 3$ of Figure 2.8 the shear modulus is inflated above its true value, caused by an error in the Laplacian but no error in sign, as the wave passes over the boundary.

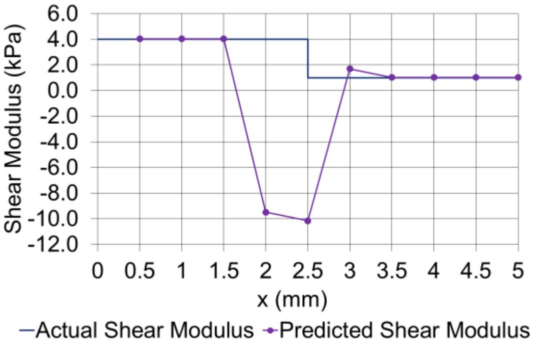

Figure 2.8: *The predicted shear moduli of the semi-infinite system described in Figure 2.6; calculated using the Helmholtz inversion algorithm.*

The observations in Figures 2.5 through to Figure 2.8 lead to a series of artefacts, which will be termed pixel artefacts. The negative shear moduli values in Figure 2.8 are known as 'black hole' artefacts and in the analysis are equated to zero. The less dramatic errors in the Laplacian for example at $x = 3$ of Figure 2.7(b) lead to over and underestimated stiffnesses. In Chapter 4, it is observed that the location of the pixelated 'black hole' artefacts changes with frequency, suggesting that these artefacts may be related to either the phase or the frequency of the wave as it passes over a boundary. Although further research would be required to confirm this, it indicates that a combination of data obtained at different frequencies could alleviate these artefacts.

Another consequence of the second order spatial derivatives, is that across an interface with a medium of no stiffness, for example the blood of the lumen, a reduced stiffness boundary artefact is generated. This is caused by the zero displacement within two pixels of the pixel of interest; the spatial derivatives, i.e. the components of the denominator in equation 2.25, are inflated and lead to underestimated shear moduli. Conversely when there is a boundary, beyond which there is a lack of information, such as at the edge of the ROI, the size of the Laplacian is reduced by the lack of information from some of its components. This leads to a boundary artefact with inflated pixels. Both the pixel artefacts and boundary artefacts can occur through the real and imaginary displacement images and hence through the shear modulus and shear viscosity elastograms.

To progress these conclusions into 2D would require the simulation of MRE through an inclusion. The wave displacement through an inclusion, as opposed to a semi-infinite domain, is governed by the strain in 2 dimensions making it much more complicated to demonstrate in the simple numerical manner employed here. Similar pixel artefacts occur around inclusions; however the specific interaction of the inversion algorithm with changes in inclusion size and stiffnesses is an ongoing area of research.

Moving back to the calculation of the shear modulus and shear viscosity; as mentioned in section 2.2.4, determining the elasticity and viscosity components from the complex modulus is based on a rheological model. In this instance the Voigt model was used, equations 2.15 and 2.18. Combining these with equation 2.25 allows the elastic shear modulus and the viscosity to be extracted from the storage and loss modulus using the equations 2.33 and 2.34. In this chapter, the shear modulus and viscosity were either plotted over the ROI or averaged using the median.

$$\mu = G^{'} \tag{2.33}$$

$$\eta = \frac{G^{''}}{\omega} \tag{2.34}$$

2.3) Results

Throughout the images in this section and future results sections, the scales have been altered, so that in some instances there are displacements or stiffnesses within the image that have larger magnitudes than that of the scale. In these cases the values have been truncated to the colour of the maximum value. In the case of wave images this has been done purely for aesthetics. In the case of elastograms it brings the primary range of stiffness values into focus. These alterations do not impinge on the quality of the visual results.

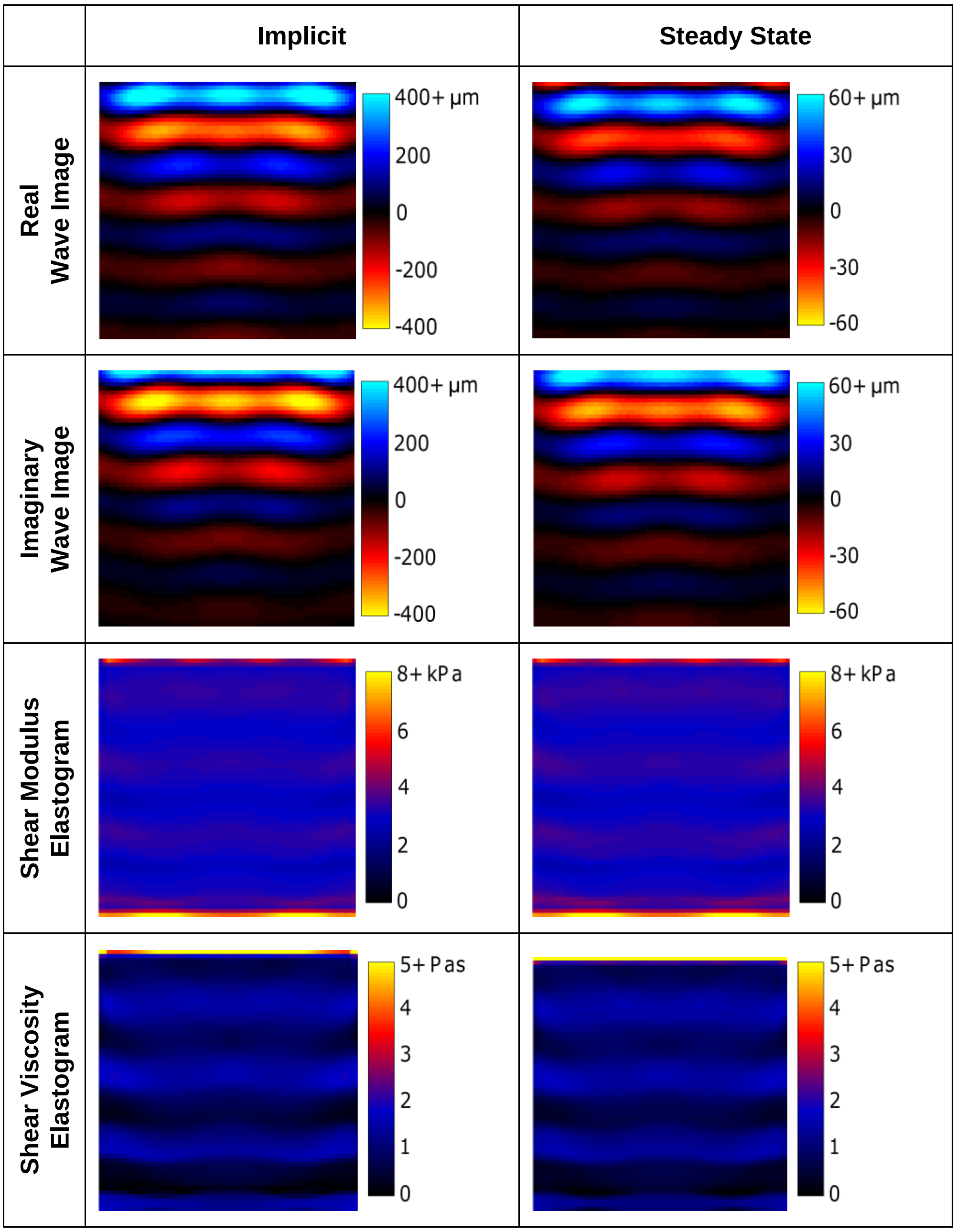

Figure 2.9: *The real and imaginary components of the complex wave images and the shear modulus and shear viscosity elastograms yielded by the implicit dynamic analysis and steady state dynamic analysis.*

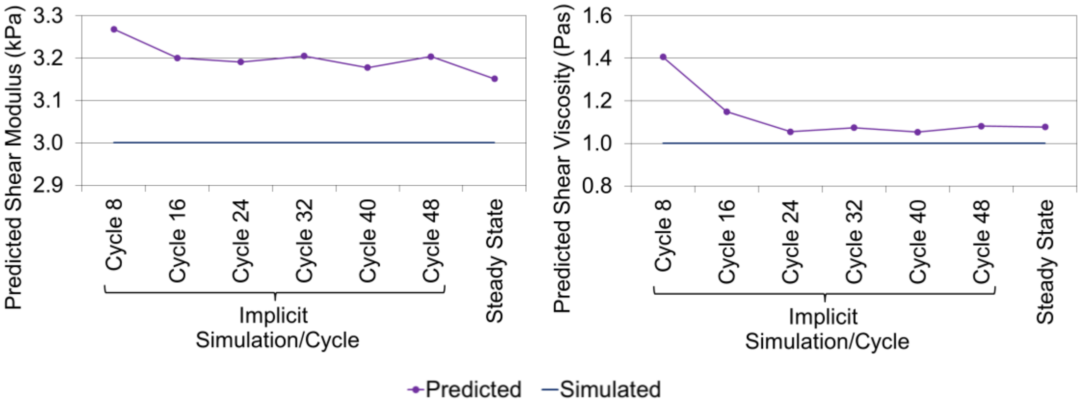

a) Shear modulus b) Shear viscosity

Figure 2.10: *The variation of shear modulus and shear viscosity with simulation type.*

2.3.1) Simulation Type

Figure 2.9 displays the real and imaginary complex wave images and the shear modulus and shear viscosity elastograms from the implicit dynamic analysis and steady state dynamic analysis. The complex wave images taken from the implicit simulation were taken from the 48th wave cycle.

Figure 2.10 shows the variation of average predicted shear modulus and shear viscosity through the ROI using the steady state dynamic analysis and the implicit analysis at wave cycles 8, 16, 24, 32, 40 and 48. The shear modulus and viscosity converge towards the steady state value, however all values remain higher than the simulated moduli. The steady state analysis offers a time efficient alternative to the implicit analysis, with qualitatively and quantitatively comparable results. The steady state analysis was taken forward for the rest of the investigation.

2.3.2) Material Properties

Figure 2.11 gives an example of the changes in the real component of the complex wave image, the shear modulus elastogram and shear viscosity elastogram with variation in the simulated shear modulus and viscosity. As the ratio of loss to storage modulus increases, the attenuation in the wave images increases and the homogeneity of the elastograms decreases.

This is also reflected in Figure 2.12 which shows the variation in the predicted shear modulus and shear viscosity as the simulated shear modulus and viscosity vary.

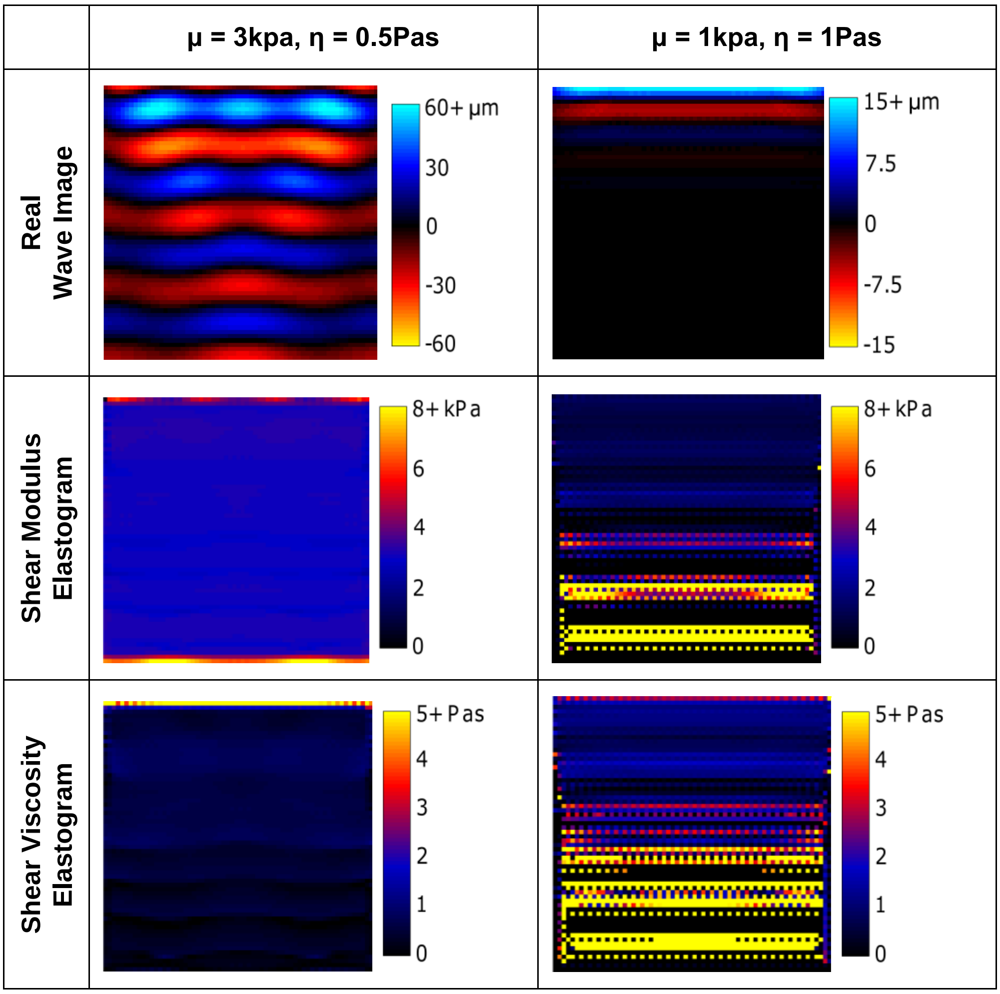

Figure 2.11: *The real component of the complex wave images and the shear modulus and shear viscosity elastograms through a linear elastic soft tissue with different material properties.*

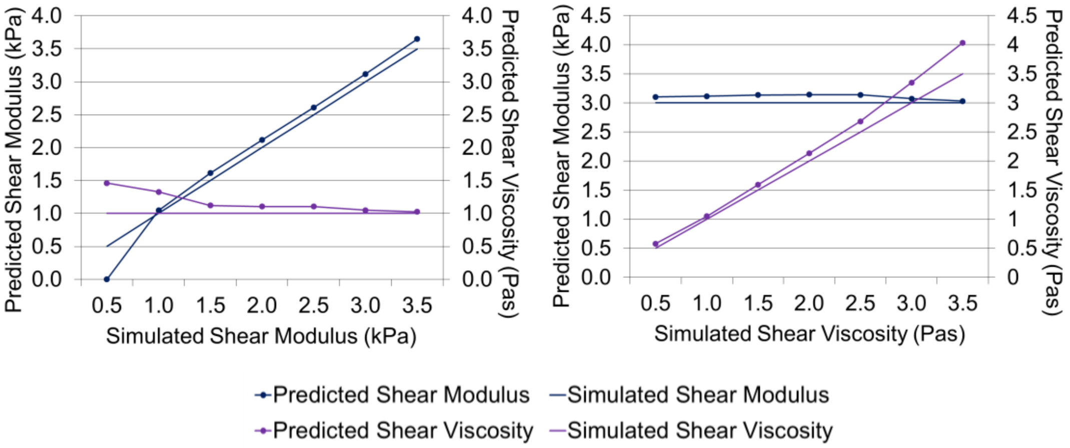

a) Varying the shear modulus b) Varying the shear viscosity

Figure 2.12: *The variation of predicted shear modulus and shear viscosity with changes in simulated shear modulus and shear viscosity.*

2.3.3) Element and Pixel Size

Figure 2.13 shows how the real component of the complex wave images, shear modulus elastograms and shear viscosity elastograms change with respect to mesh density for a fixed pixel size of 1mm^2. Figure 2.14 shows how the real component of the complex wave images, shear modulus elasotgrams and shear viscosity elastograms change with respect to pixel size for a fixed mesh density based on an element length of 1mm^2. Figure 2.15 summarises this data; displaying the numerical variation of shear modulus and shear viscosity with both element length and pixel size.

When pixels smaller than the element length are combined the finite element mesh is visible in the elastograms. This follows through to the quantitative results of Figure 2.15, where the smallest pixel size of 0.5mm^2 shows very poor accuracy and continuity. Almost all the predicted shear moduli are overestimated; this error decreases in magnitude for decreasing pixel size and increasing element length.

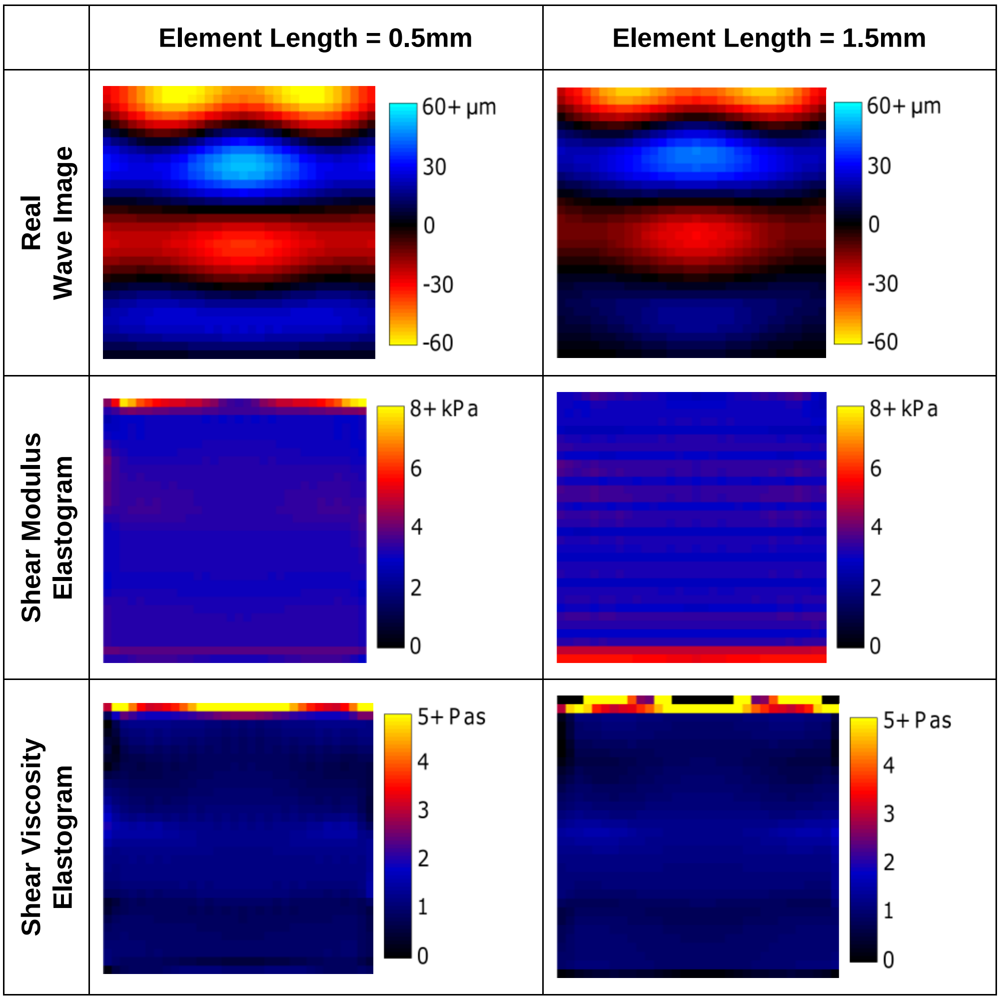

Figure 2.13: *The real component of the complex wave images and the shear modulus and shear viscosity elastograms through a mesh of various element lengths and pixel size of 1mm^2.*

2.4) Discussion

The results in this chapter suffer from some obvious artefacts. The boundary artefacts generated by a lack of displacement information beyond the ROI were discussed in section 2.2.6 and they affect both the shear modulus and shear viscosity elastograms. They present as pixels of inflated stiffness along the edges perpendicular to the wave propagation direction, primarily the top and bottom edges of the majority of the elastograms. The magnitudes of these boundary artefacts were included in the averaged results, since their presence is a true reflection of the investigation. However their inclusion leads to inflated spatially averaged results through the simulations. The data was reanalysed with regions of interest that neglect these boundary artefacts and the results were still found to be consistently overestimated when compared to the actual shear stiffness through the simulation.

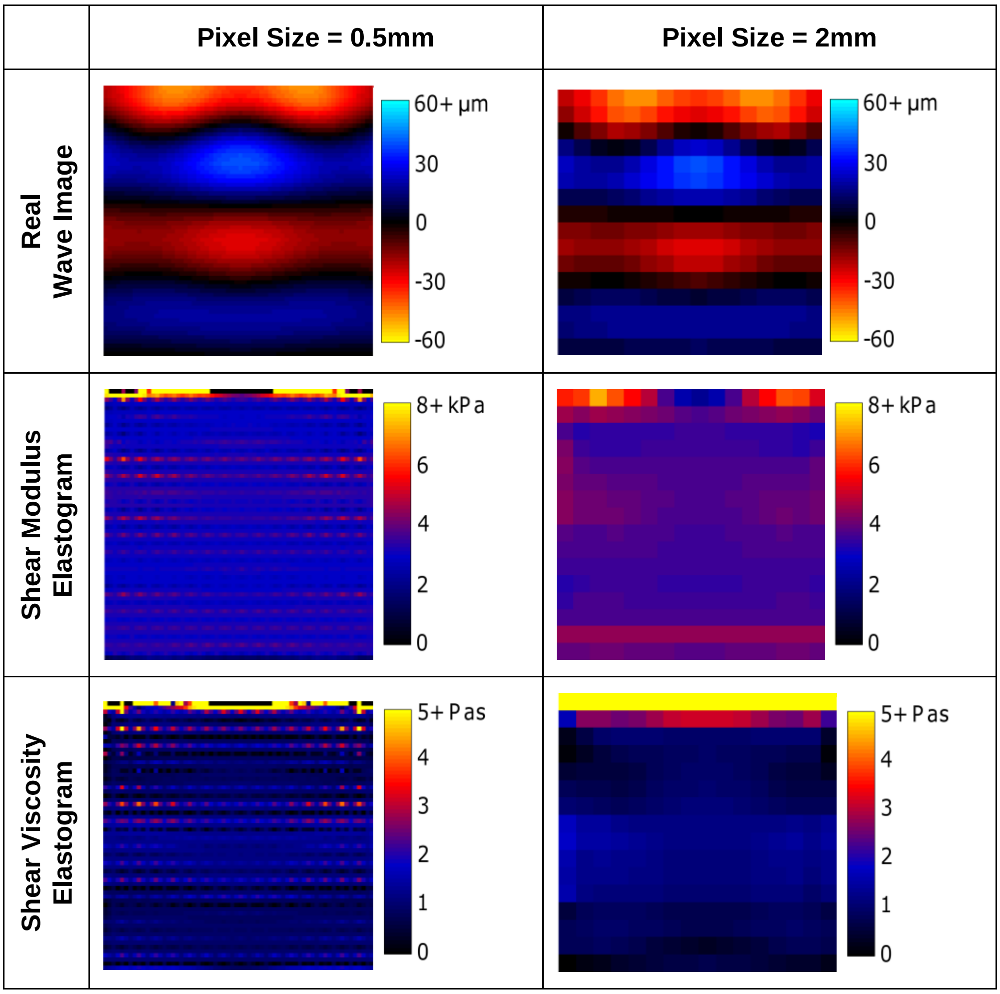

Figure 2.14: *The real component of the complex wave images and the shear modulus and shear viscosity elastograms through a 1mm element edge length mesh and various pixel sizes.*

This averaged overestimation through the ROI changes with mesh and pixel size, this is demonstrated very clearly in Figure 2.15. This would indicate that this error is linked to the wave discretization. However the results from the work of Chen et al. (2005) also show primarily overestimated wavelengths; they report that the error between the simulated and actual wavelength can vary with boundary conditions, density, the thickness of the medium and to a lesser extent element type. In Chapter 6, it is shown that the presence of encastre boundary conditions leads to inflated wavelengths through the arterial phantoms. The boundary conditions in this section, whilst approximately non-reflecting, are imperfect. In addition, it is highlighted later in this section, that there is a limit to the numerical software precision used in this analysis, most notably a single precision within the FEA itself. The results from this Chapter, Chapter 6 and Chen et al. (2005) suggest that there may be several reasons for these overestimated wavelengths. To pinpoint the exact source of this error would require a further more in depth parameter assessment.

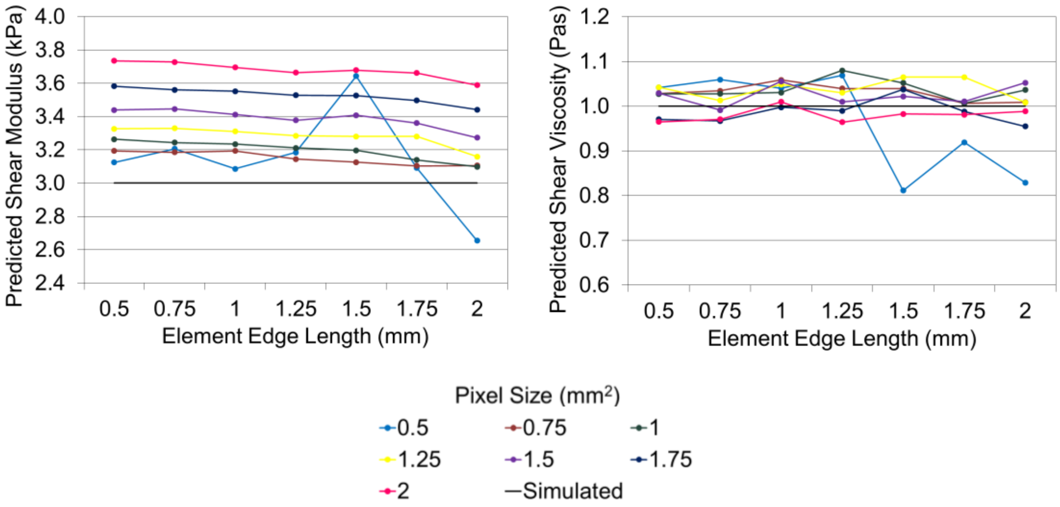

a) Shear modulus

b) Shear viscosity

Figure 2.15: *The variation of shear modulus and shear viscosity with element edge length and pixel size.*

Papazoglou et al. (2008) report that there are 5 sources of error stemming from invalidation of the Helmholtz inversion algorithm assumptions; the presence of boundaries, wave diffraction and radiation, non-planar wave propagation, a non-zero pressure field and discrete and noisy data. The errors seen in this chapter are primarily created by the discrete data and edge boundary of the ROI. The wave diffraction and deviation from planar propagation is minimal. The excitation of the wave is purely shear. As the research in this thesis continues, more of these assumptions become invalidated due to non-planar wave propagation, compressional excitation and noise.

The errors that are generated by the Helmholtz inversion algorithm in this chapter and the number of assumptions that will be invalidated by the application to arterial geometries calls into question whether another inversion algorithm would be more suitable. A range of algorithms are overview in section 1.7.2 and although alternative inversion algorithms are not investigated in this thesis, two stand out as having the potential to be more applicable. The inversion of bounded media, proposed by Kolipaka et al. (2009) could be extended to look at the cylindrical geometries of arteries. Alternatively the significant computational component in this research lends itself to expansion into the arena of inversion between experimental and FEA wave images using a minimization algorithm, as discussed in section 1.7.4.

2.4.1) Simulation Type

Figure 2.9 visually compares the complex wave image results from the dynamic implicit analysis and direct solution steady state analysis. The images between the simulations are very comparable, they are slightly out of phase with each other but nevertheless they display the same wavelength of approximately 17 pixels, matching well with the theoretically ideal wavelength of 16.9mm, calculated by equations 2.31 and 2.32. The Fourier transformed implicit simulation complex images have larger overall wave amplitudes than the complex images from the steady state analysis. This shows that the steady state simulation does not exactly replicate the Fourier transformed results taken from the time steps of the implicit analysis; however for the purpose of this study where the key parameter is wavelength, the procedures are comparable. Indeed, with experimental or computational MRE the load parameter and hence wave amplitude, is often varied to ensure the correct degree of propagation is obtained.

The propagation seen in the simulated wave images is not completely planar. This deviation from idealised planar propagation is created by gradients in the X direction which have two sources; diffraction of the wave at the edges of the actuator and the wave reflections from the simplistic method of mirroring boundary conditions. Other methods of removing wave reflections completely would be to use infinite elements (Dassault Systèmes Simulia Corp. 2010c) or a perfectly matched layer (Berenger 1994). In reality it is almost impossible to remove the presence of wave diffraction or the interaction of wave reflections in a phantom or *in vivo* experimental MRE scan, so the slight deviation from non-planar wave propagation is not considered hugely detrimental to the study.

Figure 2.9 also shows the shear modulus and viscosity elastograms resulting from both analysis methods. They are extremely comparable, with very slight differences in stiffness throughout the ROI. Figure 2.10 and Table 2.4 show that the spatially averaged stiffness values from the steady state analysis give accurate results with small errors that are comparable to the implicit simulation. The shear modulus and viscosity from the implicit analysis tends towards the steady state value over the first 16 cycles. This is to be expected as the more cycles that occur, the further from transient and the closer to steady state the simulation will become.

The errors between the predicted and simulated moduli for both analysis types are summarised in Table 2.4. They are all positive errors, the sources of which were discussed at the beginning of this section. Nevertheless the errors were found to be sufficiently small to support the use of both techniques to simulate MRE. The remaining sections of this chapter and thesis were conducted using the more time efficient steady state dynamic analysis.

Parameter	**Simulation**	**Error (%)**
Shear Modulus	Implicit Cycle 48	6.8
	Steady State	5.0
Shear Viscosity	Implicit Cycle 48	8.1
	Steady State	7.7

Table 2.4: *The errors between the simulated and average predicted moduli for the 48th cycle of the implicit dynamic analysis and the steady state dynamic analysis.*

2.4.2) Material Properties

The most pertinent observation from the results of this section is the severe attenuation of the waves at certain combinations of shear modulus and viscosity. When the loss to storage modulus ratio is high, the phase δ tends towards the viscous liquid end of the viscoelastic range, equation 2.19. The simulation of μ=1kpa, η=1Pas, shown in Figure 2.11 demonstrates such large attenuation that the wave amplitudes are barely perceptible beyond the first wave cycle. Consequently the quality of the corresponding elastograms is compromised; the homogeneity and the accuracy of the values are poor, especially at the bottom of the images. The waves of the μ=3kpa, η=0.5Pas simulation show good propagation across the whole image, therefore the corresponding elastograms are homogeneous and accurate.

In such an idealised system, theoretically the wave amplitudes in the simulation of μ=1kpa, η=1Pas should continue to propagate through the ROI, albeit at smaller and smaller values. This is where the numerical precision levels of the software used in this analysis become limiting. In this instance, the limiting precision value is within the finite element analysis itself; Abaqus/CAE has a default single precision (Dassault Systèmes Simulia Corp. 2010a). As the wave is attenuated with depth, the limiting precision level causes numerical errors in the analysis and hence the resulting wave amplitudes, so effectively the wave ceases to propagate. Future work could change the precision level to double, however in reality MRE imaging will also have a limiting threshold displacement that can be detected.

In Figure 2.12 both the fixed and variable parameters in each simulation demonstrate good correlation with the value of the simulated variable. The consistent overestimation due to the boundary artefacts and discrete analysis methods, discussed at the beginning of this section, are again visible in these results. The consequence of a high loss to storage modulus ratio can be seen clearly in both graphs of Figure 2.12. As ratio increases, the attenuation increases and the numerical precision of the technique limits wave propagation, thus the results begin to deviate significantly from the simulated properties. The other factor that affects δ is the excitation frequency; as the excitation frequency increases, the loss to storage modulus and therefore attenuation increases. Frequency has not been dealt with in this chapter but will be in Chapter 3 and 4.

2.4.3) Element and Pixel Size

An observation that was noticed in a high proportion of elastograms where the pixel size was smaller than the element size, was the visual presence of the mesh in the elastogram, this can be seen in Figure 2.13 and 2.14. The root cause of this is Laplacian operator in the inversion algorithm, which effectively highlights the changes in gradient along the finite element mesh. The effect of this on the averaged shear modulus and shear viscosity results can be seen quantitatively in Figure 2.15, where for a pixel size of 0.5mm^2, there are very high errors for the larger element sizes. The other visible errors in the elastograms of this section are the previously discussed boundary artefacts along the edges of the ROI.

The visual differences between the wave images and elastograms as the mesh varies, in Figure 2.13, are minimal and primarily due to changes in the discretization of the mesh. Close inspection of the wave images show a slight difference in phase, this is caused by slight variations between the models to accommodate the element sizes as opposed to any significant difference in the results with mesh density. Except for the faintly visible mesh in the 1.5mm element length elastogram, the elastograms are very comparable between different element lengths. The wavelengths in Figure 2.14, for a fixed mesh, are affected by pixel size in terms of the discretization of the wavelength; the $2mm^2$ pixel appears to have a longer wavelength than the $0.5mm^2$ which follows through to higher stiffnesses in shear modulus the elastogram.

Figure 2.15 shows that the overestimation error between the simulated and average predicted shear modulus changes with both element and pixel size, more noticeably with pixel size. As the pixel size decreases there is a decrease in the overestimated error, this is intuitive as the smaller pixel size can give a more accurate representation of the wavelength. As the element edge length increases, the mesh becomes less dense and presumably less accurate; however the error appears to decrease. The reason for this is not clear and requires a more detailed analysis of how the discretization of the wave combining meshing techniques and pixelated images effects the predicted moduli. Although mesh independence was not achieved with decreasing element edge length, the change in predicted shear modulus with large changes in the mesh density is quite small. This indicates that the technique should be relatively insensitive to small variations in element size through the atherosclerotic plaque geometry of future chapters.

The variation of shear viscosity with element and pixel size in Figure 2.15 is fairly random, presumed to be due to the very high sensitivity of the wave attenuation to the mesh and pixel size. However since the shear viscosity is not the primary parameter under observation in the bulk of this thesis and the errors (omitting the $0.5mm^2$ pixel results, for element lengths above 1mm, for the reasons discussed above) are within 10%, this is not considered a significant issue.

Of course, as discussed at the beginning of this chapter, a large number of additional variables are introduced into MRE when it moves into the computational domain. The parameters most specific to the work conducted in this thesis were investigated in this chapter, however there is potential for much a broader investigation.

2.5) Conclusions

The steady state dynamic analysis provides an accurate, time and memory efficient alternative to the implicit dynamic analysis. When the loss to storage modulus ratio deviates away from the solid end of the viscoelastic range the high attenuation can inhibit wave propagation and consequently disrupt shear modulus and viscosity estimations. In soft tissues which are predominately water based (Fung 1993), this is an important point. Ideally the mesh size needs to be smaller or equal to the pixel size, to avoid inaccuracies generated by the gradients of the mesh appearing in the elastograms. However the pixel size also needs to be small enough to be able to accurately resolve the length of the propagating wave accurately. All the sections of this chapter have demonstrated overestimated results thought to be linked to the discrete nature of the analysis and the sources of error discussed in (Papazoglou *et al.* 2008).

Overall the results from this chapter are very encouraging and provide a solid foundation for the computational work conducted in this thesis; an efficient analysis technique has been developed that subject to propagating waves, gives a good estimate of the viscoelastic parameters.

Chapter 3

Steady State Wave Response through Idealised Atherosclerotic Plaques

3.1) Introduction

The field of arterial magnetic resonance elastography, the literature of which was summarised in section 1.7.3, is relatively under researched. The theory of applying MRE to image the mechanical properties of atherosclerotic plaques remains, to date, completely unresearched. Ideally the feasibility of this technique needs to be assessed experimentally using arterial phantoms (Chapter 5) and healthy volunteers and patients (Chapter 7). However the concept of assessing the mechanical properties of an atherosclerotic plaque using MRE is inherently challenging. There are many potential complications including imaging resolution, the small size of the ROI, the lumen boundary, physiological motion of the arterial wall and flow artefacts created by the blood. In tandem MRE is a relatively expensive and time consuming imaging technique.

In addition to removing some of the complications associated with MRE through atherosclerotic plaques, FEA allows time and cost efficient parameter assessment in a controlled environment, in advance of experimental feasibility studies. A method of simulating MRE was proposed in Chapter 2.

A simulation of MRE through an idealised atherosclerotic plaque has an enormous amount of potential variables, listed in Table 3.1. Beyond the FEA specific parameters, which were investigated in Chapter 2, there are variables associated with the mechanical waves, MRI and the inversion algorithm. In addition there are the variables associated with the disease development of atherosclerosis. Due to the shear amount of variables to be investigated, they shall be split over chapter 3 and 4.

Chapter 3 shall investigate the variation in steady state wave response, in advance of incorporating the inversion algorithm and examining the variation of the shear modulus in Chapter 4. The steady state shear wave response is the output of the FEA and the input into the wave inversion algorithm; a highly idealised replica of the Fourier transformed phase contrast images gained from experimental MRE. Since the artery is a challenging organ to image using MRE, several studies have displayed their results in terms of wave images (Woodrum *et al.* 2006, Zheng *et al.* 2007). To date the only application of MRE to atherosclerotic plaques was conducted by Woodrum et al. (2006) who imaged waves through the fluid of thin walled, stenotic phantoms, to determine stenosis size.

The aim of this chapter is to investigate the behaviour of the steady state shear wave response through an idealised atherosclerotic plaque with variations in mechanical and geometric disease development parameters. Preliminary work into the behaviour of 1D transient shear waves passing through atherosclerotic plaque was outlined in (Thomas-Seale *et al.* 2011b) and developed into a 2D steady state analysis in (Thomas-Seale *et al.* 2011a). The models in this chapter have been developed, based on the observations from this work and throughout the course of this research.

3.2) Method

3.2.1) Overview

The methodology of this chapter is based on a truncated version of that described in section 2.2 and shown in Figure 2.1. Based on the conclusions of Chapter 2, the Abaqus/ CAE direct solution steady state analysis shall be used as a time efficient method of creating complex wave images at the corresponding excitation frequency.

The parameters to be considered in Chapter 3 and 4 are listed in Table 3.1. Chapter 3 shall consider imaging plane, wave excitation frequency, load direction and magnitude, stenosis, fibrous cap and lipid pool size. Although the imaging plane is an MRI variable, the propagation of waves through different sectional planes of the plaque was explored in order to identify the one which yields the clearest result. The variables which are not considered until Chapter 4 are shaded in Table 3.1.

Plaque rupture is associated with the composition of the plaque and properties of the components (Falk *et al.* 1995). Atherosclerotic disease development was modelled using idealised geometric variations of the stenosis, fibrous cap and lipid pool. Changes in the mechanical properties of the lipid and fibrous cap have fixed values in this chapter and are varied in Chapter 4.

	Mechanical Parameters			**Imaging and Inversion Parameters**						
Variables Under Analysis	**Load Direction**	**Load Magnitude (N)**	**Excitation Frequency (Hz)**	**Imaging Plane**	**Pixel Resolution (mm^2)**	**Averaging Method**	**Filter Limits (m^{-1})**		**Rheological Model**	**Artificial Noise (SNR)**
							Upper	**Lower**		
Imaging Plane	Shear	$6x10^{-4}$	100	X-Y/ Y-Z	1	N/A	N/A	N/A	N/A	Noiseless
Load Direction	Shear/ Compression	$6x10^{-4}$	100	Y-Z	1	N/A	N/A	N/A	N/A	Noiseless
Load Magnitude	Shear	$2/4/6/8x10^{-4}$	100	Y-Z	1	N/A	N/A	N/A	N/A	Noiseless
Stenosis	Shear	$6x10^{-4}$	100	Y-Z	1	N/A	N/A	N/A	N/A	Noiseless
Excitation Frequency/ Lipid Pool Size	Shear	$6x10^{-4}$	50/100/150/ 200	Y-Z	1	N/A	N/A	N/A	N/A	Noiseless
Fibrous Cap Thickness	Shear	$6x10^{-4}$	100	Y-Z	1	N/A	N/A	N/A	N/A	Noiseless

Table 3.1: *MRE simulation parameters: mechanical, imaging, inversion and disease. The shaded parameters are investigated in Chapter 4.*

	Disease Variables				
Variables Under Analysis	**Stenosis Size (%)**	**Lipid Pool**		**Fibrous Cap**	
		Size (mm^3)	**Cholesterol (%)**	**Thickness (mm)**	**Structure**
Imaging Plane	70	0/Total	0	0.25	Cellular
Load Direction	70	30	0	0.25	Cellular
Load Magnitude	70	30	0	0.25	Cellular
Stenosis	40/50/60/70/80	0/Total	0	0.25	Cellular
Excitation Frequency/ Lipid Pool Size	70	0/30/Total	0	0.25	Cellular
Fibrous Cap Thickness	70	0/Total	0	0.25/0.5/0.75	Cellular

Table 3.1: *(continued) MRE simulation parameters: mechanical, imaging, inversion and disease. The shaded parameters are investigated in Chapter 4.*

The results of this chapter will be displayed qualitatively; the variation of 2D shear wave images with various parameters. Consequently the parameters under investigation in Table 3.1 could not be investigated through an inclusive range or in relation to the variation of all the other parameters; otherwise there would be an excessive amount of results. Chapter 4 however displays a more diverse range of quantitative stiffness results, summarised in Table 4.1. The addition of artificial noise was omitted from this chapter. The signal to noise ratio is a parameter that may be compensated for, to some extent, by filters in the inversion algorithm parameters and so will be discussed further in Chapter 4.

The model geometry was created using the computer aided design software Rhinoceros version 3.0, (McNeel, Seattle, Washington, USA). Simulations were conducted using the finite element modelling software Abaqus/ CAE version 6.10. Complex wave image results were extracted from Abaqus/ CAE and formatted using Microsoft Office Excel and MATLAB R2011a.

3.2.2) Geometry

The arterial geometry used in this chapter was detailed but highly idealised. A plaque modelled as an eccentric stenosis, composed of fibrotic and diseased wall tissue, containing a lipid pool, was enclosed by a fibrous cap. The plaque was situated within a straight arterial vessel incorporating the three layers and embedded in an arbitrary block of tissue. The model geometry is shown in Figures 3.1 and 3.2.

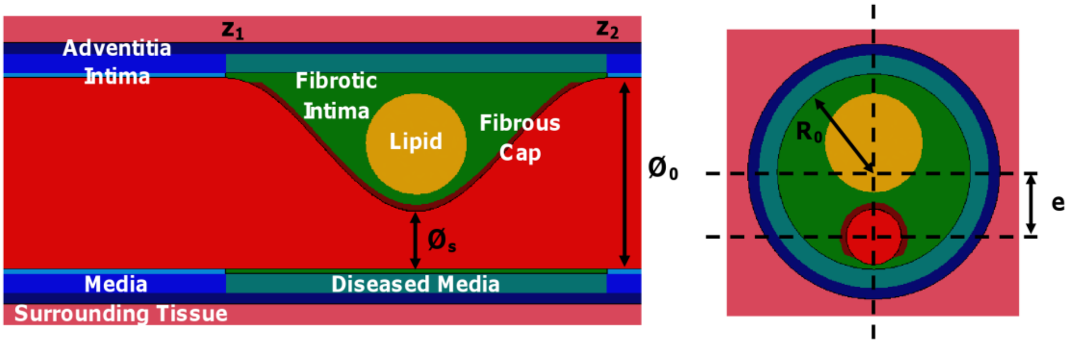

Figure 3.1: *Cross sectional idealised plaque geometry.*

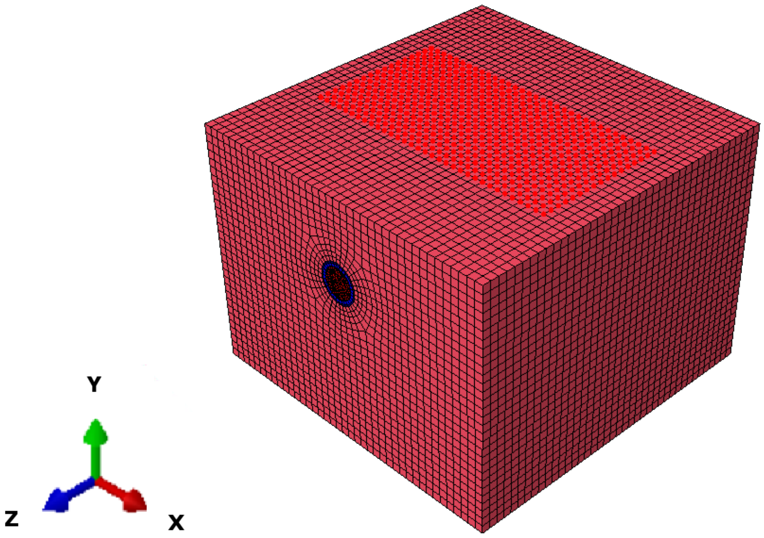

Figure 3.2: *Idealised atherosclerotic plaque, full model geometry, axes, mesh and load nodes.*

The vessel wall geometry, intima, media and adventitia were taken from histological measurement of the iliac arteries (Schulze-Bauer *et al.* 2003). The plaque was modelled as an eccentric stenosis based on equations 3.1, 3.2 and 3.3 taken from (Ahmed and Giddens 1983, Tang *et al.* 2004, Li 2007) the nomenclature of which are displayed in Figure 3.1. R_0 is the radius and ϕ_0 is the diameter of the healthy lumen, S is the stenosis and ϕ_s is the diameter of the narrowest stenosed section. $R(z)$ is the radius of the vessel, at a distance z along the length of the vessel, where z_1 and z_2 are the ends of the stenosed section. The length of the stenosis is equal to twice the diameter of the lumen. E_c is the eccentricity of the stenosis, where e is the distance between the centre point of the vessel and lumen.

$$R(z) = R_0 - SR_0 \{1 - \cos[2\pi(z - z_1)/(z_2 - z_1)]\}/2 \tag{3.1}$$

$$S = (\phi_0 - \phi_s)/\phi_0 \times 100\% \tag{3.3}$$

$$E_c = e/[(\phi_0 - \phi_s)/2] \times 100\% \tag{3.3}$$

The lipid pool was modelled as either absent, a sphere orientated on the geometric centre of the plaque or filling the entire plaque. The fibrous cap was created as a surface offset from the stenosis geometry into the plaque, the thickness of the fibrous cap was varied between 0.25mm, 0.5mm and 0.75mm (Loree *et al.* 1992). Geometric disease development was modelled by varying the degree of the stenosis, the volume of the lipid pool and thickness of the fibrous cap. An example of the vessel and plaque geometry through two cross-sectional planes can be seen in Figure 3.1; a 70% stenosis with a 30mm^3 lipid pool and 0.25mm fibrous cap.

The vessel was embedded within a homogeneous block of tissue to imitate the transmission of shear waves *in vivo*; allowing the waves to propagate from the interface of the actuator through a layer of tissue, the vessel and plaque and then on through the tissue. The location of vessel within in the tissue block can be seen in the complete model shown in Figure 3.2. A summary of all the geometric parameters can be found in Table 3.2.

Tissue	Geometric Parameter	Value
Surrounding Tissue	Length	80.00mm
	Width	80.00mm
	Depth	60.00mm
Stenosis	Length	14.52mm
Intima	Inner Radius	3.63mm*
	Thickness	0.17mm*
Media	Inner Radius	3.80mm*
	Thickness	0.73mm*
Adventitia	Inner Radius	4.53mm*
	Thickness	0.43mm*
Fibrous Cap	Thickness	0.25/0.5/0.75mm**
Lipid Pool	Volume	0/30/Total mm^3

Table 3.2: *Geometric parameters: idealised atherosclerotic plaques. *(Schulze-Bauer et al. 2003) and **(Loree et al. 1992).*

3.2.3) Material Properties

Ideally the viscoelastic properties assigned to each component of the atherosclerotic plaque would be taken from experimental work in the frequency range of interest, identifying the correct rheological model. However quantifying the *in vivo* mechanical properties of arteries via MRE or other methods, summarised in sections 1.5.3 and 1.7.3, is relatively under researched. Therefore the values and models were taken from the available literature; in some cases, the data obtained was not ideal and the required stiffness parameters had to be extrapolated.

In this study the diseased vessel was modelled as an incompressible, isotropic Hookean viscoelastic material. Viscoelasticity may be expressed using the dynamic shear modulus and a rheological model. The equations for this constitutive relationship and integration into the model are outlined in section 2.2.4; some equations are repeated here for explanatory purposes. The dynamic shear modulus, equation 3.4, is composed of the storage, G', and loss modulus, G'', defined by the amplitude of the complex modulus $|G|$, and phase by which the strain lags the stress, the loss angle δ, equations 3.5 and 3.6 (Fung 1993).

$$G = G' + iG'' \tag{3.4}$$

$$G' = |G| \cos\delta \tag{3.5}$$

$$G'' = |G| \sin\delta \tag{3.6}$$

The dynamic modulus is related to the elastic shear modulus, μ, and the viscosity, η, of the tissue by a rheological model, of which there are a variety. The Voigt and Maxwell rheological models are based upon two parameters, meaning that the shear modulus and viscosity can be calculated from the storage and loss modulus yielded by the Helmholtz inversion algorithm, equation 2.25. For the purpose of this study, this makes them more appropriate than higher order models which would require curve fitting as opposed to direct extraction.

The Voigt model, equation 3.7, used in Chapter 2, has demonstrated a good correlation to *in vivo* arterial pressure-area dynamics (Valdez-Jasso *et al.* 2009, Valdez-Jasso *et al.* 2011). However the storage modulus of the Voigt model shows no dependence on frequency, whereas it has been shown that storage modulus is frequency dependent in some very relevant biological tissues; lipid (Loree *et al.* 1994), fibrous cap (Lee *et al.* 1991), and muscle (Klatt *et al.* 2010). Therefore the Maxwell model, equation 3.8, was chosen to represent these tissues. Figure 3.3, shows that although the Maxwell model is also composed of a spring and dashpot, contrary to the Voigt model, these components act in series.

$$G(\omega) = \mu + i\omega\eta \tag{3.7}$$

$$G(\omega) = \frac{i\omega\eta\mu}{\mu + i\omega\eta} \tag{3.8}$$

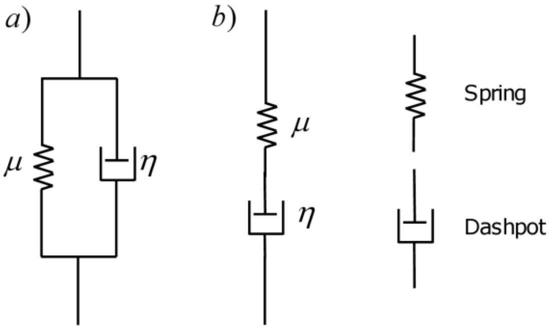

Figure 3.3: *The a) Voigt and b) Maxwell viscoelastic models.*

The Maxwell and Voigt model, demonstrate different behaviours with frequency, which hinge on the relative magnitude of the storage and loss modulus. This shall be discussed in more depth in Chapter 4, section 4.2.3, where the excitation frequency and rheological model used in the inversion algorithm shall be varied.

The shear moduli for the components of the artery wall were taken from the Neo-Hookean parameters given in (Holzapfel *et al.* 2002). The Neo-Hookean model is a hyperelastic model used to model nonlinear behaviour at large deformations. At small deformations however, this model behaves like a Hookean elastic solid (Bower 2010) and therefore provides shear moduli applicable to this study. The viscous moduli were kept constant throughout the components of the wall; based on the values in (Valdez-Jasso *et al.* 2011).

The mechanical properties of the fibrous cap and lipid pool can affect the vulnerability of atherosclerotic plaques (Falk *et al.* 1995). The variation of these properties with different compositions and frequencies are not very well documented, especially at the frequencies that are under consideration in this study. Loree et al. (1994) investigated the dynamic modulus of lipid with variations of cholesterol between 0.1 and 3Hz. Lee et al. (1991)

investigated the dynamic modulus of the fibrous cap with structure between 0.1 and 10Hz. The values taken for the modelling used in this chapter and Chapter 4 are an approximation, extrapolated from the results of the highest frequencies investigated in these studies.

Tissue	Density (kgm^{-3})	Shear Modulus (kPa)	Bulk Modulus (kPa)	Shear Viscosity (Pas)
Surrounding Tissue	1047*	2.3**	-	17.0**
Intima	1047*	150.0[+]	-	80.0[++]
Fibrotic Intima	1047*	221.0[+]	-	80.0[++]
Media	1047*	34.0[+]	-	80.0[++]
Diseased Media	1047*	757.0[+]	-	80.0[++]
Adventitia	1047*	50.0[+]	-	80.0[++]
Fibrous Cap – Cellular	1047*	208.4[#]	-	19820.0[#]
Lipid – 0% Cholesterol	1047*	0.1[##]	-	6.4[##]
Blood	1060[^]	-	2.7x10^{6}[^]	-

Table 3.3: *Material properties: idealised atherosclerotic plaques. *(Hoskins 2010), **(Klatt et al. 2010), [+](Holzapfel et al. 2002), [++](Valdez-Jasso et al. 2011), [#](Lee et al. 1991), [##](Loree et al. 1994), [^](Hoskins 2007).*

These approximations were calculated from equation 3.8 for the Maxwell model and the definition of the storage and loss moduli, equation 3.4. The values of the shear and viscous modulus extracted from (Loree *et al.* 1994) and (Lee *et al.* 1991), are based on a 0% cholesterol lipid and cellular fibrous cap respectively. Even though these values are an approximation, the shear moduli are not dissimilar to the ones outlined in (Holzapfel *et al.* 2002). In Chapter 4 the effect of changes in the mechanical properties with disease development shall also be incorporated into the analysis i.e. the cholesterol levels of the lipid pool (Loree *et al.* 1994) and the structure of the fibrous cap (Lee *et al.* 1991).

Chapter 7, explores the application of MRE to the femoral arteries of healthy volunteers and patients, therefore muscle was thought to be the most applicable surrounding tissue. Muscle however, has complicated stiffness properties; it is highly anisotropic due to its fibrous nature (Kruse *et al.* 2000). A very simplified approximation was modelled using the Maxwell model and viscoelastic properties reported from MRE literature (Klatt *et al.* 2010).

All the tissue components were modelled as incompressible, with a Poisson's ratio of 0.5, applicable due to the high water content of soft tissue (Fung 1993). They were assigned a density of 1047kgm^{-3}, the approximate average for soft tissue (Hoskins 2010). The blood was modelled as static and given acoustic properties as described in (Hoskins 2007). The material properties for each component of the model are summarised in Table 3.3.

3.2.4) Loads

Depending on the set up, the excitation load can normally be controlled to various degrees during experimental MRE. Using the equipment at the Clinical Research Imaging Centre, described in Chapter 5, section 5.2.7, the load can be tailored to create sufficient wave propagation without excessive phase wrapping. Wrapping is used to define when the phase is out of the $[-\pi, \pi)$ range and the wraps back around to create discontinuities (Wang *et al.* 2011). However, this phenomenon is more applicable to experimental work.

The actuator may be orientated to create a shear or compression load and the magnitude can be controlled using the amplifier or peak to peak amplitude of the wave form generator. However this set up also means that the exact magnitude of the load, being applied to the ROI, can-not be determined easily. Comparing the magnitude of the wave displacement with the experimental phase images seen in later chapters, can give a good approximation of the required load magnitude in the simulation, although this does vary depending on the material properties applied within the model. Consequently the load shall be applied in a compressional and shearing direction and the magnitude shall be varied through a small range of 2x10^{-4}N to 8x10^{-4}N in 2x10^{-4}N intervals.

The excitation frequency shall be varied between 50Hz and 200Hz in 50Hz intervals. This range was based upon observations from (Thomas-Seale *et al.* 2011a) where significant wave disruption was noted at frequencies above 200Hz. The frequency shall also be investigated in tandem with the lipid pool size as MRE excitation frequency and resolution are strongly linked (Sinkus *et al.* 2000, Parker *et al.* 2005, Thomas-Seale *et al.* 2011a). Frequency shall be investigated again in Chapter 4 when the shear moduli results are under observation as opposed the wave images.

3.2.5) Boundary Conditions

Symmetric boundary conditions were used to approximate non-reflecting boundaries at the edges of the surrounding tissue. The imperfect nature of this method was discussed in Chapter 2, however since reflecting boundaries also occur in MRE phantoms and *in vivo* scans, it was deemed to be a satisfactory and efficient method of avoiding wave reflections in multiple simulations.

3.2.6) Mesh

The model was meshed using linear, hybrid, tetrahedron and hexahedron elements. Where possible the geometry was partitioned to allow a structured hexahedron mesh to be used, however throughout the complicated curved geometry of the plaque an unstructured tetrahedron mesh was required. The continuity of the mesh was maintained between different parts and different mesh types.

An element edge length of 0.5mm was used to mesh the plaque geometry. This element size had to be reduced along some feature edges to allow the mesh to resolve the geometric variations of the plaque. To keep the simulation at manageable memory requirements and run times, only the plaque could be meshed with this high density. Propagating away from the plaque but within a 32mm^3 region of interest, the edge seed length was increased to 1mm. With the pixel size set at 1mm^2, this increase in element size was deemed to have a negligible effect on the accuracy of the results. Beyond the region of interest the edge seed length was increased to 2mm.

3.2.7) Results Extraction

The real and imaginary displacement results were taken through a 32 by 32 region of interest with a pixel spacing of 1mm^2. The matrix was focussed on the atherosclerotic plaque and taken through both the X-Y and Y-Z plane, with reference to the global coordinate system in Figure 3.2.

3.3) Results

All the references to planes and directions throughout this section are relative to Figure 3.2. All the wave displacement results shown in this section are the real component of the complex wave image.

3.3.1) Imaging Plane

Figure 3.4 shows the 100Hz wave propagation through the Y-Z and X-Y plane through the 70% stenosis model with a 0.25mm fibrous cap and either a fully lipid or fully fibrous composition. Of the two imaging planes, the Y-Z shows the plaque geometry the clearest. Therefore the variation of the steady state wave image with the mechanical parameters and disease variables was taken through the Y-Z plane.

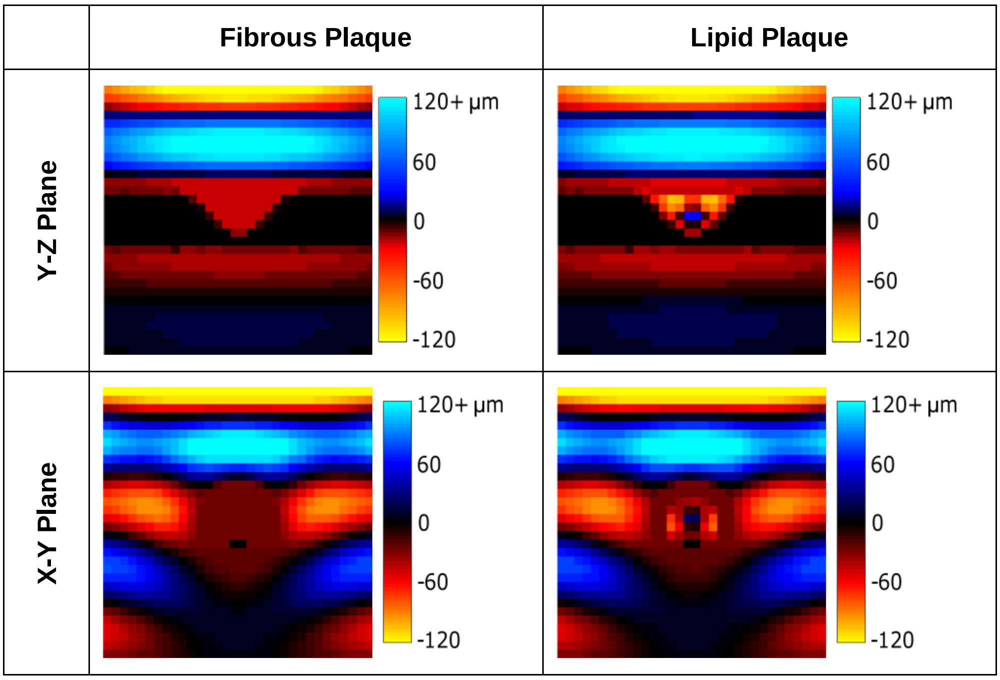

Figure 3.4: *Wave displacement through the 70% stenosis model in different planes and plaque compositions at an excitation frequency 100Hz.*

3.3.2) Mechanical Parameters

Figure 3.5 displays the wave behaviour under a shear and compression load, through all three motion directions. A shear load, with motion extracted through the Z direction gives the closest approximation of planar wave propagation. Figure 3.6 shows how the shear wave through the Z direction varies with changes in load magnitude. The magnitude of the load changes the amplitude of the wave but not the pattern of the propagation. These results were taken through a 70% stenosis with 30mm^3 lipid pool at an excitation frequency of 100Hz. The variation of the excitation frequency is displayed in tandem with changes in the lipid pool volume in section 3.3.3.

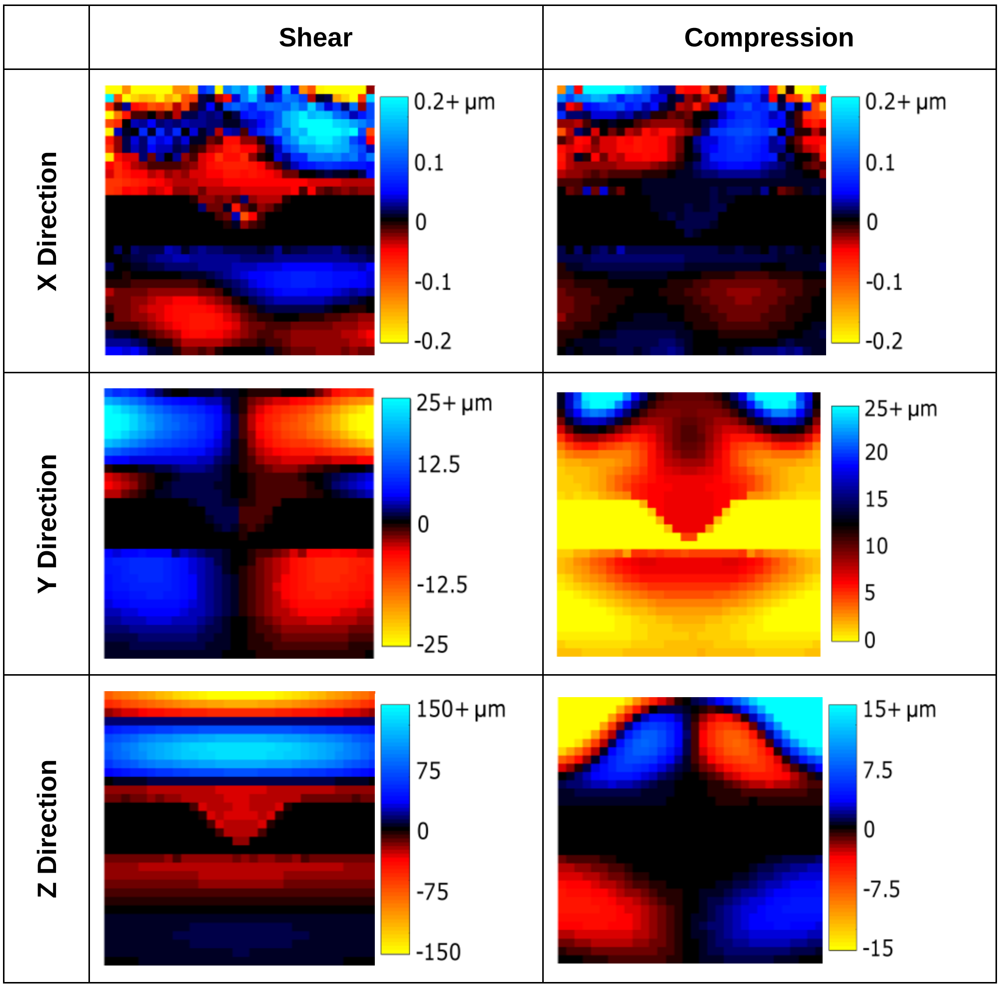

Figure 3.5: *Wave displacement through the 70% stenosis model with a 30mm^3 lipid pool through different motion directions under a 100Hz shear and compression load.*

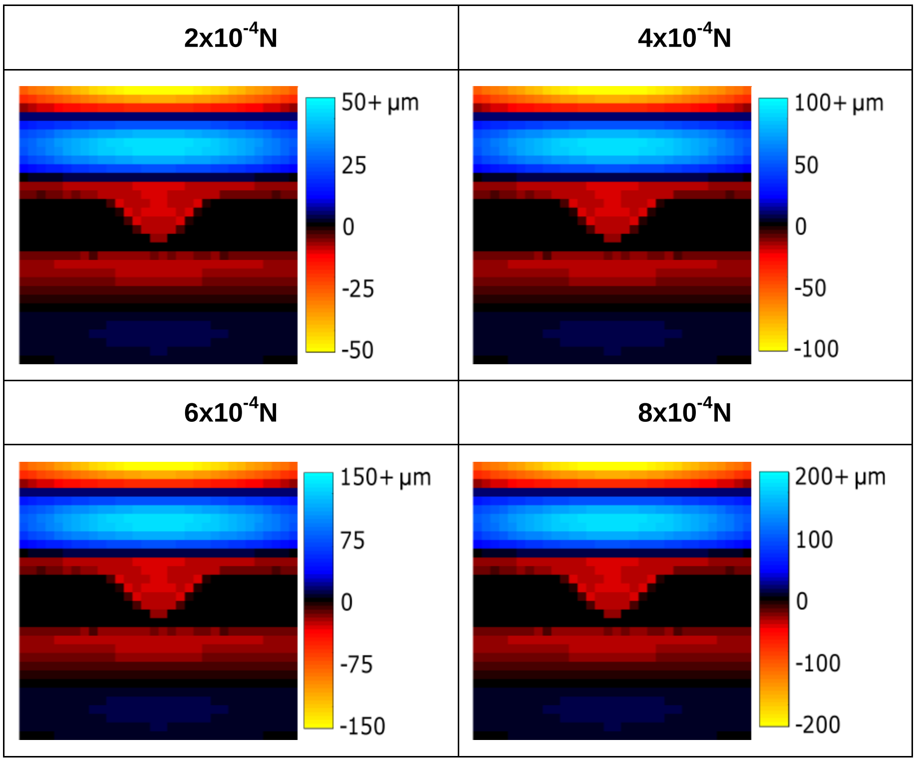

Figure 3.6: *Wave displacement through the 70% stenosis model with a 30mm*^{3} *lipid pool under a 100Hz shear load of varying magnitude.*

3.3.3) Disease Development and Excitation Frequency

The excitation frequency was varied in tandem with the lipid pool size. Figure 3.7 shows the wave behaviour through the 70% stenosis plaque, with a variety of compositions and at a selection of excitation frequencies. The amount of wave displacement through the plaque increases from negligible in the fibrous composition through to significant in the lipid composition. Though the lipid plaque peaks and trough of the wave form are clearer at the lower two frequencies, and become disrupted at the higher two frequencies.

Figure 3.8 shows how the wave behaviour at 100Hz through lipid and fibrous plaques changes with stenosis sizes. Although there are differences between the two plaques types, beyond size there are little differences between stenosis sizes of the same composition. Figure 3.9 shows the wave behaviour through 70% stenosis lipid and fibrous plaques with different fibrous cap thicknesses, at an excitation frequency of 100Hz. There is no visible change with an increase in fibrous cap thickness for the fibrous composition. In the lipid composition an increase in the fibrous cap, results in reduced wave amplitudes.

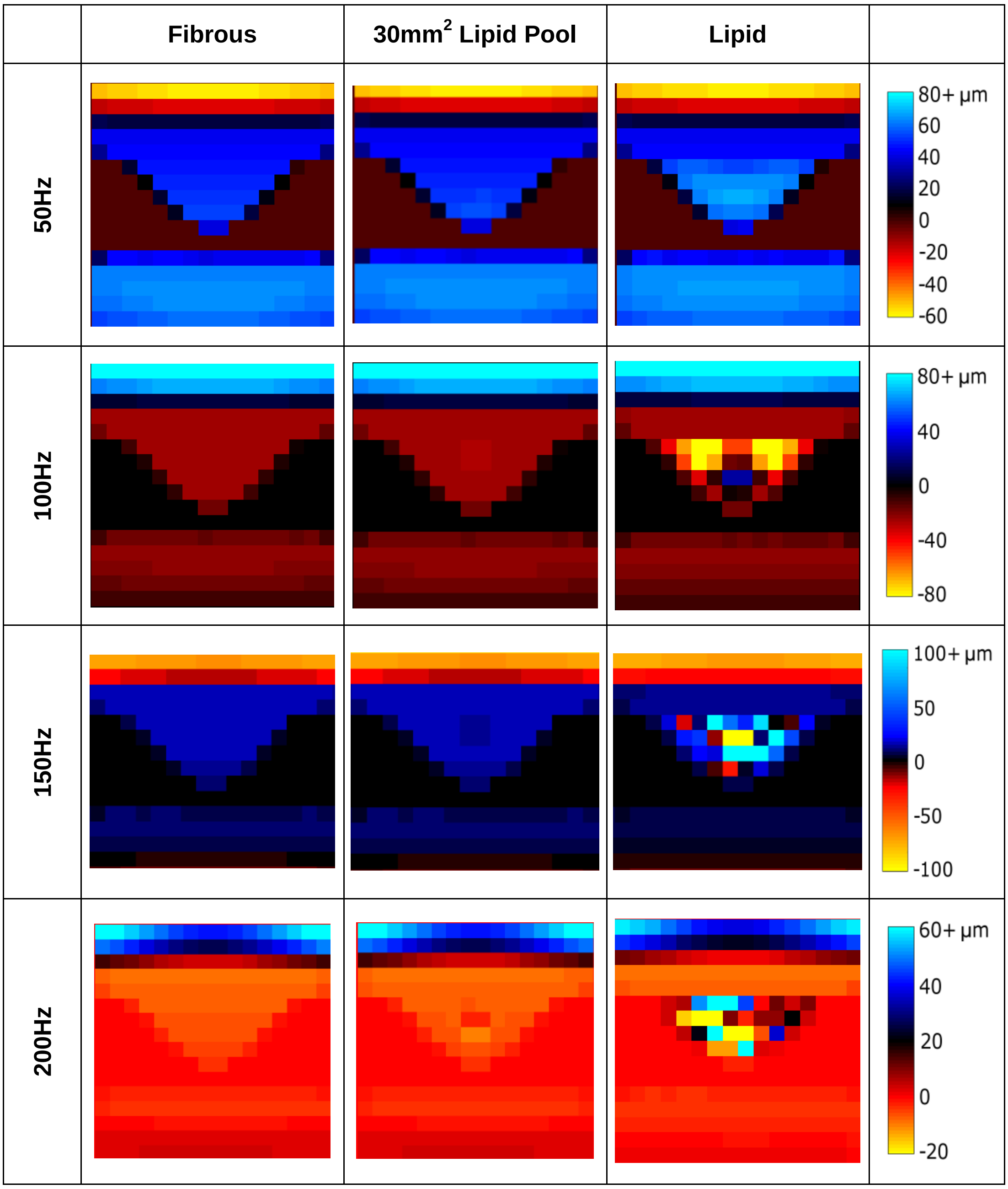

Figure 3.7: *Wave displacement through 70% stenosis plaques of different compositions and various excitation frequencies.*

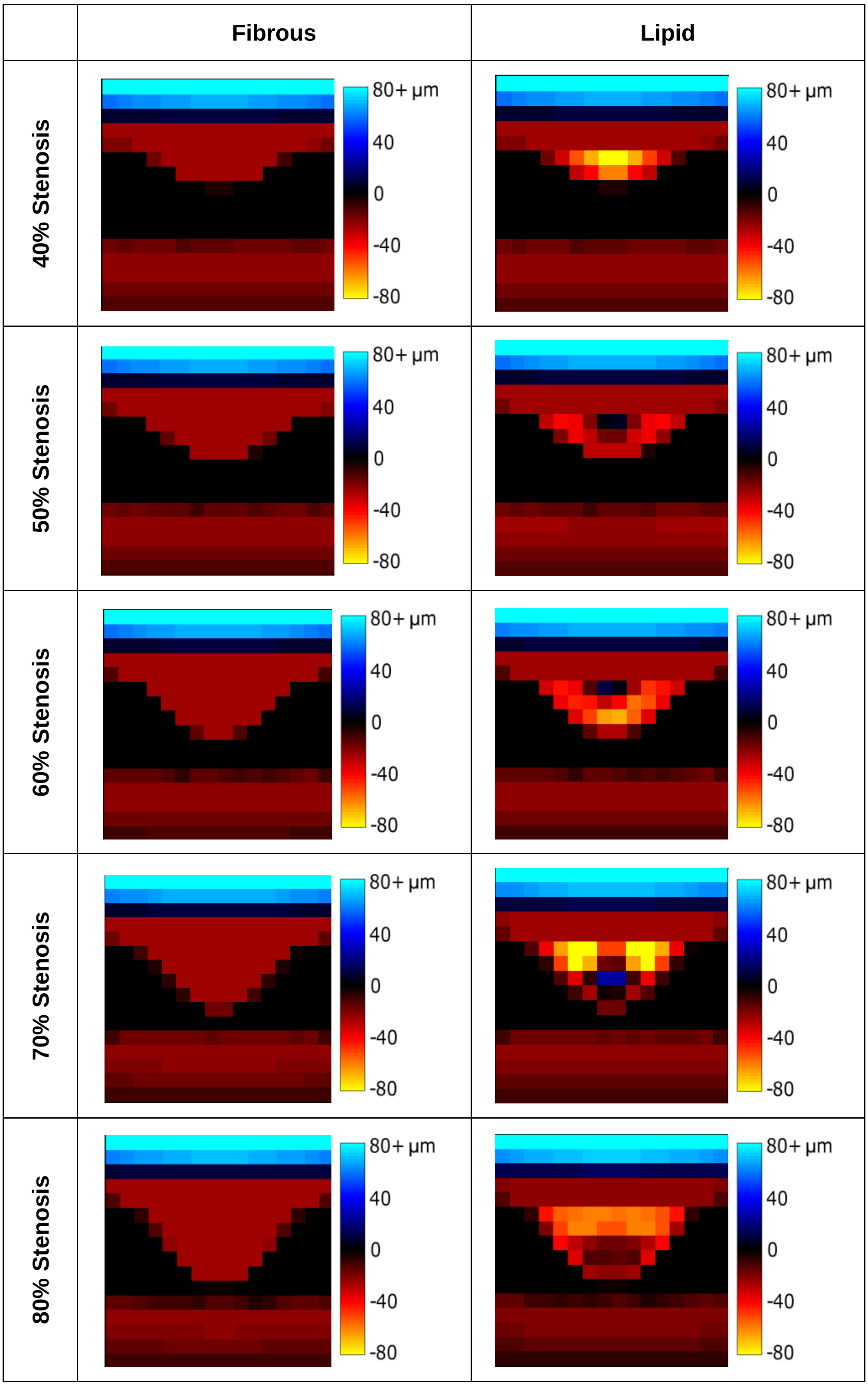

Figure 3.8: *Wave displacement through the fibrous and lipid plaques of various stenosis sizes at an excitation frequency of 100Hz.*

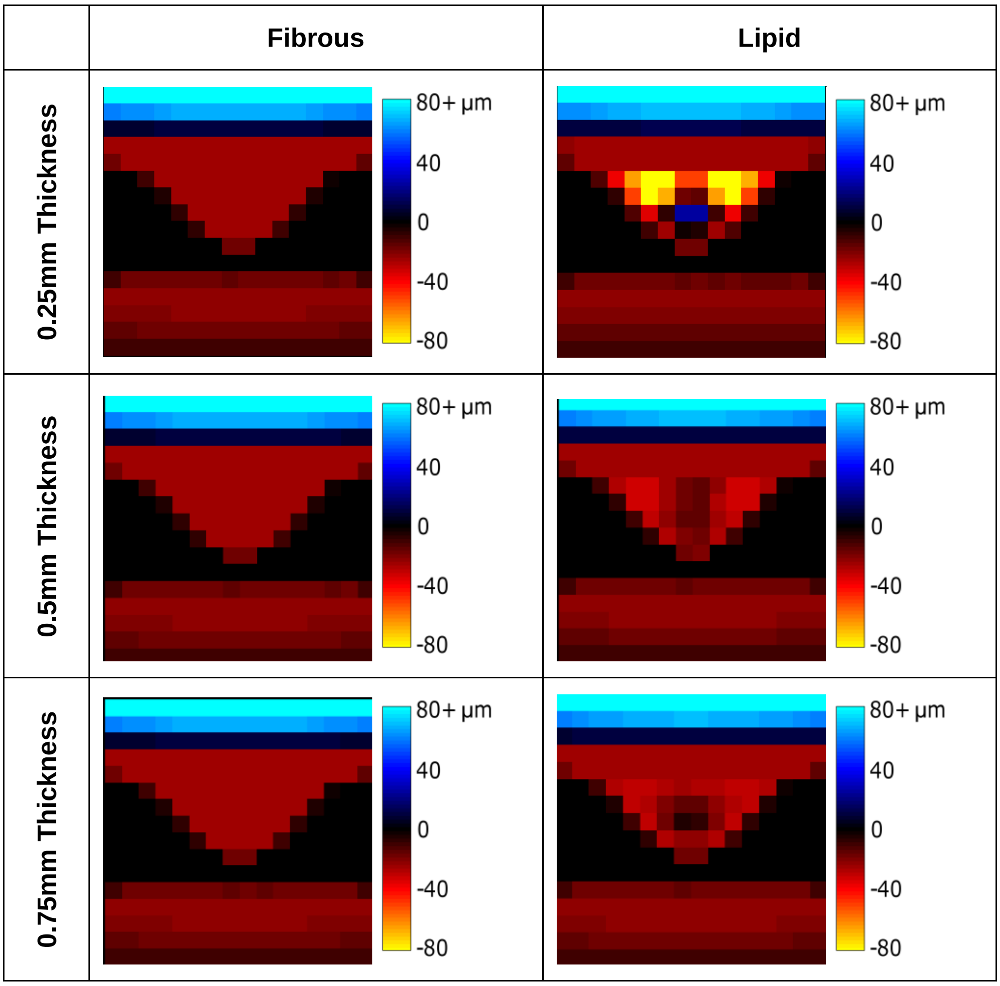

Figure 3.9: *Wave displacement through lipid and fibrous 70% stenosis plaques with different fibrous cap thicknesses at an excitation frequency of 100Hz.*

3.4) Discussion

3.4.1) Imaging Plane

By comparing the wave propagation through a fibrous and lipid plaque in different imaging planes, Figure 3.4 shows that there is significant loss of wave propagation through the Y-Z plane as opposed to the X-Y plane. This can be attributed to the presence of the lumen. In the X-Y plane, the waves throughout the surrounding tissue are also disturbed by the existence of the vessel and lumen, causing a discontinuity in the wave. Nevertheless, the vessel and plaque are the focus of this work and boundaries of these are much easier to depict against the lumen in the Y-Z plane. It was therefore decided to continue the analysis in this chapter and Chapter 4, solely through the Y-Z plane.

3.4.2) Mechanical Parameters

With reference to Figure 3.5 both the wave displacements from the shear and compression load in the X direction, are non-planar and appear to be quite disrupted above the plaque. In the Y direction the shear load creates linear wave propagation with a central discontinuity whilst the compression load shows very poor propagation below the lumen. The shear load in the Z direction shows clear planar wave propagation, although it begins to attenuate strongly below the lumen. The compression load, in the Z direction, shows symmetric waves but these are non-planar with a central discontinuity.

The combination of a shear load, with wave displacement taken through the Z direction, gives the ideal planar wave propagation. For this reason, this loading direction and displacement direction shall be taken forward. However it should be noted that these results are highly idealised, and also depend on the choice of boundary conditions. It has been shown in experimental studies that compressional wave excitation (Sinkus *et al.* 2000) and wave displacement in other planes are compatible with MRE (Papazoglou *et al.* 2008).

As discussed in Chapter 2, load magnitude is adjusted during an experimental scan to achieve the correct level of wave penetration. Figure 3.6 clearly supports this observation, as the wave patterns are exactly the same for each load magnitude, the only difference being the displacement magnitudes. For future simulations, it was decided to use a load magnitude of $6x10^4$N, because the peak wave displacements are similar to the peak phase values seen in the experimental phantoms of Chapter 5; where the displacement of the computational and phase of the experimental complex wave images both serve as the input to the inversion algorithm.

Figure 3.7 shows that an increase in excitation frequency is beneficial for resolving the 30mm^3 lipid pool. At 50Hz, there is negligible difference between the fibrous plaque and 30mm^3 lipid pool plaque but at 100Hz the presence of the 30mm^3 lipid pool becomes more clearly apparent. MRE excitation frequency has been strongly linked to spatial resolution (Sinkus *et al.* 2000, Parker *et al.* 2005) as the wavelength decreases small inclusions become more easily resolved. However, relating back to Chapter 2, as the excitation frequency increases, the loss modulus and thus attenuation increases. Following on from this, the resolution of the lower vessel wall is significantly decreased at higher frequencies, due to the increased attenuation of the wave.

It also appears that as the excitation frequency increases, the waves within the lipid become increasingly disrupted. At 50Hz and 100Hz within the lipid plaque discernible wave peaks and troughs can be seen. However at 150Hz and 200Hz the wave behaviour is much less clear. The depth of the stenosis is approximately 5mm, at 50 Hz the wavelength through the lipid pool is 6mm, at 100Hz it is 3mm, at 150Hz it is 2mm and at 200Hz it is 1.5mm. At 100Hz a full wavelength is captured within the lipid volume however as the wavelength decreases further, significant wave interference begins to occur. It is hypothesised that when the wavelength of the excitation wave through the lipid medium becomes increasingly smaller than the size of the lipid volume, the wave interference is generated by reflections at the boundary. This theory is supported by the beginning of disrupted wave behaviour that can be seen through the 80% lipid stenosis of Figure 3.8, i.e. as the lipid volume is increasing with stenosis size for a fixed excitation frequency. The 3D curvatures of the lipid volumes make it difficult to confirm this hypothesis.

Similar observations to these were made in (Thomas-Seale *et al.* 2011a). To progress the conclusions of the effect of varying frequency and lipid pool size, the methodology needs to be evolved to give an estimate of stiffness. This shall be conducted in Chapter 4.

3.4.3) Disease Development

Figure 3.7 also shows that, to a greater or lesser extent depending on frequency, that the wave disruption through the plaque increases with increased lipid composition. In Figure 3.8, there are negligible differences between the wave propagation through the fibrous plaques of different stenosis sizes. However through the lipid plaque, where the wavelength is much shorter, there are more pronounced differences between stenosis sizes; as the lipid volume increases more of the wavelength can fit within the plaque.

The lipid pool is modelled as a low stiffness solid, similar to the analysis of Holzapfel et al. (2002) and informed by the mechanical characterisation of Loree et al. (1994). However a questionable point is whether lipid should be modelled as a low stiffness solid or a liquid. In an MRE analysis this is a key definition, since shear waves can-not propagate through liquid. Further research in the mechanical characterisation of lipid in the frequency range of interest would be beneficial to future simulations of MRE through atherosclerosis.

The variation of fibrous cap thickness in a fibrous plaque creates minor differences in the wave images of Figure 3.9. This component of the plaque is very thin compared to the other plaque geometry and the pixel size, and it also has a similar shear modulus to the fibrous material within the plaque. The fibrous cap thickness creates a big difference between the wave patterns through the lipid plaques, most notably between a thickness of 0.25mm and 0.5mm. This effect is due to an overall increase in structural stability, as the fibrous cap surrounds the lipid pool in a fully lipid plaque.

3.5) Conclusion

The investigation of wave response with the variation of the imaging and mechanical MRE parameters has identified the ideal imaging plane, load direction and magnitude required to yield the clearest wave images through idealised atherosclerotic plaques, summarised in Table 3.4. The resolution of the lipid pool was shown to increase with excitation frequency.

Parameters	**Load**		**Imaging Plane**
	Direction	**Magnitude (N)**	
Ideal	Shear	$6x10^{-4}$	Y-Z

Table 3.4: *Ideal parameters: load direction, magnitude and imaging plane.*

In terms of disease development, the stenosis size was shown to affect the wave image through fully lipid plaques, only with regards to the consequent change in lipid pool size. An increase in lipid pool volume increased wave displacement through the plaque whilst an increase in fibrous cap thickness decreased wave displacement through the lipid plaque composition. To progress the conclusions drawn from the variations in geometry and excitation frequency, the quantitative change in predicted stiffness shall be investigated in Chapter 4.

Chapter 4

The Variation of Local Shear Modulus with Atherosclerotic Plaque Composition

4.1) Introduction

Identifying the change in mechanical properties of an atherosclerotic plaque with disease development is the crux of the clinical question posed in this thesis. This chapter aims to investigate whether this is possible in an idealised computational simulation of MRE. Beyond the MRE investigation by Woodrum et al. (2006) into stenosis size, this is the first application of MRE to image the elasticity of atherosclerosis. In tandem this chapter also aims to optimise some of the MRE parameters that can be varied experimentally.

Chapter 4 progresses the research that was undertaken in Chapter 3, to quantitatively analyse the variables in Table 4.1. The parameters under analysis in Chapter 4 fall into two categories. The disease development parameters incorporate the variation of plaque geometry and the composition of the components. The preliminary results of this work are displayed in (Thomas-Seale *et al.* 2013). The remaining parameters are mechanical, imaging or inversion and in theory these may be optimised. The effect of introducing artificial noise will also be investigated. The selection of parameters that were investigated to a satisfactory conclusion in Chapter 3, were fixed during this chapter. However, it was decided that incorporating the variables of excitation frequency, stenosis and lipid pool size already explored in Chapter 3, into the quantitative analysis of this chapter, could lead to more conclusive results.

Traditionally MRE and the associated inversion algorithms have been applied to predominately large, homogeneous organs such as the liver (Klatt *et al.* 2006), brain (Sack *et al.* 2008) and breast (Sinkus *et al.* 2005). Recently more complex applications have been investigated introducing additional difficulties such as smaller sizes, boundaries, physiological motion and inherent inhomogeneities for example the prostate (Sahebjavaher *et al.* 2014), aorta (Kolipaka *et al.* 2012), heart (Sack *et al.* 2009) and lungs (Mariappan *et al.* 2011).

The 2D Helmholtz inversion algorithm is constrained by a large number of assumptions which are outlined in section 2.2.6. The application of this algorithm to atherosclerotic plaques invalidates several of these due to the presence of inhomogeneities and boundaries. In addition the size of the plaque compared to the excitation wavelength limits the resolution of the technique. Whilst developing a more applicable algorithm is beyond the scope of this thesis, the simulation of MRE through idealised atherosclerotic plaques can explore the hypothesis whilst removing some of the complications and constraints that would be encountered *in vivo* such as physiological motion and imaging resolution.

4.2) Methods

4.2.1) Overview

The methodology of this chapter combines and extends what has already been described in Chapter 2 and 3; where steady state complex wave images taken through idealised atherosclerotic plaques form the input into the inversion algorithm. The variables under consideration are outlined in Table 4.1. The load direction, magnitude and imaging plane are fixed, based upon the work conducted in Chapter 3. The parameters that may be varied experimentally are investigated first; the imaging variables of pixel size and averaging method, followed by the excitation frequency, the filters of the inversion algorithm and rheological model by which the shear modulus and viscosity are extracted. The filters limits shall also be explored in terms of the signal to noise ratio of additional artificial noise. Each parameter shall be varied with respect to the lipid pool size, as this is the most straight forward way of incrementally varying the stiffness of the plaque. This will then allow the disease variables to be investigated under the identified optimum technique parameters.

The lipid pool shall be discussed in isolation once the technique parameters for this chapter have been fixed. Followed by the remaining parameters reflecting disease development; stenosis size, fibrous cap thickness, fibrous cap structure and lipid pool cholesterol. The results of this chapter will be displayed predominantly quantitatively; the variations of average shear modulus through atherosclerotic plaques with various parameters. Where relevant for explanatory purposes a selection of elastograms will also be discussed.

	Mechanical Parameters			**Imaging and Inversion Parameters**						
Variables Under Analysis	**Load Direction**	**Load Magnitude (N)**	**Excitation Frequency (Hz)**	**Imaging Plane**	**Pixel Resolution (mm^2)**	**Averaging Method**	**Upper Filter (m^{-1})**	**Lower Filter (m^{-1})**	**Rheological Model**	**Artificial Noise (SNR)**
Pixel Resolution and Averaging Method	Shear	6x10^{-4}	100	Y-Z	0.5/1/1.5/2	Mean/ Median	N/A	N/A	Voigt	Noiseless
Excitation Frequency	Shear	6x10^{-4}	50-200 (10)	Y-Z	0.5	Mean	N/A	N/A	Voigt	Noiseless
Rheological Model	Shear	6x10^{-4}	50/100/150/ 200	Y-Z	0.5	Mean	N/A	N/A	Voigt/ Maxwell	Noiseless
Filter Limits	Shear	6x10^{-4}	100	Y-Z	0.5	Mean	5-100000	25-100000	Voigt	Noiseless/ 5/40/500
Stenosis and Lipid Pool Size	Shear	6x10^{-4}	100	Y-Z	0.5	Mean	N/A	N/A	Voigt	Noiseless
Lipid Pool Cholesterol	Shear	6x10^{-4}	100	Y-Z	0.5	Mean	N/A	N/A	Voigt	Noiseless
Fibrous Cap Thickness	Shear	6x10^{-4}	100	Y-Z	0.5	Mean	N/A	N/A	Voigt	Noiseless
Fibrous Cap Structure	Shear	6x10^{-4}	100	Y-Z	0.5	Mean	N/A	N/A	Voigt	Noiseless

Table 4.1: *MRE simulation parameters: mechanical, imaging, inversion and disease. The shaded parameters were investigated in Chapter 3.*

	Disease Variables				
Variable(s) Under Analysis	**Stenosis Size (%)**	**Lipid Pool**		**Fibrous Cap**	
		Size (mm^3)	**Cholesterol (%)**	**Thickness (mm)**	**Structure**
Pixel Resolution and Averaging Method	80	0/10/20/30/40/50/Total	0	0.25	Cellular
Excitation Frequency	80	0/10/20/30/40/50/Total	0	0.25	Cellular
Rheological Model	80	0/10/20/30/40/50/Total	0	0.25	Cellular
Filter Limits	80	0/Total	0	0.25	Cellular
Stenosis and Lipid Pool Size	40/50/60/70/80	0/10/20/30/40/50/Total	0	0.25	Cellular
Lipid Pool Cholesterol	70	10/20/30/40/ Total	0/25/50	0.25	Cellular
Fibrous Cap Thickness	70	0/10/20/30/ Total	0	0.25/0.5/ 0.75	Cellular
Fibrous Cap Structure	70	0/10/20/30/40/Total	0	0.25	Cellular/ Hypocellular/ Calcified

Table 4.1: *(continued) MRE simulation parameters: mechanical, imaging, inversion and disease. The shaded parameters were investigated in Chapter 3.*

The methodology of Chapter 4 is an extension of Chapter 3. Where there are no alterations in the method, it shall not be repeated. Where it is appropriate to review the method for completeness, some aspects will be rediscussed.

The plaque geometry incorporated into the simulations was created using the computer aided design software Rhinoceros version 3.0. These simulations were then generated and run on the finite element analysis software Abaqus/ CAE version 6.10-1. The displacement results were extracted from Abaqus/ CAE and formatted using Microsoft Office Excel. The inversion algorithm was supplied by collaborators at the MR Elastography Group, Charité Univesitätsmedizin Berlin and run on MATLAB R2011a.

4.2.2) Geometry

The geometries and geometric disease development used in the simulations of Chapter 4 are exactly the same as those created in Chapter 3, discussed in section 3.2.2. The 80% stenosis geometry shall be used to assess the technique parameters, since this provides the largest range of lipid pool sizes within its structure. Beyond this, to investigate the ability of the technique to image disease development, the 70% stenosis shall be used as the primary geometry.

4.2.3) Material Properties

To repeat what was stated in the material properties section of Chapter 3; ideally the material properties and rheological models used in the simulations would be based upon informed experimental work in the desired frequency range. However to conduct this work was beyond the scope of the thesis, therefore the information was taken from the most applicable literature that was available. In some cases this has led to parameters being extrapolated and simplifications in material behaviour being assumed.

The material properties of each component of the model were the same as those described in section 3.2.3, with the exception of a variation in the lipid pool and fibrous cap compositions. The lipid composition was varied in terms of the cholesterol percentage, explored by Loree et al. (1994). The fibrous cap composition was varied in terms of structure, taken from the work of Lee et al. (1991); cellular, hypocellular or calcified. The method used to extract the material properties from the additional compositions described in these two studies, was the same as that described in section 3.2.3. Using the highest frequency under consideration in each study, the storage and loss moduli were based on the Maxwell rheological model. The material properties are summarised in Table 4.2, with the variation in lipid and fibrous cap compositions.

Tissue	Density (kgm^{-3})	Shear Modulus (kPa)	Bulk Modulus (kPa)	Shear Viscosity (Pas)
Surrounding Tissue	1047*	2.3**	-	17.0**
Intima	1047*	150.0[+]	-	80.0[++]
Fibrotic Intima	1047*	221.0[+]	-	80.0[++]
Media	1047*	34.0[+]	-	80.0[++]
Diseased Media	1047*	757.0[+]	-	80.0[++]
Adventitia	1047*	50.0[+]	-	80.0[++]
Fibrous Cap – Cellular	1047*	208.4[#]	-	19820.0[#]
Fibrous Cap – Hypocellular	1047*	375.0[#]	-	48610.0[#]
Fibrous Cap – Calcified	1047*	937.3[#]	-	121492.0[#]
Lipid – 0% Cholesterol	1047*	0.1[##]	-	6.4[##]
Lipid – 25% Cholesterol	1047*	0.2[##]	-	11.9[##]
Lipid – 50% Cholesterol	1047*	0.5[##]	-	37.6[##]
Blood	1060[^]	-	2.7x10^{6}[^]	-

Table 4.2: *Material properties: idealised atherosclerotic plaques. *(Hoskins 2010), **(Klatt et al. 2010), [+](Holzapfel et al. 2002), [++](Valdez-Jasso et al. 2011), [#](Lee et al. 1991), [##](Loree et al. 1994), [^](Hoskins 2007).*

In addition to varying the composition of the lipid pool and fibrous cap, the Voigt and Maxwell model shall be compared in terms of extracting the shear modulus and viscosity from the inversion algorithm. These models shall be discussed here and referenced in section 4.2.9, because the behaviour of these models with frequency is pertinent to the simulation as well as the extraction of the stiffness moduli. As discussed in section 2.2.4, under small-amplitude oscillatory loads, the response of a viscoelastic material depends upon the loss angle, δ, defined by the arctangent of the loss to storage modulus ratio. When the stress and strain are in phase and the loss angle is 0° the material response is purely elastic and when the loss angle is 90°, purely viscous. For completion the models shall be repeated and expanded to define the loss angle in Table 4.3.

	Voigt	**Maxwell**
$G(\omega)$	$\mu + i\omega\eta$	$\frac{i\omega\eta\mu}{\mu + i\omega\eta}$
$G'(\omega)$	μ	$\frac{\omega^2\eta^2\mu}{\mu^2 + \omega^2\eta^2}$
$G''(\omega)$	$\omega\eta$	$\frac{\omega\eta\mu^2}{\mu^2 + \omega^2\eta^2}$
δ	$a\tan\frac{\omega\eta}{\mu}$	$a\tan\frac{\mu}{\omega\eta}$

Table 4.3: *Voigt and Maxwell model.*

The Voigt and Maxwell models, in the context of the tissues used in these simulations, are arguably not sophisticated enough to model complex tissue behaviour, they are also not ideal under wide frequency ranges (Yasar *et al.* 2013). However, using these models means that the same two parameters can be extracted directly from the inversion algorithm.

The storage modulus of the surrounding tissue, fibrous cap and lipid pool, modelled using the Maxwell model, varies within 10% of the 100Hz value. The storage modulus of the Voigt model is constant. The loss angle of the Maxwell model peaks at $\omega = \frac{\mu}{\eta}$. The decreasing loss modulus with frequency dominates the loss angle making the tissues more elastic with frequency. Conversely the Voigt model demonstrates an increasing loss angle with frequency, so the tissue behaviour becomes more viscous.

The effect of the rheological model is primarily the variation of the loss modulus and hence the loss angle. With reference to the conclusions of Chapter 2, as long as the loss angle remains towards the elastic end of the viscoelastic spectrum then the simulation of MRE yields accurate results. The only materials where the rheological model defines loss angles that are beyond the range investigated in Chapter 2 are the media and adventitia. The combination of the Voigt model and relatively high shear viscosity in comparison to the shear modulus leads to high loss angles. However since these layers of the arterial wall are incredibly thin, even in comparison to the plaque and also do not occur inside the region of interest, the effect of the highly viscous behaviour of these layers should not be too detrimental to the results. The ability of the two rheological models to extract the shear modulus and viscosity from the dynamic modulus shall be also be investigated.

The main parameter under investigation is the shear modulus. In the cases where the values needed to be extrapolated from the literature, they are a good approximation for each tissue and are comparable to those described by Holzapfel et al. (2002). Research into the shear viscosity of arterial tissue is extremely limited; Valdez-Jasso et al. (2011) obtained their values for the Voigt model from arterial pressure-area dynamics. However the shear viscosity applied to the fibrous cap and lipid pool in this study, were extrapolated from the most applicable literature (Lee *et al.* 1991, Loree *et al.* 1994). Unlike the shear moduli figures, the shear viscosity approximations are much higher than those documented in other arterial literature, namely (Valdez-Jasso *et al.* 2011). This property of arterial tissue is not well researched and although the shear viscosity values for the fibrous cap and lipid pool appear to be over-estimated, it is difficult to pinpoint to what degree since there is no specific literature in the frequency range of interest. The combination of the shear modulus, shear viscosity and Maxell models in these tissues, leads to loss angles towards the elastic end of the viscoelastic range, therefore they are unlikely to suffer from the severe attenuation effects shown in Chapter 2. Although the shear viscosity is not the main parameter under investigation in this thesis, the validation of future work would require appropriate shear modulus and viscosity mechanical testing of each arterial tissue in the frequency range of interest.

4.2.4) Loads

The conclusions of Chapter 3, led to a fixed load magnitude of $6x10^{-4}$N in the shear direction. The frequency of the load was varied through 50Hz to 200Hz in 10Hz intervals.

4.2.5) Boundary Conditions

As Chapters 2 and 3 have both discussed, symmetric boundary conditions were applied as a time efficient method of approximating non-reflecting boundaries.

4.2.6) Mesh

The model was meshed in the same manner as that discussed in Chapter 3, section 3.2.6.

4.2.7) Results Extraction

Based on the results of Chapter 3, the results shall be extracted through a 2D Y-Z plane with reference to Figure 3.2, along the length of the vessel. The ROI was isolated on the atherosclerotic plaque, protruding into the lumen.

Unfortunately in reality the resolution of MRE cannot be increased without significant development to the technique. Without such development, reducing the pixel size leads to a decrease in the signal to noise ratio. The MRE pixel size, used in later experimental chapters is 1.84mm^2 by a 10mm slice thickness. When exploring the feasibility of MRE imaging atherosclerotic plaques, this imaging resolution is a limitation of the technique. The magnitudes of the atherosclerotic plaque geometry displayed in Table 3.2, range from smaller than the pixel size to marginally bigger. Since the purpose of using computational simulations to explore MRE through atherosclerosis is to identify what the optimum parameters of the technique are, this allows more flexibility when it comes to resoltion. The pixel size was varied, similarly to Chapter 2, between 0.5mm and 2mm, in increments of 0.5mm. The size of the region of interest had to be varied slightly to accommodate the pixel size. The results were extracted through a 2D plane therefore the slice thickness was not a parameter in this study.

4.2.8) Artificial Noise

Artificial noise was added to the simulated wave images of the 80% stenosis fibrous, lipid and 30mm^3 lipid pool compositions. In doing so, the accuracy of the results under the presence of a more realistic noisy data set could be explored. It also allows the effectiveness of the filters in the inversion algorithm to be assessed.

Extracting the signal to noise ratio (SNR) from MRE data is complicated; the random noise needs to be isolated from the inherently fluctuating signal. In addition the background regions of the experimental phase images in this thesis were subject to very large ghosting artefacts, which is unsurprising considering the amount of motion generated in the scan.

In the field of simulating MRE, noise has been added to idealised computational data based on various SNR values; Papazoglou et al. (2008) added SNR in the range of 3 to 100, Plewes et al. (2000) between 500 and 5000 and McGee et al. (2011) between 2 and 9. It is apparent that a diverse range of SNR values are considered appropriate to add to simulated data. Ideally the SNR values added to the simulated data in this chapter would reflect those taken from the experimental data of Chapter 5 and 7.

McGee et al. (2011) propose a method of extracting SNR from MRE data that is compatible with the experimental data collected in this thesis i.e. the noise is estimated from the background of the relatively artefact free magnitude images. This technique is explained in full in Appendix B. McGee et al. (2011) consider the standard deviation through the background of the magnitude, divided by the Rician correction factor of 1.66, equal to the standard deviation of the noise in the phase image. The Rician correction factor corrects the bias between the Rician distribution of noisy magnitude data and a Gaussian distribution (Gudbjartsson and Patz 1995). The amplitude of the first harmonic across the phase images is taken as the magnitude of the signal. Once averaged over the ROI, the SNR is then calculated as the ratio of these two values, equation 4.1.

$$SNR = \frac{\overline{A_s}}{\sigma_n} \tag{4.1}$$

$\overline{A_s}$ is the amplitude of the complex wave averaged through the ROI. σ_n is the standard deviation of the background noise through the magnitude image, taken through a region free from ghosting artefacts, averaged over each magnitude image corresponding to a phase offset and divided by the Rician correction factor.

Extracting the SNR from the data in Chapters 5 and 7, yielded values ranging between approximately 3 and 40, and 0.7 and 4 respectively; the means of these values are shown in Tables 5.5, 5.6 and 7.3. Chapter 6 discusses whether these SNR values are a true reflection of the SNRs seen in the experimental work. Values of 5, 40 and 500 were investigated in this chapter, as a representation of the SNRs extracted from later chapters.

Random normal distributed noise, with a zero mean and a standard deviation of σ_n was added to the complex wave image. σ_n was calculated for each region of interest, based upon the value of $\overline{A_s}$ averaged over an area surrounding the ROI, including the vessel wall above and below. The shear stiffness results were taken as a mean, standard deviation and a standard error averaged over 20 noisy images.

4.2.9) Image Processing

The theory of the inversion algorithm is given in detail was Chapter 2, section 2.2.6, which led to the Helmholtz inversion algorithm, equation 4.2. The inversion algorithm was programmed in MATLAB and can be found in Appendix A. The real and imaginary displacements of the complex wave image are used at the input to the inversion algorithm.

$$G(\omega) = \frac{-\rho\omega^2 U}{\nabla^2 U} \tag{4.2}$$

This chapter explores some of the variable parameters of the algorithm; the filter limits, the spatial averaging and extraction of the shear modulus and viscosity via a rheological model.

A 2D Butterworth bandpass filter is used in tandem with this algorithm, similar to other research conducted by the Berlin MR Elastography Group; it has been found to suppress noise and compression wave components (Klatt *et al.* 2006, Klatt *et al.* 2007). The Butterworth bandpass filter contains a high and low pass filter, effectively isolating the frequencies between the higher and lower frequency thresholds. The frequency response of the low and high pass Butterworth filters are displayed in equation 4.3 and 4.4 respectively (Haidekker 2010); where A_G is the gain, ω_0 the cut-off frequency and n the order. The high and low pass cut-off frequencies were varied and effect on the predicted shear modulus over the plaque explored. The orders of the filters were set at 5.

$$H_L(\omega) = \frac{A_G}{1+\left(\omega/\omega_0\right)^{2n}} \tag{4.3}$$

$$H_H(\omega) = \frac{A_G}{1+\left(\omega_0/\omega\right)^{2n}} \tag{4.4}$$

In theory the idealised wave data in these simulations should not require filters, as the results are noiseless and the tissue is modelled as incompressible. However for completion the filter limits were explored in relation to the idealised results and also those with artificial noise added to the complex wave images.

Spatial averaging using the mean and median was investigated. The median is useful when there are extreme outliers, for example noise or the artefacts seen in Chapter 2. However Chapter 2 analyses homogeneous data and the atherosclerotic plaques under analysis in this chapter are inhomogeneous, therefore the mean was also explored.

Finally to mirror the material properties of section 4.2.3, the Voigt and Maxwell rheological models shall be used to extract the shear and viscous modulus from the dynamic shear modulus, using the equations in Table 4.3.

4.3) Results

4.3.1) Spatial Resolution and Averaging

Figure 4.1 shows how the predicted plaque shear modulus varies with lipid pool size, with changes in both pixel resolution and averaging method. All pixel sizes and both averaging methods show a decrease in shear modulus between a fully fibrous and lipid plaque. The 0.5mm^2 and 1mm^2 pixel size combined with the mean averaging method capture the graduated decrease in plaque stiffness with increasing lipid composition.

4.3.2) Excitation Frequency

The changes in wave behaviour and elastograms with excitation frequency are shown in Figure 4.2. In the wave images the resolution of the lipid pool increases with frequency however the waves become disrupted at 200Hz. The quality of the elastograms are poor; they are highly inhomogeneous and dominated by pixel artefacts. Some features are recognisable and the clarity of them improves with frequencies above 100Hz; the lipid pool and the interface between the plaque and lumen.

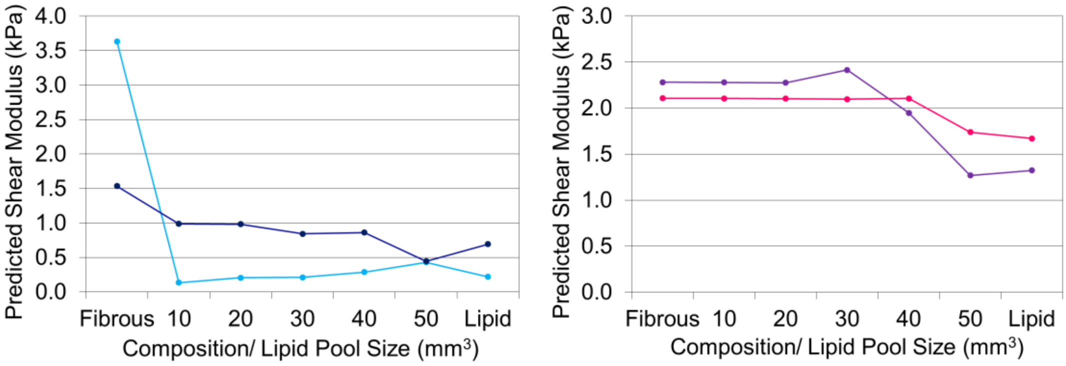

a) 0.5 and 1.0mm^2 Pixels, Median

b) 1.5 and 2.0mm^2 Pixels, Median

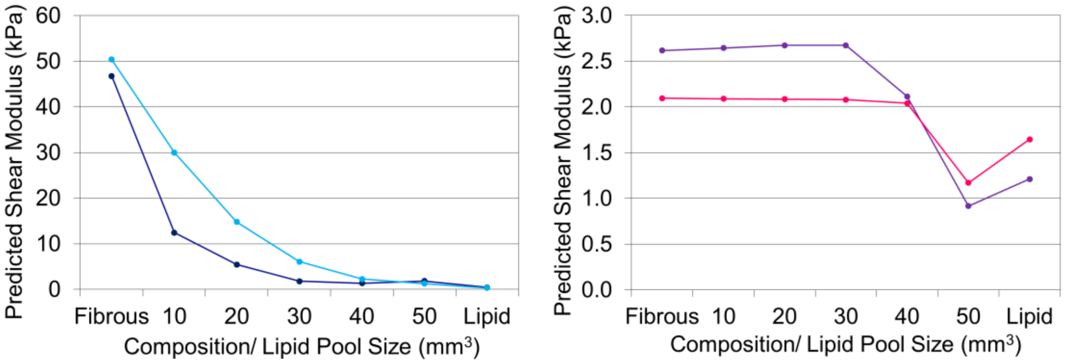

c) 0.5 and 1.0mm^2 Pixels, Mean

d) 1.5 and 2.0mm^2 Pixels, Mean

Pixel Size (mm^2) ● 1.5 ● 2.0 ● 0.5 ● 1.0

Figure 4.1: *The variation of predicted shear modulus with lipid composition through an 80% stenosis plaque at an excitation frequency of 100Hz, using different spatial resolutions and averaging methods.*

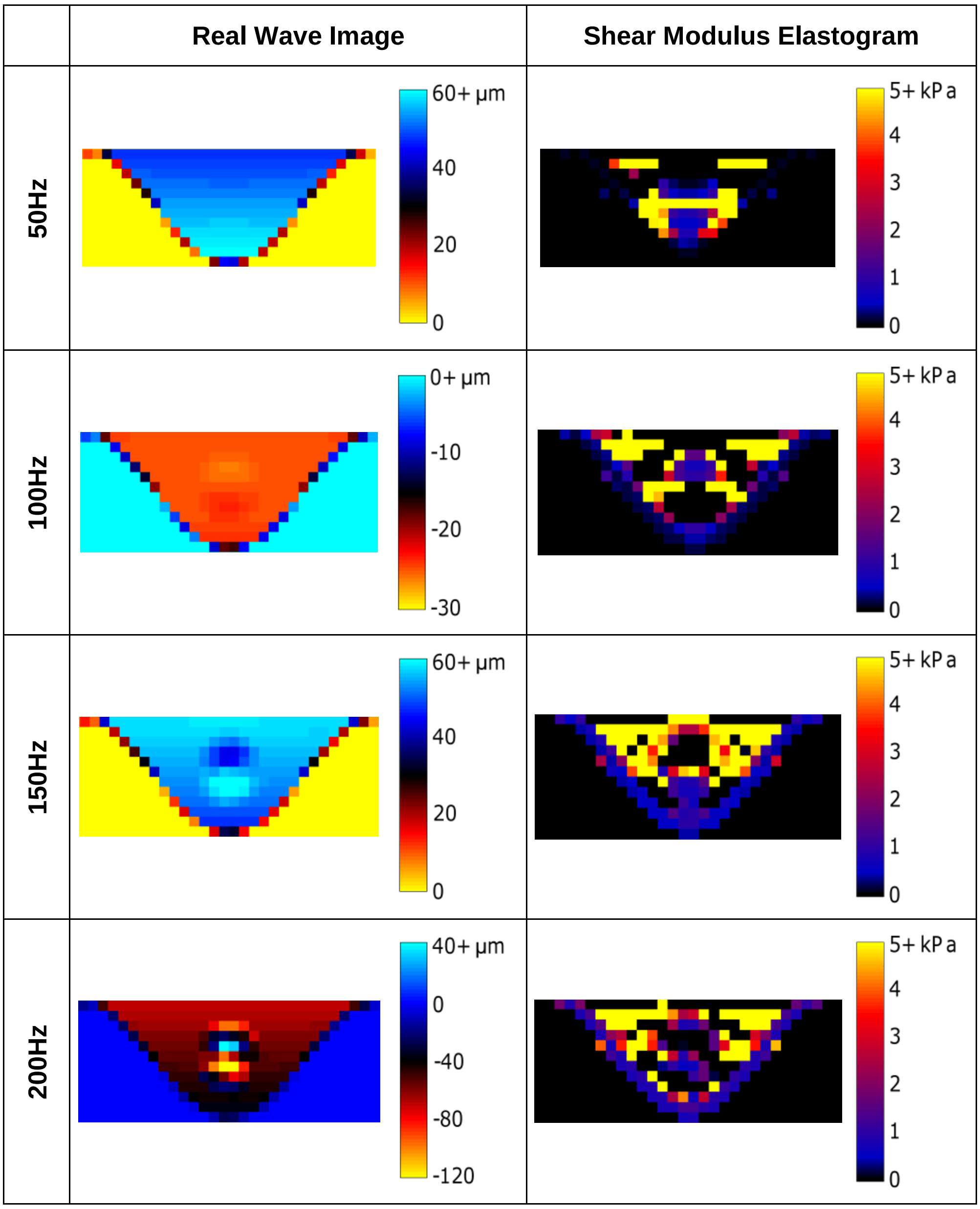

Figure 4.2: *The real component of the complex wave images and the shear modulus elastograms through an 80% stenosis plaque with a 30mm^{3}lipid pool at different excitation frequencies.*

The variation of predicted shear modulus through an 80% stenosis plaque with frequency and lipid pool size is shown in Figure 4.3. The shear modulus predication for each plaque composition varies with frequency, however all frequencies show a decrease in shear modulus with increasing lipid volume. The magnitudes of the shear moduli increase between 50Hz and 90Hz and appear to converge around 100Hz.

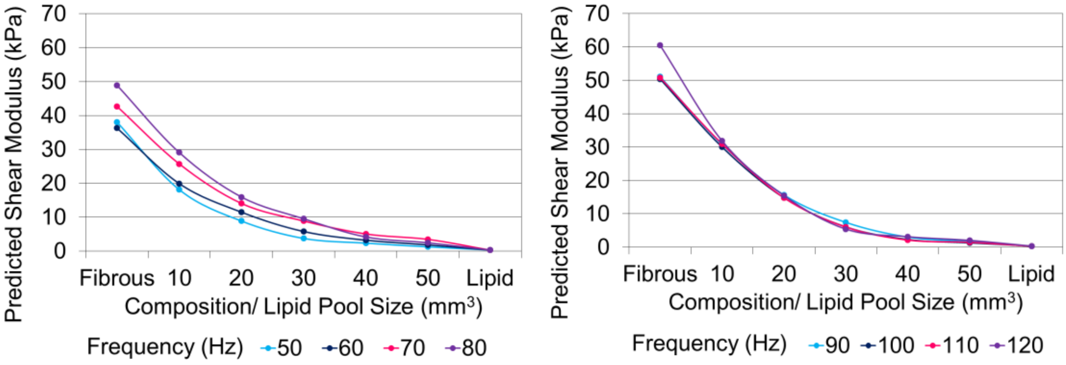

a) 50 – 80Hz b) 90 – 120Hz

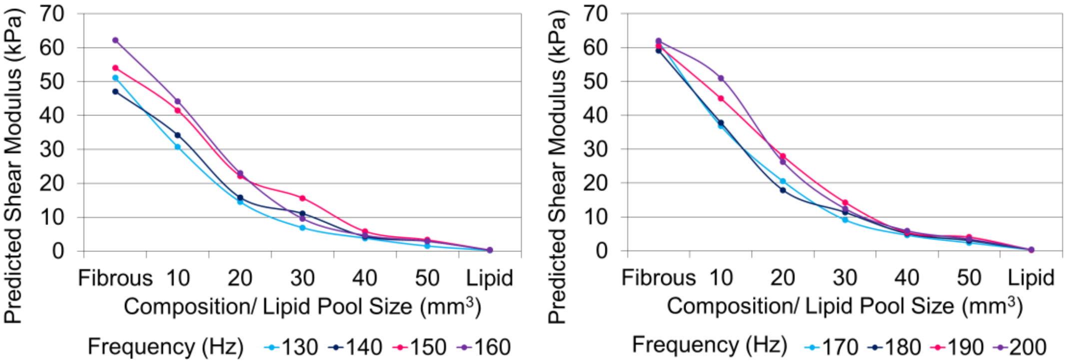

c) 130 – 160Hz d) 170 – 200Hz

Figure 4.3: *The variation of predicted shear modulus with lipid composition through an 80% stenosis plaque at different excitation frequencies, using a spatial resolution of 0.5mm^2 and the mean averaging method.*

The mean predicted shear modulus through the plaques and the standard deviation for the excitation frequencies 50Hz, 100Hz, 150Hz and 200Hz are shown in Table 4.4. The magnitudes of the predicted shear moduli are underestimated compared to the simulated values seen in Table 4.2. This is highlighted by comparing the predicted and simulated shear moduli for a fully fibrous plaque, which is dominated by fibrotic intima tissue of shear modulus 221kPa. The standard deviations are very high compared to the mean shear moduli.

4.3.3) Inversion Parameters

Figure 4.4 compares the extraction of the shear modulus using the Voigt and Maxwell rheological models. The Voigt model demonstrates a decrease in shear modulus as the composition of the plaque becomes less stiff. The Maxwell model shows a decrease in shear modulus between the fully fibrous and lipid plaques, but it does not show a clear trend for the compositions in between.

	Predicted Mean Shear Modulus (Standard Deviation) (kPa)						
	Composition/ Lipid Pool Size						
Frequency (Hz)	**Fibrous**	**$10mm^3$**	**$20mm^3$**	**$30mm^3$**	**$40mm^3$**	**$50mm^3$**	**Lipid**
50	38.0 (55.8)	18.1 (49.0)	8.9 (39.1)	3.7 (23.1)	2.3 (15.1)	1.3 (13.6)	0.3 (0.7)
100	50.4 (71.9)	30.0 (74.7)	14.8 (58.8)	6.0 (42.6)	2.3 (27.3)	1.3 (19.8)	0.3 (1.0)
150	54.0 (76.7)	41.5 (99.3)	22.2 (78.2)	**15.6** (79.9)	5.8 (43.7)	3.3 (29.6)	0.3 (0.5)
200	**62.0** (90.9)	**51.0** (141.2)	**26.3** (78.3)	12.4 (76.9)	**5.9** (42.8)	**3.5** (29.7)	**0.4** (0.8)

Table 4.4: *The mean and standard deviation of the mean predicted shear modulus through various compositions at different excitation frequencies. The highlighted values represent the closest predicted shear moduli to the simulated moduli.*

The thresholds of a high and low pass Butterworth filter were varied in the inversion algorithm, the effect that this has on the predicted shear modulus is shown in Figure 4.5. Three 80% stenosis compositions and noise levels were investigated; in each graph the change in shear modulus is only due to the filter threshold. In the results that contain noise, the mean is displayed and the standard error bars are omitted since the combination of error bars with the logarithmic scale were barely visible. The most important observation in these figures is that, under noiseless conditions, there is a definitive difference in the shear modulus of different composition plaques at very low thresholds for the high pass filter and very high thresholds for the low pass filter. As the SNR decreases, so does the ability to identify a difference in shear modulus with composition.

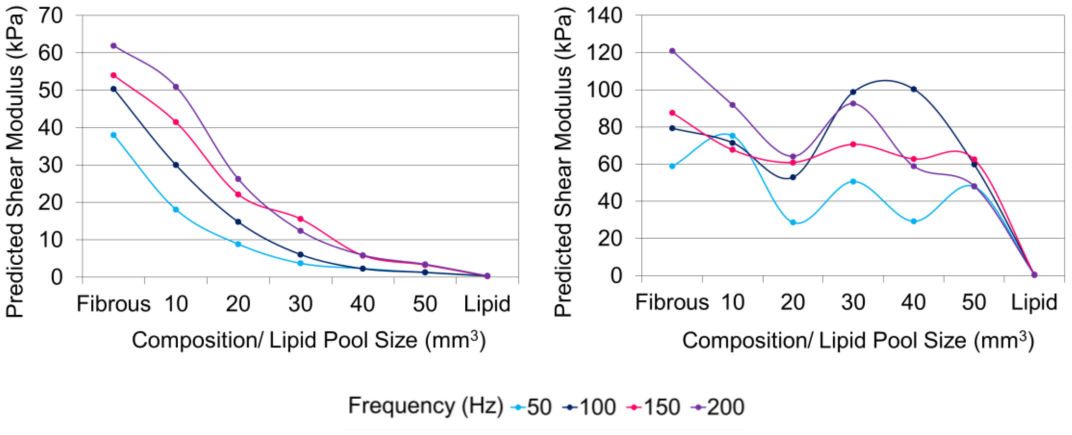

a) Voigt

b) Maxwell

Figure 4.4: *The variation of the predicted shear modulus with lipid composition, extracted using different rheological models, through an 80% stenosis plaque, at a selection of excitation frequencies.*

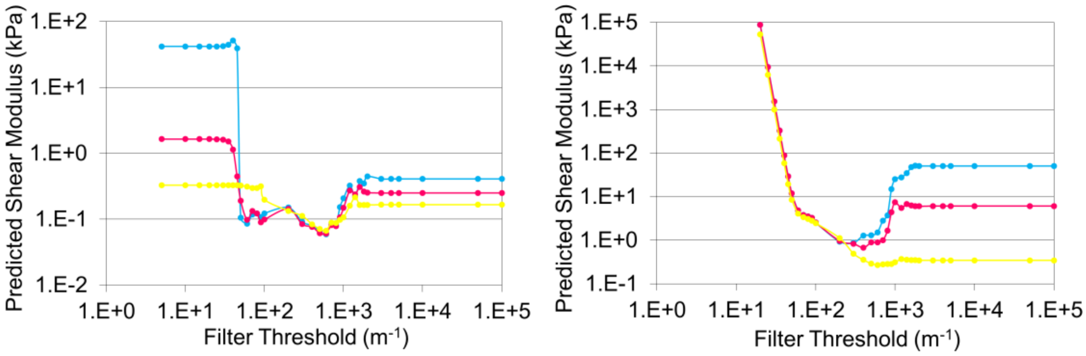

a) Noiseless, High Pass Filter

b) Noiseless, Low Pass Filter

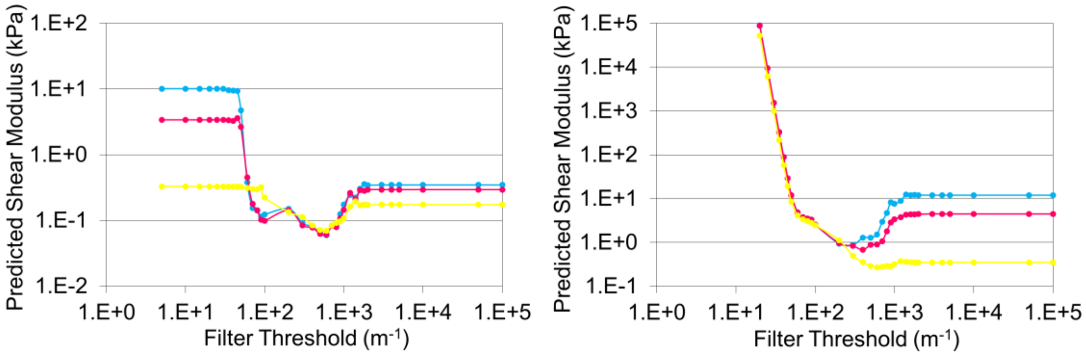

c) SNR 500, High Pass Filter

d) SNR 500, Low Pass Filter

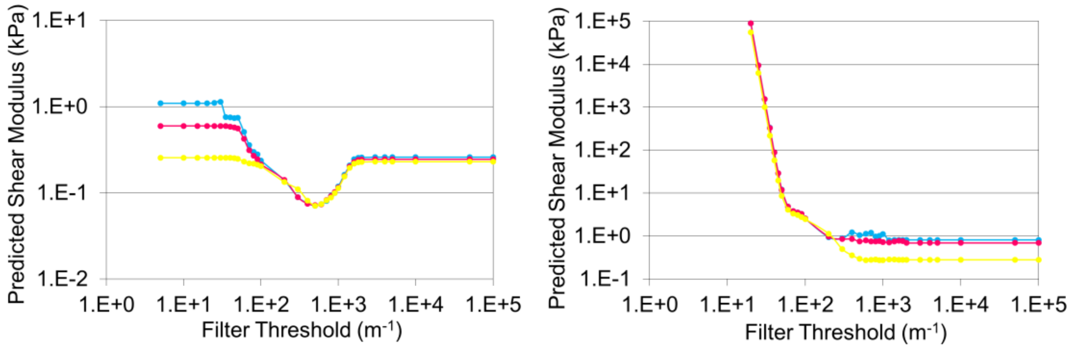

e) SNR 40, High Pass Filter

f) SNR 40, Low Pass Filter

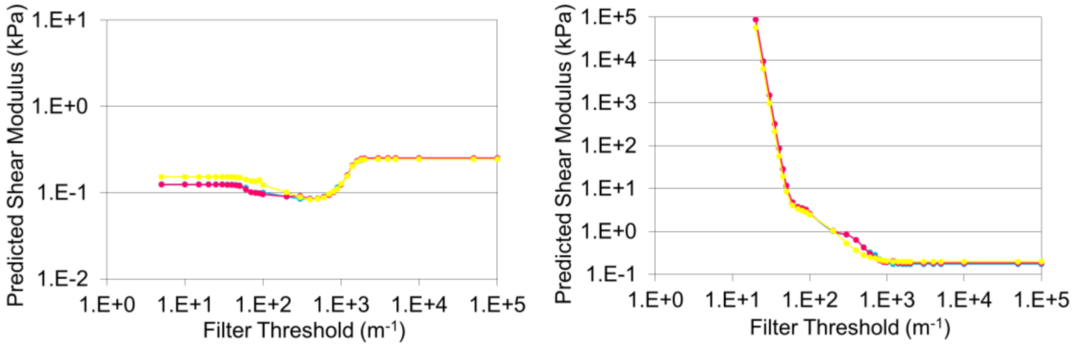

g) SNR 5, High Pass Filter

h) SNR 5, Low Pass Filter

Figure 4.5: *The variation of predicted shear modulus with high or low pass filter threshold through an 80% stenosis plaque; each image contains three different plaque compositions and each pair of images is conducted at a different SNR.*

Figure 4.6 shows the variation of the predicted shear modulus through the 80% stenosis compositions at various noise levels, with and without a Butterworth bandpass filter of thresholds 100000m^{-1} and 5m^{-1}. The plots including noise display the standard error over 20 images. The algorithms ability to detect the change in plaque composition deteriorates as the noise level increases, with and without filters. The predicted shear moduli have lower magnitudes when filters are utilised compared to the non-filtered results.

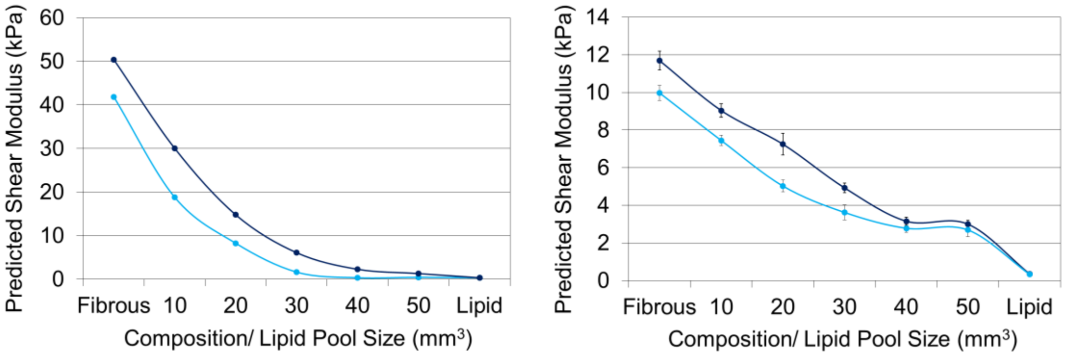

a) Noiseless

b) SNR 500

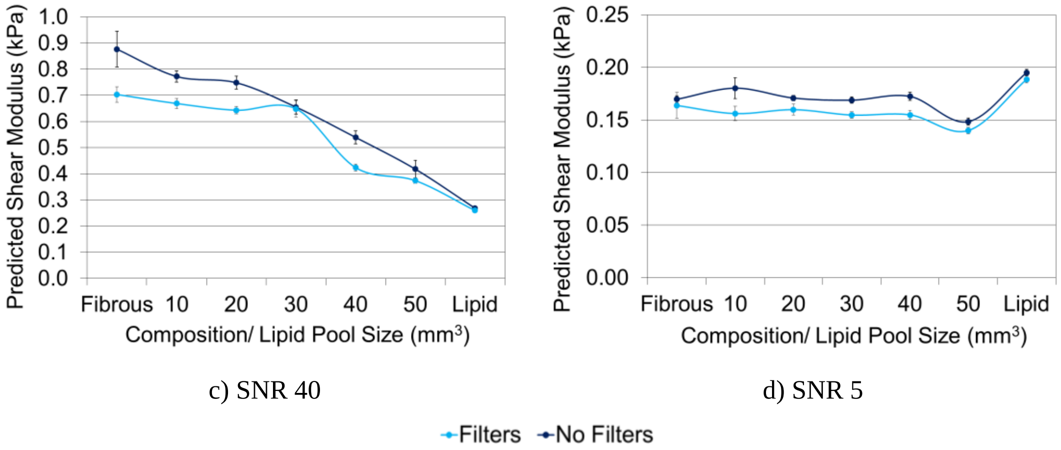

Figure 4.6: *The variation of predicted shear modulus with lipid composition through an 80% stenosis plaque, subject to different levels of SNR with and without filters.*

4.3.4) Disease Development

The disease development results are all presented at a pixel resolution of 0.5mm^2, an excitation frequency of 100Hz, omitting noise and filters and extracted using the Voigt model. Figure 4.7 shows how the predicted shear modulus through different stenosis sizes, changes with lipid pool size. In all stenosis sizes, the predicted shear modulus decreases with increasing lipid composition.

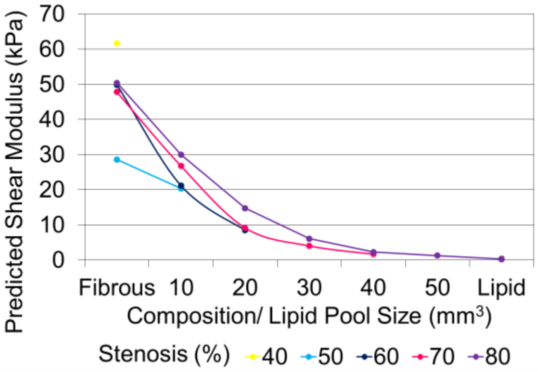

Figure 4.7: *The variation of predicted shear modulus with lipid composition through different stenosis sizes.*

The wave images and shear modulus elastograms through a 70% stenosis plaque with a fibrous and lipid composition and 10mm^3, 20.mm^3, 30mm^3 and 40mm^3 lipid pools are shown in Figure 4.8 using the identified ideal parameters of 0.5mm^2 pixel size, a mean averaging method, the Voigt model, omitted noise and no filters. The wave displacement through the lipid pool, increases with increasing lipid compositions, although this does not correspond to a more visible lipid pool in the elastogram. The elastograms of the fully fibrous and lipid plaques are noticeably more homogeneous and have less artefacts than the one containing a lipid pool volume.

Figure 4.9 demonstrates the variation of shear modulus as the cholesterol of the lipid pool changes, in a 70% stenosis plaque. The cholesterol composition ranges between 0 and 50%, with increases in cholesterol resulting in a higher shear modulus, except in the 10mm^3 lipid pool composition.

The change in shear modulus with increasing fibrous cap thickness through 70% stenosis plaques of various compositions is displayed in Figure 4.10. The fibrous cap thickness does not change the local stiffness of most plaque compositions. The difference in fibrous cap structure on the shear modulus through 70% stenosis plaques of various compositions is shown in Figure 4.11. Cellular, hypocellular and calcified fibrous cap structures were analysed; with the plaque stiffness increasing with each change in composition.

	Real Wave Image	**Shear Modulus Elastogram**
Fibrous	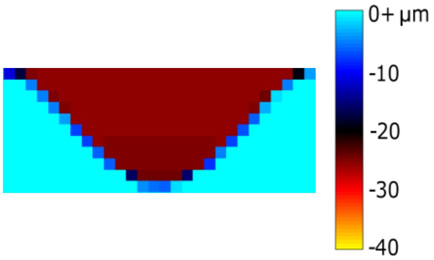	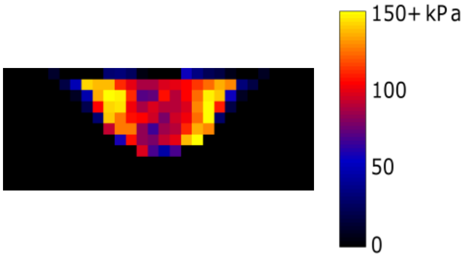
10mm^3 Lipid Pool	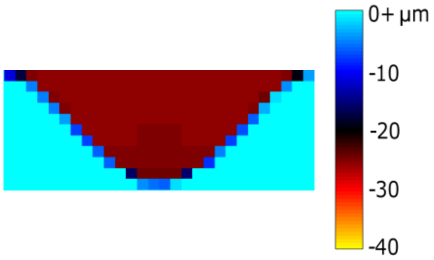	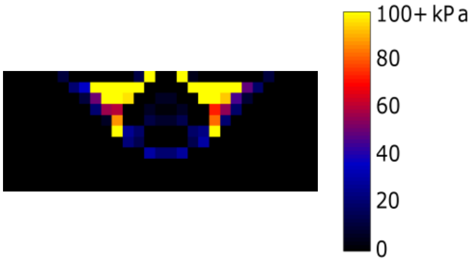
20mm^3 Lipid Pool	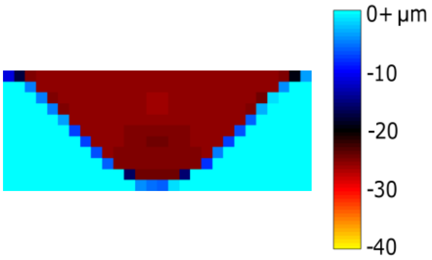	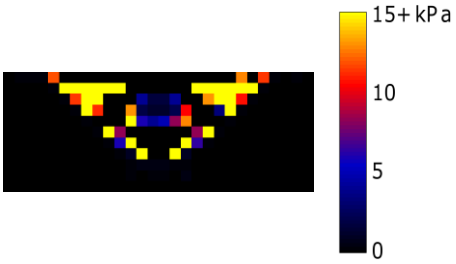
30mm^3 Lipid Pool	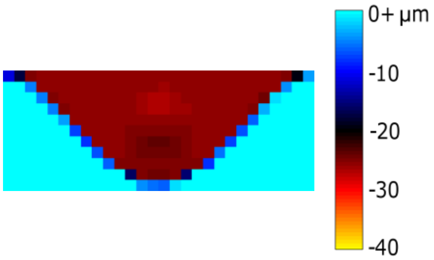	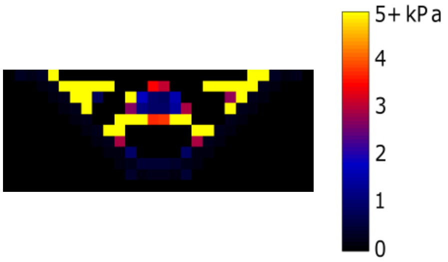
40mm^3 Lipid Pool	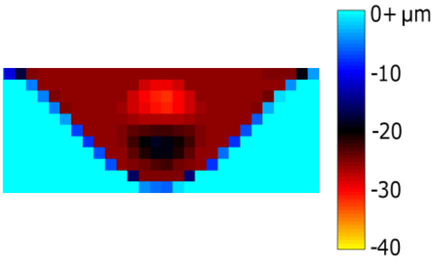	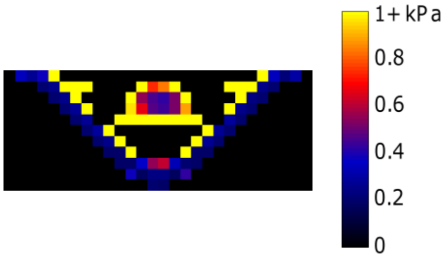

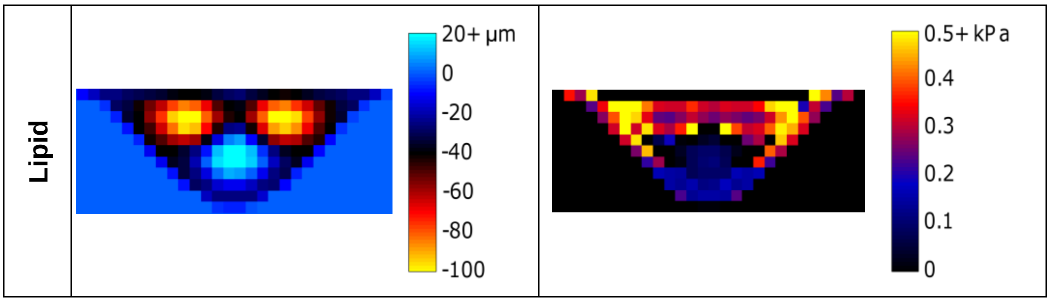

Figure 4.8: *The real component of the complex wave images and the shear modulus elastograms through a 70% stenosis plaque with different lipid compositions.*

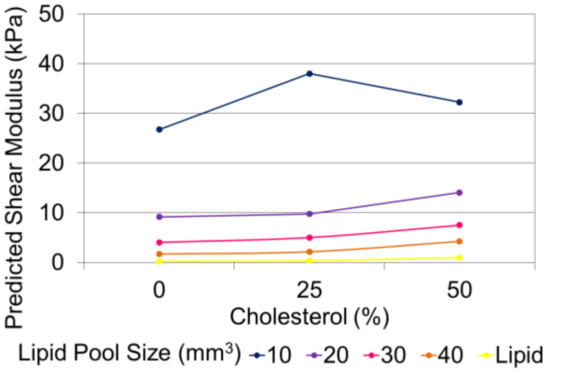

Figure 4.9: *The variation of predicted shear modulus with lipid pool cholesterol through different compositions of a 70% stenosis plaque.*

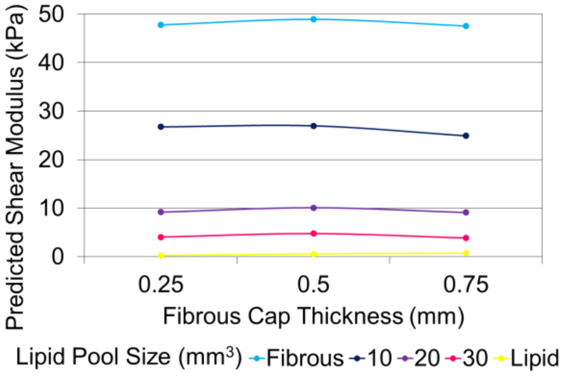

Figure 4.10: *The variation of predicted shear modulus with fibrous cap thickness through different lipid compositions of a 70% stenosis plaque.*

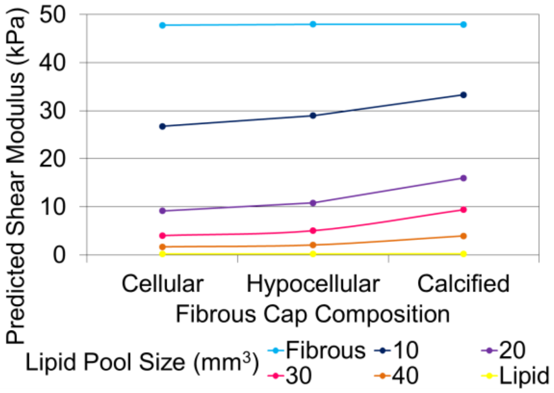

Figure 4.11: *The variation of predicted shear modulus with different fibrous cap structures through different lipid compositions of a 70% stenosis plaque.*

4.4) Discussion

The elastograms of this chapter suffer from two types of pixel artefacts. Boundary artefacts, along an interface with a medium of no stiffness, were discussed in Chapter 2, section 2.2.6. The effect of the zero displacement through the lumen creates an artefact of reduced shear moduli, two pixels deep along the interface. The artefact is generated by inflated spatial derivatives between the wave displacement in the tissue and the lack of displacement in the lumen. The spatial derivatives combine to form the Laplacian term of the inversion algorithm, equation 4.2, and hence results in underestimated shear moduli.

The artefacts caused by boundaries between different mediums present as pixels of over and under estimated stiffness, the most noticeable of which are the ‘black hole’ artefacts. The behaviour of the spatial derivatives across boundaries was demonstrated numerically in Chapter 2, section 2.2.6. The root cause of these artefacts is the second order spatial derivatives of the step change in wave behaviour over a boundary. Where there are errors in the spatial derivatives, hence the Laplacian, the shear modulus is incorrectly calculated. When the Laplacian is the incorrect sign, the shear modulus becomes negative and is equated to negligible, leading to the ‘black hole’ artefacts. For clarity, this group of artefacts will be described as pixel artefacts.

These artefacts can be seen in Figure 4.2 and they are clearly detrimental to the accuracy of the elastograms. Focussing on the ‘black hole’ artefacts; Figure 4.2 shows that for a fixed composition a change in frequency leads to elastograms with artefacts in different positions, demonstrating that these pixel artefacts are dependent not only on the position of the boundary but the specific interaction of the wave across the boundary. Whether this is due to the phase of the wave of as it passes over the boundary or the frequency of the wave is not obvious. However, if a change in frequency can lead to the presence or lack of pixel artefacts, then a combination of data obtained at different frequencies or a multi-frequency analysis could alleviate the lack of data in these ‘black hole’ pixels.

All the artefacts have been included in the spatially averaged shear modulus results through the plaques; otherwise a large amount of the ROI would be discounted. However these artefacts, in the presence of the intrinsic boundaries and homogeneities within an atherosclerotic plaque, highlight the need to develop a more applicable inversion algorithm. As proposed in Chapter 2, the theory of inverting the equation of motion specific to a shape as discussed by Kolipaka et al. (2009) could be applied to the cylindrical nature of arteries. This algorithm would intrinsically deal with the lumen boundary. The FEA based minimization inversion algorithm proposed by Van Houten et al. (2001) lends itself to well to the computational work conducted here and has also demonstrated superior handling of inhomogeneities albeit at larger sizes than the plaques under analysis in this research.

4.4.1) Spatial Resolution and Averaging

The effect of decreasing resolution can be seen as the algorithms ability to resolve the differences in plaque stiffness with reducing lipid pool size. This is most apparent in the 1.5mm^2 and 2.0mm^2 pixel trends of Figure 4.1. Using both averaging methods, the 2mm^2 pixel only shows a drop in stiffness for a 50mm^3 lipid pool and a totally lipid plaque, whereas the 1.5mm^2 pixel shows a decrease from the 40mm^3 lipid pool upwards.

The difference between the averaging methods can be seen more clearly in Figure 4.1 in the 0.5mm^2 and 1mm^2 pixel sizes. The mean averaging method can compute the higher stiffnesses of the predominately fibrous plaques. Using the mean averaging method, the two pixel sizes are showing quite similar results, with the 0.5mm^2 pixel giving a fractionally smoother trend, due to its ability to resolve the plaque composition better. Of course, the pixel resolution could have been increased further, but the magnitudes are always likely to be underestimated due to the size of the ROI relative to the wavelength.

The 0.5mm^2 pixel gives an obvious and smooth decrease in elastogram stiffness with increase in lipid pool volume, therefore was taken as the ideal resolution along with the mean averaging method.

4.4.2) Excitation Frequency

The changes in the wave images with lipid composition and excitation frequency were discussed in section 3.4.2. Similarly in Figure 4.2, as the excitation frequency increases the waves in the lipid pool become quite disrupted, to the point that in the fully lipid composition at 150Hz and 200Hz the elastogram loses its symmetry. However, conversely, at 50Hz the 30mm^3 lipid pool is barely resolved because the wavelength is so large.

The quality of the elastograms in Figure 4.2 are poor, this is due to several reasons. The small ROI, compared to the relatively larger wavelength underestimates the high stiffness components of the plaque. The inhomogeneity of the structure creates numerous ‘black hole’ artefacts and boundary with the lumen means that the fibrous cap stiffness is lost in the artefact generated by this interface. The increase in frequency alleviates the underestimated stiffnesses through the plaque and in the fibrous cap, as the wavelength shortens. In the 100Hz and above elastograms the lipid pools are just about perceptible as an area of reduced stiffness. The high stiffness of the fibrous tissue surrounding the lipid pool is coming through in the elastogram, although again the clarity is disrupted by the boundary between the two tissues.

Figure 4.3 confirms these observations. Overall each frequency shows a decrease in plaque stiffness with a reduction in lipid pool size. Increasing the frequency between 50Hz and 90Hz significantly increases the predicted shear moduli in each composition. Between 90Hz and 110Hz the trend appears to converge along a smooth curve, with very little difference between the three frequencies. Above 120Hz, the shear moduli increase again but the curves become much less smooth, this coincides with the disrupted waves noted at higher frequencies. Based on this, 100Hz was chosen as the optimum frequency to take forward.

Comparing Table 4.4 and Table 4.2 shows that the mean predicted shear moduli are largely underestimated. For example the fully fibrous plaques are composed of fibrotic intima 221kPa and surrounded by a fibrous cap of 208kPa, yet the inversion algorithm is yielding values between 38kPa and 62kPa. The fully lipid plaques, with a lipid shear modulus of 107Pa, combined with the fibrous cap, gives values between 200-500Pa, much closer to the values that you would expect. Of course all the plaques are highly inhomogeneous so direct comparison of the simulated plaque stiffness with the stiffness predicted by the MRE procedure would be extremely difficult. Overall the predicted shear moduli in Table 4.4 increase with frequency, particularly through the more fibrous compositions. Since all the magnitudes are underestimated, the highest frequency, bar one composition, demonstrates the predicted values that are closest to the simulated ones.

There is an apparent increase in accuracy with both lipid composition and frequency. These are linked to the resolution of the technique with frequency. Although the 2D Helmholtz algorithm is subject to several limitations, stemming from inhomogeneities and boundaries, even if the resulting artefacts were omitted, there is a question of detectability in terms of the small size of the plaque. Parker et al. (2005) explain this phenomenon in terms of shear wave theory, one that is applicable to all elastography techniques that are founded upon shear waves. Inhomogenieties create a local disturbance in the displacement wave field, the strength of this disturbance increases with increasing frequency, leading to increased contrast and detectability (Parker *et al.* 2005). This leads to a trade-off between frequency and attenuation; increasing the frequency increases detectability but also increases the attenuation of the wave and thus decreases penetration depth (Parker *et al.* 2005).

Atherosclerotic plaques have more complicated features over inclusion studies that have been conducted in the literature (Sinkus *et al.* 2000, Van Houten *et al.* 2001). Beyond the many prior mentioned complications, atherosclerotic plaques can be relatively less stiff that the surrounding vessel wall, whereas MRE techniques are often aimed at pathologic tissues with an increased stiffness such as cancerous lesions or fibrosis. In this Chapter, more accurate stiffness predictions have been noted with frequency and an increasing lipid composition. Frequency and wavelength are inversely proportional, so where an increase in frequency leads to an increased detectability, a decrease in wavelength is also seen. Since lower a shear modulus also results in a decrease in wavelength, it is hypothesised that the wavelength could be the common factor between the changes in accuracy with frequency and composition. More in-depth research into the interaction of the inversion algorithm with inclusion size, stiffness and excitation frequency is required to confirm this.

Table 4.4 also demonstrates the behaviour of the standard deviation through the elastograms with frequency and composition. The overriding impression from this data is that the standard deviations are very high, larger than the means. The artefacts that appear in the elastograms were discussed in detail at the beginning of this section and are the cause of these large standard deviations. In some cases the standard deviation increases with frequency and composition stiffness, but it is difficult to identify whether this is a separate observation or one tied to the increased the magnitude of the mean.

4.4.3) Inversion Parameters

It is clear from Figure 4.4, that the Voigt model is best suited to extracting the shear modulus from the dynamic modulus yielded by the computational MRE technique. With reference to Table 4.3, the Maxwell storage and loss moduli are dependent on both the shear modulus and viscosity and the relationship between the parameters are more complicated than the Voigt model. It can be seen in Figure 4.2 that the elastograms of the plaques, from which the average material properties are taken, are far from ideal; they grossly underestimate the tissue stiffness, contain artefacts and are highly susceptible to changes in frequency and boundaries. Combining this with a more complex rheological model, where the shear modulus depends upon both the storage and loss moduli via a second order equation leads to enhanced errors which begin to show through to the mean values over the region of interest.

This section adds weight to the conclusion that superior material models and viscosity data are required to accurately model the behaviour of waves through atherosclerotic plaques. For this study the Voigt model was carried forward as the method of extracting the shear modulus.

Figure 4.5 shows that under noiseless conditions a low high pass filter and a high low pass filter result in a definitive stiffness difference between the shear modulus of the three plaque compositions. As artificial noise is introduced the stiffness difference between compositions decreases, as do the overall magnitudes. At an SNR of 5 there is no distinct difference in the behaviour of the shear modulus between each composition over the filter ranges. It should be noted that varying the low pass filter can yield just about any shear modulus magnitude, and therefore should be applied with care.

Figure 4.6 shows that the addition of filters to the inversion algorithm results in a reduction in the shear modulus over the range of compositions and noise conditions. The shear moduli in the noisy data sets decrease with decreasing SNR and are much lower than the magnitudes programmed into the simulation and those extracted from the noiseless data. The noiseless results show a progressive decrease in shear modulus with increasing lipid composition. In the presence of SNR 500 and 40, even taking into account the standard error, the algorithm can still detect the change in composition. However the reduction of the shear modulus with increasing lipid composition is not as smooth as the noiseless conditions. The data with SNR 5 shows no trend with composition.

Since in theory, the noiseless data from an incompressible model should not require filtering to remove noise and the compression wave components, the remaining idealised results in this chapter were assessed without adding filters.

4.4.4) Disease Development

The effect of the lipid pool size upon the local plaque stiffness has been demonstrated in relation to a number of variables. Upon optimising the technique variables, it can clearly be seen in Figure 4.7 that the plaque stiffness decreases in all stenosis sizes with an increasing volume of low stiffness lipid. Figure 4.7 also shows that as the stenosis size decreases, with the same lipid pool volume, the percentage of lipid in the composition increases and hence the stiffness decreases. It is difficult to discern a clear trend between lipid pool size and local plaque stiffness in the smaller stenosis sizes since they do not have enough volume to contain a variety of lipid pool sizes. However even with a reduced number of points, they all show a decreased stiffness with increasing lipid composition.

Figure 4.8 shows the waves images and elastograms through a series of 70% plaque compositions. As the composition becomes more lipid the wavelength in the lipid pool becomes more and more visible. The fibrous plaque barely shows any changes in wave amplitude, demonstrating how little of the wavelength is contained within the ROI. The lipid plaque on the other hand contains a full wavelength due to its much reduced stiffness. Tying this back into discussion of section 4.4.2, the amount of the wavelength contained in the plaque clearly affects the accuracy of inversion algorithm, with the lipid plaques giving far more realistic shear moduli values than the fibrous plaques.

The elastograms of the fibrous and lipid plaques are by far the clearest of the set. The elastograms of plaques containing lipid pools have one extra boundary and are consequently of inferior quality, suffering from large areas of ‘black hole’ artefacts.

Figure 4.9 shows that for the most part an increase in lipid pool cholesterol level shows an increase in local plaque shear modulus. The anomalous result in this section is the 10mm^3

lipid pool with a 25% cholesterol lipid composition. Looking at the elastograms in Figure 4.8, and the other results in this chapter, it can be seen that although there are identifiable trends they are not always smooth and certainly do not always have the correct magnitude when compared with those in the simulation, especially for the stiffer plaque compositions.

Figure 4.10 shows that the only composition that shows a trend with fibrous cap thickness is the fully lipid plaque. The fibrotic intima surrounding the lipid pools and fibrous cap has a similar shear stiffness, 221kPa and 208kPa, respectively. Therefore it is not surprising that changes in the fibrous cap thickness do not create any definitive changes in stiffness, especially when the local stiffness predictions are far below their actual values. In the fully lipid composition the marked change in stiffness between the fibrous cap and 107Pa lipid, means that as the fibrous cap increases in thickness the overall plaque does show an increase in stiffness. The 40mm^3 lipid pool size had to be omitted in this investigation as the thicker 0.75mm fibrous cap would have led to overlapping geometry.

In Figure 4.11 each plaque containing a lipid pool shows an increase in stiffness as the fibrous cap structure varies from cellular, to hypocellular and calcified, with a material stiffness of 208kPa, 375kPa and 937kPa respectively. The only composition which does not follow this trend is the fully fibrous cap which keeps approximately the same stiffness regardless of fibrous cap structure. As previously discussed the average estimated stiffness through the fibrous plaques are far below the actual values programmed into the simulation. Therefore a small change in the stiffness of the very thin fibrous cap within a fully fibrous structure may not create a quantifiable change in the estimated average stiffness.

There are three noteworthy limitations to the methodology of Chapters 3 and 4. Firstly the effect of changes in the wave behaviour through the surrounding tissue prior to propagation through the plaque has not been investigated. Different wave patterns, dependent on patient specific geometries would certainly be encountered during an *in vivo* investigation. Secondly the shear viscosity has not been varied since Chapter 2 however during that chapter it was acknowledged that this parameter can strongly affect the accuracy of the technique. The shear viscosity values were based upon values quoted in or extrapolated from the literature. There is scope for these two limitations to be explored in future research.

The final limitation was the extraction of the results across a 2D plane which is significantly different to the 10mm slice thickness used during experimental MRE. Whilst this may not be a limiting factor through the homogeneous tissue blocks of Chapter 2, this would almost certainly lead to idealised computational results through models of vessels with diameters in the region of 7mm. This parameter could be incorporated into future work, to guide the required slice thickness resolution for experimental research.

4.5) Conclusions

In addition to the ideal imaging plane, load direction and magnitude yielded by Chapter 3, Chapter 4 has identified the optimum pixel resolution, averaging method, rheological model and excitation frequency in a simulation of MRE through idealised atherosclerotic plaques, summarised in Table 4.5 and 4.6.

Parameters	**Load**		
	Direction	**Magnitude (N)**	**Frequency (Hz)**
Ideal	Shear	6×10^{-4}	100

Table 4.5: *Ideal mechanical parameters.*

Parameters	**Imaging Plane**	**Pixel Resolution (mm^2)**	**Averaging Method**	**Rheological Model**
Ideal	Y-Z	0.5	Mean	Voigt

Table 4.6: *Ideal imaging and inversion parameters.*

MRE through simulated idealised atherosclerotic plaques can detect a change in stiffness between a fully fibrous and fully lipid plaque at pixel resolutions between 0.5 and 2mm^2. There is a graduated decrease in plaque stiffness as the lipid pool volume increases using a mean spatial average and a pixel size of 1mm^2 and 0.5mm^2.

Simulated MRE through idealised atherosclerotic plaques at a pixel resolution of 0.5mm^2 has demonstrated that it can identify an overall change in plaque stiffness with disease development; specifically the lipid pool size, cholesterol percentage and fibrous cap structure. The fibrous cap cannot be identified in the elastogram. Above 100Hz the lipid pool can be depicted on the wave image, and to the informed eye, it can be identified in the elastograms as well.

It is worth summarising before progressing into the experimental feasibility of the technique, the limitations that have been identified. The more successful results of this chapter were obtained at almost a quarter of the 1.84mm^2 pixel size seen experimentally, the accuracy of the technique decreased with increasing pixel size. In the presence of inhomogeneous media and a small region of interest, the inversion algorithm introduces large errors into the technique, resulting in underestimated mean shear moduli and unclear elastograms prone to artefacts. In addition the introduction of noise to the simulated data reduces the accuracy of the results, even at a high resolution.

This chapter has optimised the computational procedure and under idealised parameters the results give strength to the hypothesis that MRE has the potential to identify changes in plaque stiffness. The results do not retain their accuracy in the face of some realistic limitations, identifying three key areas that require development; resolution, SNR and an inversion algorithm applicable to inhomogeneous media.

In the following chapters, this research shall move on to investigate the experimental feasibility of the technique. Where possible the ideal parameters shown in Table 4.5 and 4.6 shall be utilised. However the acknowledged limitations prevent the research from being conducted under all the idealised parameters identified in the last two chapters.

Chapter 5

Magnetic Resonance Elastography through Diseased Arterial Phantoms

5.1) Introduction

Whilst computational research allows a detailed sensitivity analysis of all the variable factors in arterial MRE, experimental investigation is important to assess the real world feasibility of the technique. The next intuitive step, to assess the application of a new imaging technique, is to scan a simple phantom. Imaging phantoms for investigation and validation purposes is common practise in MRE (Sinkus *et al.* 2000, Papazoglou *et al.* 2008).

The concept of applying MRE to atherosclerotic plaques is inherently complex when compared to studies in larger, homogeneous organs. Progressing onto imaging phantoms, prior to an *in vivo* study, allows some the associated complications such as resolution, noise, plaque size and lumen boundary to be assessed, whilst omitting others. MRE shall be conducted on static flow arterial phantoms; thus the *in vivo* difficulties of physiological motion and flow artefacts will be neglected.

A large number of materials have been used to mimic the components of diseased arteries, reviewed extensively in (Hoskins 2008). For this particular study, the key characteristic required by the arterial phantom is the ability to vary the plaque stiffness. Polyvinyl alcohol cryogel (PVA-C) is a well-established vessel mimicking material (Surry *et al.* 2004, Dineley *et al.* 2006) and was chosen for this study for several reasons; elastic properties comparable with arterial tissue (Li 2007), variable mechanical properties (King *et al.* 2011) and MRI compatibility (Chu and Rutt 1997). Previous studies have used PVA-C to generate 3D fibrous and lipid occlusions by either differing the number of freeze-thaw cycles between the plaque and wall (Surry *et al.* 2004, Dumont *et al.* 2009) or incorporating an alternative lipid based substance (Pazos *et al.* 2010). To date the only application of MRE to vessel phantoms was conducted by Woodrum et al. (2006) who calculated stenosis size from an analysis of wave reflections.

The aim of this chapter is to create arterial phantoms containing plaques of various size and stiffness for the purpose of validating the application of magnetic resonance elastography to atherosclerosis. An example of the results from this chapter can be seen in (Thomas-Seale *et al*. 2013).

5.2) Method

5.2.1) Overview

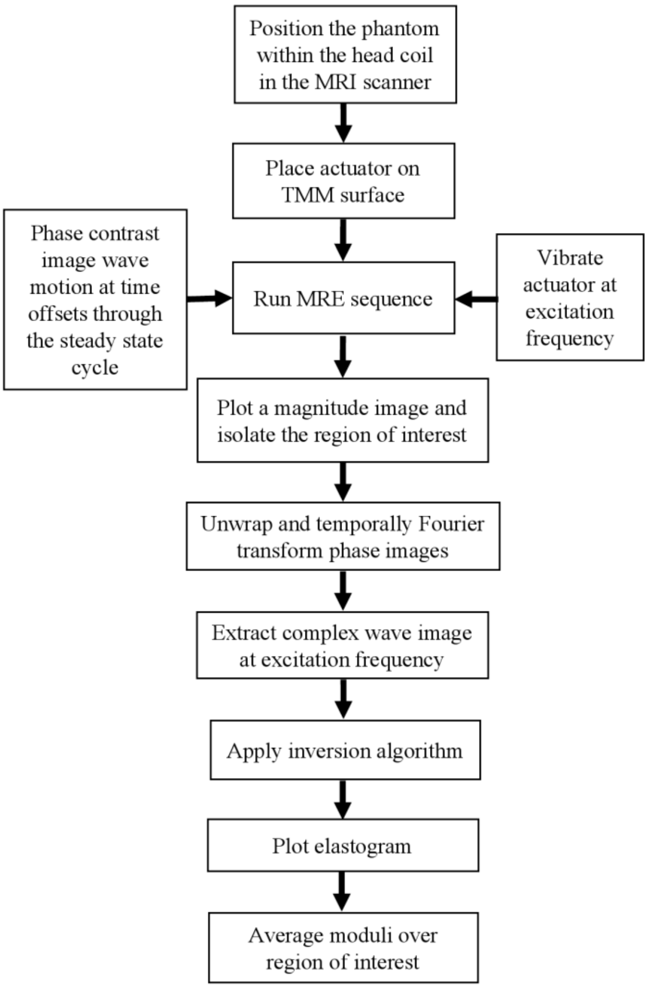

Figure 5.1: *MRE methodology: arterial phantoms.*

The methodology of MRE was outlined in Figure 2.1 in comparison to the computational methodology. Figure 5.1 has been adjusted to represent the experimental methodology used in the arterial phantoms scans.

Ten arterial phantoms were created, a healthy vessel phantom and 9 diseased vessel phantoms incorporating one of the three plaque sizes and three stiffnesses. As a control experiment, a homogeneous phantom, composed of just tissue mimicking material (TMM), was constructed. Each phantom was scanned at three frequencies, 75Hz, 100Hz and 125Hz in three motion encoding directions.

Since MRE of a relatively small plaque interfacing with a liquid boundary is a challenging application in terms of imaging resolution and inversion algorithm applicability, this chapter will focus on the behaviour of the wave images and elastograms over the whole phantom as opposed to isolating a very small ROI. The qualitative and quantitative results are displayed and averaged over a ROI incorporating the majority of the phantom. Disturbances in the image due to presence of the actuator and any image artefacts around the edges of the phantom shall be omitted.

The homogeneous TMM and healthy vessel phantoms were used to identify the clearest wave images in terms of excitation frequency and motion encoding direction. The SNR through each data set was calculated to support this work. The optimal parameters were then used to display qualitative results of wave images and elastograms through phantoms of varying stenosis size and composition.

The arterial phantoms were designed and manufactured with assistance from Tom Anderson (School of Cardiovascular Sciences, Queen’s Medical Research Institute, University of Edinburgh, Edinburgh, UK) and Stan Loneskie (NHS Medical Physics Workshop, The Royal Infirmary of Edinburgh, Edinburgh, UK). The MRE scans were conducted by Paul Kennedy (Clinical Research Imaging Centre, Queen’s Medical Research Institute, University of Edinburgh, Edinburgh, UK) on a 3 Tesla Magnetom Verio MRI research scanner (Siemens AG, Erlangen, Germany). The MRE equipment, imaging protocol and inversion methodology was based upon the research and set up in collaboration with the MR Elastography Group, Charité Univesitätsmedizin Berlin. The mechanical MRE equipment was designed and manufactured by Steven Hammer (Institute of Mechanical, Process and Energy Engineering, School of Engineering and Physical Sciences, Heriot-Watt University, Edinburgh, UK). The inversion algorithm was run on the programming software MATLAB R2011a.

5.2.2) Arterial Phantom Design

Atherosclerotic disease was modelled as an eccentric stenosis embedded in the wall of an otherwise straight vessel. Three stenosis sizes were created, 50%, 60% and 70%, and combined with three plaque stiffnesses to represent a homogeneous stenosis, a lipid based plaque and fibrous plaque. The vessel mimicking material (VMM) PVA-C was used to create the 10 vessel phantoms; 1 healthy and 9 variations of a diseased artery. Each vessel was embedded in a block of TMM to recreate the propagation of waves through the surrounding tissue *in vivo*. An example of a fully constructed phantom is shown in Figure 5.2.

The shear moduli of the phantom materials were restricted to the ranges available for each of the manufacturing methodologies; the tissue mimic was controlled by composition, and the vessel mimic by the number of freeze-thaw cycles. In this phantom study, motion generated by blood flow was neglected; the lumen was filled with water, which beyond any interaction with the waves, was assumed to remain static.

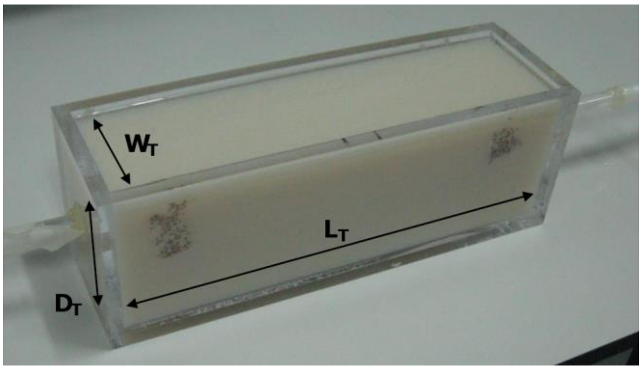

Figure 5.2: *Arterial phantom, surrounded by tissue mimicking material.*

5.2.3) Vessel Mimicking Material

The mechanical properties of PVA-C can be manipulated by the number of freeze-thaw cycles it undergoes during manufacture. Polyvinyl alcohol (PVA) is a gel like substance that is converted into a cryogel when crystal nuclei, generated during freezing, grow into crystals that act as polymer cross-linking sites during thawing (Chu and Rutt 1997). Each additional freeze-thaw cycle increases the size and/or the number of cross-linking sites, which increases the stiffness of the cryogel (Chu and Rutt 1997). This particular property makes PVA-C ideally suited to this study, allowing easy manipulation of the vessel stiffness properties. The drawbacks of the vessel mimic were minimal, however it was noted during manufacture that during the repeated freeze-thaw cycles, the vessel mimic undergoes shrinkage (Chu and Rutt 1997) causing slight deviations from the original moulded shapes.

To be suitable for a validation study, it is important to be able to quantify the mechanical properties of the vessel phantom. Beyond the absolute number of freeze-thaw cycles, studies have shown that the concentration (King *et al.* 2011) and rate of thaw (Wan *et al.* 2002) also affect the properties of the cryogel. To ascertain the mechanical properties per number of freeze-thaw cycles, the concentration and methodology outlined by King et al. (2011) was employed and the relevant Young’s moduli per freeze-thaw cycle are summarised in Table 5.2.

The general manufacturing method for each section of the vessel, regardless of the number of freeze-thaw cycles was taken from (King *et al.* 2011) and is outlined as follows. 10% wt. PVA in a loosely sealed container was heated in a water bath at 100±1ºC for 60 minutes. Upon heating, the viscosity of PVA decreases allowing it to flow more easily and be injected into the required mould. The moulds were lubricated in advance with silicon grease to allow the cryogel to be removed easily after manufacture. Where appropriate the syringe and mould were heated in advance to maintain the PVA at a high temperature and low viscosity. The mould was allowed to stand for 24 hours at room temperature 22±0.5ºC to allow any air bubbles to rise to the surface. The freeze-thaw cycle involved a freezing stage at -20ºC for 14 hours and a thawing stage at room temperature 22±0.5ºC for 10 hours (King *et al.* 2011). The number of times the sample underwent the freeze-thaw process was dependent on the desired mechanical properties, outlined in section 5.2.4. Once the required number of freeze-thaw cycles had been completed, the sample was removed from the mould and stored in water to prevent dehydration.

To support the aim of validating the application of MRE to atherosclerosis, mechanical testing of PVA-C samples was conducted. However problems such as crushing and ripping of the samples were encountered due to the use of tensile testing clamps that were not specialised for tissue samples. Future work would be strengthened by quantification of the mechanical properties of samples of the PVA-C and TMM used specifically in this research.

5.2.4) Vessel Manufacture

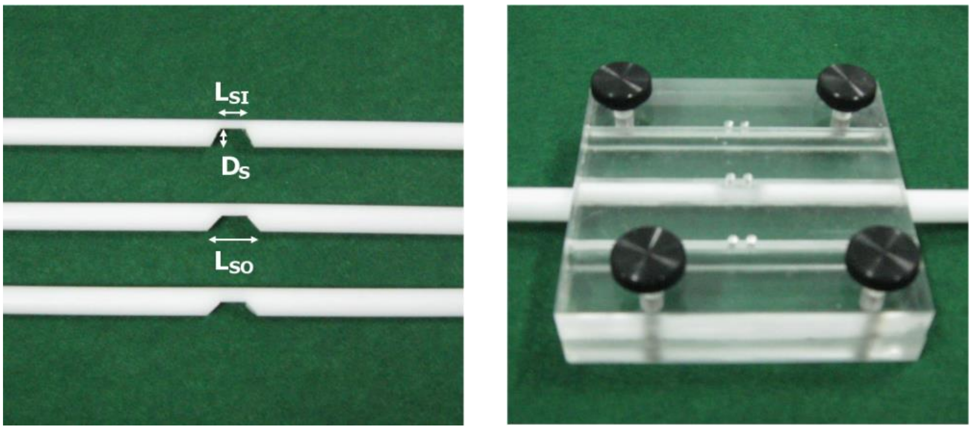

(a) Stenosis moulds

(b) Plaque mould

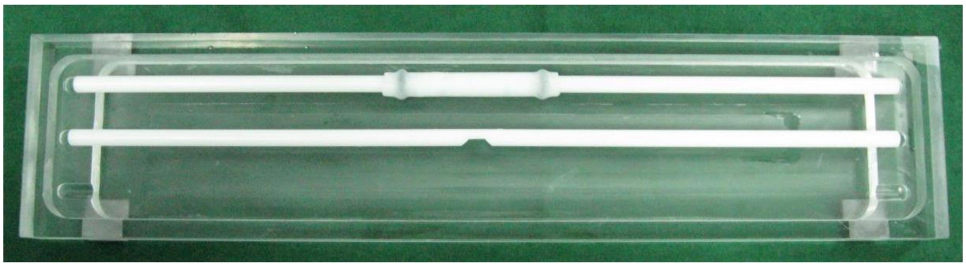

(c) Water bath

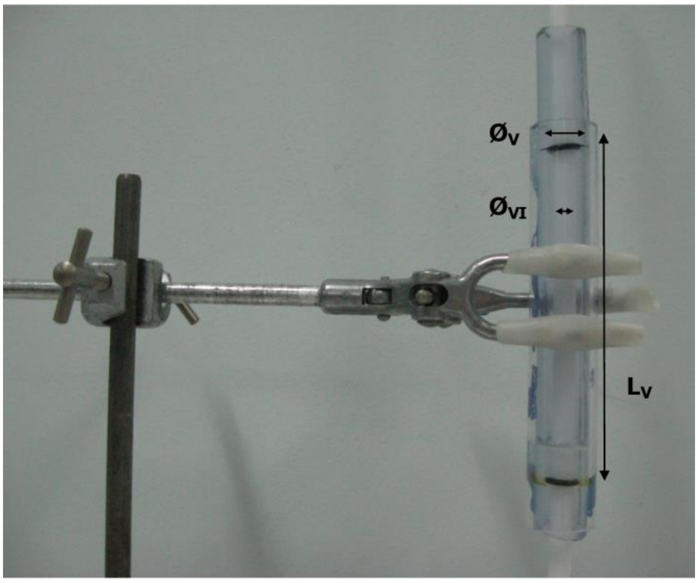

(d) Vessel wall mould

Figure 5.3: *Vessel and plaque moulds.*

Material	Phantom Component		Length, L (mm)		Width, W (mm)	Depth, D, (mm)	Diameters, Ø (mm)	
			Inner	Outer			Inner	Outer
Tissue Mimic	Surrounding Tissue		N/A	300.0 ± 1.0	80 ± 1.0	100 ± 1.0	N/A	N/A
Vessel Mimic	Wall		N/A	80.0 ± 10.0	N/A	N/A	8.0	13.0
	Stenosis	50%	8.0	14.6	N/A	3.9	N/A	N/A
		60%	8.0	15.3	N/A	4.8	N/A	N/A
		70%	8.0	13.0	N/A	5.6	N/A	N/A

Table 5.1: *Tissue and vessel mimic mould dimensions.*

Material	Phantom Component	Freeze-Thaw Cycles	Moduli (kPa)		Error (kPa)	
			Shear	Young's	Positive	Negative
Tissue Mimic*	Surrounding Tissue	N/A	16.8	-	0.8	0.8
Vessel Mimic**	Wall	3	-	102.5	8.9	15.9
	Fibrous Plaque	5	-	160.1	18.1	13.6
	Lipid Plaque	1	-	18.9	2.9	4.7

Table 5.2: *Material properties: tissue and vessel mimic. *(Hamhaber et al. 2003) **(King et al. 2011) and correspondence with Jacinta Browne (Medical Ultrasound Physics and Technology Group, Dublin Institute of Technology, Dublin 8, Ireland).*

The manufacturing steps involved in creating each vessel were based on the methodology described in section 5.2.3; heating the PVA, a rest period to allow the air bubbles to escape and then the required number of freeze-thaw cycles. A series of moulds were designed and manufactured; a 50%, 60% and 70% stenosis mould, Figure 5.3(a), a compatible plaque mould, Figure 5.3(b), a water bath, Figure 5.3(c) and a vessel mould, Figure 5.3(d). These moulds facilitated the construction of a range of vessels containing plaques of different size and stiffness, the properties of which are summarised in and Table 5.1 and 5.2. The nomenclature for these dimensions can be seen in Figure 5.3.

Healthy and Homogeneous Stenosed Vessels

The straight vessel wall, with thickness 2.5 mm was created using a hollow cylindrical outer mould of inner diameter 13 mm combined with a circular acrylic rod of outer diameter 8mm. The outer mould was composed of polyvinyl chloride tubing reinforced by an acrylic tube. This combination eased the extraction of the PVA-C vessel from the mould. The inner rod was placed within the outer wall mould and sealed using one rubber o-ring at the bottom. PVA was heated as described in section 5.2.3 and injected into the top of the mould. Once the mould was filled, the inner rod was aligned concentrically using a second rubber o-ring. These o-rings also allowed the PVA to expand upon freezing. An example of the vessel mould is shown in Figure 5.3(d). To create homogeneous vessels containing a plaque, the acrylic stenosis moulds of 50%, 60% and 70%, Figure 5.3(a), were combined with the outer mould. The homogeneous stenosed vessels and healthy vessel underwent 3 freeze-thaw cycles.

Fibrous Plaque

Fibrous plaques were created to be relatively stiffer than the vessel wall. They therefore required additional freeze-thaw cycles compared to the vessel wall. The size appropriate stenosis mould was placed in a compatible plaque mould, shown in Figure 5.3(b). The plaque and stenosis mould were covered in silicon grease to create an air tight seal. The heated PVA was injected through an injection hole, allowing air to escape through the second hole. The fibrous plaque was then subjected to 2 freeze-thaw cycles. The stenosed rod, containing the plaque, was removed from the plaque mould and placed inside an outer wall mould and secured using a rubber o-ring. Heated PVA gel was injected into the mould, around the stenosis mould containing the fibrous plaque. The stenosed rod was then concentrically aligned using the second o-ring. The mould was placed in the freezer for a further 3 freeze-thaw cycles. The result of this methodology was a fibrous plaque having undergone 5 free-thaw cycles, embedded in a vessel wall having undergone 3 freeze-thaw cycles.

Lipid Plaque

The opposite approach was taken to create a lipid plaque, which required relatively less stiff properties than the wall. A straight vessel wall was created as described above and placed in the freezer for 2 freeze-thaw cycles. The cryogel vessel was removed from the moulds and placed around a rod containing the required size of stenosis. O-rings were required to create a seal between the stenosis mould and the PVA-C vessel, and the model was suspended in the water bath as displayed in Figure 5.3(c). Heated PVA gel was injected through the wall into the hollow created by the stenosis. This procedure had to be done in several stages to allow all the air bubbles to escape. The water bath was then filled with water to cover the PVA-C vessel and prevent dehydration during the freeze-thaw process. The vessel was frozen and thawed once resulting in a vessel wall having undergone 3 freeze-thaw cycles containing a lipid plaque having undergone 1 freeze-thaw cycle.

The limitation of this approach is that the PVA-C will have a slower rate of thaw when submerged in the water bath, as opposed to thawing whilst exposed directly to room temperature. Pazos et al. (2009) report that a decrease in the rate of thaw leads to an increase in the stiffness of the cryogel. Therefore the properties listed in Table 5.2 may not be accurate for the lipid plaque and surrounding vessel wall.

5.2.5) Tissue Mimic and Manufacture

A very simple agar based tissue mimicking material was used to surround the vessel phantom. A concentration of 1% agar was used, corresponding to a shear modulus of 16.8kPa, as imaged using elastography at 125Hz (Hamhaber *et al.* 2003). A preservative, Rodalon, at a concentration of 0.3% was added to extend the life span of the tissue mimic. The agar, water and preservative were mixed thoroughly and heated in a water bath up to 96.9°C and allowed to cook for 1 hour. The tissue mimic was allowed to cool down to 42°C at which point it was ready to be poured. At approximately 40°C liquid agar changes to a solid state via chemical cross-linking (Hamhaber *et al.* 2003).

5.2.6) Phantom Construction

Once a PVA-C vessel as per section 5.2.3 and 5.2.4 and TMM, ready to pour, as per section 5.2.5 had been created, they were combined to create an arterial phantom. The containers that were used had previously been designed to support a range of arterial phantoms; with two tubes at each end aligned along the centre of the container. In order to pour the TMM around the vessel without collapsing the tube, the vessel was supported by rods aligning it with the tubes at either end of the container, Figure 5.4. The stenosis was aligned with a mark on the outside of the container to aid the imaging process. Once the TMM had been poured and set, this rod was carefully removed leaving the vessel embedded in the tissue mimic, as can be seen in Figure 5.2. To ensure that the PVA-C did not dry out, the lumen was filled with water and sealed at each end.

In addition a simple homogeneous TMM phantom, without a vessel, was created in a container measuring approximately 200mm by 120mm by 85mm in depth; shown in Figure 5.5(b). All the phantoms were covered with a thin layer of water to prevent dehydration.

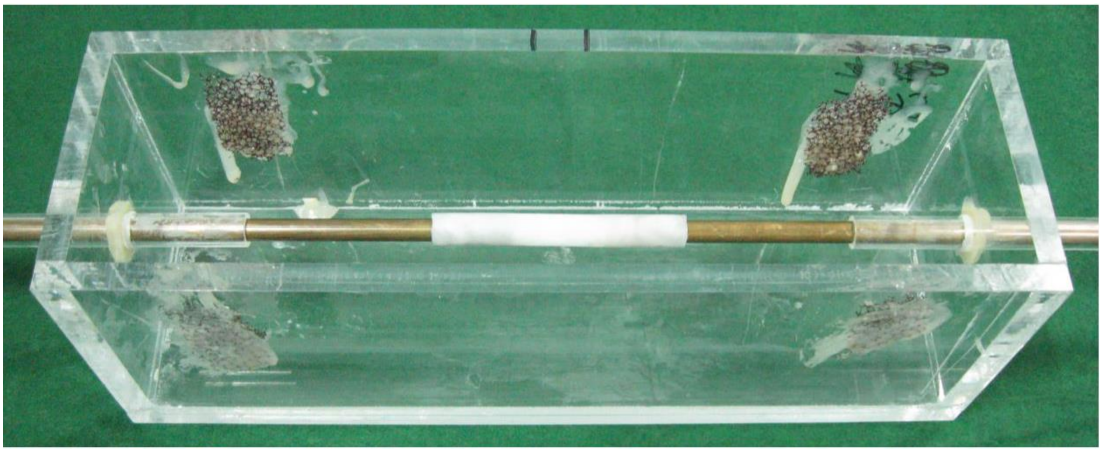

Figure 5.4: *Arterial phantom construction.*

5.2.7) Magnetic Resonance Elastography

MRE Set Up

The MRE equipment used at The University of Edinburgh is shown in Figure 5.5; set up for the homogeneous phantom scan. The phantoms were placed inside a 12 channel head coil, shown in Figure 5.5(b). The phantoms were constrained as much as possible using blocks of padding. A custom designed artery actuator was placed on the surface of the TMM, above and slightly offset from the region of interest, indicated in Figure 5.5(b) and (c).

Harmonic, sinusoidal waves were generated by a waveform generator and passed through an audio amplifier to a subwoofer (Carpower Raptor Mk-12, Monacor, Germany) situated outside the 5 Gauss line in the MRI scan room. These waves were synchronised with the imaging sequence via a trigger signal between the MRI operating station and the waveform generator. The waves were transferred to the actuator from the subwoofer via a carbon-fibre piston. The subwoofer and piston in related to the MRI scanner are shown in Figure 5.5(a); the subwoofer is situated inside a transportable frame.

Due to the consistency and high water content of agar based TMM; the surface of the phantoms was extremely smooth and covered in a thin layer of water, making excitation in the shear direction almost impossible without causing significant damage to the phantom. Therefore compressional excitation was used to transmit waves into the phantom. To create these waves the subwoofer was orientated to vibrate the piston in the direction indicated on Figure 5.5(a). To try and control excessive vibration of the actuator, for example bouncing, the piston was lightly constrained in the compression direction.

This method of excitation was enforced due to the lack of friction on the surface of the phantoms however, compressional excitation has been shown to effectively excite mechanical waves that may be imaged and inverted using MRE (Sinkus *et al.* 2000). In reality, a finite, harmonic source exciting in the shear or longitudinal direction will intrinsically excite a secondary wave in other directions (Carstensen *et al.* 2008). For example, in the case of a finite rectangular actuator, at the edge of the area over which the compression force is applied, there will be a shearing force between medium that is immediately displaced and the non-displaced medium a distance from the actuator. However, under harmonic excitation the longitudinal wave, compared to the shear displacement field, is so large that it effectively has a uniform phase (Carstensen *et al.* 2008).

Although the Helmholz inversion algorithm neglects compression wave components, by the fair assumption of incompressibility, not all inversion algorithms do. Sinkus et al (2000) used compressional excitation and do not neglect compressional wave components in their inversion algorithm. The Helmholtz algorithm can either be applied under pure shear wave excitation or combined with longitudinal or curl filtering (Mariappan *et al.* 2010). In this research, longitudinal wave filtering was applied, section 5.2.9.

MRE Protocol

The MRE protocol used at The University of Edinburgh consists of a 3 tesla echo planar imaging sequence combined with a motion encoding gradient (MEG). Initially a localising sequence was used to select the appropriate imaging plane through the ROI. A sagittal slice was taken along the length of the vessel phantoms and homogeneous phantom as this provided the clearest wave images.

The parameters of the protocol are summarised in Table 5.3. The acquisition through the imaging plane was repeated 40 times, with an increasing time offset between the start of the harmonic wave and the MEG. This provided 40 sampling points for the movement of the sinusoidal wave through the TMM. The amplitude of the harmonic wave was controlled by the wave generator and set at 4V peak to peak voltage. This generated good wave penetration through the TMM without excessive phase wrapping. This protocol was repeated nine times; for the frequencies 75Hz, 100Hz, and 125Hz and within each frequency for the three motion encoding directions. The motion encoding directions are shown in Figure 5.5(c) and defined as follows; slice select (SS), perpendicular to the image, phase encoding (PE), parallel to the vessel and read out (RO). The actuator was vibrated in the RO direction. The field of view (FoV) was 235mm^2, with a matrix size of 128 x 128 yielding a pixel size of 1.84mm^2. The slice thickness was 10mm.

At this point, it is valuable to mention that during this study the possibility of scanning at an increased 256 x 256 resolution was investigated superficially. However, it was visually apparent that signal to noise ratio was not sufficient to distinguish the wave propagation properly. The possibility of scanning at an increased resolution could not be investigated further due to funding constraints.

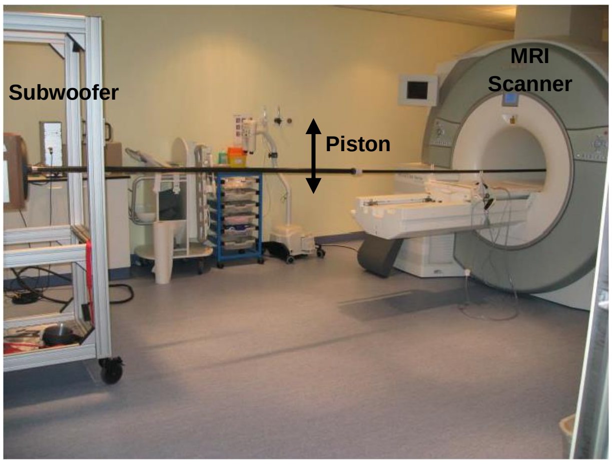

(a) MRE set up; subwoofer, piston and MRI scanner

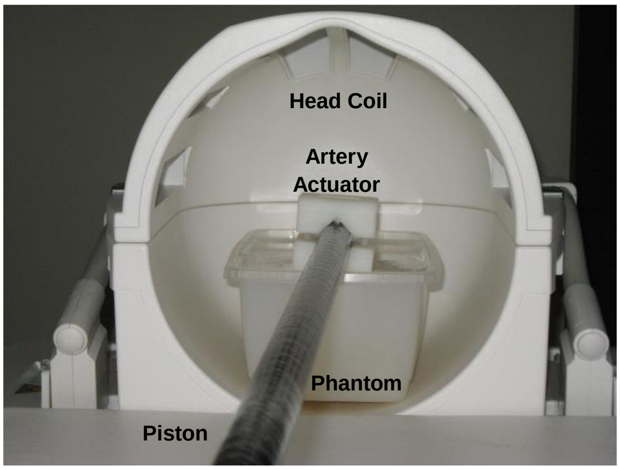

(b) Actuator and homogeneous phantom inside the head coil

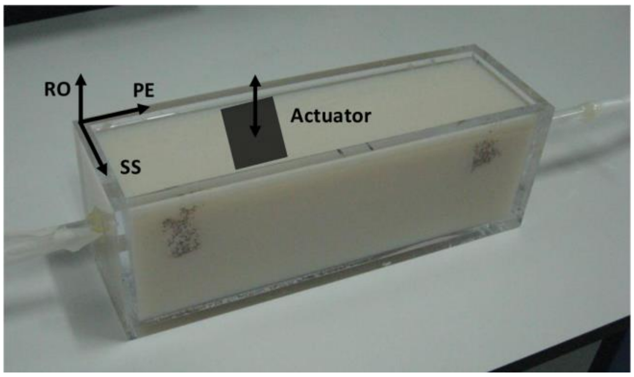

(c) Imaging and excitation directions relative to an arterial phantom

Figure 5.5: *MRE equipment: arterial phantoms.*

Repetition Time (TR)	1600ms
Echo Time (TE)	56ms
MEG Cycles (75/100/125Hz)	1/1/2
MEG Amplitude	35mT/m
FoV	235mm x 235mm
Matrix Size	128 x 128
Slice Thickness	10 mm

Table 5.3: *MRE acquisition parameters: arterial phantoms.*

5.2.8) Signal to Noise Ratio

The signal to noise ratio through the MRE data was calculated, as per the methodology outlined in section 4.2.8 and Appendix B taken from (McGee *et al.* 2011). These values were used to inform not only the discussion of this chapter but also work conducted in Chapters 4 and 6. To summarise the noise analysis; equation 5.1 was informed by $\overline{A_s}$ the amplitude of the complex wave image averaged through the ROI and σ_n, the standard deviation of the background pixels through the magnitude image, averaged over all time steps and divided by the Rician correction factor 1.66.

$$SNR = \frac{\overline{A_s}}{\sigma_n} \tag{5.1}$$

5.2.9) Image Processing

The image processing method used in experimental MRE is the same as that described in Chapters 2 and 4. The inversion algorithm is programmed in MATLAB and can be found in Appendix A. The theory and mathematics behind the inversion algorithm is given in detail in section 2.2.6, a description of the filters is given in section 4.2.9. In addition the experimental methodology incorporates a technique known as phase unwrapping.

The MRE acquisition process yielded a set of 40 magnitude and positive phase images corresponding to time steps through the wave cycle. The magnitude image was used to identify the geometry of the plaque and to create a mask to isolate the ROI. First the phase images were unwrapped. Phase wrapping occurs when the phase is out of the $[-\pi, \pi)$ range; the phase wraps back around into this range creating discontinuities (Wang *et al.* 2011). Phase unwrapping was achieved using a Flynn's 2D minimum discontinuity algorithm, integrated into the inversion algorithm (Hamhaber *et al.* 2007). The phase images were temporally Fourier transformed and the complex wave image corresponding to the excitation frequency was extracted to serve as the input to the inversion algorithm.

In this phantom study, the excitation wave is generated in the compression direction and the experimental nature means that the phase images are also subjected to noise. A high pass filter is required to remove noise and a low pass filter is required to remove compression wave components (Klatt *et al.* 2007). However the work conducted in Chapter 4 demonstrated that the filters need to be used with care, as to some extent the average stiffness of an elastogram can be manipulated by filter thresholds. Filtering of the phantom wave images at the thresholds used in the literature (Klatt *et al.* 2007) resulted in excessive smoothing and the wave disturbances from the lumen became undetectable. Therefore the high pass and low pass 2D Butterworth filters, discussed in more detail in section 4.2.9, were set at the wide thresholds of 5m^{-1} and 100000m^{-1} respectively. Even though these generous limits may lead to insufficient filtering of the compression and noise components, the wave image will not be changed too dramatically from the raw data.

$$G(\omega) = \frac{-\rho\omega^2 U}{\nabla^2 U} \tag{5.2}$$

$$G(\omega) = \mu + i\omega\eta \tag{5.3}$$

The inversion algorithm was based upon the Helmholtz equation 5.2, from which the shear moduli were extracted using the rheological Voigt model, equation 5.3. The shear moduli were spatially averaged over the regions of interest using the mean and standard deviation.

5.3) Results

The results show the variation in filtered wave images, elastograms and averaged shear modulus with respect to excitation frequency and motion encoding direction, plaque size and stiffness. For reference a recreated computational image of the cross sectional phantom geometries can be seen alongside Figures 5.6 to 5.11. These images show how the phantom geometry lines up with the results images; the ROI has been highlighted. The approximate position of the actuator and direction of the vibration is marked by an arrow. This actuator can also be seen in each of the images by the indent where the ROI has avoided an area full of motion artefacts. The legends of the wave images and elastograms have been truncated below their maximum value; this is to improve image clarity and has been indicated in the accompanying legends.

The actual mean shear modulus values are based upon an estimated figure. Taking into account the resolution of the scan, motion artefacts blurring the edges of the phantom and indenting where the actuator is positioned, shrinkage of the VMM and TMM during manufacture; to calculate an exact average stiffness through the phantom would be almost impossible. The values in this results section are an approximate, based upon average sizes of the regions of interest and vessel lengths, provided for reference.

The averaged shear moduli through the elastograms are noticeably less than the actual mean stiffness through the phantoms. In each set of results, the largest value of the mean shear modulus data appears to be the most accurate because it is closer to the actual value. In light of the very high standard deviations generated by the zero and inflated stiffness pixels in the elastograms, discussed in section 4.4, the highest stiffness values shall not be considered the most accurate unless they demonstrate other factors that support this conclusion.

5.3.1) Signal to Noise Ratio

The SNRs through the homogeneous phantom at each frequency and motion encoding direction are shown in Table 5.4. Table 5.5 gives the mean SNR through all the arterial phantoms at each frequency and motion encoding direction. The SNR decreases with increasing frequency in all the phantoms. The SNR is the highest through the read out direction in the homogeneous phantom and the phase encoding direction in the arterial phantoms.

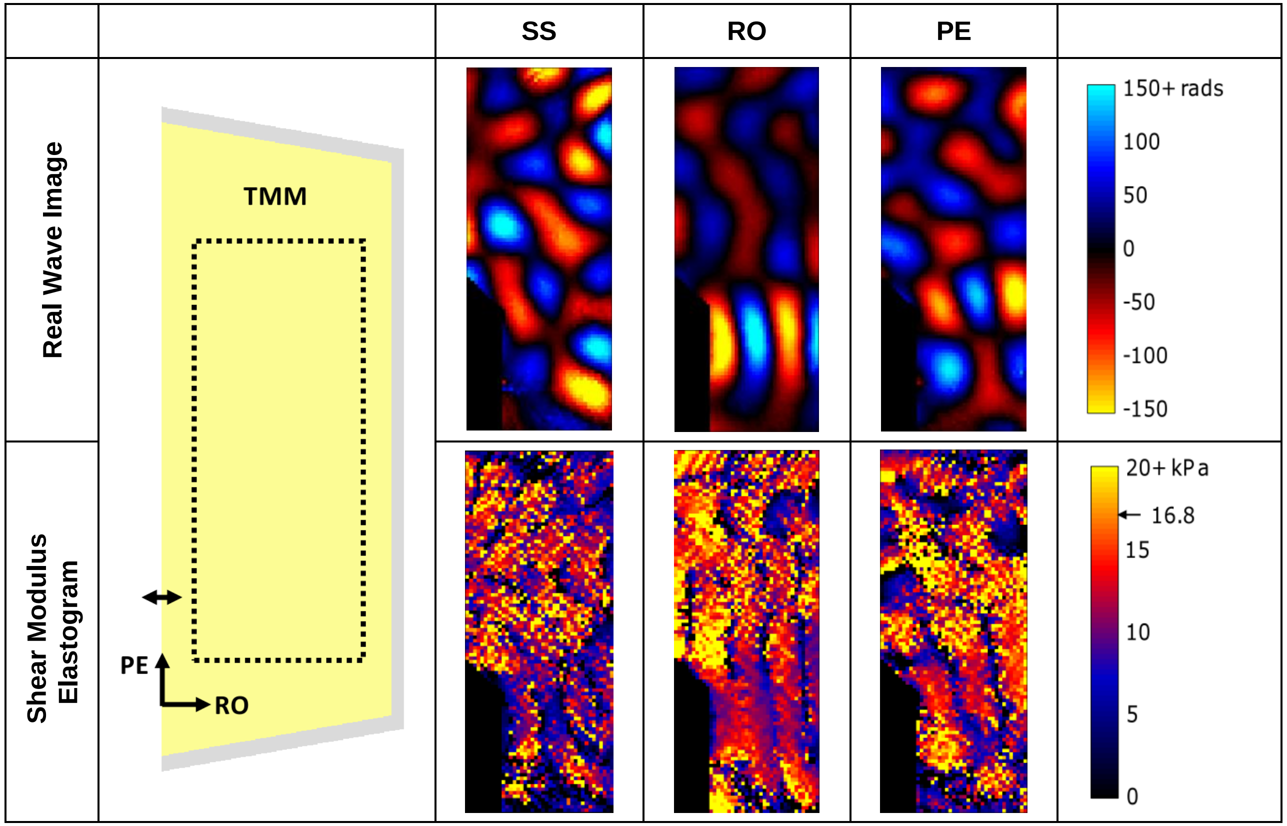

Figure 5.6: *The real component of the complex wave images and the shear modulus elastograms through the homogeneous phantom at 100Hz through each motion encoding direction. The true value of the shear modulus is indicated.*

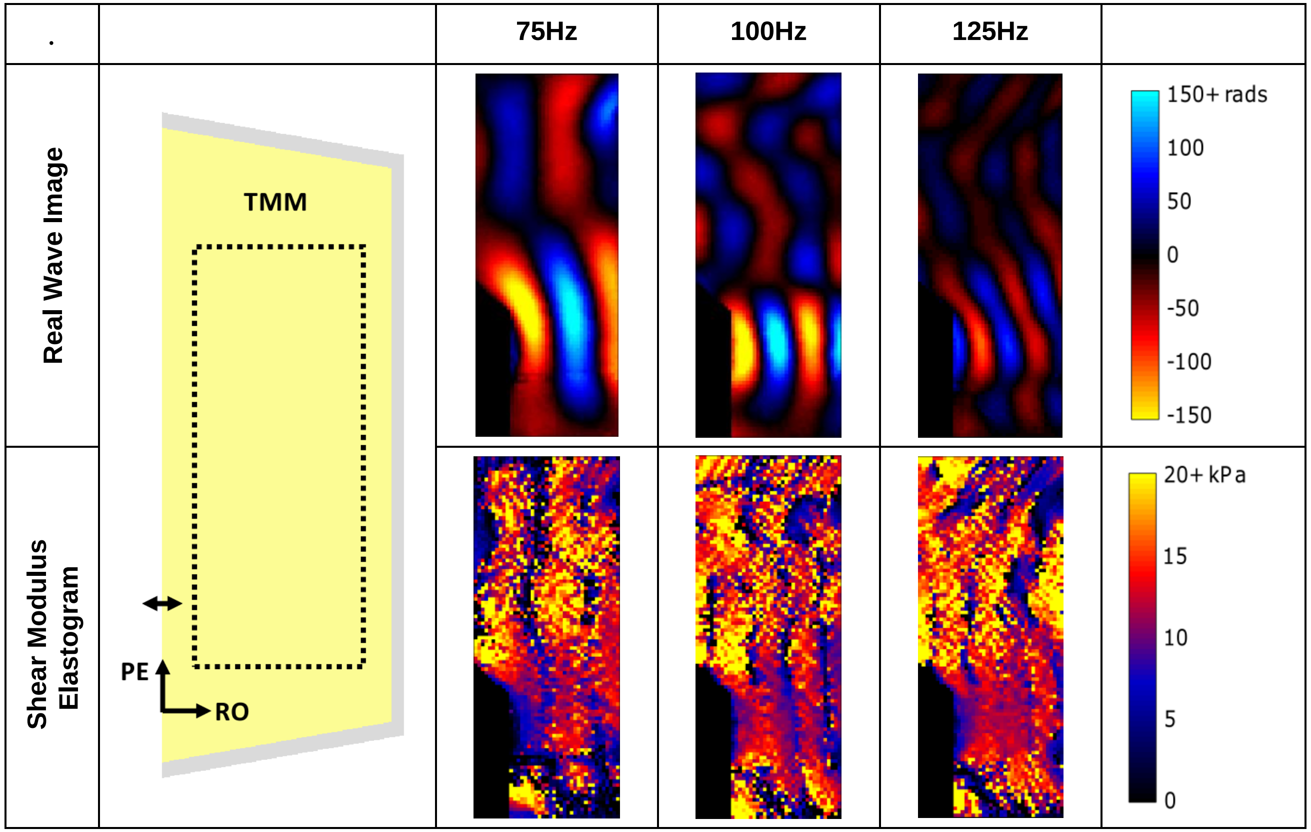

Figure 5.7: *The real component of the complex wave images and the shear modulus elastograms through the homogeneous phantom at each frequency in the read out motion encoding direction.*

Frequency (Hz)	**SNR**		
	Motion Encoding Directions		
	PE	**RO**	**SS**
75	13.7	22.9	8.3
100	10.1	18.4	5.7
125	5.4	11.4	4.2

Table 5.4: *The SNR through the wave images of the homogeneous phantom for each frequency and motion encoding direction.*

Frequency (Hz)	**Mean SNR**		
	Motion Encoding Directions		
	PE	**RO**	**SS**
75	41.9	26.6	11.3
100	28.1	19.2	11.5
125	9.7	7.4	3.7

Table 5.5: *The mean SNR through the wave images of the arterial phantoms for each frequency and motion encoding direction.*

5.3.2) The Homogeneous Phantom

The wave images and elastograms through the homogeneous TMM phantom at an excitation frequency of 100Hz and all motion encoding directions are shown in Figure 5.6. Of the three directions, read out gives a good approximation to planar wave propagation. This observation can be seen in the elastogram, with an area free from ‘black hole’ artefacts just below the actuator. The slice select direction shows reduced wave amplitudes.

The mean and standard deviation through these elastograms are summarised in Table 5.6. The mean averaging method through the read out direction gives the closest approximation of 13.5kPa to the true value of 16.8kPa the tissue mimic; appearing to correspond with the planar wave propagation seen in Figure 5.6, the highest SNR in Table 5.4 and the lowest standard deviation in Table 5.6.

The wave images and elastograms through the homogeneous TMM phantom at excitation frequencies of 75Hz, 100Hz and 125Hz and the read out motion encoding direction are shown in Figure 5.7. All three frequencies demonstrate a good approximation to planar wave propagation, with the clearest area just below the actuator translating to an area of the elastogram relatively free from ‘black hole’ artefacts. The 125Hz wave image shows notably reduced wave amplitudes.

Motion Encoding Directions	**Mean (kPa)**	**Standard Deviation (kPa)**	**Actual Stiffness (kPa)**
SS	11.2	13.7	16.8
RO	13.5	9.9	16.8
PE	12.6	11.9	16.8

Table 5.6: *The mean and standard deviation of the shear modulus through the elastograms of the homogenous phantom at a frequency of 100Hz in each motion encoding direction.*

Frequency (Hz)	**Mean (kPa)**	**Standard Deviation (kPa)**	**Actual Stiffness (kPa)**
75	12.1	10.5	16.8
100	13.5	9.9	16.8
125	13.8	10.5	16.8

Table 5.7: *The mean and standard deviation of the shear modulus through the elastograms of the homogenous phantom at each excitation frequency in the read out motion encoding direction.*

The mean and standard deviation through these elastograms are summarised in Table 5.7. The increasing frequency appears to result in a higher mean shear modulus however the standard deviations through the elastograms are so high that this observation may not be a true reflection of the data.

5.3.3) The Healthy Vessel Phantom

Figure 5.8 shows the wave images and elastograms through the healthy vessel phantom at an excitation frequency of 100Hz and all motion encoding directions. Contrary to section 5.3.1 the phase encoding direction gives the closest approximation to planar wave propagation. Similar to section 5.3.1, the slice select direction has the poorest signal. The mean and standard deviation through these elastograms are summarised in Table 5.8. Again mirroring the observations of section 5.3.2, the motion encoding direction with the most planar wave propagation, i.e. phase encoding, has the lowest standard deviation.

Motion Encoding Directions	Mean (kPa)	Standard Deviation (kPa)	Actual Mean Stiffness (kPa)
SS	9.1	8.1	13.8
RO	8.8	6.3	13.8
PE	9.0	4.7	13.8

Table 5.8: *The mean and standard deviation of the shear modulus through the elastograms of the healthy vessel phantom at a frequency of 100Hz in each motion encoding direction.*

Frequency (Hz)	Mean (kPa)	Standard Deviation (kPa)	Actual Mean Stiffness (kPa)
75	8.7	9.8	13.8
100	8.8	6.3	13.8
125	9.7	9.6	13.8

Table 5.9: *The mean and standard deviation of the shear modulus through the elastograms of the healthy vessel phantom at each excitation frequency through the read out motion encoding direction.*

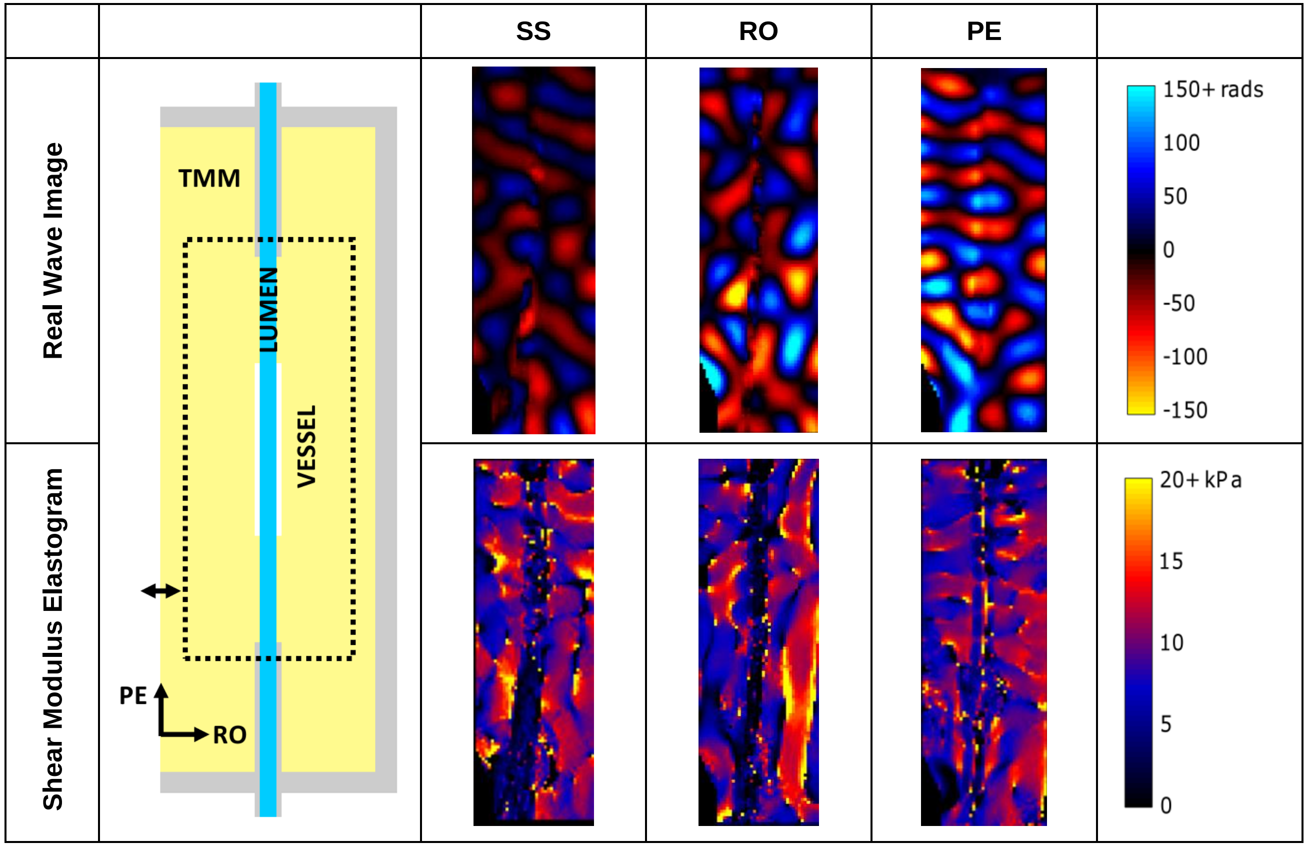

Figure 5.8: *The real component of the complex wave images and the shear modulus elastograms through the healthy vessel phantom at 100Hz through each motion encoding direction.*

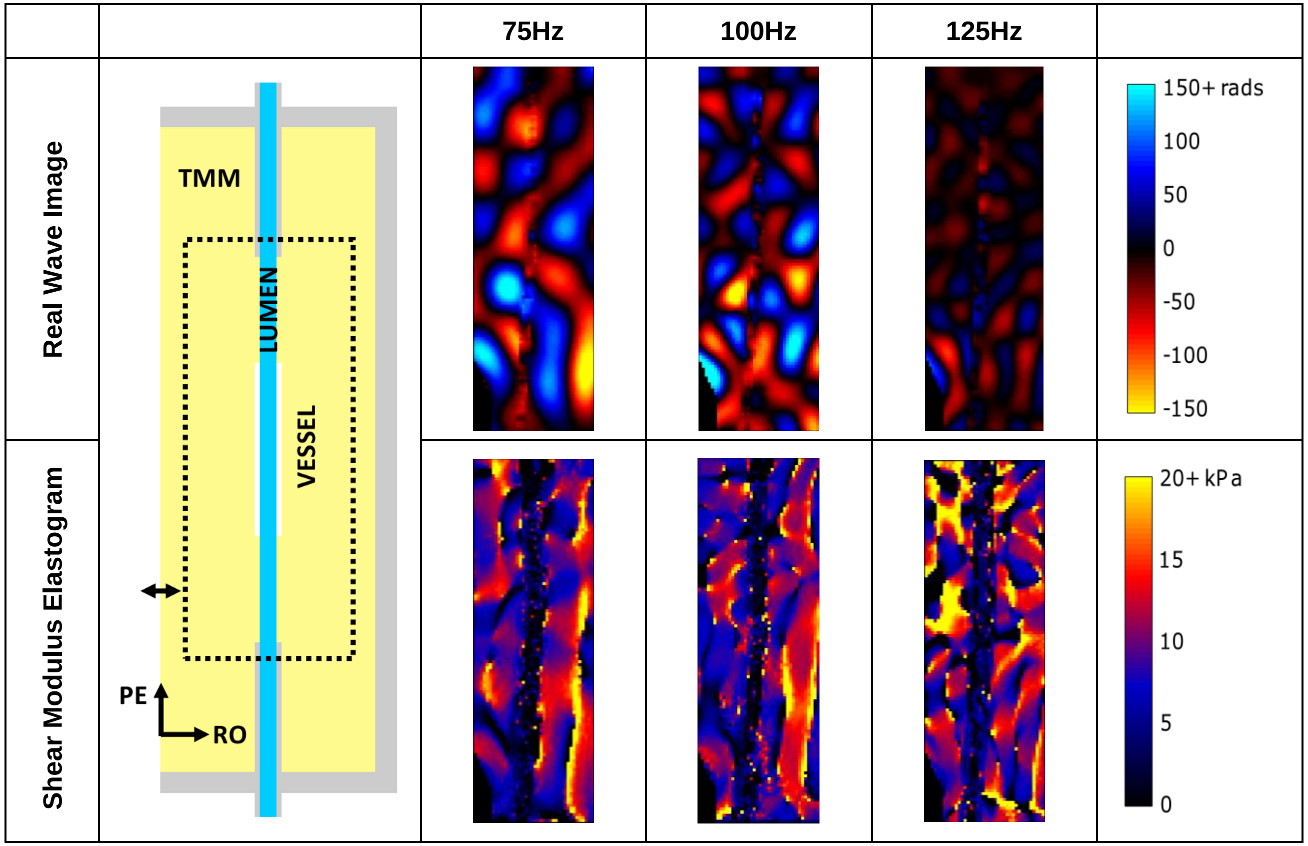

Figure 5.9: *The real component of the complex wave images and the shear modulus elastograms through the healthy vessel phantom at each frequency in the read out motion encoding direction.*

The wave images and elastograms through the healthy vessel arterial phantom at excitation frequencies of 75Hz, 100Hz and 125Hz and the read out motion encoding direction are shown in Figure 5.9. The 75Hz waves appear the most planar. The 125Hz show the lowest signal. The mean and standard deviation through these elastograms are summarised in Table 5.9. Unlike in Table 5.7, the shear stiffness does not increase with frequency.

5.3.4) Stenosis Size and Composition

Tables 5.6 to 5.9 show that the standard deviation of the results are very high, in some cases higher than the mean, due to the nature of the elastograms with artefacts of extremely high, or zero stiffness. The standard deviations of the elastograms appear to decrease when the wave propagation through the phantom is more planar. However this data does not add much more value to the analysis and therefore shall be omitted from this section. As an example of the wave images and elastograms through the plaque phantoms, the 100Hz and read out results shall be displayed.

The wave images and elastograms through the phantoms containing the healthy vessel and three sizes of stenosis with a homogeneous plaque, at an excitation frequency of 100Hz through the read out motion encoding direction are shown in Figure 5.10. The lumens of the phantoms are visible in the wave images and elastograms. The vessel wall and stenosis of each phantom are not visible in either image. The average shear moduli over the elastograms, Table 5.10, do not agree with the magnitude of the averaged stiffnesses through the phantom nor do they show any correlation with the stenosis size, for any combination of imaging parameters.

The wave images and elastograms through the three compositions of the 70% stenosis, at an excitation frequency of 100Hz through the read out motion encoding direction are shown in Figure 5.11. The mean shear moduli through the elastograms are shown in Table 5.11, alongside the approximated mean average stiffness through the imaged area. The wave images and elastograms do not show any obvious differences with changes in plaque stiffness. The average shear moduli results do not correlate with the magnitudes or trends of the actual averaged stiffnesses, for any combination of imaging parameters.

Stenosis Size (%)	**Mean (kPa)**									**Actual Mean Stiffness (kPa)**
	SS			**RO**			**PE**			
	Frequency (Hz)									
	75	**100**	**125**	**75**	**100**	**125**	**75**	**100**	**125**	
Healthy Vessel	9.1	9.1	11.7	8.7	8.8	9.7	9.4	9.0	10.1	13.8
50	7.4	7.5	9.7	7.7	7.4	8.6	8.2	7.9	8.6	14.0
60	7.4	8.1	11.4	9.5	9.1	9.1	9.3	9.9	9.8	14.0
70	8.4	9.0	10.3	10.1	9.2	9.4	10.1	10.6	10.0	14.0

Table 5.10: *The mean shear modulus through the elastograms of the healthy vessel and homogeneous 50%, 60% and 70% stenosis phantoms, through all motion encoding directions, at all excitation frequencies.*

Plaque	**Mean (kPa)**									**Actual Mean Stiffness (kPa)**
	SS			**RO**			**PE**			
	Frequency (Hz)									
	75	**100**	**125**	**75**	**100**	**125**	**75**	**100**	**125**	
Lipid	8.1	8.8	10.9	9.6	8.4	9.3	9.4	9.5	10.6	13.8
Homo-geneous	8.4	9.0	10.3	10.1	9.2	9.4	10.1	10.6	10.0	14.0
Fibrous	8.7	8.8	9.5	8.9	8.3	8.8	9.3	9.1	9.8	14.1

Table 5.11: *The mean shear modulus of the elastograms through the 70% stenosis phantoms with each plaque composition, through all motion encoding directions, at all excitation frequencies.*

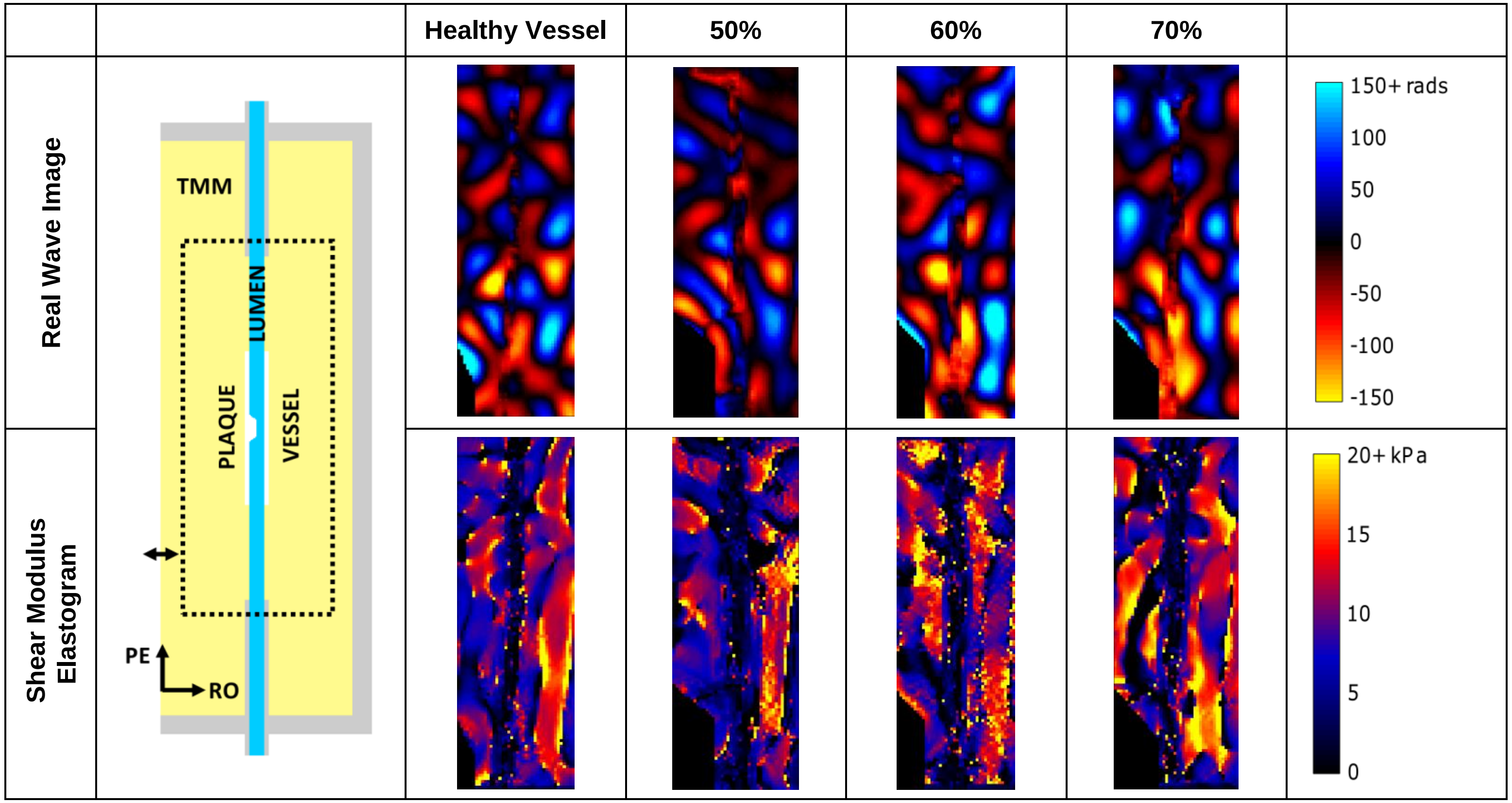

Figure 5.10: *The real component of the complex wave images and the shear modulus elastograms through the healthy vessel and three homogeneous plaque phantoms, at 100Hz through the read out motion encoding direction.*

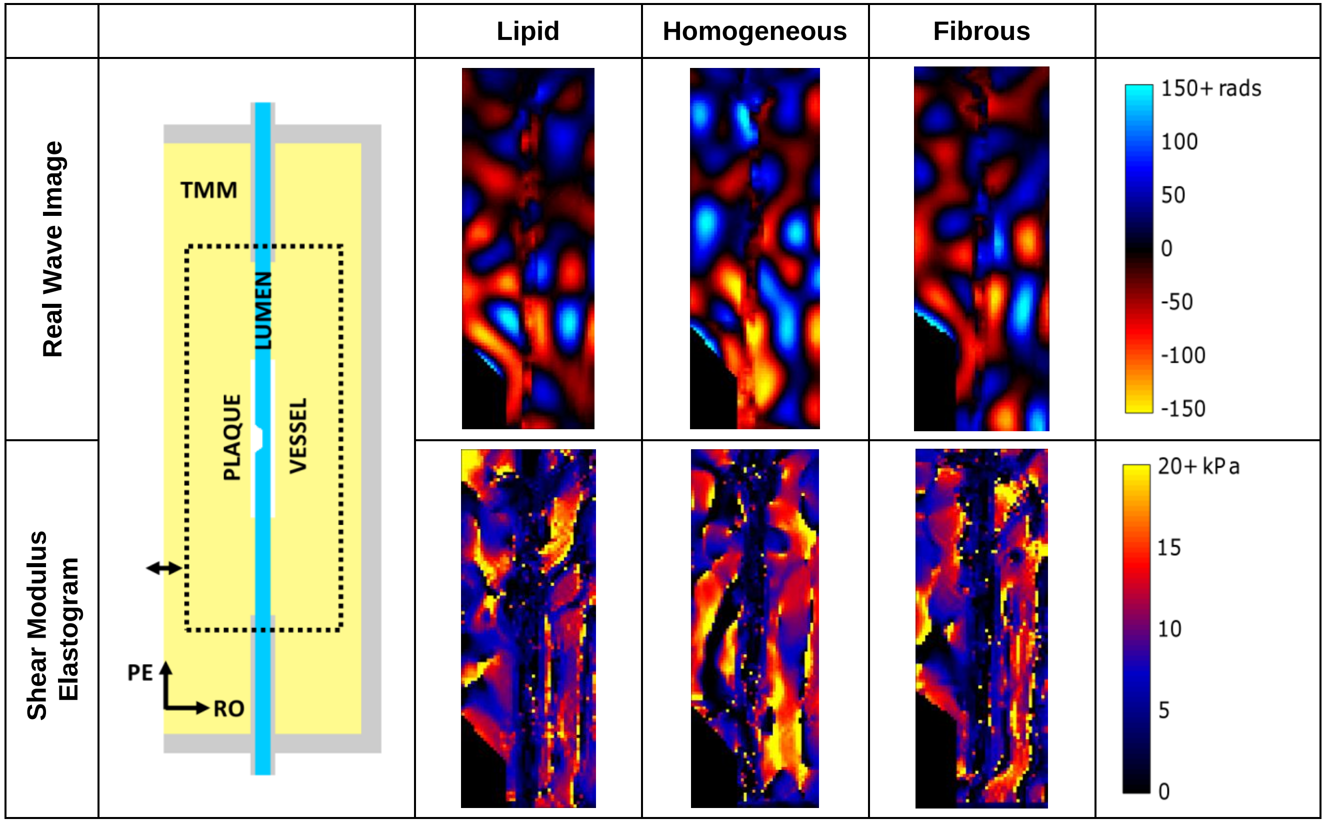

Figure 5.11: *The real component of the complex wave images and the shear modulus elastograms through three compositions of the 70% stenosis, at 100Hz through the read out motion encoding direction.*

5.4) Discussion

Although it cannot be seen in the wave images of this results section, due to the isolated regions of interest, the MRE wave images were subject to motion artefacts. Although the phantom was constrained as much as possible during the scan, the MRE actuator caused some rigid body motion which is visible as ghosting artefacts in the background of the phase images. The effect of these artefacts is hard to pinpoint within the body of the phantom, since motion is inherently present, however this overall motion of the phantom will have had a detrimental effect on the accuracy at which the waves were imaged.

The pixel artefacts discussed in Chapter 2, section 2.2.6, are also present in this data. In addition to the boundaries, seen also in the simulations of Chapter 4, the results of this chapter also suffer from the presence of non-planar wave propagation, wave reflections and noise, which exasperate the errors in the Laplacian creating more ‘black hole’ and inflated stiffness pixel artefacts and leading to extremely noisy elastograms.

Another potential source of error is the use of wide thresholds in the Butterworth filter. As just discussed, the presence of noise in experimental data can lead to artefacts generated by errors in the Laplacian. The Helmholtz inversion algorithm also neglects the effects of compressional wave components, so when waves are generated using compressional excitation, the filters are particularly important to its integrity. The use of wide filter thresholds was designed to avoid over smoothing of waves through inhomogeneous phantoms, however in doing so this may have led to increasing the errors created by noise and compressional wave components.

5.4.1) Signal to Noise Ratio

The SNRs in Tables 5.4 and 5.5 increase with decreasing frequency. The wave images of Figure 5.7 show that the wave amplitude decreases with increasing frequency, corresponding to a reduction in the amplitude of the signal across the ROI and leading to a lower SNR.

Through the homogeneous phantom the read out motion encoding direction yields a superior SNR, Table 5.4. Figure 5.6 shows that the wave propagation encoded along the read out direction, is quite planar, leading to the higher signal amplitude through the region of interest. The waves through the read out direction are most planar just under the actuator. As they propagate away from this area, the planar nature deteriorates. It can be concluded that this optimum wave propagation is due to the vibrations of the actuator being in the same direction as the motion encoding.

This observation does not hold through the arterial phantoms where the phase encoding direction yields approximately planar wave propagation and therefore the highest SNRs of the three motion encoding directions; Table 5.5 and Figure 5.8. The phase encoding direction is parallel to the long axis of the phantom and vessel and is therefore subject to the least amount of wave interference cause by reflections.

The applicability of the SNR extraction technique (McGee *et al.* 2011) is investigated in Chapter 6. The results shown in Table 5.4 and 5.5 are shown to be grossly underestimated; careful inspection of the wave images in Figure 5.6 to 5.11 supports this, as the wave images have very low levels of random noise, in some cases almost imperceptible. Even though the noise levels yielded by the SNR calculation are inaccurate, the SNR results do provide a method of comparing relative signal levels through the wave images.

5.4.2) The Homogeneous Phantom

Figure 5.6 quite clearly shows that through the homogeneous phantom, the read out motion encoding direction captures the best approximation of planar wave motion. Even through a simple rectangular block of TMM, the waves through the slice select and phase encoding direction are less than ideal. The phase encoding direction approaches planar wave motion just beneath the actuator. Following this through to the elastograms the smoothest, most artefact free regions correspond to areas which have the most planar wave motion; notably, underneath the actuator of the read out image. Confirming this observation, the standard deviation in Table 5.6, although large in all the images, is the lowest in the read out direction, followed by phase encoding and lastly the slice select direction.

$$\lambda = \frac{c_s}{f} \tag{5.4}$$

$$c_s = \sqrt{\frac{G}{\rho}} \tag{5.5}$$

None of the motion encoding directions or frequencies comes very close to true stiffness of the TMM; Table 5.6 and 5.7. The shear stiffness of the TMM is 16.8kPa, at 75Hz, 100Hz and 125Hz. This corresponds to wavelengths of 53mm, 40mm, 32mm respectively; equation 5.4 and 5.5. The approximate wavelengths through the homogeneous phantom just underneath the actuator, in the read out direction at 75Hz, 100Hz and 125Hz, are 48mm, 35mm and 29mm respectively. These wavelengths measured manually through the wave images, correlate well with the average stiffness values in Table 5.7. This indicates that although the elastograms have low homogeneity and obvious artefacts they are inverting the wave accurately. In light of this, the real stiffness of the tissue mimic becomes uncertain and future work would look to clarify this with additional mechanical testing. The quoted stiffness was based upon the manufacturing method and elastography stiffness imaging of Hamhaber et al. (2003).

All three excitation frequencies of Figure 5.7 show a similar approximately planar wave propagation. The wave amplitudes decrease with frequency, which affects the SNRs shown in Table 5.5. The averaged shear modulus increases and standard deviation decreases as frequency increases. However this observation it is not repeated in Table 5.7. Hamhaber et al. (2003) report that the viscous mechanical properties of the tissue mimic has little influence in the frequency range 125Hz – 400Hz.

5.4.3) The Healthy Vessel Phantom

Figure 5.8 shows that contrary to the homogeneous phantom, the healthy vessel phantom shows the more planar wave propagation through the phase encoding direction, which ties in with the superior average SNR seen through this direction in Table 5.5. The phase encoding direction is parallel to the long axis of the phantom and also the vessel, therefore sees the least amount of boundaries and wave reflection, leading to the smoother propagation.

Similar to the homogeneous phantom the slice select direction shows a decrease in wave amplitude and SNR in Table 5.5. The slice select direction encodes motion perpendicular to the plane of the image; the motion in this direction is neither parallel to the excitation wave nor in the long axis of the phantom. Therefore the waves in this direction are secondary waves subject to a large amount of wave interference generated by multiple boundaries.

The quality of the elastograms in Figure 5.8 is poor, the only identifiable feature is the lumen. The smooth wave propagation through the phase encoding direction makes even the lumen hard to discern in the elastogram. The average stiffnesses of the healthy vessel in

Table 5.8 are far below the approximate real stiffness through the ROI. The standard deviation again demonstrates a reduction through the motion encoding direction that shows the most planar wave propagation.

The wave images of Figure 5.9 do not show any substantial differences with increasing frequency, except for an expected reduction in wavelength amplitude; supported by the SNR results of Table 5.5. The elastograms are all of a similar poor quality, which is not alleviated by changes in frequency. The quantitative data in Table 5.8 and 5.9 show no preferential imaging direction or excitation frequency.

5.4.4) Stenosis Size and Composition

MRE of the phantoms containing vessels have yielded disappointing results. The lumen is visible in the wave and elastograms images, but the vessel wall and plaques are not. The magnitude of the averaged shear moduli through the elastograms are far below their real value. It is difficult to identify if any parameters yield more accurate results because, as Tables 5.6 to 5.9 show, the standard deviations of the elastograms are so high.

The 'black hole' and overestimated magnitude artefacts, seen and discussed in Chapter 4, dominate the vessel elastograms in Figures 5.8 to 5.11; where the lack of planar wave propagation through highly inhomogeneous media invalidates several assumptions of the inversion algorithm. The average stiffness values of Table 5.10 and 5.11 are far below their approximate actual mean stiffness. Although the stiffness of the TMM has been questioned, the quantitative results show no correlation with size or stiffness of plaque, or indeed with the presence of a plaque compared to the healthy vessel phantom. This conclusion remains true even when the ROI is isolated to just the plaque or vessel wall. For these reasons the quantitative analysis of the experimental results was taken no further.

In the presence of relatively more planar wave propagation, i.e. in the phase encoding direction, the elastograms start to lose their depiction of the lumen, which arguably makes the results worse, with no significant improvement in the quantitative results. This highlights the inapplicability of the inversion algorithm, it requires planar waves to invert them properly, but in having planar waves the inhomogeneous detail of the medium is lost.

The one positive observation that can be taken away from these results is that to a more or less degree, the lumen can be identified in both the wave images and elastograms. The wave images show the lumen as an obvious disruption running through the length of the image. The lumen appears as a region of zero stiffness in the elastograms, which is identifiable even in the presence of the 'black hole' artefacts. Therefore non-planar waves passing through a highly inhomogeneous phantom with multiple boundaries, can still detect the absence of tissue stiffness.

5.5) Conclusions

Chapter 4 demonstrated that the accuracy of MRE suffers with the increasing pixel size and the presence of noise and indicated that development on the imaging side of the technique to increase SNR and resolution is required. Qualitative analysis of MRE through a homogeneous TMM phantom and selection of vessel phantoms has shown that the quality of the elastograms is further compromised by low levels of noise, rigid body motion artefacts, non-planar wave propagation and inhomogeneous media.

It has been noted that the presence of inhomogeneous tissue and the boundary between the plaque and lumen leads to artefacts in the elastogram. This chapter has highlighted that in order to invert wave images through atherosclerotic plaques the inversion algorithm also needs to be able to deal with the more realistic non-planar wave propagation seen experimentally. The wave propagation *in vivo* may actually be subject to less wave interference since a four sided plastic box is an extreme set of boundary conditions. However the interference caused by the presence of the lumen and inhomogeneous tissue would still be present in an *in vivo* scan and thus to develop this area of research a more applicable inversion algorithm needs to be utilised.

A technique to create a series of arterial phantoms containing plaques of various size and stiffness was proposed to validate the application of MRE to atherosclerosis. Although the validation was unsuccessful, areas for development in the phantom validation and imaging methodology have been highlighted.

Chapter 6
Comparison of Computational and Experimental Magnetic Resonance Elastography

6.1) Introduction

Computational simulations and experimental phantoms are often used as methods of validation. Simulating MRE through replicated models of the experimental phantoms in Chapter 5 offers an opportunity to compare the experimental and computational results; giving insight into the realism of the simulation results.

Replicating the experimental phantoms as closely as possible, in terms of geometry, material properties, loads, noise and pixel size, will allow the results to be assessed without rigid body motion and the ghosting artefacts seen experimentally. To some extent this could support the proposal of the technique outlined in Chapter 5 as a future validation methodology for arterial MRE. In addition comparison of the experimental wave images and computational waves images with the same extracted and added SNR, will allow the accuracy of the noise analysis to be reviewed.

The aim of this chapter is to computationally simulate MRE through replicated models of the phantoms in Chapter 5 and in doing so, validate the noise analysis method, the realism of the computational simulations and assess the potential of the experimental technique outlined in Chapter 5 under more idealised conditions, to identify a change in plaque stiffness.

6.2) Method

6.2.1) Overview

The methodology for conducting a simulation of MRE has been discussed in depth throughout Chapters 2, 3 and 4. The same methodology was applied in this chapter with each parameter tailored to reflect the experimental set up in Chapter 5. As discussed in Chapter 2, the units of the experimental and computational complex wave images are radians and displacement respectively. These are a comparable inputs into the inversion algorithm and proportional via equation 6.1 (Klatt 2010). Φ, A, ω, γ, K_0 and q refer to the wave phase, wave amplitude, excitation frequency, gyromagnetic ratio, motion encoding gradient frequency and number of motion encoding gradient cycles, respectively.

$$A = \Phi \frac{\omega}{2\pi\gamma K_0 q} \tag{6.1}$$

The computational simulations shall incorporate the geometry, material properties, loads, boundary conditions, SNR and pixel size of the experimental study. While every effort shall be made to replicate the experimental phantoms there are uncertainties in the experimental methodology that cannot be accounted for in a precise computational model. Examples include, unquantified shrinkage of the tissue and vessel mimic during manufacture and load applied by the actuator on the surface of the tissue mimicking material. The load shall be tailored to induce a similar wave displacement in the simulations as the phase of the waves seen in Chapter 5.

The effect of noise on computational and experimental MRE has been discussed in Chapter 4 and Chapter 5. It has been mentioned that the method of extracting SNR from experimental data may not be ideal, the consequence of which has led to discrepancies between the values of SNR taken from the experimental data and those added to the computational data. This issue will be discussed and investigated in this chapter, since the comparison of replicated simulated images with the original experimental data provides the perfect platform to qualitatively compare the noise levels.

The wave images, elastograms and mean predicted shear modulus through the experimental and computational healthy volunteer phantom shall be used to compare the results in each motion direction and at each excitation frequency. The variation of the computational results through the phantoms with changes in plaque size and stiffness shall be assessed both globally and locally. This will ascertain whether the removal of complications which caused additional image and wave disruption would allow MRE through arterial phantoms to yield a correlation between plaque stiffness and composition.

Computationally, the model geometry was created using the computer aided design software Rhinoceros version 3.0. The simulations were run on the finite element analysis software Abaqus/ CAE version 6.10-1. The inversion algorithm was developed by collaborators at the

MR Elastography Group, Charité Univesitätsmedizin Berlin. The data was formatted using Microsoft Office Excel before being imported into MATLAB R2011a to run the inversion algorithm.

6.2.2) Geometry

The phantom geometry was based upon the dimensions of the tissue and vessel mimicking materials of the phantoms in Chapter 5. The values are outlined in Table 6.1, and the simulated phantom geometry and nomenclature is shown in Figure 6.2. The global axes of the model and their synonymous imaging directions are shown in 6.1(b).

Material	**Phantom Component**		**Length, L (mm)**		**Width, W (mm)**	**Depth, D (mm)**	**Diameters, Ø (mm)**	
			Inner	**Outer**			**Inner**	**Outer**
Tissue Mimic	Surrounding Tissue		N/A	300.0	80.0	100.0	N/A	N/A
Vessel Mimic	Wall		N/A	80.0	N/A	N/A	8.0	13.0
	Stenosis	50%	8.0	14.6	N/A	3.9	N/A	N/A
		60%	8.0	15.3	N/A	4.8	N/A	N/A
		70%	8.0	13.0	N/A	5.6	N/A	N/A

Table 6.1: *Tissue and vessel mimic mould dimensions.*

Atherosclerosis was modelled as an eccentric stenosis embedded in the wall of an otherwise healthy and straight vessel. A 50%, 60% and 70% stenosis was combined with three stiffnesses to represent a homogeneous plaque (with the same properties as the wall), a lipid based plaque and fibrous plaque. The vessel was embedded within tissue mimicking material. Similarly to the phantom study, blood flow was neglected and the lumen was filled with water, which was assumed to remain static unless interacting with the excitation waves.

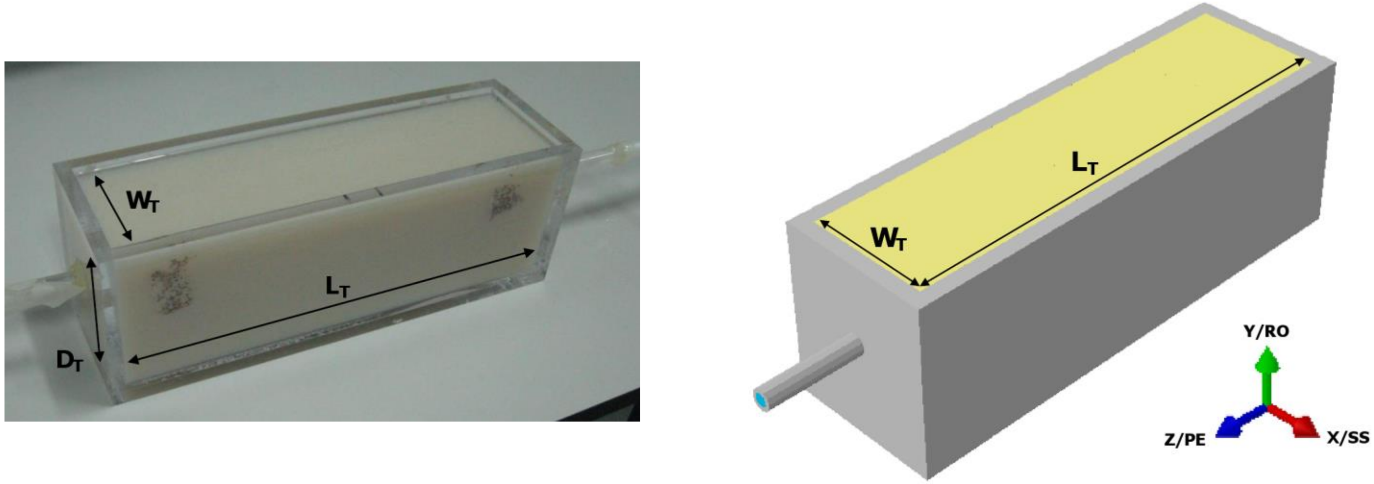

(a) Arterial phantom

(b) Isometric view of phantom model

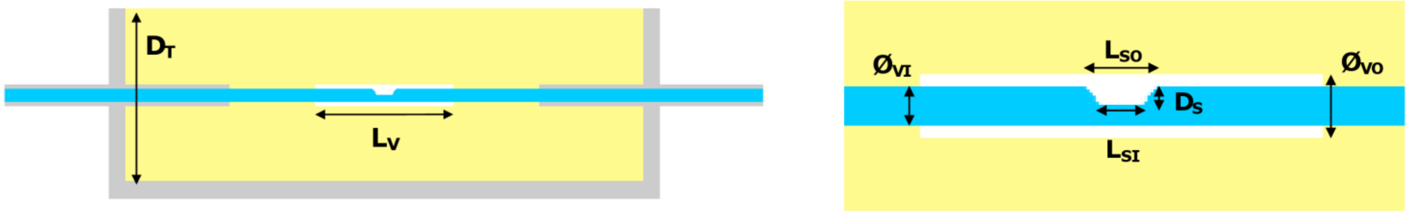

(c) Sectional view of phantom model

(d) Sectional view of vessel geometry

Figure 6.1: *Simulation and phantom geometry.*

6.2.3) Material Properties

The material properties used in the simulations are focussed upon the shear modulus properties of the tissue mimic and vessel mimic, Table 5.2. The shear viscosity values are not defined for the materials that were used to construct the phantoms and were therefore given an arbitrary value of 3Pas taken from MRE literature (Klatt *et al.* 2007).

The Voigt model was used to model the viscosity, unifying the modelling technique with the inversion algorithm. The tissue and vessel mimic were modelled with a density of 1047kgm^{-3} (Hoskins 2010) and as incompressible; an assumption that is applicable due to high water content tissues (Fung 1993). The lumen was modelled with the density and bulk modulus of water (Hoskins 2008), and the phantom container with the properties of acrylic. The material properties used in the simulation are summarised in Table 6.2.

Material	**Phantom Component**	**Density (kgm^{-3})**	**Moduli**			
			Young's (kPa)	**Shear (kPa)**	**Viscous (Pas)**	**Bulk (kPa)**
Tissue Mimic	Surrounding Tissue	1047	-	16.8	3.0	-
Vessel Mimic	Wall	1047	-	34.2	3.0	-
	Fibrous Plaque	1047	-	53.4	3.0	-
	Lipid Plaque	1047	-	6.3	3.0	-
Water	Lumen	1000	-	-	-	2.2 x10^{6}
Acrylic	Phantom Container	1180	3.2 x10^{6}	-	-	-

Table 6.2: *Material properties: arterial phantom simulations.*

6.2.4) Loads

The load nodes were chosen to represent the approximate contact area between the actuator and tissue mimic; 47mm by 32mm. The load nodes were placed above and off centre to the plaque, similar to the position of the actuator during the experimental scans. A 10N load was applied at each node to replicate the amplitude of the wave deformation through the phantoms seen experimentally. The load was applied at 75Hz, 100Hz and 125Hz.

6.2.5) Boundary Conditions

Unlike the previous computational chapters, wave reflections were not avoided in these simulations. The boxes used to hold the experimental phantoms were constructed from acrylic and therefore created multiple hard surfaces that encourage reflection of the excitation wave. Therefore to create similar wave reflections, the phantom container was constrained on all surfaces, in all directions. The remaining components of the phantom, the tissue and vessel mimic and the water filled lumen were constrained by tying the nodes to adjacent parts.

6.2.6) Mesh

The size of the computational models in this chapter, compared to models in previous chapters, was very large. This put restrictions on the mesh density, in terms of the time and memory resources required to run the simulation. The element edge length was 0.5mm around the plaque, increasing to 1mm through vessel wall surrounding it. In the surrounding tissue mimic the element length had to be increased to 2mm and then again to 3.6mm towards the outer edges of the block. These larger element lengths reduced the size of the models and in tandem the simulation time and memory requirements. However as shown in Chapter 2, an element size that is larger than the proposed pixel size, creates visible errors in elastograms and also the average shear modulus. It was felt that since the surrounding tissue was meshed with predominately 2mm element lengths which are only fractionally bigger than the experimental pixel size of 1.84mm^2, this was an acceptable reduction in accuracy.

The mesh was structured and comprised of hexahedron elements wherever possible, however around some of cylindrical and stenosis geometry an unstructured mesh composed of tetrahedral elements was used. The elements used to model the tissue and vessel mimic were hybrid elements and the elements used to model the water in the lumen were acoustic elements.

6.2.7) Results Extraction

Results were extracted through the experimental pixel value of 1.84mm^2, used in Chapter 5. The results were extracted over two regions of interest. The first was of a similar size to that seen in Chapter 5, incorporating the whole vessel and surrounding tissue. The results through this region shall be referred to as the global phantom. The second region shall focus specifically on the plaque, similar to the region of interest in Chapter 4. The results through this region shall be known as the local plaque.

6.2.8) Artificial Noise

The method of SNR extraction from experimental MRE data and addition to computational data has been discussed in sections 4.2.8, 5.2.8 and is explained in detail in Appendix B (McGee *et al.* 2011). Wave and elastogram images taken from the experimental scans and replicated computational simulations were compared at the same SNR to assess the applicability of the noise extraction technique.

6.2.9) Image Processing

The image processing methodology is exactly the same as that described in section 2.2.6 incorporating the filters described in section 4.2.9. The algorithm is described in MATLAB code format in Appendix A. A 2D Butterworth bandpass filter with thresholds 5m^{-1} and 100000m^{-1} was applied to the wave images after artificial noise had been added but prior to inversion. The shear moduli were assessed over the global and local regions of interests, using the mean, standard deviation and standard error over 20 cycles containing additional random noise.

6.3) Results

6.3.1) Signal to Noise Ratio Comparison

Figure 6.2 compares the wave images and elastograms through a homogeneous section of the experimental and computationally simulated phantoms. These images were all taken through the homogeneous 70% stenosis geometry, at an excitation frequency of 100Hz, with motion extracted through the read out and corresponding Y direction, relative to Figure 6.1(b).

Scrutinising the experimental wave images show almost imperceptible levels of random noise. This follows through to an elastogram with very little speckle. The corresponding computational wave image at SNR 33 has an obvious scattering of random noise that is seriously detrimental to the quality of the elastogram. The experimental and computational data at a SNR of 33 obviously do not have the same level of noise; therefore the noise extraction technique and addition technique to and from the experimental and computational data, are not comparable.

As the SNR through the computational images increases, the noise level appears to visually become more in line with what can be seen through the experimental images. An SNR of 500 through the computational images looks to be an approximate good match. Therefore the computational results were continued with artificial noise added at this SNR.

6.3.2) Comparisons through the Healthy Vessel Phantom

Figure 6.3 and 6.4 compare the waves images and elastograms through the experimental phantoms and computational simulations with variations in motion direction at 100Hz. The X/slice select direction shows reduced wave amplitudes in both the experimental and computational wave images. In the case of the simulations this also follows through to produce a noisy elastogram. Overall the computational simulations show more planar wave propagation than the experimental wave images and higher stiffness values and homogeneity through the tissue mimic of the phantom. The lumen is clearer in the computational wave images and elastograms compared to those yielded by experimental MRE.

Figures 6.5 and 6.6 compare the wave images and elastograms through the experimental phnatoms and the computational simulations with variations in excitation frequency through the Y/read out direction. Even though they do not display the same wave propagation both the computational and experimental wave images show a decrease in wavelength with increasing frequency, and a notable reduction in wave amplitude at 125Hz. The wavelengths in the computational image are longer than in the experimental image for the same frequency. This follows through to elastograms displaying higher stiffnesses than the experimental ones.

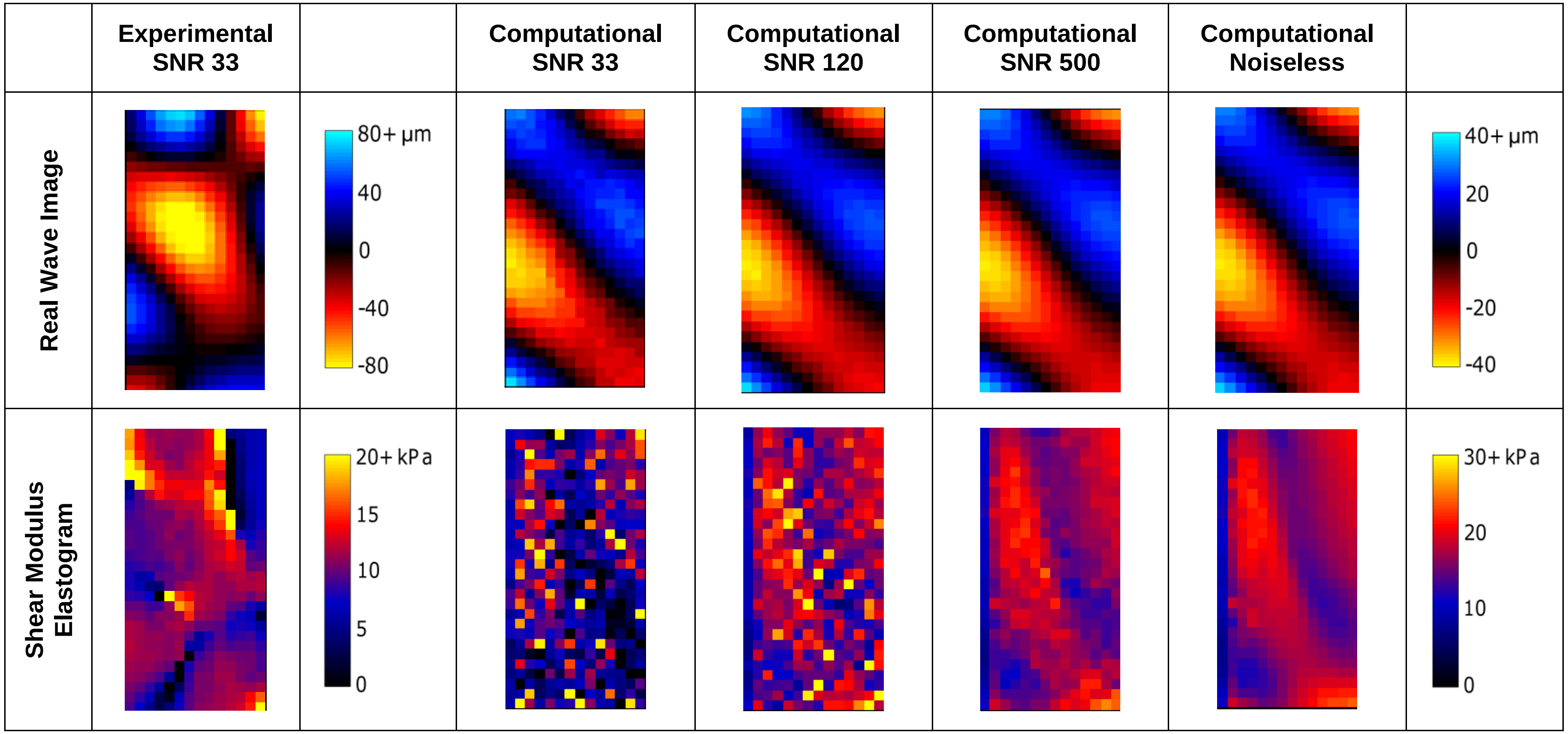

Figure 6.2: *The real component of the complex wave images and the shear modulus elastograms through the experimental and computational healthy vessel phantom, at 100Hz in the Y/read out motion direction. The results are presented at a pixel size of 1.84mm^2 and various SNRs to compare the noise level in the experimental and computational images.*

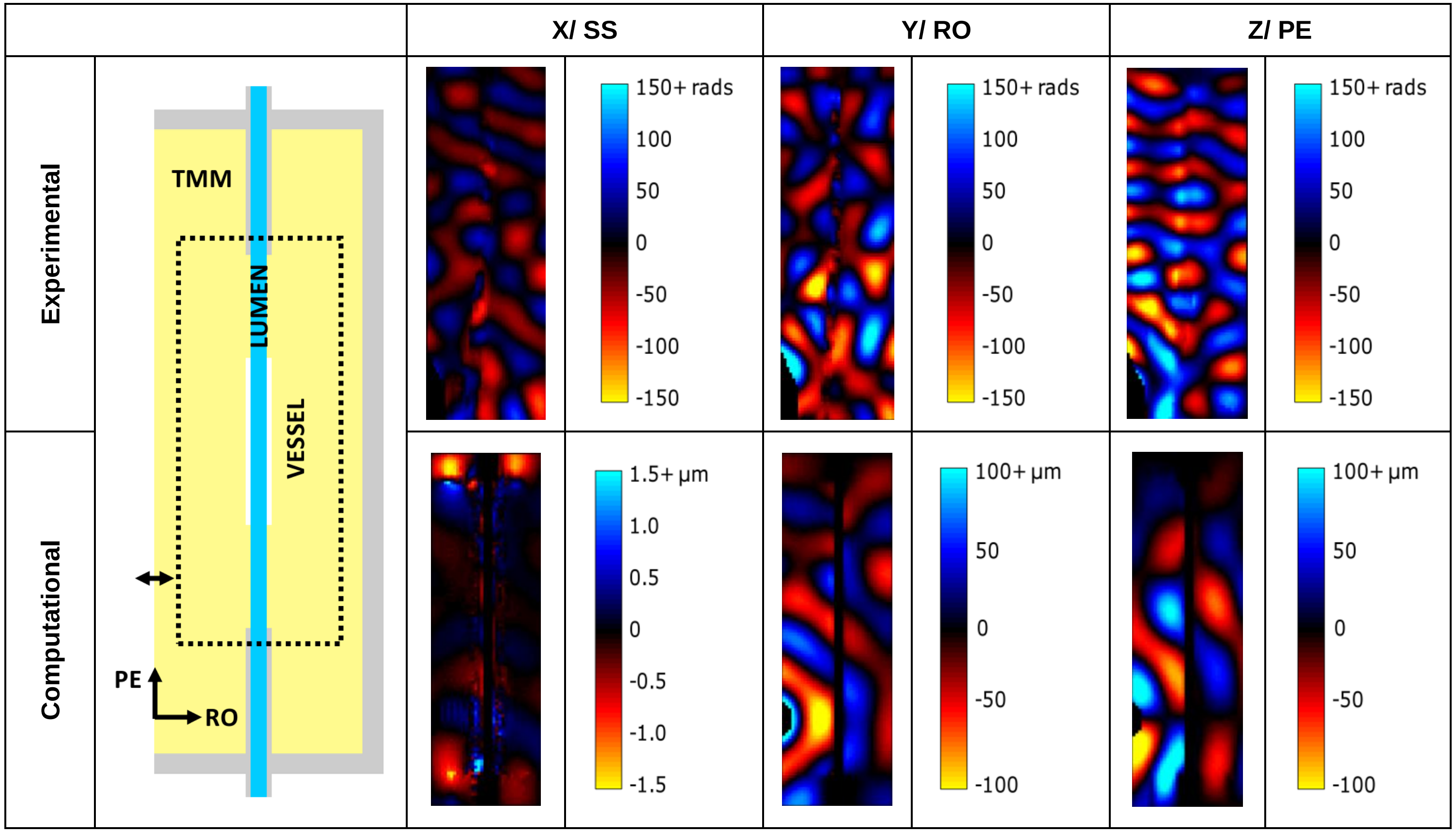

Figure 6.3: *The real component of the complex wave images through the experimental and computational healthy vessel phantoms, at 100Hz through each motion direction.*

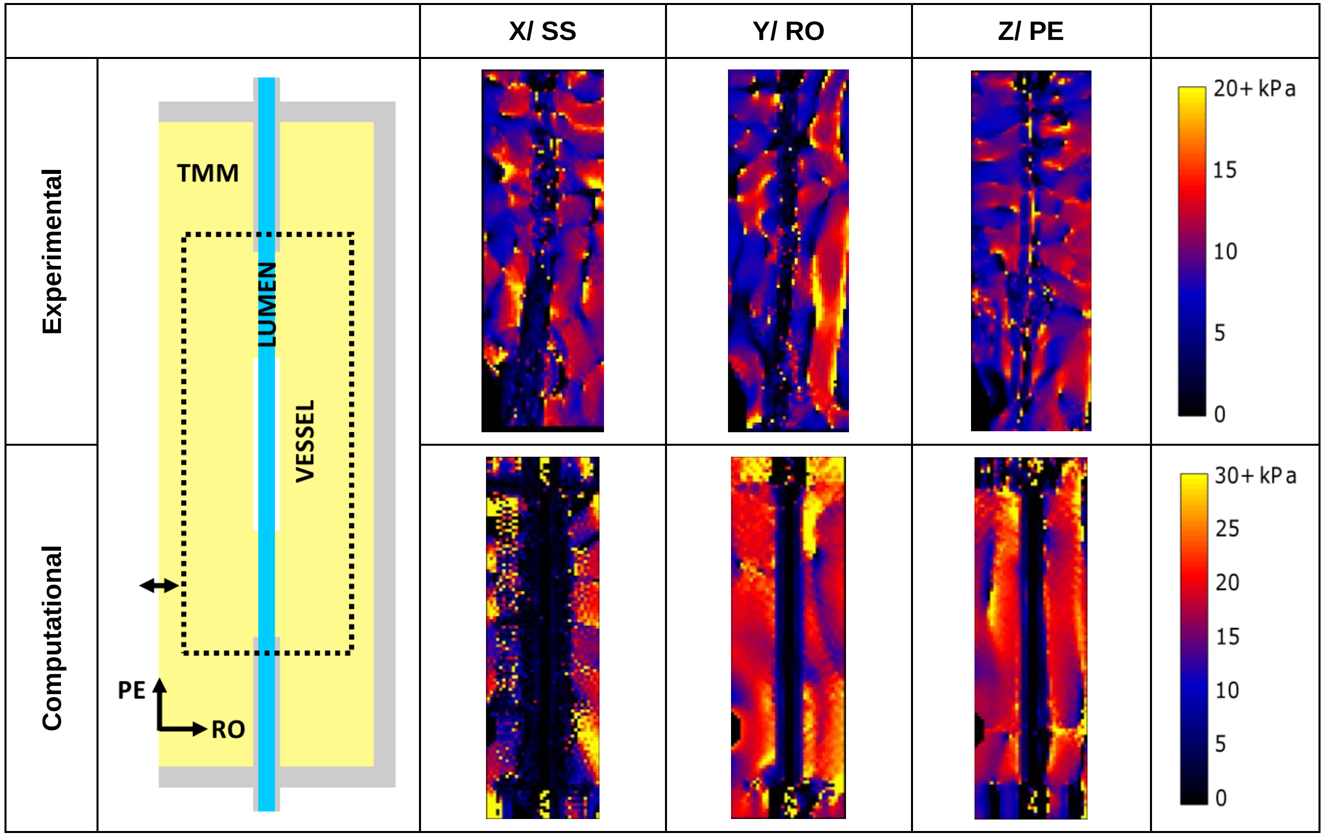

Figure 6.4: *The shear modulus elastograms through the experimental and computational healthy vessel phantoms, at 100Hz through each motion direction.*

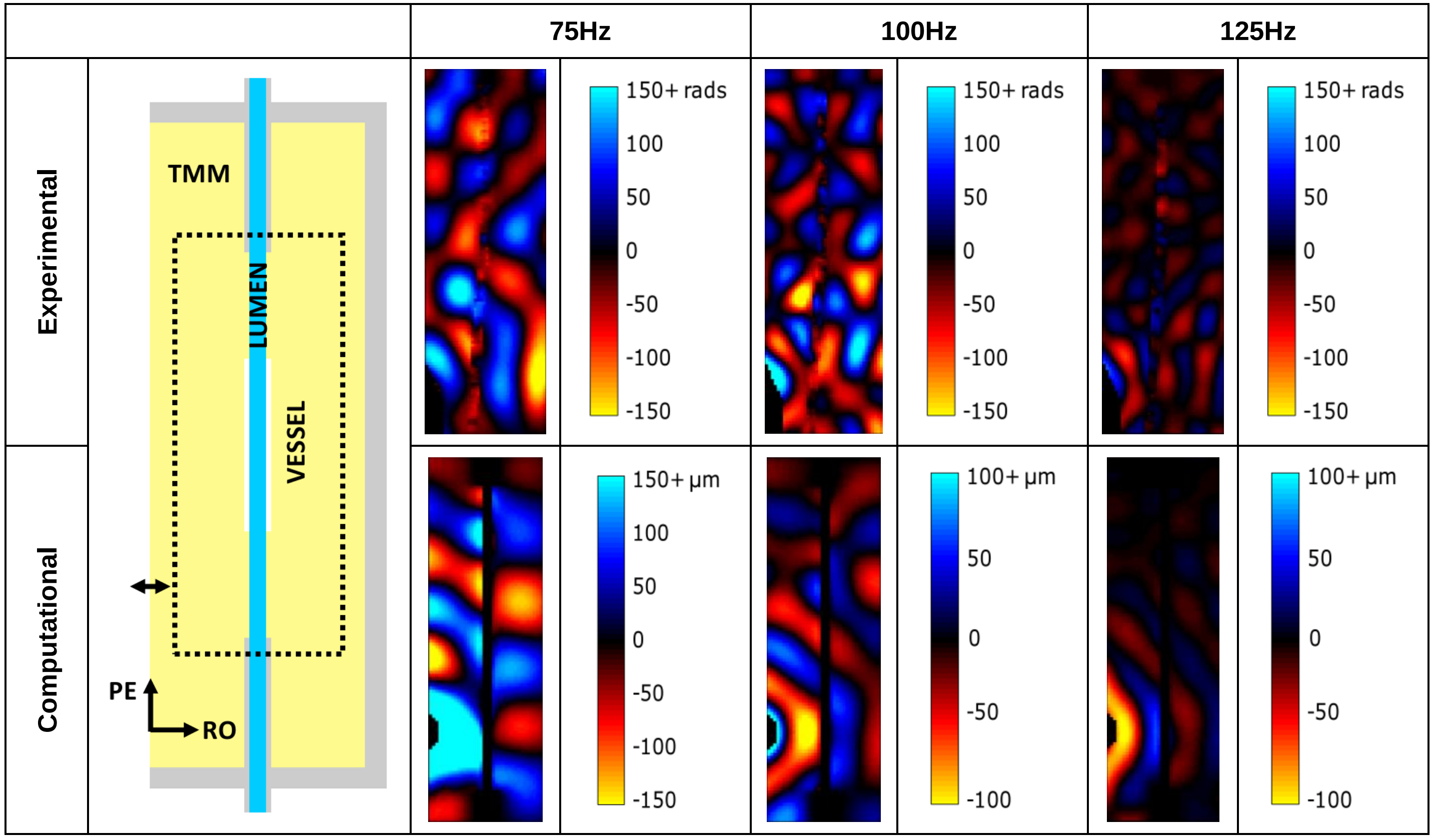

Figure 6.5: *The real component of the complex wave images through the experimental and computational healthy vessel phantoms, at each frequency through the Y/read out motion direction.*

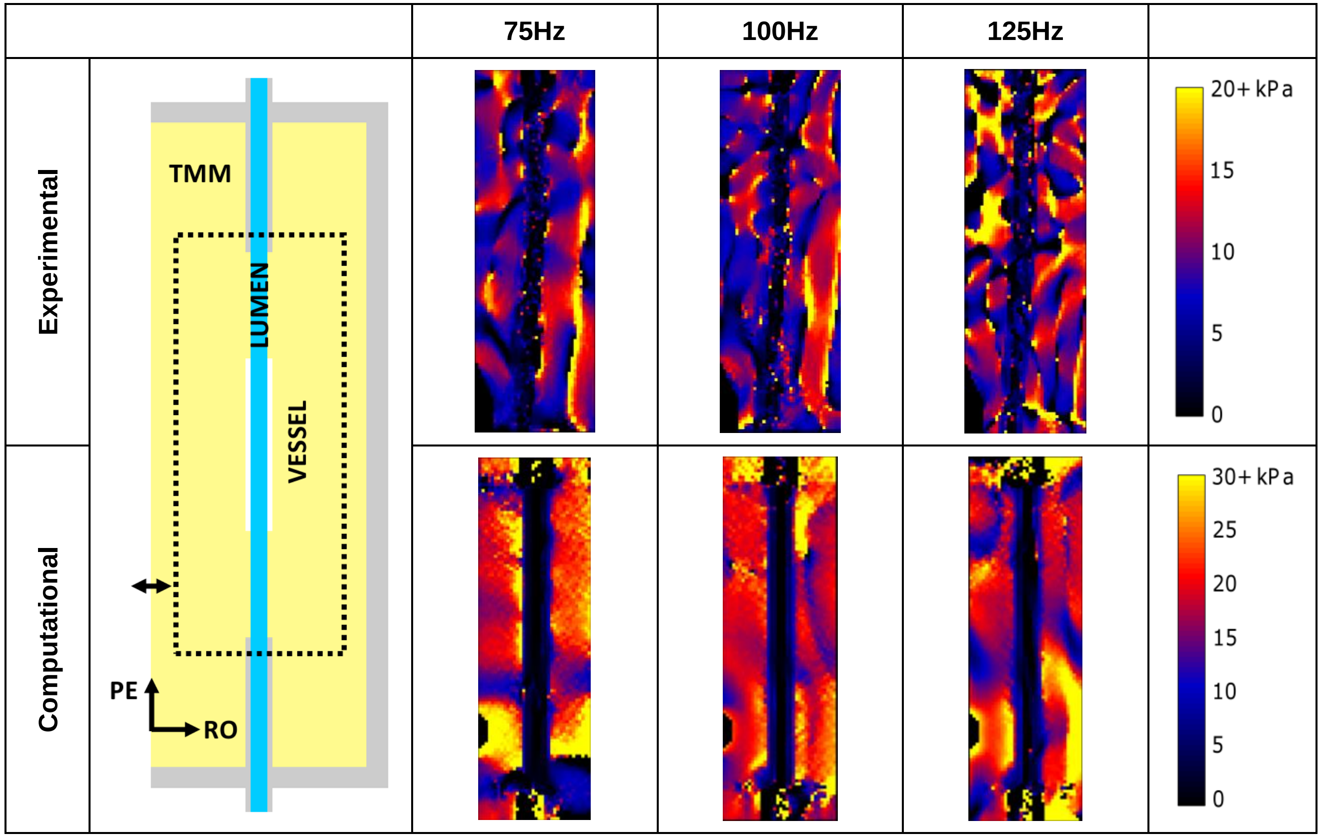

Figure 6.6: *The shear modulus elastograms through the experimental and computational healthy vessel phantoms, at each frequency through the Y/read out motion direction.*

	Motion Encoding Directions	**Mean (kPa)**	**Standard Deviation (kPa)**	**Standard Error over 20 Images (kPa)**	**Approximate Actual Mean Stiffness (kPa)**
Experimental	Slice Select (X)	9.1	8.1	N/A	13.8
	Read Out (Y)	8.8	6.3	N/A	13.8
	Phase Encoding (Z)	9.0	4.7	N/A	13.8
Computational	X (Slice Select)	11.6	32.3	0.10	13.6
	Y (Read-Out)	16.9	17.6	0.05	13.6
	Z (Phase Encoding)	14.8	14.0	0.04	13.6

Table 6.3: *The mean, standard deviation and standard error of the shear modulus through the elastograms of the experimental and computational healthy vessel phantoms at a frequency of 100Hz through each motion direction.*

	Frequency (Hz)	**Mean (kPa)**	**Standard Deviation (kPa)**	**Standard Error over 20 Images (kPa)**	**Approximate Actual Mean Stiffness (kPa)**
Experimental	75	8.7	9.8	N/A	13.8
	100	8.8	6.3	N/A	13.8
	125	9.7	9.6	N/A	13.8
Computational	75	16.8	18.5	0.03	13.6
	100	16.9	17.6	0.05	13.6
	125	18.0	18.0	0.09	13.6

Table 6.4: *The mean, standard deviation and standard error of the shear modulus through the elastograms of the experimental and computational healthy vessel phantoms at each excitation frequency through the Y/ read out motion direction.*

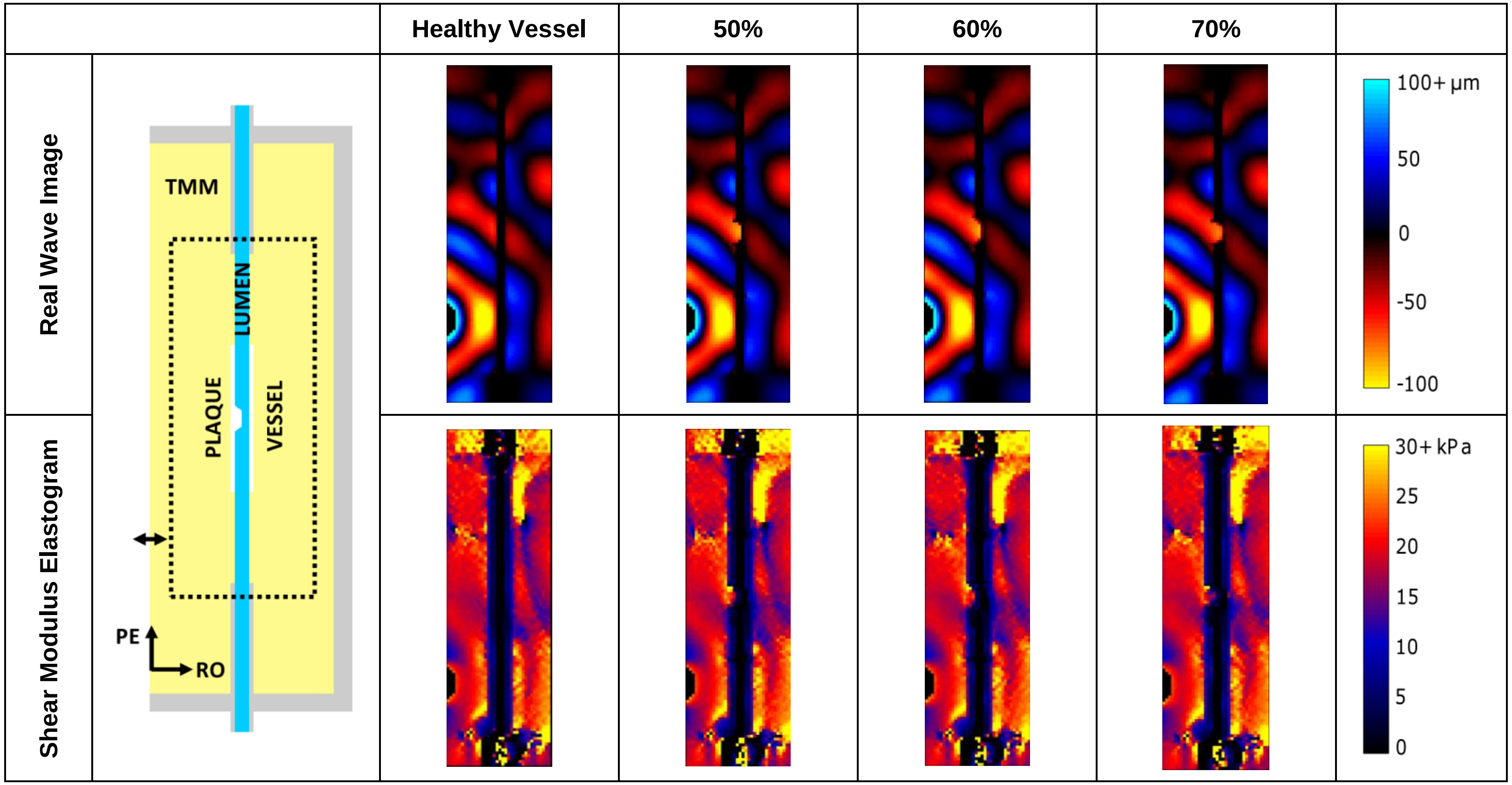

Figure 6.7: *The real component of the complex wave images and shear modulus elastograms through the computational healthy vessel and three homogeneous plaque phantoms, at 100Hz through the Y motion direction.*

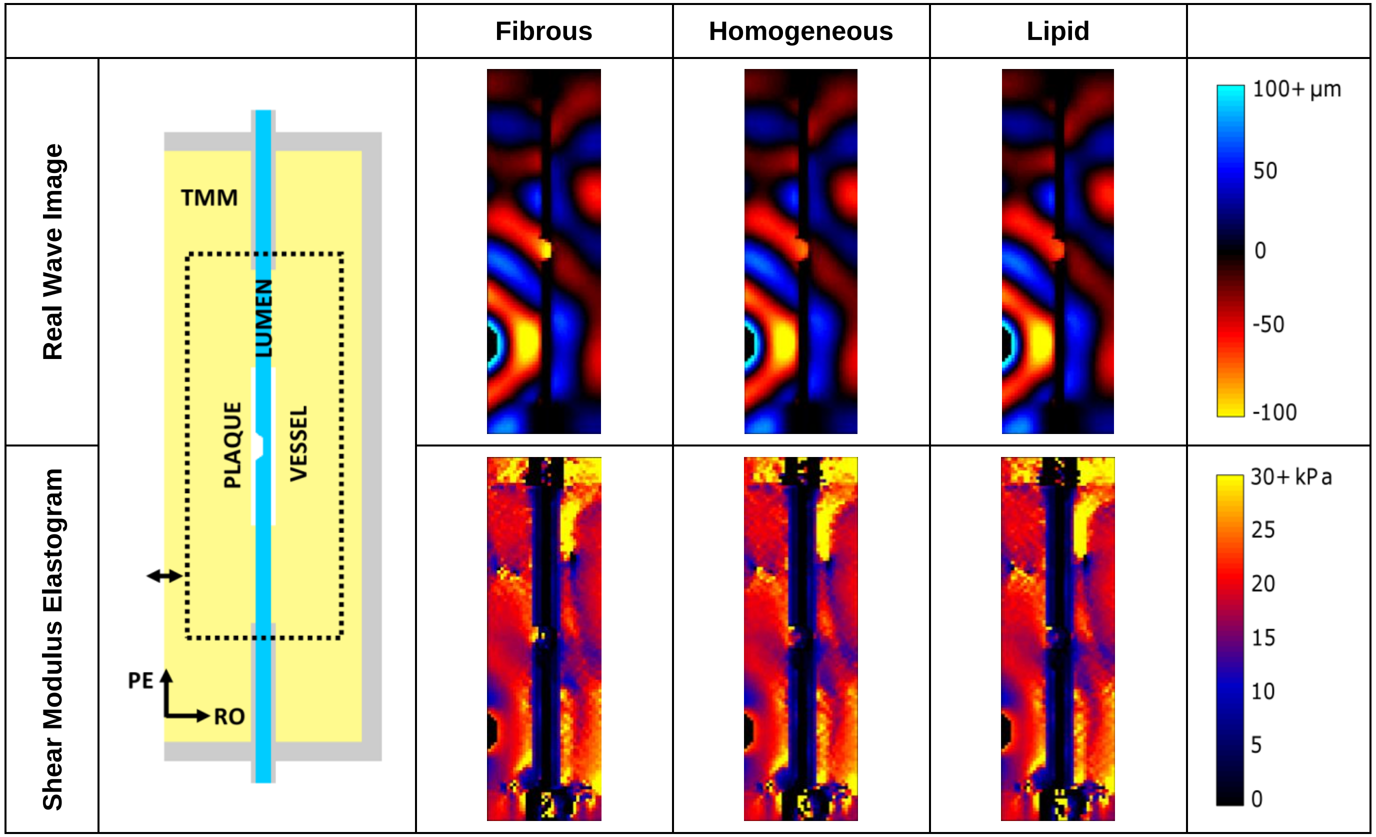

Figure 6.8: *The real component of the complex wave images and shear modulus elastograms through each composition of the computational 70% stenosis phantom, at 100Hz through the Y motion direction.*

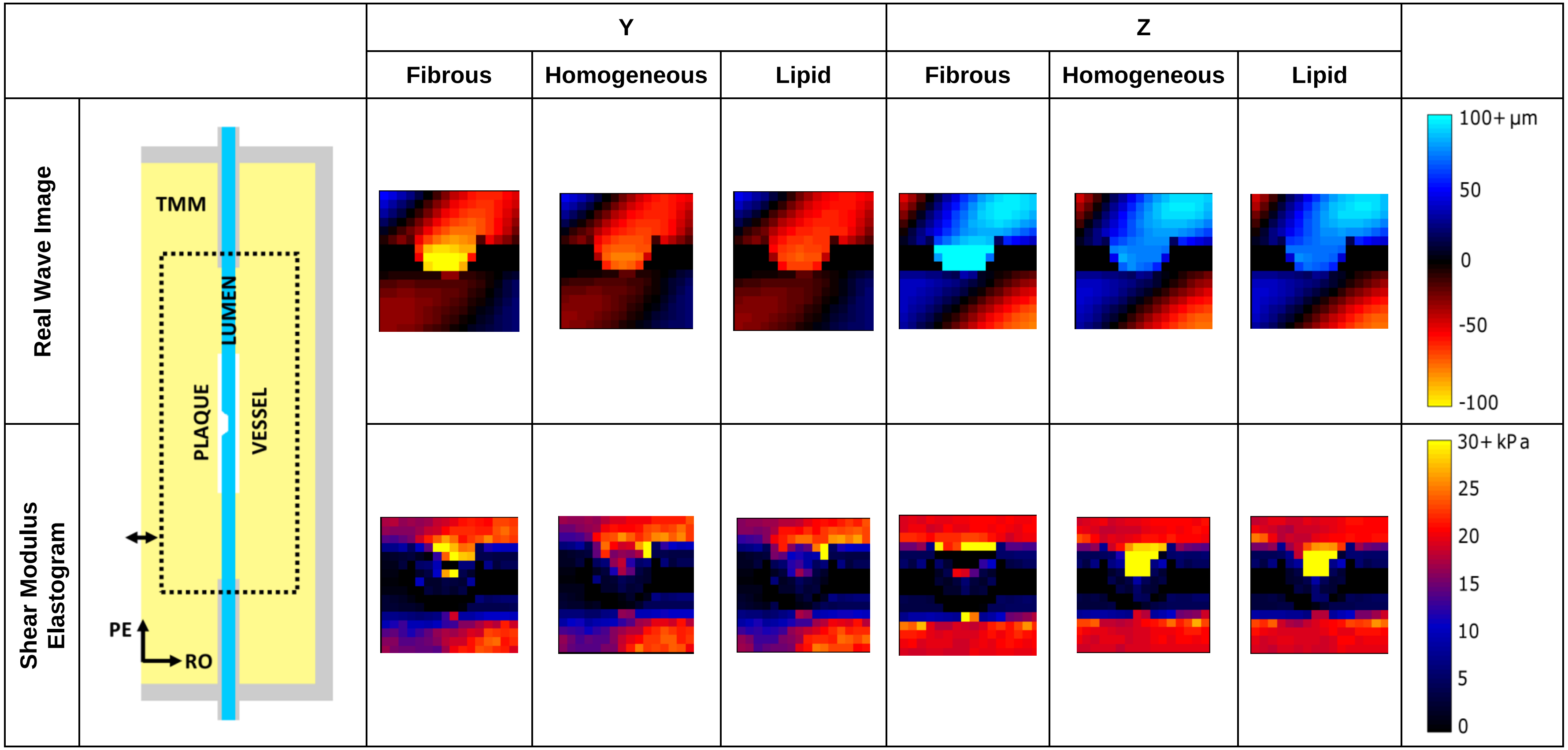

Figure 6.9: *The real component of the complex wave images and shear modulus elastograms through each composition of the computational 70% stenosis plaque, at 100Hz in the Y and Z motion directions.*

Table 6.3 and 6.4 compare the experimental and computational variation of the mean and standard deviation through the elastograms with motion direction and frequency. The standard errors over 20 cycles of added artificial SNR are low. The standard deviations of the computational elastograms are very high, on a par with the magnitudes of the means values. Bar a few exceptions, this is also seen in the experimental data. Overall the computational elastograms have a higher mean than the experimental ones; in the majority of cases this exceeds the approximate actual mean stiffness through the simulated phantom.

6.3.3) Computational Simulations through Global Arterial Phantoms

Considering the low magnitudes seen in the X direction wave images of Figure 6.3 and consequent low quality elastogram in Figure 6.4, the results were continued considering the Y and Z direction only.

Figure 6.7 and 6.8 show the variation of the computational wave images and elastograms with the stenosis size and stiffness. As noted in section 6.3.2, the computational images show clearer depiction of the lumen, and in this section the plaques are also well resolved. The wave images and elastograms show continuity between plaque sizes and compositions; the differences between the images are localised to the stenosis.

Stenosis Size (%)	**Mean (kPa)**						**Approximate Actual Mean Stiffness (kPa)**
	Y			**Z**			
	75 Hz	**100Hz**	**125Hz**	**75 Hz**	**100Hz**	**125Hz**	
Healthy Vessel	16.8	16.9	18.0	14.9	14.8	17.8	13.6
50	16.8	16.9	18.6	15.3	14.9	17.6	13.8
60	16.6	16.9	18.7	15.3	14.8	17.6	13.8
70	16.7	16.9	18.3	15.3	14.8	17.6	13.9

Table 6.5: *The mean shear modulus of the elastograms through the healthy vessel and homogeneous 50%, 60% and 70% stenosis simulations through the Y and Z motion directions.*

Stenosis Composition	**Mean (kPa)**						**Approximate Actual Mean Stiffness (kPa)**
	Y			**Z**			
	75 Hz	**100Hz**	**125Hz**	**75Hz**	**100Hz**	**125Hz**	
Lipid	16.6	16.7	18.2	15.3	14.7	17.9	13.6
Homogeneous	16.7	16.9	18.3	15.3	14.8	17.6	13.6
Fibrous	16.7	16.8	18.3	15.2	14.9	17.7	14.0

Table 6.6: *The mean shear modulus of the elastograms through 70% stenosis phantoms with each plaque composition, through the Y and Z motion directions.*

Table 6.5 and 6.6 summarise the change in global stiffness, averaged over the whole phantom with changes in stenosis size and stiffness. The magnitude of the average stiffness through the elastograms is higher than that of the approximate actual mean stiffness. There is little variation and no identifiable trends with stenosis size or stiffness with the average predicted stiffness results through the simulations.

6.3.4) Computational Simulations through Local Atherosclerotic Plaques

Computational simulations yield much higher clarity wave images and elastograms, meaning that in this chapter the stiffness local to the plaque could be explored in isolation. Figure 6.9 shows wave images and elastograms through the region surrounding the 70% stenosis of various compositions. The region of interest was extended around the plaque in these images; because the plaque is only 3 pixels deep, it is difficult to visualise wave propagation through one alone. Both motion directions show increased wave displacement through the lipid plaque and the Z direction yields elastograms with increased shear moduli through the homogenous and fibrous plaques.

Figure 6.10 shows the variation of the averaged elastogram stiffness through the 70% stenosis with changes in composition. The Y direction does not show a correlation between plaque composition and predicted shear modulus. The Z direction shows a trend of increasing predicted shear modulus through the elastogram as the true stiffness value of the plaque increases. The magnitudes in both motion directions and all frequencies are lower than their true values for the homogeneous and fibrous plaques.

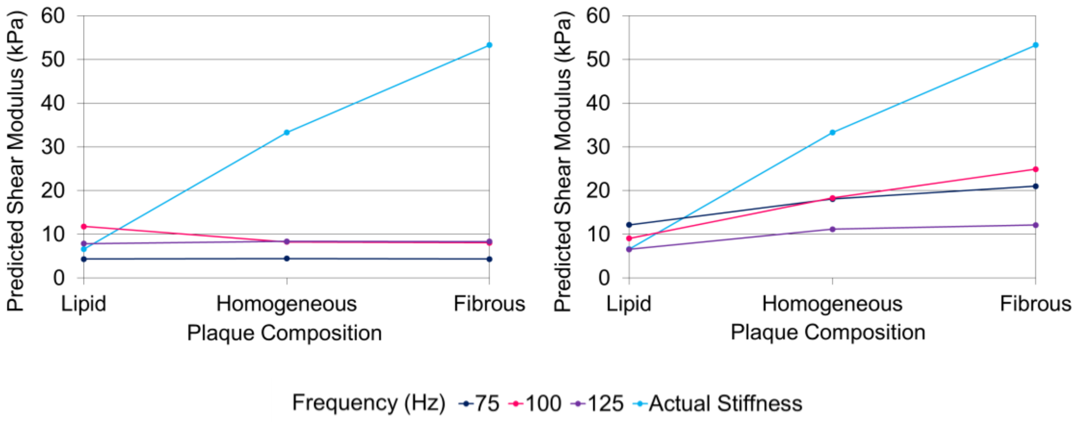

a) Y Direction b) Z Direction

Figure 6.10: *The variation of the local predicted shear modulus with plaque composition through a 70% stenosis, at a selection of excitation frequencies through the Y and Z motion directions.*

6.4) Discussion

The artefacts and reduction in accuracy caused by the sources of error discussed in Chapter 2, 4 and 5, are also relevant to the results of this chapter; imaging, boundary, and pixel artefacts, insufficient resolution and invalidations of inversion algorithm assumptions by non-planar wave propagation, inhomogeneities, boundaries, the non-zero pressure field, compressional excitation without sufficient filtering, discrete analysis of the data and noise.

6.4.1) Signal to Noise Ratio Comparison

Figure 6.2 quite clearly shows that the application of the SNR extraction outlined in (McGee *et al.* 2011) from the experimental data in Chapter 5, does not a give a good representation of the noise level through the complex wave image. When the values are reapplied as random noise through simulated data the SNR levels are visibly higher. McGee et al. (2011) caution the applicability of this technique in the presence of a spatially invariant noise distribution. The background of the magnitude and phase images are subject to higher levels of noise than is present through the body of the phantom, which leads to SNR ratios that are much lower than the actual noise level through the experimental phantom images.

With respect to the SNR values discussed in Chapter 5, displayed in Table 5.4 and 5.5; presuming that the noise levels are approximately equal in the background of all the magnitude images, although not numerically correct, this extracted SNR value is useful for comparing relative SNR levels. The other notable point in Figure 6.2 is how sensitive the homogeneity of the elastograms are to noise levels. Even when the noise in the wave images is almost imperceptible to the eye, there are under and over-estimated pixels through the elastograms. As the noise levels increases, the ‘black hole’ artefacts discussed in Chapter 2 and 4 become visible. The presence of noise affects the inversion algorithm similarly to inhomogenieties, causing errors in the spatial derivatives that present as pixel artefacts. A SNR of 500 added to the computational wave images was visually estimated to be equivalent to the SNR seen in the experimental image.

6.4.2) Comparisons through the Healthy Vessel Phantom

Figure 6.3 and 6.5 compares the waves images through the experimental and computational healthy vessel phantoms. The waves are more planar and the wavelengths are longer in the computational images. This improved wave behaviour is still in the presence of multiple reflective boundaries, nonhomogeneous media, added noise and generated by a compressional wave; a replica of the experimental system. The main difference is that the experimental images are also subject to rigid body motion of the phantom container, motion within the lumen and possible MR imaging artefacts. These artefacts are hard to pinpoint in the body of the phantom, although they are obvious through the background of the image.

This is a positive observation, since due to financial constraints on the research, the manufacture and imaging of the phantoms in Chapter 5 were subject to no optimisation, improvements or repetition. There is scope to improve the methods proposed in Chapter 5; to increase the constraints on the phantom to prevent rigid body motion, to improve the method of sealing the water within the lumen to reduce fluid motion and investigate if the imaging parameters can alleviate some of the MR ghosting artefacts. These results indicate that if these issues were alleviated then the wave images could tend towards the propagation seen through the computational simulations.

Alternatively, the effects of rigid body motion could be modelled and explored computationally, providing insight into their effects on the experimental results. To incorporate the head coil, padding, actuator and surrounding air to give the container realistic degrees of freedom as per the experimental set-up, would require an extremely large model. To extend the system beyond the edges of the phantom container, in order to model the rigid body effects, would require significantly more computational resources than were available in this research, however this is a potential avenue for future research.

In Figure 6.3 the motion through the X/ slice select direction has reduced wave amplitudes in the experimental wave image and to a greater extent in the computational image. In Chapter 5 it was discussed that this direction is perpendicular to the load and is along a short axis of the phantom; the waves in this direction are secondary generated by reflections of the excitation wave. In the experimental phantoms, the rigid body motion generates a lot more wave interference which is not present in the computational simulation, meaning that the amplitude of the waves in this direction remain low. The computational elastogram based on the X direction motion, in Figure 6.4, is noisy and does not show the width of the lumen correctly, this is unsurprising considering the poor quality of the wave image that it is based upon. These observations follow through to a reduced averaged stiffness through the computational elastogram in the X motion direction, Table 6.3.

The lumen is much more visible in the computational images compared to the experimental ones. In the experimental phantoms the rigid body motion and presence of air pockets in the lumen increases the fluid motion. However it is felt that the lack of motion within the lumen of the computational images is too idealised and unlikely to occur in real life. Generating a FSI model of blood flow through the lumen in tandem with arterial wall motion and MRE excitation could be of benefit to this area of research, although this was far beyond the scope of this thesis.

The Y and Z computational elastograms in Figure 6.4 show a much higher level of homogeneity compared to the experimental elastograms. This is due to planar wave propagation that is more applicable to the inversion algorithm. The interfaces with the lumen are subject to boundary artefacts, similar to those seen in Chapter 4, where the lack of motion in the lumen creates an incorrect Laplacian. The edges of the computational elastograms, corresponding to either end of the lumen, show a reduction in homogeneity and contain some artefacts. This is due to both wave interference with the plastic of the phantom container protruding into the TMM and a reduced mesh density, larger than the pixel size, which as discussed in Chapter 2 is detrimental to elastogram accuracy. Computational memory and run time requirements restricted the maximum number of elements within the model, meaning that away from the main ROI that element size had to be increased.

The wave images of Figure 6.5 show that both the experimental and computational waves decrease in wavelength and amplitude with frequency; however in all images the computational wavelength is longer that the experimental one. The theoretically ideal wavelengths through the 16.8kPa TMM at 75Hz, 100Hz and 125Hz are 53mm, 40mm, 32mm respectively. It is difficult to measure the experimental wavelengths through vessel phantoms with any accuracy, due to the highly disrupted waves and large pixel size. However a selection of the computational wavelengths were measured in Abaqus/ CAE, and were found to be equal to or longer than the theoretical ideals. Since the experimental wavelengths are so much shorter, it brings into questions whether the experimental TMM had an accurate stiffness of 16.8kPa, an observation which was also noted in Chapter 5, any future work into MRE phantoms should include tensile testing of the tissue mimic.

In these simulations the viscous modulus was given an arbitrary value, one which when combined with the Voigt model, results in materials that tend towards the elastic end of the viscoelastic spectrum. As was noted in Chapter 2, this results in low attenuation of the wave and good estimates of stiffness. Looking specifically at the 125Hz wave images in Figure 6.5, the attenuation of the wave actually appears to be higher in the simulations as opposed to the experimental phantoms, suggesting that the viscous modulus through the tissue mimic should be lower to reflect the attenuation correctly. Although the mechanical testing in this research was unsuccessful, as discussed in section 5.2.3, ideally the tissue and vessel mimic would need to undergo mechanical testing to accurately measure both the shear and viscous modulus.

The elastograms in Figure 6.6 display the patches of increased and decreased stiffness that are generated where the wave deviates from planar propagation and slight changes occur in the wavelengths due to interference. The computational elastograms suffer from this less than the experimental ones and also display less of the ‘black hole’ artefacts discussed in section 2.2.6; a product of the more applicable wave propagation. However the computational elastograms show stiffnesses through the main body of the phantom that are higher that the true value of the tissue mimic; corresponding to wavelengths equal or longer than the theoretical. The observations of the wavelengths and quality of the elastogram and their effect on the mean stiffness values through the global region of interest can also be seen in Tables 6.3 and 6.4.

Before this chapter, analysis has taken place upon simulations of tissues blocks with or without embedded vessels, surrounded by symmetric boundary conditions. The edges of the tissue mimic in this simulation are tied to a plastic phantom container, which is subjected to encastre boundary conditions. A tissue mimicking material subject to encastre boundary conditions will be able to resist deformation, more than one which is subjected to symmetric, non-reflecting boundary conditions. Hence the wavelengths through the tissue mimic give a higher apparent stiffness than the true stiffness.

The reality of the situation is that the TMM is highly water based, and has a low friction coefficient and although it is constrained within the phantom by the geometry, there will be a degree of motion relative to the TMM and phantom container. To develop this research further, the boundary conditions of the simulation would need to be more sophisticated to reflect this.

Another limitation that was highlighted by this study was the difference in experimental and computational results extraction methodology. Although the pixel resolution of the experimental results and computational results were equal, the depth of the resolution was very different. The slice thickness of the experimental images was 10mm, whereas the computational results were extracted across a 2D plane. MRE resolution was identified in Chapter 4 as an area that would benefit from development; this is applicable to the slice thickness as well as the matrix size. In tandem the realism of the computational MRE technique could be improved by incorporating depth into the results extraction procedure.

Additional things to note in Table 6.3 and 6.4 are that the standard errors over 20 cycles of noise added to the computational data are low, indicating minimal variation of the results with noise. The standard deviations discussed in Chapter 5, predominately had a similar magnitude to the means, with smaller or larger values corresponding to the more or less planar nature of the wave propagation. A similar trend exists in the computational results, with the X results displaying a high standard deviation due to the noisy low amplitude wave propagation through this direction. The other standard deviations display values in line with or slightly higher than the means. The increased standard deviations are thought to be due to the increased amount of low values through the lumen, and high values at each end of the phantoms.

6.4.3) Computational Simulations through Global Arterial Phantoms

The wave images and elastograms in Figure 6.7 and 6.8 show that changes in stenosis size and shape do not have a huge effect on the global wave and elastogram images. Nevertheless the plaques are well resolved in all images, showing an increase in wave amplitude through the lipid plaque.

The average global stiffnesses of Tables 6.5 and 6.6 through the phantoms do not show an increase in stiffness with increase in stenosis size or stiffness, mirroring the results of section 5.3.3. The stiffnesses do however show a strong continuity through each simulation for a certain frequency and motion direction; reflecting how little the wave images alter with changes in plaque size and stiffness.

6.4.4) Computational Simulations through Local Atherosclerotic Plaques

Where computational simulations have a huge advantage over their experimental equivalent is the fact that the plaque may be very easily identified and analysed in isolation. The plaques were almost impossible to identify in the experimental wave images of Chapter 5 due to highly disrupted waves and motion through the lumen.

Figure 6.9 shows the wave propagation and elastograms through the stenosis, displayed as images including the region surrounding the plaques. The increased wave displacement through the lower stiffness lipid plaque can be visualised. The elastograms are less clear, although through Z direction the homogenous and fibrous show a notable increase in stiffness.

Quantitatively, Figure 6.10 displays the variation of elastogram stiffness through the plaques with composition. It can be seen that the ability of the technique to identify the increased stiffness of the homogeneous and fibrous plaques, is dependent on the direction of the wave propagation. Figure 6.9 shows that the wave patterns through the Y and Z directions are quite similar; the wave propagates through the plaque at roughly a 45^o angle with wavelengths and amplitude of a comparable size. Since the presence of the trend is also not dependent on the frequency, the only difference is the direction in which the waves oscillate; the Y direction is through the depth of the plaque whilst the Z is along the length. Upon close inspection of the wave images, the only identifiable difference in wave between each direction, is that the fibrous and homogeneous plaques display equal to or more displacement relative to the adjacent tissue in the Y direction and equal to or less motion in the Z direction; thus the Z direction can detect the increase in stiffness whilst the Y cannot.

This leads onto a previously undiscussed subject; the fact that structure can affect the stiffness as much as the material properties can. A tube with no internal pressure is less able to withstand a radial force than it is a compressional force along the length, hence the increased motion of the plaque in the Y direction. In reality there is a pressure force within the lumen, generated by the cardiac cycle, that however is another in-depth area that has the potential to be researched.

The magnitudes of the averaged moduli are much lower than their true magnitude; since the depth of the 70% stenosis is approximately 3 pixels and a 2 pixel artefact is generated along the boundary with the lumen.

6.5) Conclusions

Comparison of the experimental and computational MRE images through phantoms, has allowed reflection upon some of the techniques and methods used throughout the thesis.

The noise extraction methodology taken from (McGee *et al.* 2011) has been shown to be inappropriate to the experimental MRE results through phantoms. The SNR through these phantoms is surprisingly high, considering the amount of random noise present in the background of these images.

The realism of boundary conditions used in the computational simulations throughout the thesis have been questioned; encastre has been shown to lead to inflated stiffnesses through the tissue mimic and the previously applied symmetric has limited applicability in real life. The lack of motion throughout the lumen is a gross over simplification, and the lack of pressure within the lumen has shown to be detrimental to the wave analysis under compressional loading. The 2D extraction of the computational results compared to the 10mm slice thickness of the experimental results is a limitation of the computational technique. There is scope here to improve the realism of the simulations by incorporating realistic boundary conditions, slice thickness, blood flow and the wall motion of the cardiac cycle.

The wave disturbances and impact on the elastograms, generated by the additional complications present in an experimental procedure compared to the computational replica have been shown. The improved wave images, elastograms and ability to identify a local change in stiffness through the plaque, through the computational simulations, has shown that there is a lot of room to improve upon the procedures conducted in Chapter 5. The removal of rigid body motion, ghosting artefacts and improvement of realism of the motion within the lumen has the potential to lead to more successful results.

Chapter 7

Magnetic Resonance Elastography through Healthy and Diseased Peripheral Arteries

7.1) Introduction

The majority of this thesis has been focussed on tackling the concept of applying MRE to atherosclerosis, subject to a large number of simplifying assumptions. To assess the feasibility of applying this technique clinically, a series of *in vivo* scans were conducted. Moving into an *in vivo* study introduces further complications in terms of wall motion and blood flow artefacts that may corrupt the quality of the MRE data. However in doing so, all the limitations that are present in the technique at this stage can be assessed. This will provide a clear platform for future development of the imaging and inversion methodology.

The application of MRE to arteries has been approached in a few recent studies; the healthy (Xu *et al.* 2013) and hypertensive aorta (Kolipaka *et al.* 2012) and the femoral artery (Woodrum *et al.* 2006, Zheng *et al.* 2007). In order to develop the *in vivo* imaging protocol, the technique was first evaluated on the peripheral arteries of two healthy volunteers. The results from healthy volunteer 1 can be seen in (Thomas-Seale *et al.* 2013); through the read out motion direction at an excitation frequency of 100Hz, Figure 7.7. This protocol was then used to scan the peripheral arteries of three peripheral artery disease patients. This will be the first study to apply MRE to the peripheral arteries of PAD patients.

The aim of this chapter is to develop an imaging protocol to apply MRE to atherosclerosis in the peripheral arteries and to test the feasibility and assess the limitations of the technique on PAD patients.

7.2) Method

7.2.1) Overview

The imaging protocol was developed and tested on two healthy volunteers, followed by three feasibility scans on PAD patients. The imaging methodology in Figure 7.1 is very similar to that discussed in Chapter 5, with an additional MRA scan used to locate the appropriate section of the peripheral artery and adjust the imaging plane.

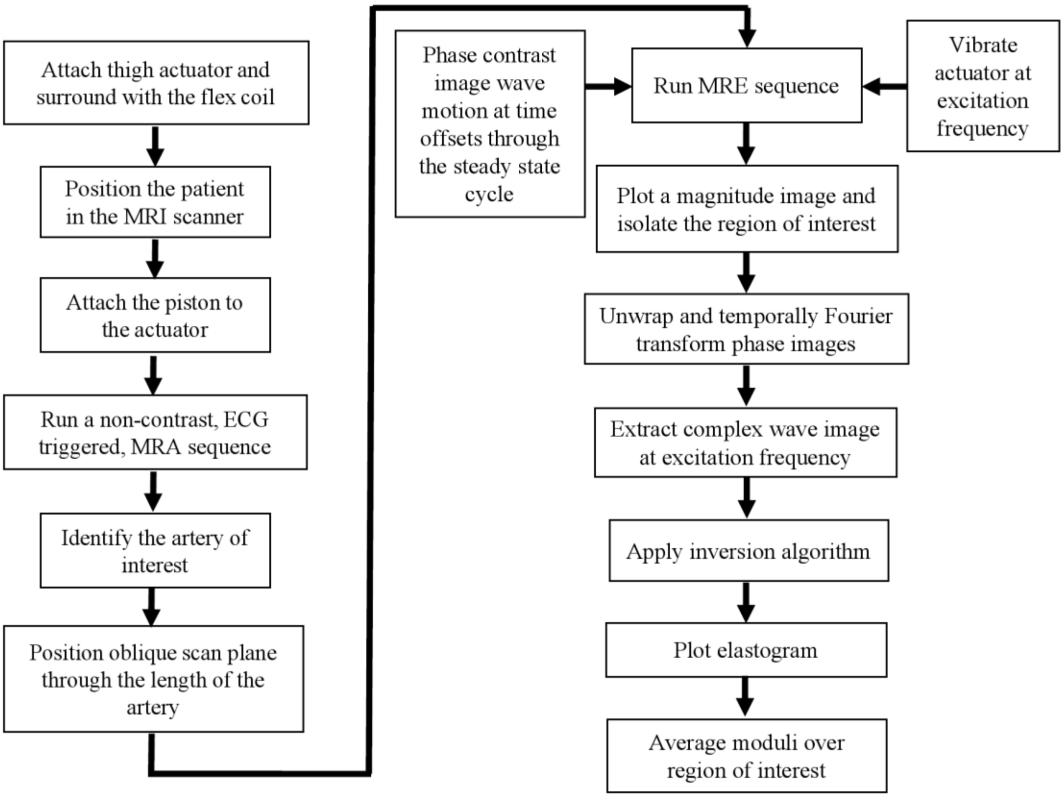

Figure 7.1: *MRE methodology: peripheral arteries.*

The *in vivo* results are subject to a whole host of additional issues that can degrade the quality of the images; from the physiological motion of the artery and flow artefacts generated by the blood, to motion of the limb whilst in the scanner. Combining these limitations with those identified in previous chapters, it was not possible to identify an overall frequency or motion encoding direction that gave the best quality results. Through the extensive analysis of simulated and experimental wave images in this thesis, it has become apparent what type of wave behaviour will invert into a good quality elastograms; propagating, planar waves. Therefore the real complex wave images of the healthy volunteers and patients, at each frequency and motion encoding direction, were first observed to identify which appears to be the most promising wave image. These data sets were then inverted to analyse the elastograms.

The imaging protocol for MRE through the peripheral artery was developed and conducted by Scott Semple, Annette Cooper, Saeed Mirsadraee and Paul Kennedy (Clinical Research Imaging Centre, Queen’s Medical Research Institute, University of Edinburgh, Edinburgh, UK) on a 3 Tesla Magnetom Verio MRI research scanner. The MRE equipment, imaging protocol and inversion methodology was based upon the research and set up in collaboration with the MR Elastography Group, Charité Univesitätsmedizin Berlin. The mechanical MRE equipment was designed and manufactured by Steven Hammer. The inversion algorithm was run on the programming software MATLAB R2011a. Patient recruitment was conducted by Christopher Hay (NHS Lothian, Royal Infirmary of Edinburgh, Edinburgh, UK). All volunteers and patients gave written informed consent and the study was conducted with the approval of the South East Scotland Research Ethics Committee. The favourable ethics approval can been found in Appendix C.

7.2.2) Magnetic Resonance Imaging

MRA Protocol

Before the MRE acquisition, the correct imaging plane needed to be identified; an oblique plane along the length of the artery. In the healthy volunteers this was through the femoral artery of the left leg. In the PAD patients an appropriate section of diseased artery was identified in advance by a clinical radiologist. A Siemens 3D NATIVE SPACE, non-contrast enhanced, MRA acquisition was used to highlight the lumens of the peripheral arteries. This acquisition was echocardiogram triggered and conducted using both an 8 channel spine coil and 4 channel flex coil. The imaging parameters are summarised in Table 7.1.

TR	930ms
TE	81ms
FoV	440mm x 440mm
Matrix Size	384 x 384
Slice Thickness	1.3mm

Table 7.1: *MRA acquisition parameters.*

(a) Healthy volunteer 1

(b) Healthy volunteer 2

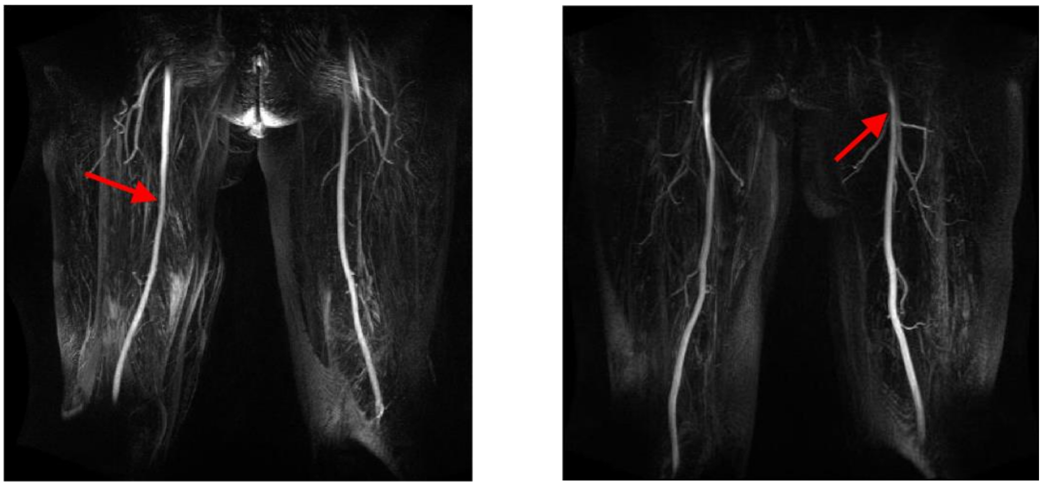

(c) Patient 1

(d) Patient 2

(e) Patient 3

Figure 7.2: *MRA MIPs through the healthy volunteers and patients.*

The maximum intensity projections (MIP) of the NATIVE MRAs through the thighs of each healthy volunteer and patient are shown in Figure 7.2; the section of the vessel under analysis in each subject is indicated. In the patients, this section also corresponds to the atherosclerosis.

a) MRE set-up; Subwoofer, piston and MRI scanner

b) Thigh actuator

c) Thigh actuator, piston and flex coil

Figure 7.3: *MRE equipment: peripheral arteries.*

MRE Set Up

The MRE set up, protocol and inversion algorithm were explained in detail in Chapter 5 section 5.2.7. They shall be reiterated here, for clarity, in reference to this *in vivo* study. The

MRE equipment used for an *in vivo* peripheral artery scan is shown in Figure 7.3. The actuator was placed around the upper thigh and surrounded by a 4 channel flex coil. In addition an 8 channel spine coil was activated underneath the thigh.

The actuator was attached to the subwoofer, situated at the edge of the MRI scanner room, by a carbon-fibre piston. Harmonic, sinusoidal waves were generated in the subwoofer by a waveform generator and amplifier. These vibrations were synchronised with the imaging sequence via a trigger signal from the MRI operating station. Waves were generated in the shearing direction, along an axis in line with the bore of the scanner.

MRE Protocol

Once the MRA images had been used to orientate the imaging plane at an oblique angle along the length of the artery of interest, the MRE scan was able to commence. The protocol utilised a 3 tesla, echo planar imaging sequence with a motion encoding gradient. The parameters of the MRE protocol are summarised in Table 7.2.

TR	1600ms
TE	56ms
MEG Cycles (75/100/125Hz)	1/1/2
MEG Amplitude	35mT/m
FoV	235mm x 235mm
Matrix Size	128 x 128
Slice Thickness	10mm

Table 7.2: *MRE acquisition parameters: peripheral arteries.*

16 sampling points were acquired for the movement of the sinusoidal wave through the artery, by repeating the acquisition 16 times with an increasing time offset between the start of the harmonic wave and the MEG. The amplitude of the harmonic wave was controlled by the wave generator and set at 4V peak to peak voltage. The protocol was repeated nine times; for each motion encoding direction and the frequencies 75Hz, 100Hz, and 125Hz. This protocol yielded 16 magnitude and phase images for each healthy volunteer and patient,

frequency and motion encoding direction; corresponding to different time offsets through the wave cycle. The motion encoding directions are defined as follows; slice select, perpendicular to the image, phase encoding, approximately parallel to the artery, and the read out direction perpendicular to this in the plane of the image.

The resolution was based on a field of view of 235mm^2, with a matrix size of 128 x 128 yielding a pixel size of 1.84mm^2. The slice thickness was 10mm.

7.2.3) Signal to Noise Ratio

The signal to noise ratio in each wave image was assessed using the noise analysis method outlined in section 4.2.8, 5.2.8 and Appendix B taken from (McGee *et al.* 2011). Chapter 6 highlighted that this extraction methodology was not applicable to the experimental wave images in Chapter 5, and led to underestimated SNRs. It's usefulness for comparing relative SNRs between data sets was noted and was therefore similarly used to analyse the *in vivo* wave images of this chapter.

7.2.4) Image Processing

The image processing methodology is exactly the same as that outlined in Chapter 5, section 5.2.9. The inversion algorithm code, programmed in MATLAB, can be found in Appendix A. The theory and mathematics behind the algorithm is explained in section 2.2.6.

Due to time constraints the MRE image sequence used for the healthy volunteers and patients, yielded a set of 16 magnitude and positive phase images, as opposed to the 40 taken in Chapter 5. The application of filter thresholds was discussed in detail in Chapters 4 and 5. The high pass and low pass 2D Butterworth filters, were similarly set with the wide thresholds of 5m^{-1} and 100000m^{-1} respectively.

The results of this chapter were purely qualitative, based on the results of Chapter 5 a quantitative analysis was not expected to add any value. Where possible the ROI was focused upon a section of the healthy or diseased vessel that displayed the clearest waves and least artefacts.

7.3) Results

For each participant the angiography image of the vessel with relation to the leg anatomy was displayed in Figure 7.2. The wave images and elastograms shall be viewed next to a magnitude image of the vessel through the same oblique imaging plane. The resolution of the magnitude image is too low to identify the components of the artery wall, but the location of the lumen is highlighted by the blood flow. The legends have been truncated below their maximum values to improve the clarity of the wave images and elastograms.

The magnitude and real complex wave images through each motion encoding direction through the healthy volunteers 1 and 2 (HV 1 and HV2) and patients 1, 2 and 3 (P1, P2 and P3) are shown in Figure 7.4, 7.5 and 7.6 for excitation frequencies 75Hz, 100Hz and 125Hz respectively. The corresponding SNR values, averaged over the healthy volunteers and patients, are displayed in Table 7.3.

On the whole, the healthy volunteer wave images have a higher SNR than patient wave images. The lumen is visible on most of the healthy volunteer images as line of disruption through the waves. Regions of planar wave propagation and disruptions through the lumen are visible in some of the patient images, but most are dominated by noise.

	Signal to Noise Ratio								
	75Hz			**100Hz**			**125Hz**		
	SS	**RO**	**PE**	**SS**	**RO**	**PE**	**SS**	**RO**	**PE**
Healthy Volunteers	3.8	2.5	3.7	3.2	2.7	4.1	1.6	1.9	2.2
Patients	1.0	1.2	1.2	0.9	0.8	0.8	0.5	0.7	0.4

Table 7.3: *The mean SNR through the wave images of the healthy volunteers and patients for each frequency and motion encoding direction.*

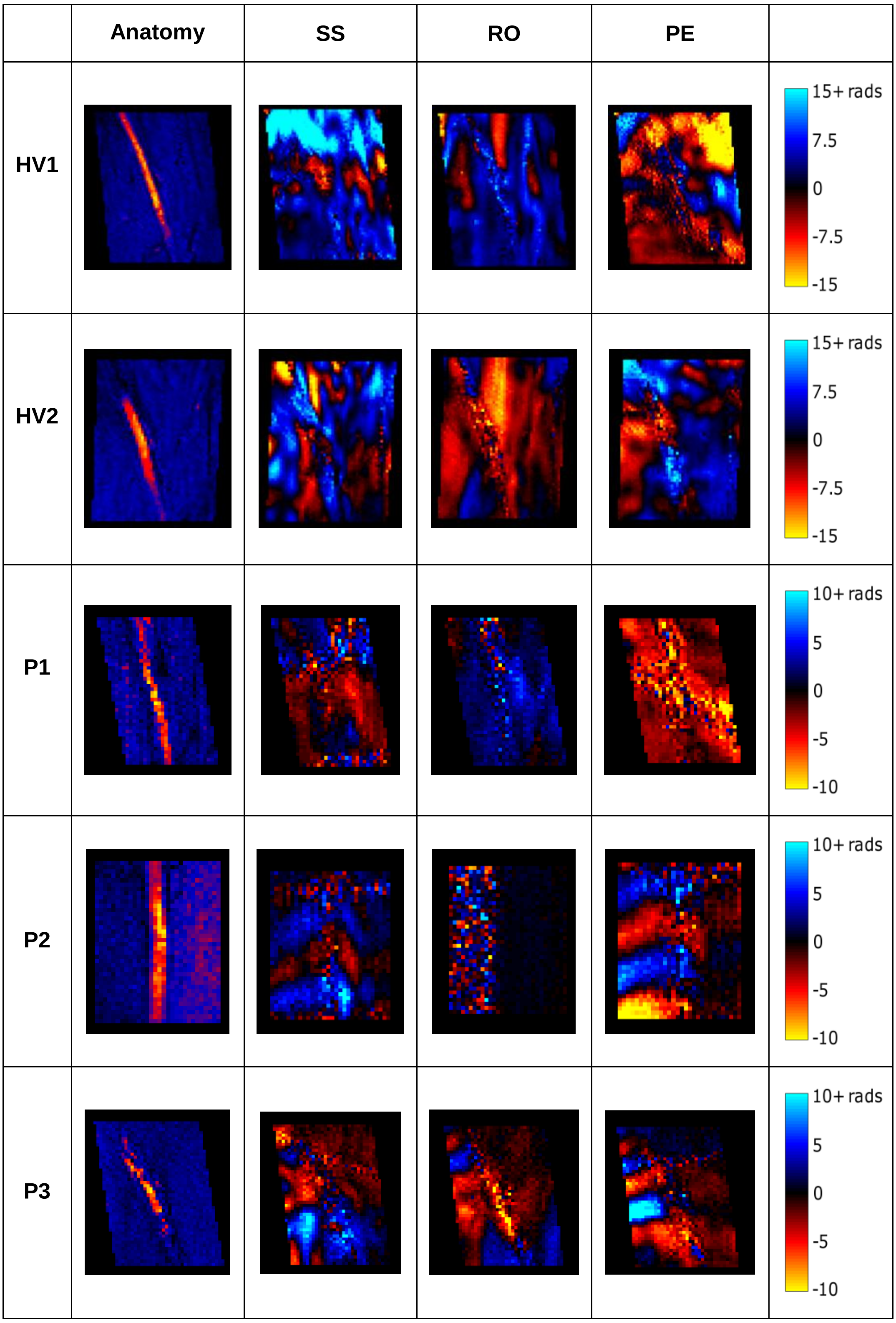

Figure 7.4: *The real component of the complex wave images through the artery and surrounding muscle of each subject, through each motion encoding direction at 75Hz.*

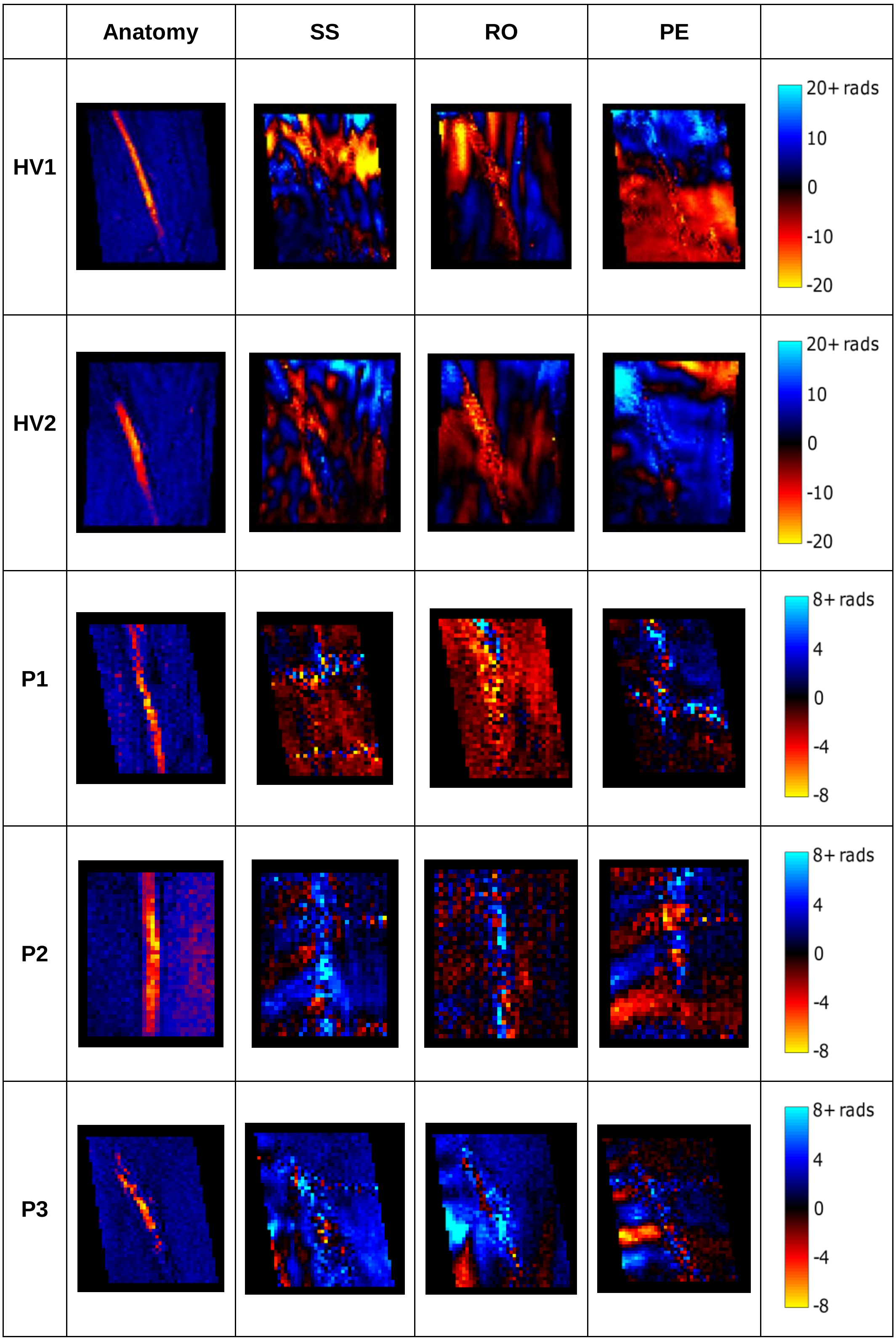

Figure 7.5: *The real component of the complex wave images through the artery and surrounding muscle of each subject, through each motion encoding direction at 100Hz.*

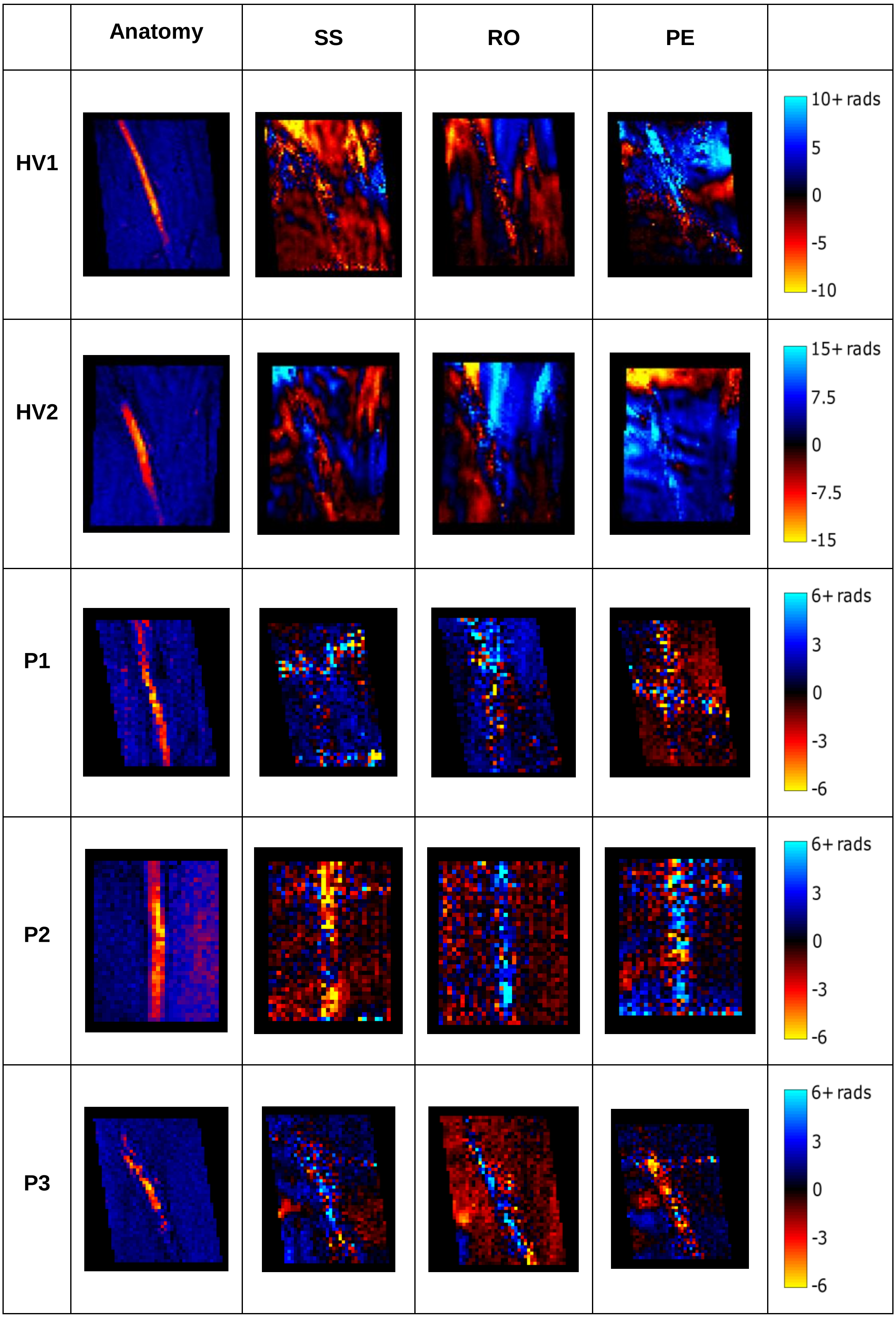

Figure 7.6: *The real component of the complex wave images through the artery and surrounding muscle of each subject, through each motion encoding direction at 125Hz.*

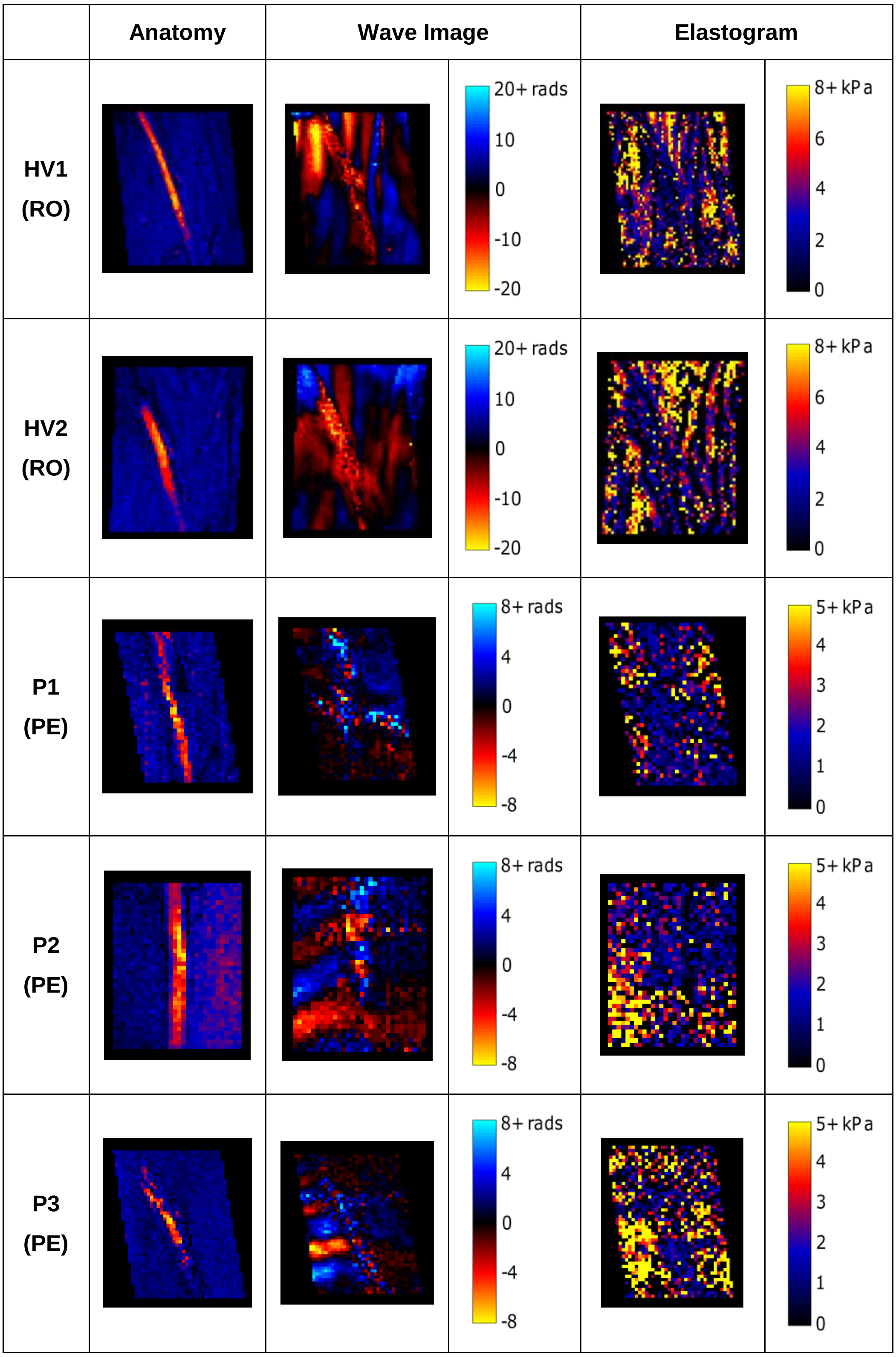

Figure 7.7: *The real component of the complex wave images and shear modulus elastograms for each subject through the specified motion encoding direction at 100Hz.*

The magnitude, wave image of interest and elastogram images through the healthy volunteers 1 and 2 and patients 1, 2 and 3 are shown in Figure 7.7 at an excitation frequency of 100Hz through the specified motion encoding directions. The elastograms are of poor quality; they show no homogeneity through the surrounding muscle and contain large amounts of speckle. The lumens of the healthy volunteers are only identifiable with reference to the anatomy image. The patient elastograms do not show anything significant.

7.4) Discussion

Though the wave images of Chapter 5 could not be described as ideal, when compared to the level of noise and in some cases complete lack of visible wave propagation in the *in vivo* images, it becomes apparent why phantoms are a good progressive step between computational and *in vivo* MRE. Comparing the values in Table 5.5 with 7.3 shows a distinct reduction in SNR. Similar to the values seen in the arterial phantoms, the SNR appears to decrease with increasing frequency.

Due to the low image clarity, analysis had to be conducted through the clearest section of the vessel in the magnitude and phase images. It is difficult to identify the exact position of the atherosclerosis in the MRE magnitude and phase images through the oblique plane. In patients 1 and 3, any deviation of the selected ROI from the diseased section of the artery will be minor as the image is centered on the stenosed region. In patient 2 however, the stenosed length of the vessel is much higher up the peripheral artery, shown in Figure 7.3. Although the actuator was placed around the upper thigh, the waves did not propagate up that far. The region of interest analysed in this patient had to therefore be taken distal to the location of the atherosclerosis.

In the *in vivo* results the wave amplitudes are low, the images are noisy, the lumen is not well defined, in some images there is wave propagation but in some there appears to be almost none. The MRE sequence was not gated so the quality of the wave images depend upon where in the cardiac cycle the imaging series falls. The series of magnitude images corresponding with the phase images, display various degrees of flow artefacts through the lumen, and it can be assumed that these are also present in the phase images. In addition to errors created by arterial wall motion and flow artefacts, there are other sources of physiological motion during *in vivo* scans such as unconsciously tensing muscles or moving limbs. Under such a host of potential errors, it was impossible to pinpoint exactly what was the optimum excitation frequency and motion encoding direction.

Looking at the results of the healthy volunteers first; the wave propagation through the phase encoding direction is the poorest of the three motion encoding directions. The read out direction gives fractionally more planar wave propagation than slice select, with a more obvious wave disruption through the lumen. When looking at waves images that are so far from ideal, identifying the best quality of wave image becomes almost subjective. From the author’s perspective, the read out 100Hz and 125Hz images look the clearest. The read out 100Hz wave images were taken forward to analyse the elastograms, a decision also based upon the results of Chapter 4 and 5 which yielded the best results at this frequency.

These observations do not hold for the patient wave images. They are subject to even lower SNR, less clear wave propagation and in some cases large motion artefacts, meaning that the regions of interest had to be considerably smaller than in the healthy volunteers. The majority of wave images have barely perceptible waves. It is unclear why this has occurred, possible reasons stem from the fact that the two healthy volunteers were young, informed adults. Therefore the image degradation could be due to more patient motion than the healthy volunteers, more complex wave interactions through the diseased as opposed to the healthy artery or increased inhomogeneity of the muscle stiffness with age (Domire *et al.* 2009). The attenuation in the higher frequency scans appears to be more significant in the patient wave images with the 125Hz data sets showing the worst image qualities and lowest wave amplitudes.

In the read out 75Hz scan, patient 2 may have moved and caused a very large artefact across the wave image, effectively invalidating the results. Patients 2 and 3, demonstrate good wave propagation on the left hand side of the lumen, through the phase encoding direction at 75Hz and 100Hz. Patient 1, shows particular poor wave images across the whole set of results, the only image where waves are barely perceptible are 100Hz through the phase encoding direction. The 100Hz and PE images were inverted into elastograms.

It was noted, in the patient scans, that where planar waves exist, regardless of the wavelength or noise level of the image, they appear significantly reduced on one side of the lumen compared to the other. This would indicate that as the waves pass through the section of diseased artery, they are disrupted and/or attenuated far more that passing through the healthy volunteer arteries, which show approximately equal wave clarity both sides of the lumen. Calcification is a symptom of peripheral artery disease and it can be particularly severe in patients with long-standing diabetes and renal failure (Hirsch *et al.* 2006). It is hypothesised, that the fact that waves appear to be more damped as they pass through the patient arteries as opposed to the healthy volunteers, could be due to the presence of calcification in the peripheral arteries. Ideally, a medical diagnosis or additional MRI composition imaging would be available to confirm this. However the ethics approval did not extend to granting this information or conducting additional imaging. Future work could look to confirming this hypothesis by conducting a much larger study, involving additional composition imaging and repeatability studies. Age matched studies between the healthy volunteers and patients could clarify whether this observation is due to disease or age.

The elastograms are very noisy, with poor resolution of the lumen, corresponding to the quality of the wave images. With reference to the anatomy images, the lumens of the healthy volunteers are just about identifiable by a section of reduced stiffness, along the vessel length. As opposed to any correlation with actual stiffness of the vessel or plaques, the patient elastograms show areas of increased stiffness where the wave propagation is clear and planar. Patient 3, whose wave image has both sections of propagating waves and wave disruption through the lumen, is the only patient elastogram where the length of the lumen is just about perceptible.

These results are disappointing when compared to studies that have successfully imaged the stiffness of the arterial wall (Kolipaka *et al.* 2012, Xu *et al.* 2013). These studies focus on the relatively larger aortic artery as opposed to the peripherals, although MRE waves have been imaged through the peripheral arteries in other studies (Woodrum *et al.* 2006, Zheng *et al.* 2007), they did not progress onto inversion. Kolipaka et al. (2012) and Xu et al. (2013) also focus on inverting waves propagating through the lumen and artery wall, as opposed to purely focussing on the artery wall, as the research in this thesis has done. In addition Xu et al. (2013) incorporated cardiac gating into their technique. Although this chapter and this thesis has had a focus on identifying the reasons why the technique has not been successful experimentally, the existence of other studies with more positive outcomes shows that with further development there is the potential for success.

7.5) Conclusions

The healthy volunteer elastograms showed a length of reduced stiffness along the position of the vessel, making the lumen identifiable to the trained eye. This change in stiffness is likely to be due to the presence of motion artefacts as much as the lack of shear stiffness through the blood. A good number of patient wave images showed a distinct reduction of planar wave propagation on one side of the lumen, suggesting that the diseased vessels may disrupt or attenuate the waves much more than the healthy vessels which did not demonstrate this feature.

Numerous sources of errors exist in arterial MRE *in vivo* scans due to physiological motion, not just arterial wall motion and flow artefacts but also subject limb motion as well. The wave images vary greatly between excitation frequencies, motion encoding gradients and each subject. Identifying the optimum parameters or wave image for inversion is not as straight forward when compared to phantoms and computational work.

Imaging protocol to apply MRE to the peripheral arteries was developed and the feasibility of the technique was tested on healthy volunteers and PAD patients. The stiffness of the artery wall and atherosclerosis could not be identified. In addition to the technique developments identified in previous chapters, this chapter has identified that a good step towards improving the MRE arterial sequence would be cardiac gating.

Chapter 8

Conclusions and Future Work

8.1) Discussion

The aim of this thesis was to investigate the application of magnetic resonance elastography to image the mechanical properties of atherosclerotic plaques. This aim was satisfied using the series of objectives below; to guide computational simulations, experimental phantoms and preliminary *in vivo* work.

1) Develop a method of computationally simulating MRE using 3D FEA.
2) Conduct a computational sensitivity study on the geometric, mechanical, imaging and inversion parameters of MRE applied to idealised atherosclerotic plaques.
3) Design a series of arterial phantoms with variable plaque size and stiffness, to aid experimental validation of the technique.
4) Test the experimental feasibility of the technique on arterial phantoms; gain insight on both the experimental and computational work by comparison with replicated simulations.
5) Conduct an *in vivo* feasibility study on healthy volunteers and PAD patients.

A method of computationally simulating MRE was described in Chapter 2; satisfying objective 1. The computational parameters were assessed through a homogeneous block of tissue; providing an informed framework on which to base the computational arterial MRE analysis. Chapter 3 and 4 focussed on objective 2; a sensitivity study was conducted on the mechanical, imaging and inversion parameters of computational MRE with respect to idealised atherosclerotic disease variables. A selection of optimised parameters were identified and where possible, taken forward and used experimentally. The deterioration of the inversion algorithm's ability to detect changes in plaque stiffness with composition, as the SNR and resolution decreased, was highlighted.

Chapter 5 outlined the design and manufacture of a series of arterial phantoms with variable plaque sizes and stiffnesses. Objective 3 was satisfied by proposing a validation technique, although the validation itself was not successful. These arterial phantoms were experimentally imaged and replicated in the simulations of Chapter 6. Although the experimental elastograms of the arterial phantoms struggled to resolve anything but the presence of the lumen, the simulations showed that with some changes to the methodology the proposed technique has the potential to identify changes in plaque stiffness with composition. Chapter 6 also provided insight into the realism of the computational technique and applicability of the SNR extraction methodology to MRE data. Thus objective 4 was satisfied.

Chapter 7 and objective 5 tested the *in vivo* feasibility of MRE; scanning the femoral artery of healthy volunteers and PAD patients. The addition of physiological motion and increased noise levels made even the lumen difficult to identify in the *in vivo* elastograms.

Throughout the course of this thesis the inherent complications of applying MRE to atherosclerosis have been introduced into the investigation methodically. Chapter 3 and 4 dealt with the presence of an inhomogeneous region of interest, the boundary of the lumen and the size of the plaque whilst investigating the effect of varying the imaging resolution and SNR. Chapters 5 and 6 investigated the presence and removal of motion artefacts with experimental and realistic simulated levels of noise, resolution and non-planar wave propagation. Chapter 7 combined all the previously mentioned complications with physiological motion and flow artefacts. Introducing the complications in a graduated manner has allowed the limitations of the technique and inversion algorithm to be assessed systematically.

8.2) Conclusions

Atherosclerosis creates a huge burden on the worldwide economy. It is a global arterial disease, leading to a number of debilitating, if not fatal conditions. Current diagnosis techniques image the stenosis size of atherosclerotic plaques, which has been shown to have a limited correlation with plaque rupture (Ricotta *et al.* 2008).

The rupture risk of atherosclerotic plaques have been associated with the mechanical properties (Falk *et al.* 1995). The application of MRE to image the change in the mechanical properties of atherosclerotic plaques was proposed. The ability to identify a change in the shear modulus with disease development was demonstrated computationally. Preliminary experimental work was conducted, however in the face of numerous complications, the results were not successful. Nevertheless the progression of the thesis through the applications of simulations, phantoms, healthy volunteers and patients has introduced complications gradually, allowing their limiting effects to be assessed and highlighting many areas that can be developed and improved. The continuation of this challenging area of research must be weighed up against the diagnostic benefits of being able to clinically image the mechanical properties of atherosclerotic plaques.

8.3) Future Work

To date, the work conducted during the development of this thesis is the only research into the application of MRE to the mechanical properties of atherosclerosis. It provides a foundation for future work in this area of imaging whilst also identifying a number of key areas to be developed.

Development in the area of arterial computational MRE should focus on improving the realism of the simulations. Patient specific modelling could be integrated to improve the realism of the plaque and vessel geometry. The accuracy of modelling the material properties and boundary conditions could be increased. Incorporating 3D results extraction through a slice of the model would unify the experimental and computational methodology. Ideally *in vivo* arterial MRE would be conducted using a gated sequence, so it is questionable how much value there would be in incorporating FSI models to investigate effects of wall and blood motion.

The experimental work in this thesis was highly constrained by research funding. There was limited development time on the MRI scanner and only enough resources to scan each phantom and human once. The MRE set up and sequence at the Clinical Research Imaging Centre is tailored to applications in the brain, muscle and liver; the parameters for arterial phantoms were guided by the computational analysis and the *in vivo* procedure was developed whilst scanning the healthy volunteers in advanced of the patients. This means that there is a huge scope for improving the experimental work.

In terms of the arterial phantoms, firstly the tissue and vessel mimic need mechanical testing to establish their true shear and viscous modulus. Secondly the method of modelling blood could be vastly improved by incorporating the higher viscosity of blood mimic as opposed to water, to alleviate some of the unrealistic motion in the lumen. In addition a flow pump could be incorporated to simulate the motion of the blood during the cardiac cycle. The constraints upon the arterial phantoms during the MRE scan need to be improved to remove rigid body motion. Alternatively the effects of rigid body motion could be investigated computationally.

It was shown computationally that increasing the resolution of MRE has a huge benefit on the imaging methods ability to detect a change in shear modulus with plaque composition. However halving the field of view for a fixed matrix size results in quartering the SNR (McRobbie 2007). It was shown computationally that a reduction in SNR also has a detrimental effect on the quality of the elastograms. Development in this area would require a higher SNR before the resolution could be increased; otherwise it would be unlikely to yield any improvements in the results. The wave images through the patient scans are both noisier and more damped through the artery than the healthy volunteer images, further investigation could broach whether this is due to calcification or age. *In vivo* imaging would also benefit from the addition of cardiac gating to allow the motion from the MRE waves to be isolated from the cardiac cycle.

Limitations in the inversion algorithm were a reoccurring theme in both the experimental and computational chapters. There are a wide variety of inversion algorithms and they are overviewed in section 1.7.2. Research into a more applicable method of inverting shear waves through atherosclerotic plaques would be key to progressing this area of research. Since computational simulations have formed a large portion of this research, a logical extension of this would be to incorporate the FEA inversion methodologies discussed in section 1.7.4. The structural stiffness of the artery was briefly mentioned in Chapter 6. Since arteries are tubes their stiffness is dependent on structure as well as material properties, they are also highly orthotropic, resisting forces in certain directions much more than others. Kolipaka et al. (2009) have proposed algorithms that are more specific to the shape of the organ; this method of inverting waves could be applicable in arteries.

In this thesis the only artery, commonly subjected to atherosclerosis, that was appropriate to image was the femoral. The depth of the aorta and position of the actuator required to excite the carotid made these arteries difficult to image during this study. However, the aorta has been successfully imaged by other research groups (Kolipaka *et al.* 2012, Xu *et al.* 2013). Arterial disease in the aorta also comes in the form of abdominal aortic aneurysms. Similar to atherosclerotic plaques, current diagnosis of rupture risk is largely based upon a measurement of their size. The advantage that aneurysms offer over atherosclerosis as an MRE application is their size. The amount of research required to successfully apply MRE to aneurysms would be substantially less if the issue of increasing the resolution was removed. In tandem, whilst developing the application of MRE through aneurysms, the research area could move closer to successfully imaging atherosclerotic plaques.

Appendix A
MATLAB Functions: 2D Helmholtz Inversion Algorithm

The MATLAB code for the 2D Helmholtz inversion algorithm was supplied by collaborators at the MR Elastography Group, Charité Univesitätsmedizin Berlin. Sections A.1 to A.4 display and annotate the series of MATLAB functions that are required to invert a set of echo planar imaging MRE phase images into an elastogram. The code in section A.1 and A.2 imports and unwraps the phase images. The Helmholtz inversion algorithm is coded in section A.3, incorporating equation A.1, and the spatial filtering function in A.4. The phase unwrapping code in section A.2 is based on Flynn’s 2D minimum discontinuity algorithm (Ghiglia and Pritt 1998, Hamhaber *et al.* 2007) and calls a black box function ‘Flynn.exe’. The functions utilised in the inversion of computational MRE complex wave images into elastograms are based on the same code, without the application of sections A.1 and A.2.

$$G(\omega) = \frac{-\rho\omega^2 U}{\nabla^2 U} \tag{A.1}$$

A.1) Importing EPI Phase Images

```
function [cw] = import_EPI(pth,sr1,BW)

% cw: complex wave images
% w: unwrapped phase images
% w_nw: raw phase images
% pth: path subdirectory
% sr1: folder name
% BW: region of interest in logical format

% Importing the phase images
w = [];
        cd([pth '\' sr1])
        lst = list;
        lst_length = length(lst);
for k = 1:length(lst(:,1))
```

```
    w(:,:,k) = double(dicomread(lst(k,:)));
end
w_nw = w;

% Unwrapping the phase images
w = w/4096*2*pi;
w = unwrap_images(w,BW);

% Calculating the complex wave images via Fourier transform
cw = fft(w,[],3);

% Deleting the temporary files
delete('tmp_out', 'tmp_in')
```

A.2) Unwrapping the Phase Images

```
function [w]=unwrap_images(W,BW)

% w: unwrapped phase images
% W: raw phase images
% BW: region of interest in logical format

% Formatting the data
% Calling Flynn's minimum discontinuity algorithm
w=zeros(size(W));
for k=1:size(W,3)
    f = fopen ('tmp_in','w' );
    fwrite (f, W(:,:,k), 'float32' );
    fclose (f);
    command = ['C:\MATLAB\Flynn.exe -input ','tmp_in',' -format ','float',' -output
    ','tmp_out',' -xsize ',num2str(size(W,1)),' -ysize ',num2str(size(W,2))];
    dos (command);
    f = fopen ('tmp_out', 'r');
    [t,blubb] = fread (f,size(W,1)*size(W,2), 'float32' );
    tmp = reshape (t,size(W,1),size(W,2));
    fclose (f);
    if nargin > 1
        w(:,:,k)=tmp-mean(tmp(find(BW)));
    else
         w(:,:,k)=tmp;
    end
end
```

A.3) 2D Helmholtz Inversion Algorithm

```
function [G] = helmholtzG(cw,rho,freq,BW,pix,lambda1,lambda2)

% cw: complex wave image, 2D array at respective frequency
% rho: Density (kg/m^3)
% freq: frequency (Hz)
% BW: region of interest in logical format
% pix: Pixel spacing (mm)
% lambda1: low pass filter threshold (m)
% lambda2: high pass filter threshold (m)

omega = 2*pi*freq;
dx = pix/1000;

% Spatial filtering the complex wave image
[W] = spatialfilter(cw.*BW,[dx; dx],1/lambda1,5,1/lambda2,5,'bwbwband');

% Inversion
[wx, wy] = gradient(W,dx,dx);
[wxx, wxy] = gradient(wx,dx,dx);
[wyx, wyy] = gradient(wy,dx,dx);
DW = wxx + wyy;
G = -rho*omega^2*W./DW;

% Equating negative stiffnesses to negligible
G(find(real(G)<0))=0;
G(find(real(G)==0))=0.000001;
G(find(imag(G)<0))=conj(G(find(imag(G)<0)));
G(find(imag(G)==0))=0.000001;
```

A.4) Spatial Filtering

```
function [imaf]=spatialfilter(ima, samplingintervals, SFlowcut, SFloworder, SFhighcut, SFhighorder, SFmode);

% imaf: Filtered image data
% ima: Image data
% samplingintervals: Column vector of sampling intervals over the image grid (m)
% SFlowcut: Low pass filter threshold (1/m)
% SFloworder: Order of the low pass filter
% SFhighcut: High pass filter threshold (1/m)
% SFhighorder: Order of the high pass filter
```

```
% SFmode: Name of spatial filter ’bwlow’ ‘bwhigh’ ‘bwbwband’
        % ‘bwlow’: Butterworth low pass filter
        % ’bwhigh’: Butterworth high pass filter
        % ‘bwbwband’: Butterworth bandpass filter

matsize = size(ima)';
samplinglengths = matsize .* samplingintervals;

% Fast Fourier transform
% Shift zero frequency component to centre of spectrum
Ima = fftshift(fftn(ima));

% Data formatting prior to filtering
origin=floor(matsize./2)+1;
[x1,x2] = ndgrid(1-origin(1):matsize(1)-origin(1), 1-origin(2):matsize(2)-origin(2));
x1 = samplingintervals(1).*x1;
x2 = samplingintervals(2).*x2;
u1 = zeros(matsize');
u2 = zeros(matsize');
u1 = (1/(samplinglengths(1)*samplingintervals(1)))*x1;
u2 = (1/(samplinglengths(2)*samplingintervals(2)))*x2;
clear('x*');
uabs = zeros(matsize');
uabs = sqrt(u1.*u1+u2.*u2);
clear('u1','u2');

% Spatial filter
SF = ones(matsize');
SFlow = ones(matsize');
SFhigh = ones(matsize');
switch SFmode
        case 'bwlow'
        SF = SF./(1+(uabs/SFlowcut).^(2*SFloworder));
        case 'bwhigh'
        SF = SF./(1+(SFhighcut*SF./(uabs+eps)).^(2*SFhighorder));
        case 'bwbwband'
        SFlow = SFlow./(1+(uabs/SFlowcut).^(2*SFloworder));
        SFhigh = SFhigh./(1+(SFhighcut*SFhigh./(uabs+eps)).^(2*SFhighorder));
        SF = SFlow .* SFhigh;
        SF = SF/max(max(SF));
        otherwise
end
```

```
% Inverse fast Fourier transform
Imaf = Ima .* SF;
imaf = ifftn(ifftshift(Imaf));
```

Appendix B

Extraction of Signal to Noise Ratio from Magnetic Resonance Elastography Images

The methodology for extracting the signal to noise ratio is taken from the work of McGee et al. (2011). Figure B.1 shows, for one pixel, the relationship between the magnitude, phase, real and imaginary values in the presence of Gaussian noise. The possible values of each component may vary within the circular 'Gaussian cloud' around the noise free complex vector, assuming that the noise is uncorrelated between the real and imaginary channels and spatially invariant (McGee *et al.* 2011).

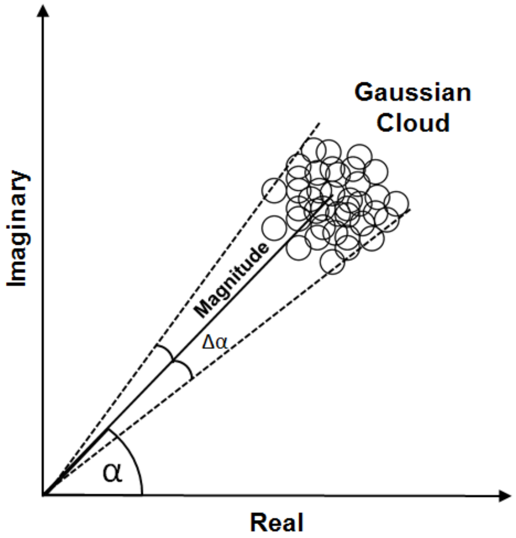

Figure B.1: *Spatially invariant Gaussian cloud based upon the magnitude of the real and imaginary components of the complex signal, where* $\Delta\alpha$*, the standard deviation of the cloud is equal to the noise in the phase. Replicated and adapted from* (McGee *et al.* 2011)

These observations led to the conclusion that the standard deviation of the noise in the direction of the real, imaginary and magnitude components are equal and may be estimated either from background pixels averaged through the real and imaginary images or in the magnitude image divided by the Rician correction factor 1.66 (McGee *et al.* 2011). The Rician correction factor takes into account the difference in the Gaussian distributions displayed by noisy data in the the real and imaginary channels and the Rician distribution seen in magnitude image (Gudbjartsson and Patz 1995). The magnitude of the signal is taken from the first harmonic fit across the phase offsets (McGee *et al.* 2011).

The assumptions of this technique include the magnitude vector being greater than 3 and spatially invariant noise that is uncorrelated in the real and imaginary planes (McGee *et al.* 2011). In noisy MRE data, the magnitude is not always above 3, however McGee et al. (2011) state that even when the magnitude falls below this threshold, the SNR extraction methodology is still useful for comparing relative noise levels. Spatially invariant, uncorrelated noise depends on the uniformity of the signal reception throughout the region of interest. This assumption can begin to breakdown in large field of view imaging.

Appendix C
Favourable Ethical Opinion

The favourable ethical opinion of the South East Scotland Research Ethics Committee 02 is detailed in Figure C.1.

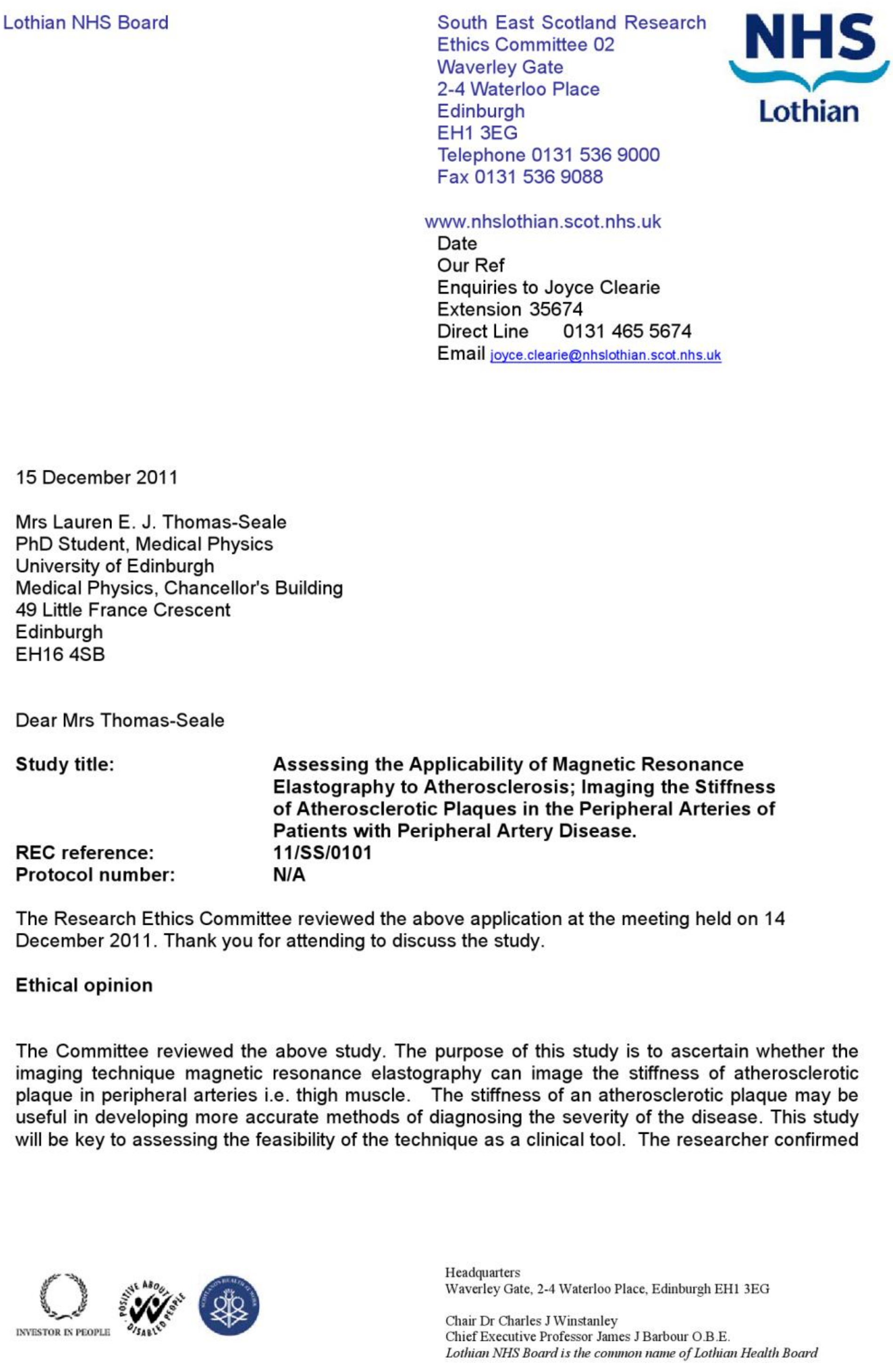

Lothian NHS Board

South East Scotland Research
Ethics Committee 02
Waverley Gate
2-4 Waterloo Place
Edinburgh
EH1 3EG
Telephone 0131 536 9000
Fax 0131 536 9088

NHS
Lothian

www.nhslothian.scot.nhs.uk
Date
Our Ref
Enquiries to Joyce Clearie
Extension 35674
Direct Line 0131 465 5674
Email joyce.clearie@nhslothian.scot.nhs.uk

15 December 2011

Mrs Lauren E. J. Thomas-Seale
PhD Student, Medical Physics
University of Edinburgh
Medical Physics, Chancellor's Building
49 Little France Crescent
Edinburgh
EH16 4SB

Dear Mrs Thomas-Seale

Study title:	**Assessing the Applicability of Magnetic Resonance Elastography to Atherosclerosis; Imaging the Stiffness of Atherosclerotic Plaques in the Peripheral Arteries of Patients with Peripheral Artery Disease.**
REC reference:	**11/SS/0101**
Protocol number:	**N/A**

The Research Ethics Committee reviewed the above application at the meeting held on 14 December 2011. Thank you for attending to discuss the study.

Ethical opinion

The Committee reviewed the above study. The purpose of this study is to ascertain whether the imaging technique magnetic resonance elastography can image the stiffness of atherosclerotic plaque in peripheral arteries i.e. thigh muscle. The stiffness of an atherosclerotic plaque may be useful in developing more accurate methods of diagnosing the severity of the disease. This study will be key to assessing the feasibility of the technique as a clinical tool. The researcher confirmed

INVESTOR IN PEOPLE

Headquarters
Waverley Gate, 2-4 Waterloo Place, Edinburgh EH1 3EG

Chair Dr Charles J Winstanley
Chief Executive Professor James J Barbour O.B.E.
Lothian NHS Board is the common name of Lothian Health Board

a) Page 1

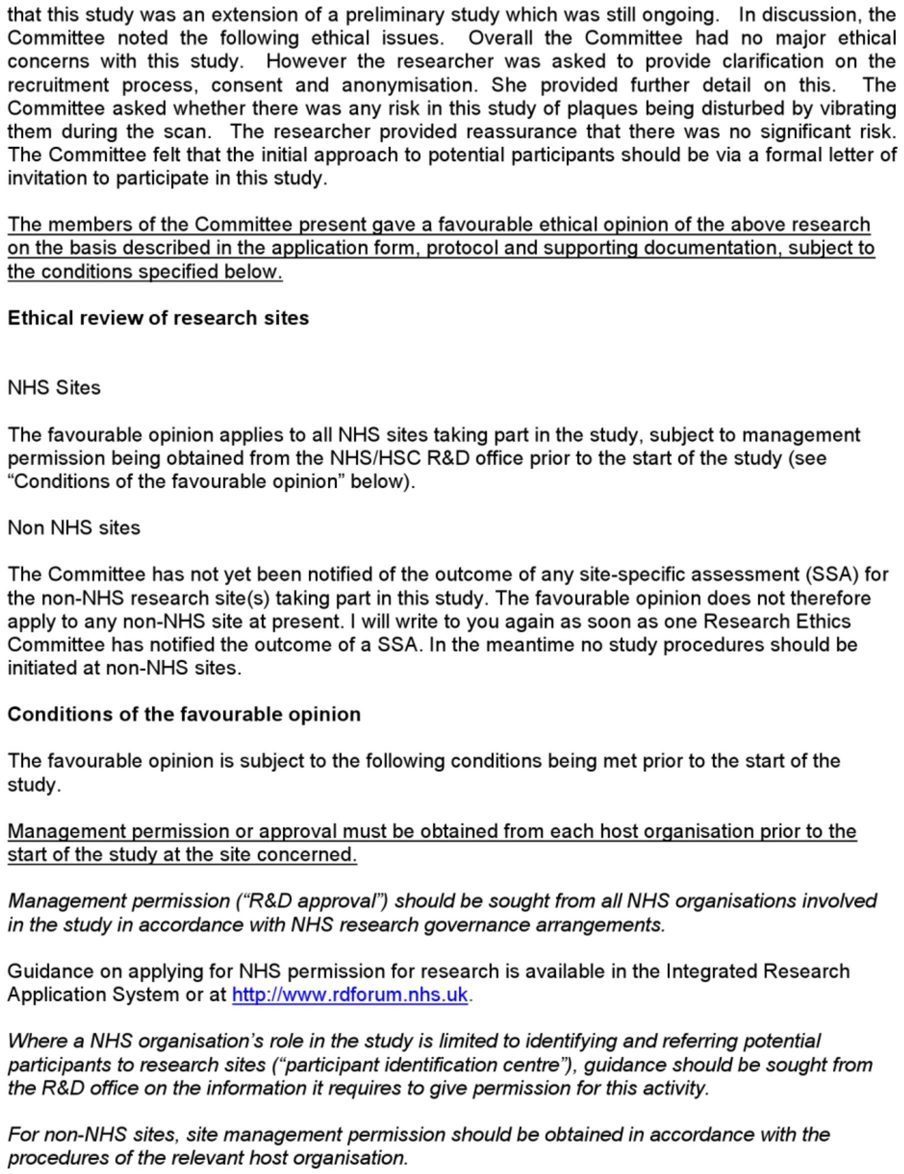

that this study was an extension of a preliminary study which was still ongoing. In discussion, the Committee noted the following ethical issues. Overall the Committee had no major ethical concerns with this study. However the researcher was asked to provide clarification on the recruitment process, consent and anonymisation. She provided further detail on this. The Committee asked whether there was any risk in this study of plaques being disturbed by vibrating them during the scan. The researcher provided reassurance that there was no significant risk. The Committee felt that the initial approach to potential participants should be via a formal letter of invitation to participate in this study.

The members of the Committee present gave a favourable ethical opinion of the above research on the basis described in the application form, protocol and supporting documentation, subject to the conditions specified below.

Ethical review of research sites

NHS Sites

The favourable opinion applies to all NHS sites taking part in the study, subject to management permission being obtained from the NHS/HSC R&D office prior to the start of the study (see "Conditions of the favourable opinion" below).

Non NHS sites

The Committee has not yet been notified of the outcome of any site-specific assessment (SSA) for the non-NHS research site(s) taking part in this study. The favourable opinion does not therefore apply to any non-NHS site at present. I will write to you again as soon as one Research Ethics Committee has notified the outcome of a SSA. In the meantime no study procedures should be initiated at non-NHS sites.

Conditions of the favourable opinion

The favourable opinion is subject to the following conditions being met prior to the start of the study.

Management permission or approval must be obtained from each host organisation prior to the start of the study at the site concerned.

Management permission ("R&D approval") should be sought from all NHS organisations involved in the study in accordance with NHS research governance arrangements.

Guidance on applying for NHS permission for research is available in the Integrated Research Application System or at http://www.rdforum.nhs.uk.

Where a NHS organisation's role in the study is limited to identifying and referring potential participants to research sites ("participant identification centre"), guidance should be sought from the R&D office on the information it requires to give permission for this activity.

For non-NHS sites, site management permission should be obtained in accordance with the procedures of the relevant host organisation.

b) Page 2

Sponsors are not required to notify the Committee of approvals from host organisations

Other conditions specified by the REC –

- Add "I understand that relevant sections of my medical notes and data collected during the study may be looked at by the study researchers and individuals from the Sponsor, regulatory authorities or from the NHS organisation, where it is relevant to my taking part in this research. I give permission for these individuals to have access to my records." to the Consent Form
- Please provide an appropriate letter of invitation
- Please do a final typographical/grammatical check of all supporting documents and amend appropriately. Technical terms such as atherosclerotic plaques should be explained in lay language.
- Please be consistent over use of terms such as MRI and MRE

.

It is responsibility of the sponsor to ensure that all the conditions are complied with before the start of the study or its initiation at a particular site (as applicable).

You should notify the REC in writing once all conditions have been met (except for site approvals from host organisations) and provide copies of any revised documentation with updated version numbers. Confirmation should also be provided to host organisations together with relevant documentation

Approved documents

The documents reviewed and approved at the meeting were:

Document	*Version*	*Date*
GP/Consultant Information Sheets	1	25 November 2011
Investigator CV	CI Thomas Seale	25 November 2011
Investigator CV	Hoskins	
Participant Consent Form: PCF	1	30 November 2011
Participant Information Sheet: PIS	1	29 November 2011
Protocol	1	20 September 2011
REC application		25 November 2011

Membership of the Committee

The members of the Ethics Committee who were present at the meeting are listed on the attached sheet.

Statement of compliance

c) Page 3

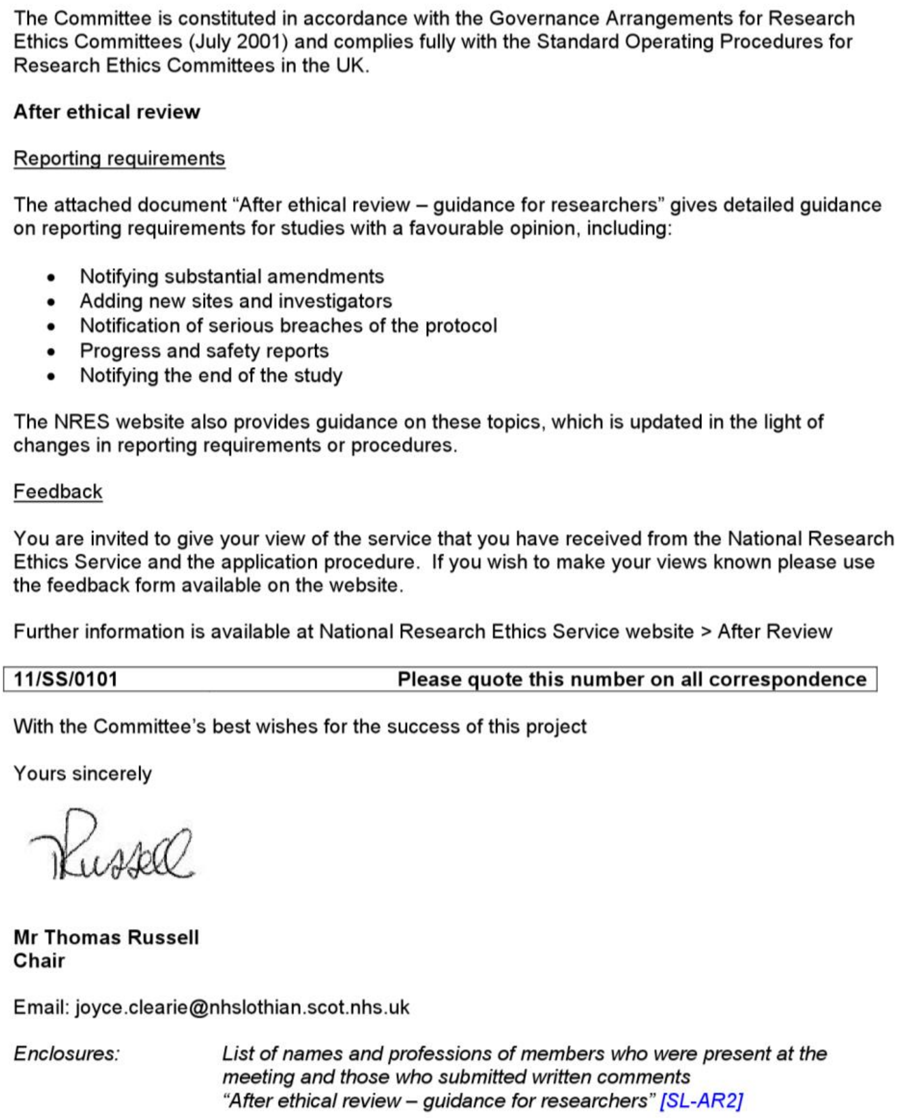

The Committee is constituted in accordance with the Governance Arrangements for Research Ethics Committees (July 2001) and complies fully with the Standard Operating Procedures for Research Ethics Committees in the UK.

After ethical review

Reporting requirements

The attached document "After ethical review – guidance for researchers" gives detailed guidance on reporting requirements for studies with a favourable opinion, including:

- Notifying substantial amendments
- Adding new sites and investigators
- Notification of serious breaches of the protocol
- Progress and safety reports
- Notifying the end of the study

The NRES website also provides guidance on these topics, which is updated in the light of changes in reporting requirements or procedures.

Feedback

You are invited to give your view of the service that you have received from the National Research Ethics Service and the application procedure. If you wish to make your views known please use the feedback form available on the website.

Further information is available at National Research Ethics Service website > After Review

11/SS/0101	**Please quote this number on all correspondence**

With the Committee's best wishes for the success of this project

Yours sincerely

Russell

Mr Thomas Russell
Chair

Email: joyce.clearie@nhslothian.scot.nhs.uk

Enclosures:	*List of names and professions of members who were present at the meeting and those who submitted written comments* *"After ethical review – guidance for researchers" [SL-AR2]*

d) Page 4

Figure C.1: *The favourable ethical opinion of the South East Scotland Research Ethics Committee 02.*

Appendix D
Publications

D.1) Papers

- Thomas-Seale, L. E. J., Klatt, D., Pankaj, P., Roberts, N., Sack, I. and Hoskins, P. R. (2011) ‘A simulation of magnetic resonance elastography steady state wave response through idealised atherosclerotic plaques’, *IAENG International Journal of Computer Science*, 38 (4), 394-400.

D.2) Conference Proceedings

- Thomas-Seale, L. E. J., Kennedy, P., Klatt, D., Anderson, T., Hammer, S., Semple, S., Mirsadraee, S., Sack, I., Pankaj, P., Roberts, N. and Hoskins, P. R. (2013) ‘Magnetic resonance elastography through atherosclerosis: The progression from computational simulations to experimental feasibility’, *Proceedings of the 12th International Tissue Elasticity Conference,* 1st-4th October, Lingfield, UK, 45.
- Thomas-Seale, L. E. J., Pankaj, P., Roberts, N. and Hoskins, P. R. (2011) ‘Computational modelling of magnetic resonance elastography shear wave behaviour through atherosclerotic plaque with disease development’, *Lecture Notes in Engineering and Computer Science: Proceedings of the World Congress on Engineering,* 6th-8th July, 2011, London, UK, 2636-2639. (Best paper award)

D.3) Conference Presentations

- Thomas-Seale, L. E. J., Klatt, D., Sack, I. Roberts, N. Pankaj, P. and Hoskins, P. R. (2012) ‘Simulating magnetic resonance elastography through idealised atherosclerotic plaques: Stiffness variation with disease development’, *Bioengineering 2012,* 6th-7th September, Oxford, UK. (Oral presentation)
- Thomas-Seale, L. E. J., Klatt, D., Sack, I., Pankaj, P., Roberts, N and Hoskins, P. R. (2011) ‘A preliminary computational simulation of MR elastography through patient

specific diseased arterial geometry', *EPSRC Network Meeting, Patient Specific Modelling,* 28th-29th September, Edinburgh, UK. (Poster presentation)

- Thomas-Seale, L. E. J., Klatt, D., Sack, I. Roberts, N. Pankaj, P. and Hoskins, P. R. (2011) 'Can a loudspeaker diagnose stroke risk: A computational simulation of magnetic resonance elastography applied to an idealised atherosclerotic plaque', *The University of Edinburgh, School of Engineering, Postgraduate Conference,* 27th April, Edinburgh, UK. (Poster presentation)
- Thomas-Seale, L. E. J., Roberts, N., Pankaj, P. and Hoskins, P. R. (2010) 'Varying the frequency of MRE shear waves through an idealised computational model of atherosclerotic plaque', *International Society for Magnetic Resonance in Medicine, British Chapter, Annual Scientific Meeting,* 1st-3rd September, Nottingham, UK. (Poster presentation)
- Thomas-Seale, L. E. J., Roberts, N., Pankaj, P. and Hoskins, P. R. (2010) 'Computational modelling of arterial MRE through atherosclerotic plaques: A feasibility study', *Scottish Imaging Network, Annual Scientific Meeting,* 16th June, Edinburgh, UK. (Poster presentation)

Bibliography

Ahmed, S. A. and Giddens, D. P. (1983) 'Velocity-measurements in steady flow through axisymmetric stenoses at moderate Reynolds-numbers', *Journal of Biomechanics,* 16(7), 505-516.

Alger, J. and Frew, A. (2007) 'Advanced MRI applications' in Caner, A., Lemoigne, Y. and Rahal, G., eds., *Physics for medical imaging applications,* Dordrecht, The Netherlands: Springer.

Alizad, A., Fatemi, M., Whaley, D. H. and Greenleaf, J. F. (2003) 'Detection of calcified arteries in breast tissue by vibro-acoustography: Implications on diagnosis of coronary artery diseases', *Proceedings of IEEE International Ultrasonics Symposium,* 5th-8th October, Honalulu, Hawaii, 1515-1518.

Anderson, J. L., Adams, C. D., Antman, E. M., Bridges, C. R., Califf, R. M., Casey, D. E., Jr., Chavey, W. E., 2nd, Fesmire, F. M., Hochman, J. S., Levin, T. N., Lincoff, A. M., Peterson, E. D., Theroux, P., Wenger, N. K. and Wright, R. S. (2007) 'ACC/AHA 2007 guidelines for the management of patients with unstable angina/non-ST-elevation myocardial infarction: A report of the American College of Cardiology/American Heart Association task force on practice guidelines', *Journal of the American College of Cardiology,* 50(7), e1-e157.

Baldewsing, R. A., Danilouchkine, M. G., Mastik, F., Schaar, J. A., Serruys, P. W. and van der Steen, A. F. W. (2008) 'An inverse method for imaging the local elasticity of atherosclerotic coronary plaques', *IEEE Transactions on Information Technology in Biomedicine,* 12(3), 277-289.

Baldewsing, R. A., de Korte, C. L., Mastik, F., Schaar, J. A. and van der Steen, A. F. W. (2002) 'Comparison of finite elements model elastograms and IVUS elastograms acquired from phantoms and arteries', *Proceedings of IEEE International Ultrasonics Symposium,* 8th-11th October, Munich, Germany, 1921-1924.

Baldewsing, R. A., De Korte, C. L., Schaar, J. A., Mastik, F. and Van Der Steen, A. F. W. (2004a) 'A finite element model for performing intravascular ultrasound elastography of human atherosclerotic coronary arteries', *Ultrasound in Medicine and Biology,* 30(6), 803-813.

Baldewsing, R. A., De Korte, C. L., Schaar, J. A., Mastik, F. and van der Steen, A. F. W. (2004b) 'Finite element modeling and intravascular ultrasound elastography of vulnerable plaques: parameter variation', *Ultrasonics,* 42, 723-729.

Baldewsing, R. A., Mastik, F., Schaar, J. A., Serruys, P. W. and van der Steen, A. F. W. (2006) 'Young's modulus reconstruction of vulnerable atherosclerotic plaque components using deformable curves', *Ultrasound in Medicine and Biology,* 32(2), 201-210.

Baldewsing, R. A., Schaar, J. A., Mastik, F., Oomens, C. W. J. and van der Steen, A. F. W. (2005) 'Assessment of vulnerable plaque composition by matching the deformation of a parametric plaque model to measured plaque deformation', *IEEE Transactions on Medical Imaging,* 24(4), 514-528.

Balocco, S., Basset, O., Courbebaisse, G., Boni, E., Frangi, A. F., Tortoli, P. and Cachard, C. (2010) 'Estimation of the viscoelastic properties of vessel walls using a computational model and Doppler ultrasound', *Physics in Medicine and Biology,* 55(12), 3557-3575.

Barbee, K. A., Davies, P. F. and Lal, R. (1994) 'Shear stress-induced reorganisation of the surface-topography of living endothelial-cells imaged by atomic-force microscopy', *Circulation Research,* 74(1), 163-171.

Barnes, H. A., Hutton, J. F. and Walters, K. (1989) *An Introduction to Rheology, Rheology Series, Volume 3,* Oxford, UK: Elsevier.

Barnett, H. J. M., Taylor, W., Eliasziw, M., Fox, A. J., Ferguson, G. G., Haynes, R. B., Rankin, R. N., Clagett, G. P., Hachinski, V. C., Sackett, D. L., Thorpe, K. E. and Meldrum, H. E. (1998) 'Benefit of carotid endarterectomy in patients with symptomatic moderate or severe stenosis', *New England Journal of Medicine,* 339(20), 1415-1425.

Barrett, S. R. H., Sutcliffe, M. P. F., Howarth, S., Li, Z. Y. and Gillard, J. H. (2009) 'Experimental measurement of the mechanical properties of carotid atherothrombotic plaque fibrous cap', *Journal of Biomechanics,* 42(11), 1650-1655.

Behler, R. H., Nichols, T. C., Merricks, E. P., Dumont, D. M., Gallippi, C. M. and Ieee (2006) 'ARFI Ultrasound for Characterizing Atherosclerosis', *Proceedings of IEEE International Ultrasonics Symposium,* 3rd-6th October, Vancouver, Canada, 722-727.

Behler, R. H., Nichols, T. C., Zhu, H., Merricks, E. P. and Gallippi, C. M. (2009) 'ARFI imaging for noninvasive material charaterization of atherosclerosis part II: Toward in vivo characterisation', *Ultrasound in Medicine and Biology,* 35(2), 278-295.

Berenger, J. P. (1994) 'A perfectly matched layer for the absorption of electromagnetic waves', *Journal of Computational Physics,* 114(2), 185-200.

Berenson, G. S., Srinivasan, S. R., Bao, W. H., Newman, W. P., Tracy, R. E. and Wattigney, W. A. (1998) 'Association between multiple cardiovascular risk factors and atherosclerosis in children and young adults', *New England Journal of Medicine,* 338(23), 1650-1656.

Bergel, D. H. (1961a) 'Dynamic elastic properties of arterial wall', *Journal of Physiology,* 156(3), 458-469.

Bergel, D. H. (1961b) 'Static elastic properties of arterial wall', *Journal of Physiology,* 156(3), 445-457.

Bertoglio, C., Barber, D., Gaddum, N., Valverde, I., Rutten, M., Beerbaum, P., Moireau, P., Hose, R. and Gerbeau, J. F. (2014) 'Identification of artery wall stiffness: In vitro validation and in vivo results of a data assimilation procedure applied to a 3D fluid-structure interaction model', *Journal of Biomechanics,* 47(5), 1027-1034.

Bouvier, A., Deleaval, F., Doyley, M. M., Tacheau, A., Finet, G., Le Floc'h, S., Cloutier, G., Pettigrew, R. I. and Ohayon, J. (2014) 'A new finite element method for inverse problems in structural analysis: application to atherosclerotic plaque elasticity reconstruction', *Computer Methods in Biomechanics and Biomedical Engineering,* 17, 16-17.

Bower, A. F. (2010) *Applied mechanics of solids,* Boca Raton, Florida: CRC Press.

Braun, J., Braun, K. and Sack, I. (2003) 'Electromagnetic actuator for generating variably oriented shear waves in MR elastography', *Magnetic Resonance in Medicine,* 50(1), 220-222.

Braun, J., Buntkowsky, G., Bernarding, J., Tolxdorff, T. and Sack, I. (2001) 'Simulation and analysis of magnetic resonance elastography wave images using coupled harmonic oscillators and Gaussian local frequency estimation', *Magnetic Resonance Imaging,* 19(5), 703-713.

Cai, J. M., Hatsukami, T. S., Ferguson, M. S., Kerwin, W. S., Saam, T., Chu, B. C., Takaya, N., Polissar, N. L. and Yuan, C. (2005) 'In vivo quantitative measurement of intact fibrous cap and lipid-rich necrotic core size in atherosclerotic carotid plaque - Comparison of high-resolution, contrast-enhanced magnetic resonance imaging and histology', *Circulation,* 112(22), 3437-3444.

Caro, C. G., Fitz-Gerald, J. M. and Schroter, R. C. (1971) 'Atheroma and arterial wall shear observation, correlation and proposal of a shear dependent mass transfer mechanism for atherogenesis', *Proceedings of the Royal Society. Series B, Biological Sciences,* 177, 109-133.

Carstensen, E. L., Parker, K. J. and Lerner, R. M. (2008) 'Elastography in the management of liver disease', *Ultrasound in Medicine and Biology,* 34(10), 1535-1546.

Chandran, K. B., Mun, J. H., Choi, K. K., Chen, J. S., Hamilton, A., Nagaraj, A. and McPherson, D. D. (2003) 'A method for in-vivo analysis for regional arterial wall material property alterations with atherosclerosis: preliminary results', *Medical Engineering & Physics*, 25(4), 289-298.

Chau, A. H., Chan, R. C., Shishkov, M., MacNeill, B., Iftimiia, N., Tearney, G. J., Kamm, R. D., Bouma, B. E. and Kaazempur-Mofrad, M. R. (2004) 'Mechanical analysis of atherosclerotic plaques based on optical coherence tomography', *Annals of Biomedical Engineering,* 32(11), 1494-1503.

Chen, Q. S., Ringleb, S. I., Manduca, A., Ehman, R. L. and An, K. N. (2005) 'A finite element model for analyzing shear wave propagation observed in magnetic resonance elastography', *Journal of Biomechanics,* 38(11), 2198-2203.

Chen, Q. S., Ringleb, S. I., Manduca, A., Ehman, R. L. and An, K. N. (2006) 'Differential effects of pre-tension on shear wave propagation in elastic media with different boundary conditions as measured by magnetic resonance elastography and finite element modeling', *Journal of Biomechanics,* 39(8), 1428-1434.

Cheng, G. C., Loree, H. M., Kamm, R. D., Fishbein, M. C. and Lee, R. T. (1993) 'Distribution of circumferential stress in ruptured and stable atherosclerotic lesions. A structural analysis with histopathological correlation', *Circulation,* 87(4), 1179-1187.

Choi, C. D., Skovoroda, A. R., Emelianov, S. Y. and O'Donnell, M. (2002) 'An integrated compliant balloon ultrasound catheter for intravascular strain imaging', *IEEE Transactions on Ultrasonics Ferroelectrics and Frequency Control,* 49(11), 1552-1560.

Chu, K. C. and Rutt, B. K. (1997) 'Polyvinyl alcohol cryogel: An ideal phantom material for MR studies of arterial flow and elasticity', *Magnetic Resonance in Medicine,* 37(2), 314-319.

Claridge, M. W., Bate, G. R., Hoskins, P. R., Adam, D. J., Bradbury, A. W. and Wilmink, A. B. (2009) 'Measurement of arterial stiffness in subjects with vascular disease: Are vessel wall changes more sensitive than increase in intima-media thickness?', *Atherosclerosis,* 205(2), 477-480.

Clayton, E. H., Okamoto, R. J. and Bayly, P. V. (2013) 'Mechanical properties of viscoelastic media by local frequency estimation of divergence-free wave fields', *Journal of Biomechanical Engineering - Transactions of the ASME,* 135, 021025 1-6.

Corti, R. and Fuster, V. (2011) 'Imaging of atherosclerosis: magnetic resonance imaging', *European Heart Journal,* 32, 1709-1719.

Dahl, J. J., Dumont, D. M., Allen, J. D., Miller, E. M. and Trahey, G. E. (2009) 'Acoustic radiation force impulse imaging for noninvasive characterisation of carotid artery atherosclerotic plaques: A feasbility study', *Ultrasound in Medicine and Biology,* 35(5), 707-716.

Dart, A. M. and Kingwell, B. A. (2001) 'Pulse pressure - A review of mechanisms and clinical relevance', *Journal of the American College of Cardiology,* 37(4), 975-984.

Dassault Systèmes Simulia Corp. (2010a) *Abaqus 6.10 Documentation, Abaqus Analysis User Manual, Volume I: Introduction, Spatial Modelling, Execution and Output,* Providence, Rhode Island: Dassault Systèmes Simulia Corp.

Dassault Systèmes Simulia Corp. (2010b) *Abaqus 6.10 Documentation, Abaqus Analysis User Manual, Volume II: Analysis,* Providence, Rhode Island: Dassault Systèmes Simulia Corp.

Dassault Systèmes Simulia Corp. (2010c) *Abaqus 6.10 Documentation, Abaqus Analysis User Manual, Volume IV: Elements,* Providence, Rhode Island: Dassault Systèmes Simulia Corp.

De Jong, N., Bom, N., Schaar, J., Goertz, D., Frijlink, M. and Van Der Steen, A. (2007) 'Intravasular imaging' in Caner, A., Lemoigne, Y. and Rahal, G., eds., *Physics for medical imaging applications,* Dordrecht, The Netherlands: Springer.

De Korte, C. L., Carlier, S. G., Mastik, F., Doyley, M. M., Van Der Steen, A. F. W., Serruys, P. W. and Bom, N. (2002) 'Morphological and mechanical information of coronary arteries obtained with intravascular elastography - Feasibility study in vivo', *European Heart Journal,* 23(5), 405-413.

De Korte, C. L., Cespedes, E. I., Van Der Steen, A. F. W. and Lancee, C. T. (1997) 'Intravascular elasticity imaging using ultrasound: Feasibility studies in phantoms', *Ultrasound in Medicine and Biology,* 23(5), 735-746.

De Korte, C. L., Hansen, H. H. G. and Van Der Steen, A. F. W. (2011) 'Vascular ultrasound for atherosclerosis imaging', *Interface Focus,* 1(4), 565-575.

De Korte, C. L., Pasterkamp, G., Van Der Steen, A. F. W., Woutman, H. A. and Bom, N. (2000) 'Characterization of plaque components with intravascular ultrasound elastography in human femoral and coronary arteries in vitro', *Circulation,* 102(6), 617-623.

Dineley, J., Meagher, S., Poepping, T. L., McDicken, W. N. and Hoskins, P. R. (2006) 'Design and characterisation of a wall motion phantom', *Ultrasound in Medicine and Biology*, 32(9), 1349-1357.

Doherty, J. R., Dumont, D. M., Trahey, G. E. and Palmeri, M. L. (2013) 'Acoustic radiation force impulse imaging of vulnerable plaques: a finite element method parametric analysis', *Journal of Biomechanics*, 46(1), 83-90.

Domire, Z. J., McCullough, M. B., Chen, Q. S. and An, K. N. (2009) 'Feasibility of using magnetic resonance elastography to study the effect of aging on shear modulus of skeletal muscle', *Journal of Applied Biomechanics*, 25(1), 93-97.

Doyle, B. J., Cloonan, A. J., Walsh, M. T., Vorp, D. A. and McGloughlin, T. M. (2010) 'Identification of rupture locations in patient-specific abdominal aortic aneurysms using experimental and computational techniques', *Journal of Biomechanics*, 43(7), 1408-1416.

Draney, M. T., Arko, F. R., Alley, M. T., Markl, M., Herfkens, R. J., Pelc, N. J., Zarins, C. K. and Taylor, C. A. (2004) 'Quantification of vessel wall motion and cyclic strain using cine phase contrast MRI: In vivo validation in the porcine aorta', *Magnetic Resonance in Medicine*, 52(2), 286-295.

Dumont, D., Behler, R. H., Nichols, T. C., Merriciks, E. P. and Gallippi, C. M. (2006) 'ARFI imaging for noninvasive material characterization of atherosclerosis', *Ultrasound in Medicine and Biology*, 32(11), 1703-1711.

Dumont, D., Dahl, J., Miller, E., Allen, J., Fahey, B. and Trahey, G. (2009) 'Lower-limb vascular imaging with acoustic radiation force elastography: Demonstration of in vivo feasibility', *IEEE Transactions on Ultrasonics Ferroelectrics and Frequency Control*, 56(5), 931-944.

Early, M. and Kelly, D. J. (2010) 'The role of vessel geometry and material properties on the mechanics of stenting in the coronary and peripheral arteries', *Proceedings of the Institution of Mechanical Engineers Part H - Journal of Engineering in Medicine*, 224, 465-476.

Eskandari, H., Salcudean, S. E., Rohling, R. and Bell, I. (2011) 'Real-time solution of the finite element inverse problem of viscoelasticity', *Inverse Problems*, 27, 1-16.

Falk, E., Shah, P. K. and Fuster, V. (1995) 'Coronary plaque disruption', *Circulation*, 92(3), 657-671.

Farr, R. F. and Allisy-Roberts, P. J. (1997) *Physics for medical imaging*, London, UK: Saunders.

Farrell, B., Fraser, A., Sandercock, P., Slattery, J. and Warlow, C. P. (1998) 'Randomised trial of endarterectomy for recently symptomatic carotid stenosis: Final results of the MRC European carotid surgery trial (ECST)', *Lancet,* 351, 1379-1387.

Fatemi, M. and Greenleaf, J. F. (1998) 'Ultrasound-stimulated vibro-acoustic spectrography', *Science,* 280, 82-85.

Fatemi, M. and Greenleaf, J. F. (2000) 'Probing the dynamics of tissue at low frequencies with the radiation force of ultrasound', *Physics in Medicine and Biology,* 45(6), 1449-1464.

Fayad, Z. A., Nahar, T., Fallon, J. T., Goldman, M., Aguinaldo, J. G., Badimon, J. J., Shinnar, M., Chesebro, J. H. and Fuster, V. (2000) 'In vivo magnetic resonance evaluation of atherosclerotic plaques in the human thoracic aorta - A comparison with transesophageal echocardiography', *Circulation*, 101(21), 2503-2509.

Franquet, A., Avril, S., Le Riche, R. and Badel, P. (2012) 'Identification of heterogeneous elastic properties in stenosed arteries: a numerical plane strain study', *Computer Methods in Biomechanics and Biomedical Engineering,* 15(1), 49-58.

Franquet, A., Avril, S., Le Riche, R., Badel, P., Schneider, F. C., Boissier, C. and Favre, J. P. (2013a) 'Identification of the in vivo elastic properties of common carotid arteries from MRI: A study on subjects with and without atherosclerosis', *Journal of the Mechanical Behavior of Biomedical Materials,* 27, 184-203.

Franquet, A., Avril, S., Le Riche, R., Badel, P., Schneider, F. C., Li, Z. Y., Boissier, C. and Favre, J. P. (2013b) 'A new method for the in vivo identification of mechanical properties in arteries from cine MRI images: Theoretical framework and validation', *IEEE Transactions on Medical Imaging,* 32(8), 1448-1461.

Fraser, K. H. (2007) 'Computational estimation of haemodynamics and tissue stresses in abdominal aortic aneurysms', PhD Thesis, The University of Edinburgh.

Fung, Y. C. (1993) *Biomechanics: Mechanical Properties of Living Tissues,* New York: Springer-Verlag.

Fung, Y. C., Fronek, K. and Patitucci, P. (1979) 'Pseudoelasticity of arteries and the choice of its mathematical expression', *American Journal of Physiology,* 237(5), H620-H631.

Gao, H., Long, Q., Graves, M., Gillard, J. H. and Li, Z. Y. (2009) 'Carotid arterial plaque stress analysis using fluid-structure interactive simulation based on in-vivo magnetic resonance images of four patients', *Journal of Biomechanics,* 42(10), 1416-1423.

Gasser, T. C., Ogden, R. W. and Holzapfel, G. A. (2006) 'Hyperelastic modelling of arterial layers with distributed collagen fibre orientations', *Journal of the Royal Society Interface,* 3(6), 15-35.

Ghiglia, D. C. and Pritt, M. D. (1998) *Two-dimensional phase unwrapping : theory, algorithms, and software,* New York: Wiley.

Glaser, K. J., Manduca, A. and Ehman, R. L. (2012) 'Review of MR elastography applications and recent developments', *Journal of Magnetic Resonance Imaging,* 36(4), 757-774.

Go, A. S., Mozaffarian, D., Roger, V. L., Benjamin, E. J., Berry, J. D., Blaha, M. J., Dai, S. F., Ford, E. S., Fox, C. S., Franco, S., Fullerton, H. J., Gillespie, C., Hailpern, S. M., Heit, J. A., Howard, V. J., Huffman, M. D., Judd, S. E., Kissela, B. M., Kittner, S. J., Lackland, D. T., Lichtman, J. H., Lisabeth, L. D., Mackey, R. H., Magid, D. J., Marcus, G. M., Marelli, A., Matchar, D. B., McGuire, D. K., Mohler, E. R., Moy, C. S., Mussolino, M. E., Neumar, R. W., Nichol, G., Pandey, D. K., Paynter, N. P., Reeves, M. J., Sorlie, P. D., Stein, J., Towfighi, A., Turan, T. N., Virani, S. S., Wong, N. D., Woo, D. and Turner, M. B. (2014) 'Heart disease and stroke statistics - 2014 update. A report from the American Heart Association', *Circulation,* 129(3), E28-E292.

Golledge, J. and Siew, D. A. (2008) 'Identifying the carotid 'high risk' plaque: is it still a riddle wrapped up in an enigma?', *European Journal of Vascular and Endovascular Surgery,* 35(1), 2-8.

Greenleaf, J. F. (2003) 'Applications of ultrasound stimulated vibro-acoustography', *Proceedings of IEEE International Ultrasonics Symposium,* 5th-8th October, Honalulu, Hawaii, 1058-1061.

Greenleaf, J. F. and Fatemi, M. (1998) 'Ultrasound-stimulated vibro-acoustic imaging in vivo', *Proceedings of IEEE International Ultrasonics Symposium,* 5th-8th October, Sendai, Japan, 1635-1638.

Greenleaf, J. F., Fatemi, M. and Insana, M. (2003) 'Selected methods for imaging elastic properties of biological tissues', *Annual Review of Biomedical Engineering,* 5, 57-78.

Gudbjartsson, H. and Patz, S. (1995) 'The Rician distribution of noisy MRI data', *Magnetic Resonance in Medicine,* 34(6), 910-914.

Guo, Z., You, S., Wan, X. and Bicanic, N. (2010) 'A FEM-based direct method for material reconstruction inverse problem in soft tissue elastography', *Computers & Structures,* 88, 1459-1468.

Haidekker, M. A. (2010) *Advanced biomedical image analysis,* Hoboken, New Jersey.: John Wiley & Sons,.

Hamhaber, U., Grieshaber, V. A., Nagel, J. H. and Klose, U. (2003) 'Comparison of quantitative shear wave MR-elastography with mechanical compression tests', *Magnetic Resonance in Medicine,* 49(1), 71-77.

Hamhaber, U., Sack, I., Papazoglou, S., Rump, J., Klatt, D. and Braun, J. (2007) 'Three-dimensional analysis of shear wave propagation observed by in vivo magnetic resonance elastography of the brain', *Acta Biomaterialia,* 3(1), 127-137.

Hamilton, A. J., Kim, H., Nagaraj, A., Mun, J. H., Yan, L. J. L., Roth, S. I., McPherson, D. D. and Chandran, K. B. (2005) 'Regional material property alterations in porcine femoral arteries with atheroma development', *Journal of Biomechanics,* 38(12), 2354-2364.

Hamilton, P. K., Lockhart, C. J., Quinn, C. E. and McVeigh, G. E. (2007) 'Arterial stiffness: clinical relevance, measurement and treatment', *Clinical Science,* 113(3-4), 157-170.

Hansen, H. H. G., Lopata, R. G. P. and de Korte, C. L. (2009) 'Noninvasive carotid strain imaging using angular compounding at large beam steered angles: Validation in vessel phantoms', *IEEE Transactions on Medical Imaging,* 28(6), 872-880.

Hansen, H. H. G., Richards, M. S., Doyley, M. M. and de Korte, C. L. (2013) 'Noninvasive vascular displacement estimation for relative elastic modulus reconstruction in transversal imaging planes', *Sensors,* 13(3), 3341-3357.

Hansson, G. K. (2005) 'Mechanisms of disease - Inflammation, atherosclerosis, and coronary artery disease', *New England Journal of Medicine,* 352(16), 1685-1695.

Hayashi, K. (1993) 'Experimental approaches on measuring the mechanical properties and constitutive laws of arterial walls', *Journal of Biomechanical Engineering - Transactions of the ASME,* 115(4), 481-488.

Himburg, H. A., Grzybowski, D. M., Hazel, A. L., LaMack, J. A., Li, X. M. and Friedman, M. H. (2004) 'Spatial comparison between wall shear stress measures and porcine arterial endothelial permeability', *American Journal of Physiology - Heart and Circulatory Physiology,* 286(5), H1916-H1922.

Hirsch, A. T., Haskal, Z. J., Hertzer, N. R., Bakal, C. W., Creager, M. A., Halperin, J. L., Hiratzka, L. F., Murphy, W. R. C., Olin, J. W., Puschett, J. B., Rosenfield, K. A., Sacks, D., Stanley, J. C., Taylor, L. M., White, C. J., White, J. and White, R. A. (2006) 'ACC/AHA 2005 practice guidelines for the management of patients with peripheral arterial disease (lower extremity, renal, mesenteric, and abdominal aortic)', *Circulation,* 113, E463-E654.

Hirsch, S., Guo, J., Reiter, R., Papazoglou, S., Kroencke, T., Braun, J. and Sack, I. (2014) 'MR elastography of the liver and the spleen using a piezoelectric driver, single-shot wave-field acquisition, and multifrequency dual parameter reconstruction', *Magnetic Resonance in Medicine,* 71(1), 267-277.

Hollis, L., Thomas-Seale, L., Conlisk, N., Roberts, N., Pankaj, P. and Hoskins, P. (2015) 'A 3-dimensional transient explicit technique to simulate magnetic resonance elastography', *International Journal of Numerical Methods in Biomedical Engineering,* (Submitted).

Holzapfel, G. A. and Gasser, T. C. (2001) 'A viscoelastic model for fiber-reinforced composites at finite strains: Continuum basis, computational aspects and applications', *Computer Methods in Applied Mechanics and Engineering,* 190(34), 4379-4403.

Holzapfel, G. A., Gasser, T. C. and Ogden, R. W. (2000) 'A new constitutive framework for arterial wall mechanics and a comparative study of material models', *Journal of Elasticity,* 61, 1-48.

Holzapfel, G. A., Gasser, T. C. and Ogden, R. W. (2004a) 'Comparison of a multi-layer structural model for arterial walls with a fung-type model, and issues of material stability', *Journal of Biomechanical Engineering - Transactions of the ASME,* 126(2), 264-275.

Holzapfel, G. A., Gasser, T. C. and Stadler, M. (2002a) 'A structural model for the viscoelastic behavior of arterial walls: Continuum formulation and finite element analysis', *European Journal of Mechanics A/Solids,* 21, 441-463.

Holzapfel, G. A., Sommer, G. and Regitnig, P. (2004b) 'Anisotropic mechanical properties of tissue components in human atherosclerotic plaques', *Journal of Biomechanical Engineering - Transactions of the ASME,* 126(5), 657-665.

Holzapfel, G. A., Stadler, M. and Schulze-Bauer, C. A. J. (2002b) 'A layer-specific three-dimensional model for the simulation of balloon angioplasty using magnetic resonance imaging and mechanical testing', *Annals of Biomedical Engineering,* 30(6), 753-767.

Hoskins, P. R. (2007) 'Physical properties of tissues relevant to arterial ultrasound imaging and blood velocity measurement', *Ultrasound in Medicine and Biology,* 33(10), 1527-1539.

Hoskins, P. R. (2008) 'Simulation and validation of arterial ultrasound imaging and blood flow', *Ultrasound in Medicine and Biology,* 34(5), 693-717.

Hoskins, P. R. (2010) 'Elastography' in Hoskins, P. R., Martin, K. and Thrush, A., eds., *Diagnostic Ultrasound: Physics and Equipment*, 2nd ed., Cambridge, UK: Cambridge University Press.

Hoskins, P. R. and Bradbury, A. W. (2012) 'Wall motion analysis' in Nicolaides, A., Beach, K. W., Kyriacou, E. and Pattichis, C. S., eds., *Ultrasound and carotid bifurcation atherosclerosis* [text], London, UK: Springer, 1 online resource (xvii, 649 pages).

Hoskins, P. R. and Hardman, D. (2009) 'Three-dimensional imaging and computational modelling for estimation of wall stresses in arteries', *British Journal of Radiology,* 82, S3-S17.

Hyde, D. E., Fox, A. J., Gulka, I., Kalapos, P., Lee, D. H., Pelz, D. M. and Holdsworth, D. W. (2004) 'Internal carotid artery stenosis measurement - Comparison of 3D computed rotational angiography and conventional digital subtraction angiography', *Stroke,* 35(12), 2776-2781.

Kanai, H., Hasegawa, H., Ichiki, M., Tezuka, F. and Koiwa, Y. (2003) 'Elasticity imaging of atheroma with transcutaneous ultrasound preliminary study', *Circulation,* 107(24), 3018-3021.

Kates, B. (2011) 'Magnetic resonance elastography for measuring the compliance of chronic total occlusions', Masters of Health Science Thesis, University of Toronto.

King, D. M., Moran, C. M., McNamara, J. D., Fagan, A. J. and Browne, J. E. (2011) 'Development of a vessel-mimicking material for use in anatomically realistic doppler flow phantoms', *Ultrasound in Medicine and Biology,* 37(5), 813-826.

Klatt, D. (2010) 'Development and Application of Multifrequency Magnetic Resonance Elastography', Doctor rerum naturalium in Physics, Humboldt-Universität zu Berlin.

Klatt, D., Asbach, P., Rump, J., Papazoglou, S., Somasundaram, R., Modrow, J., Braun, J. and Sack, I. (2006) 'In vivo determination of hepatic stiffness using steady-state free precession magnetic resonance elastography', *Investigative Radiology,* 41(12), 841-848.

Klatt, D., Hamhaber, U., Asbach, P., Braun, J. and Sack, I. (2007) 'Noninvasive assessment of the rheological behavior of human organs using multifrequency MR elastography: a study of brain and liver viscoelasticity', *Physics in Medicine and Biology,* 52(24), 7281-7294.

Klatt, D., Papazoglou, S., Braun, J. and Sack, I. (2010) 'Viscoelasticity-based MR elastography of skeletal muscle', *Physics in Medicine and Biology,* 55(21), 6445-6459.

Klein, C., Hain, E. G., Braun, J., Riek, K., Mueller, S., Steiner, B. and Sack, I. (2014) 'Enhanced adult neurogenesis increases brain stiffness: In vivo magnetic resonance elastography in a mouse model of dopamine depletion', *Plos One,* 9(3), e92582 1-10.

Kolipaka, A., McGee, K. P., Manduca, A., Romano, A. J., Glaser, K. J., Araoz, P. A. and Ehman, R. L. (2009) 'Magnetic Resonance Elastography: Inversions in Bounded Media', *Magnetic Resonance in Medicine,* 62(6), 1533-1542.

Kolipaka, A., Woodrum, D., Araoz, P. A. and Ehman, R. L. (2012) 'MR elastography of the in vivo abdominal aorta: A feasibility study for comparing aortic stiffness between hypertensives and normotensives', *Journal of Magnetic Resonance Imaging,* 35(3), 582-586.

Lally, C., Dolan, F. and Prendergast, P. J. (2005) 'Cardiovascular stent design and vessel stresses: a finite element analysis', *Journal of Biomechanics,* 38(8), 1574-1581.

Laurent, S., Cockcroft, J., Van Bortel, L., Boutouyrie, P., Giannattasio, C., Hayoz, D., Pannier, B., Vlachopoulos, C., Wilkinson, I. and Struijker-Boudier, H. (2006) 'Expert consensus document on arterial stiffness: methodological issues and clinical applications', *European Heart Journal,* 27, 2588-2605.

Leclerc, G. E., Charleux, F., Ho Ba Tho, M.-C. and Bensamoun, S. F. (2013) 'Identification process based on shear wave propagation within a phantom using finite element modelling and magnetic resonance elastography', *Computer Methods in Biomechanics and Biomedical Engineering,* 18(5), 485-491.

Lee, R. T., Grodzinsky, A. J., Frank, E. H., Kamm, R. D. and Schoen, F. J. (1991) 'Structure-dependent dynamic mechanical behaviour of fibrous caps from human atherosclerotic plaques', *Circulation,* 83(5), 1764-1770.

Li, M. (2007) 'Numerical simulation of blood flow and vessel wall stresses in stenosed arteries', PhD Thesis, The University of Edinburgh.

Li, R. X., Luo, J., Balaram, S. K., Chaudhry, F. A., Shahmirzadi, D. and Konofagou, E. E. (2013) 'Pulse wave imaging in normal, hypertensive and aneurysmal human aortas in vivo: a feasibility study', *Physics in Medicine and Biology,* 58(13), 4549-4562.

Li, Y. and Snedeker, J. G. (2011) 'Elastography: modality-specific approaches, clinical applications, and research horizons', *Skeletal Radiology,* 40(4), 389-397.

Li, Z. Y., Howarth, S., U-King-Im, J. and Gillard, J. (2005) 'Atheroma: Is calcium important or not? A modelling study of stress within the atheromatous fibrous cap in relation to position and size of calcium deposits', *Proceedings of 27th Annual Conference of the IEEE Engineering in Medicine and Biology,* 1st-4th September, Shanghai, China, 2236-2239.

Li, Z. Y., Howarth, S. P. S., Tang, T., Graves, M. J., U-King-Im, J., Trivedi, R. A., Kirkpatrick, P. J. and Gillard, J. H. (2007) 'Structural analysis and magnetic resonance imaging predict plaque vulnerability: A study comparing symptomatic and asymptomatic individuals', *Journal of Vascular Surgery,* 45(4), 768-775.

Libby, P. (2001) 'Current concepts of the pathogenesis of the acute coronary syndromes', *Circulation,* 104(3), 365-372.

Libby, P., Ridker, P. M. and Maseri, A. (2002) 'Inflammation and atherosclerosis', *Circulation,* 105(9), 1135-1143.

Lin, K., Hsu, P. P., Chen, B. P., Yuan, S., Usami, S., Shyy, J. Y. J., Li, Y. S. and Chien, S. (2000) 'Molecular mechanism of endothelial growth arrest by laminar shear stress', *Proceedings of the National Academy of Sciences of the United States of America,* 97(17), 9385-9389.

Loree, H. M., Grodzinsky, A. J., Park, S. Y., Gibson, L. J. and Lee, R. T. (1994a) 'Static circumferential tangential modulus of human atherosclerotic tissue', *Journal of Biomechanics,* 27(2), 195-204.

Loree, H. M., Kamm, R. D., Stringfellow, R. G. and Lee, R. T. (1992) 'Effects of fibrous cap thickness on peak circumferential stress in model atherosclerotic vessels', *Circulation Research,* 71(4), 850-858.

Loree, H. M., Tobias, B. J., Gibson, L. J., Kamm, R. D., Small, D. M. and Lee, R. T. (1994b) 'Mechanical properties of model atherosclerotic lesion lipid pools', *Arteriosclerosis and Thrombosis,* 14(2), 230-234.

Lusis, A. J. (2000) 'Atherosclerosis', *Nature,* 407, 233-241.

Manduca, A., Lake, D. S., Kruse, S. A. and Ehman, R. L. (2003) 'Spatio-temporal directional filtering for improved inversion of MR elastography images', *Medical Image Analysis,* 7(4), 465-473.

Manduca, A., Oliphant, T. E., Dresner, M. A., Mahowald, J. L., Kruse, S. A., Amromin, E., Felmlee, J. P., Greenleaf, J. F. and Ehman, R. L. (2001) 'Magnetic resonance elastography: Non-invasive mapping of tissue elasticity', *Medical Image Analysis,* 5(4), 237-254.

Mariappan, Y. K., Glaser, K. J. and Ehman, R. L. (2010) 'Magnetic resonance elastography: A review', *Clinical Anatomy,* 23(5), 497-511.

Mariappan, Y. K., Glaser, K. J., Hubmayr, R. D., Manduca, A., Ehman, R. L. and McGee, K. P. (2011) 'MR elastography of human lung parenchyma: Technical development, theoretical modeling and in vivo validation', *Journal of Magnetic Resonance Imaging,* 33(6), 1351-1361.

Marshall, I., Zhao, S. Z., Papathanasopoulou, P., Hoskins, P. and Xu, X. Y. (2004) 'MRI and CFD studies of pulsatile flow in healthy and stenosed carotid bifurcation models', *Journal of Biomechanics,* 37(5), 679-687.

Martin, K. (2010) 'Introduction to B-mode Imaging' in Hoskins, P. R., Martin, K. and Thrush, A., eds., *Diagnostic Ultrasound: Physics and Equipment*, 2nd ed., Cambridge, UK: Cambridge University Press.

Maurice, R. L. and Bertrand, M. (1999) 'Speckle-motion artifact under tissue shearing', *IEEE Transactions on Ultrasonics Ferroelectrics and Frequency Control,* 46(3), 584-594.

Maurice, R. L., Daronat, M., Ohayon, J., Stoyanova, E., Foster, F. S. and Cloutier, G. (2005) 'Non-invasive high-frequency vascular ultrasound elastography', *Physics in Medicine and Biology,* 50(7), 1611-1628.

Maurice, R. L., Fromageau, J., Cardinal, M.-H. R., Doyley, M., de Muinck, E., Robb, J. and Cloutier, G. (2008) 'Characterization of atherosclerotic plaques and mural thrombi with intravascular ultrasound elastography: A potential method evaluated in an aortic rabbit model and a human coronary artery', *IEEE Transactions on Information Technology in Biomedicine,* 12(3), 290-298.

Maurice, R. L., Ohayon, J., Finet, G. and Cloutier, G. (2004a) 'Adapting the Lagrangian speckle model estimator for endovascular elastography: Theory and validation with simulated radio-frequency data', *Journal of the Acoustical Society of America,* 116(2), 1276-1286.

Maurice, R. L., Ohayon, J., Fretigny, Y., Bertrand, M., Soulez, G. and Cloutier, G. (2004b) 'Noninvasive vascular elastography: Theoretical framework', *IEEE Transactions on Medical Imaging,* 23(2), 164-180.

McGarry, M. D. J. and Van Houten, E. E. W. (2008) 'Use of a Rayleigh damping model in elastography', *Medical & Biological Engineering & Computing,* 46(8), 759-766.

McGee, K. P., Lake, D., Mariappan, Y., Hubmayr, R. D., Manduca, A., Ansell, K. and Ehman, R. L. (2011) 'Calculation of shear stiffness in noise dominated magnetic resonance elastography data based on principal frequency estimation', *Physics in Medicine and Biology,* 56(14), 4291-4309.

McRobbie, D. W. (2007) *MRI from picture to proton,* 2nd ed., Cambridge, UK: Cambridge University Press.

Mendis, S., Puska, P. and Norrving, B. (2011) *Global atlas on cardiovascular disease and control,* Geneva: World Health Organisation.

Migliavacca, F., Petrini, L., Colombo, M., Auricchio, F. and Pietrabissa, R. (2002) 'Mechanical behavior of coronary stents investigated through the finite element method', *Journal of Biomechanics,* 35(6), 803-811.

Miller, Y. I., Chang, M. K., Binder, C. J., Shaw, P. X. and Witztum, J. L. (2003) 'Oxidized low density lipoprotein and innate immune receptors', *Current Opinion in Lipidology,* 14(5), 437-445.

Mulder, W. J. M., Jaffer, F. A., Fayad, Z. A. and Nahrendorf, M. (2014) 'Imaging and Nanomedicine in Inflammatory Atherosclerosis', *Science Translational Medicine,* 6(239), 1-11.

Murad, M. H., Flynn, D. N., Elamin, M. B., Guyatt, G. H., Hobson, R. W., Erwin, P. J. and Montori, V. M. (2008) 'Endarterectomy vs stenting for carotid artery stenosis: A systematic review and meta-analysis', *Journal of Vascular Surgery,* 48(2), 487-493.

Nagaraj, A., Kim, H. G., Hamilton, A. J., Mun, J. H., Smulevitz, B., Kane, B. J., Yan, L. J., Roth, S. I., McPherson, D. D. and Chandran, K. B. (2005) 'Porcine carotid arterial material property alterations with induced atheroma: An in vivo study', *Medical Engineering & Physics,* 27(2), 147-156.

Nederveen, A. J., Avril, S. and Speelman, L. (2014) 'MRI strain imaging of the carotid artery: Present limitations and future challenges', *Journal of Biomechanics,* 47(4), 824-833.

Nightingale, K., Soo, M. S., Nightingale, R. and Trahey, G. (2002) 'Acoustic radiation force impulse imaging: In vivo demonstration of clinical feasibility', *Ultrasound in Medicine and Biology,* 28(2), 227-235.

Nightingale, K. R., Palmeri, M. L., Nightingale, R. W. and Trahey, G. E. (2001) 'On the feasibility of remote palpation using acoustic radiation force', *Journal of the Acoustical Society of America*, 110(1), 625-634.

Oliphant, T. E., Manduca, A., Ehman, R. L. and Greenleaf, J. F. (2001) 'Complex-valued stiffness reconstruction for magnetic resonance elastography by algebraic inversion of the differential equation', *Magnetic Resonance in Medicine,* 45(2), 299-310.

Ophir, J., Cespedes, I., Ponnekanti, H., Yazdi, Y. and Li, X. (1991) 'Elastography - A quantitative method for imaging the elasticity of biological tissues', *Ultrasonic Imaging,* 13(2), 111-134.

Packard, R. R. S. and Libby, P. (2008) 'Inflammation in atherosclerosis: From vascular biology to biomarker discovery and risk prediction', *Clinical Chemistry,* 54(1), 24-38.

Papazoglou, S., Hamhaber, U., Braun, J. and Sack, I. (2008) 'Algebraic Helmholtz inversion in planar magnetic resonance elastography', *Physics in Medicine and Biology,* 53(12), 3147-3158.

Parker, K. H. (2009a) 'A brief history of arterial wave mechanics', *Medical & Biological Engineering & Computing,* 47(2), 111-118.

Parker, K. H. (2009b) 'An introduction to wave intensity analysis', *Medical & Biological Engineering & Computing,* 47(2), 175-188.

Parker, K. J., Taylor, L. S., Gracewski, S. and Rubens, D. J. (2005) 'A unified view of imaging the elastic properties of tissue', *Journal of the Acoustical Society of America,* 117(5), 2705-2712.

Pazos, V., Mongrain, R. and Tardif, J. C. (2009) 'Polyvinyl alcohol cryogel: Optimizing the parameters of cryogenic treatment using hyperelastic models', *Journal of the Mechanical Behavior of Biomedical Materials,* 2(5), 542-549.

Pazos, V., Mongrain, R. and Tardif, J. C. (2010) 'Mechanical characterization of atherosclerotic arteries using finite-element modeling: Feasibility study on mock arteries', *IEEE Transactions on Biomedical Engineering,* 57(6), 1520-1528.

Pepper, D. W. and Heinrich, J. C. (1992) *The finite element method: Basic concepts and applications,* Washington D.C., Washington: Hemisphere Publishing Corporation.

Petrov, A., Chase, G., Sellier, M., Latta, P., Gruwel, M., McGarry, M. and Van Houten, E. (2012) 'Subzone based multi-frequency magnetic resonance elastography using a Rayleigh damped material model', *34th Annual International Conference of the IEEE Engineering in Medicine and Biology Society,* 28th August - 1st September, San Diego, California, 436-439.

Pinton, G. F., Palmeri, M. L., McAleavey, S. A., Nightingale, K. R. and Trahey, G. E. (2003) 'ARFI imaging of the cardiovascular system', *Proceedings of IEEE International Ultrasonics Symposium,* 5th-8th October, Honalulu, Hawaii, 228-231.

Pislaru, C., Kantor, B., Kinnick, R. R., Anderson, J. L., Aubry, M.-C., Urban, M. W., Fatemi, M. and Greenleaf, J. F. (2008) 'In vivo vibroacoustography of large peripheral arteries', *Investigative Radiology,* 43(4), 243-252.

Plewes, D. B., Bishop, J., Samani, A. and Sciarretta, J. (2000) 'Visualization and quantification of breast cancer biomechanical properties with magnetic resonance elastography', *Physics in Medicine and Biology,* 45(6), 1591-1610.

Raghavan, M. L., Trivedi, S., Nagaraj, A., McPherson, D. D. and Chandran, K. B. (2004) 'Three-dimensional finite element analysis of residual stress in arteries', *Annals of Biomedical Engineering,* 32(2), 257-263.

Ribbers, H., Lopata, R. G. P., Holewijn, S., Blankensteijn, J. D. and De Korte, C. L. (2005) 'Non-invasive two dimensional elastography of the carotid artery', *Proceedings of IEEE International Ultrasonics Symposium,* 18th-21st Sepetember, Rotterdam, The Netherlands, 1113-1116.

Ricotta, J., Pagan, J., Xenos, M., Alemu, Y., Einav, S. and Bluestein, D. (2008) 'Cardiovascular disease management: The need for better diagnostics', *Medical & Biological Engineering & Computing,* 46(11), 1059-1068.

Ringleb, S. I., Chen, Q. S., Lake, D. S., Manduca, A., Ehman, R. L. and An, K. N. (2005) 'Quantitative shear wave magnetic resonance elastography: Comparison to a dynamic shear material test', *Magnetic Resonance in Medicine,* 53(5), 1197-1201.

Romano, A. J., Abraham, P. B., Rossman, P. J., Bucaro, J. A. and Ehman, R. L. (2005) 'Determination and analysis of guided wave propagation using magnetic resonance elastography', *Magnetic Resonance in Medicine,* 54(4), 893-900.

Romano, A. J., Shirron, J. J. and Bucaro, J. A. (1998) 'On the noninvasive determination of material parameters from a knowledge of elastic displacements: Theory and numerical simulation', *IEEE Transactions on Ultrasonics Ferroelectrics and Frequency Control,* 45(3), 751-759.

Ross, R. (1993) 'The pathogenesis of atherosclerosis - A perspective for the 1990s', *Nature,* 362, 801-809.

Ross, R. (1999) 'Mechanisms of disease - Atherosclerosis - An inflammatory disease', *New England Journal of Medicine,* 340(2), 115-126.

Rothwell, P. M., Eliasziw, M., Gutnikov, S. A., Fox, A. J., Taylor, D. W., Mayberg, M. R., Warlow, C. P., Barnett, H. J. M. and Carotid Endarterectomy Trialists, C. (2003a) 'Analysis of pooled data from the randomised controlled trials of endarterectomy for symptomatic carotid stenosis', *Lancet,* 361, 107-116.

Rothwell, P. M., Gutnikov, S. A., Warlow, C. P. and European Carotid Surgery, T. (2003b) 'Reanalysis of the final results of the European Carotid Surgery Trial', *Stroke,* 34(2), 514-523.

Saam, T., Hatsukami, T. S., Takaya, N., Chu, B. C., Underhill, H., Kerwin, W. S., Cai, J. M., Ferguson, M. S. and Yuan, C. (2007) 'The vulnerable, or high-risk, atherosclerotic plaque: Noninvasive MR imaging for characterization and assessment', *Radiology,* 244(1), 64-77.

Sack, I., Beierbach, B., Hamhaber, U., Klatt, D. and Braun, A. (2008) 'Non-invasive measurement of brain viscoelasticity using magnetic resonance elastography', *NMR in Biomedicine,* 21(3), 265-271.

Sack, I., Rump, J., Elgeti, T., Samani, A. and Braun, J. (2009) 'MR elastography of the human heart: Noninvasive assessment of myocardial elasticity changes by shear wave amplitude variations', *Magnetic Resonance in Medicine,* 61(3), 668-677.

Sahebjavaher, R. S., Frew, S., Bylinskii, A., Ter Beek, L., Garteiser, P., Honarvar, M., Sinkus, R. and Salcudean, S. (2014) 'Prostate MR elastography with transperineal electromagnetic actuation and a fast fractionally encoded steady-state gradient echo sequence', *NMR in Biomedicine,* 27(7), 784-794.

Sanz, J. and Fayad, Z. A. (2008) 'Imaging of atherosclerotic cardiovascular disease', *Nature,* 451(7181), 953-957.

Schaar, J. A., De Korte, C. L., Mastik, F., Strijder, C., Pasterkamp, G., Boersma, E., Serruys, P. W. and Van Der Steen, A. F. W. (2003) 'Characterizing vulnerable plaque features with intravascular elastography', *Circulation,* 108(21), 2636-2641.

Schulze-Bauer, C. A. J., Morth, C. and Holzapfel, G. A. (2003) 'Passive biaxial mechanical response of aged human iliac arteries', *Journal of Biomechanical Engineering - Transactions of the ASME,* 125(3), 395-406.

Seneviratne, A., Hulsmans, M., Holvoet, P. and Monaco, C. (2013) 'Biomechanical factors and macrophages in plaque stability', *Cardiovascular Research,* 99(2), 284-293.

Shahmirzadi, D., Narayanan, P., Li, R. X., Qaqish, W. W. and Konofagou, E. E. (2013) 'Mapping the longitudinal wall stiffness heterogeneities within intact canine aortas using pulse wave imaging (PWI) ex vivo', *Journal of Biomechanics,* 46(11), 1866-1874.

Sinkus, R., Lorenzen, J., Schrader, D., Lorenzen, M., Dargatz, M. and Holz, D. (2000) 'High-resolution tensor MR elastography for breast tumour detection', *Physics in Medicine and Biology,* 45(6), 1649-1664.

Sinkus, R., Tanter, M., Catheline, S., Lorenzen, J., Kuhl, C., Sondermann, E. and Fink, M. (2005) 'Imaging anisotropic and viscous properties of breast tissue by magnetic resonance-elastography', *Magnetic Resonance in Medicine,* 53(2), 372-387.

Skovoroda, A. R., Emelianov, S. Y., Lubinski, M. A., Sarvazyan, A. P. and Odonnell, M. (1994) 'Theoretical analysis and verification of ultrasound displacement and strain imaging', *IEEE Transactions on Ultrasonics Ferroelectrics and Frequency Control,* 41(3), 302-313.

Slager, C. J., Wentzel, J. J., Gijsen, F. J. H., Thury, A., van der Wal, A. C., Schaar, J. A. and Serruys, P. W. (2005) 'The role of shear stress in the destabilization of vulnerable plaques and related therapeutic implications', *Nature Clinical Practice Cardiovascular Medicine,* 2(9), 456-464.

Stanton, A. V. (1999) 'Haemodynamics, wall mechanics and atheroma: a clinician's perspective', *Proceedings of the Institution of Mechanical Engineers Part H - Journal of Engineering in Medicine*, 213, 385-390.

Stary, H. C., Chandler, A. B., Dinsmore, R. E., Fuster, V., Glagov, S., Insull, W., Rosenfeld, M. E., Schwartz, C. J., Wagner, W. D. and Wissler, R. W. (1995) 'A definition of advanced types of atherosclerotic lesions and a histological classification of atherosclerosis - A report from the committee on vascular lesions of the council on arteriosclerosis, American Heart Association', *Circulation*, 92(5), 1355-1374.

Stary, H. C., Chandler, A. B., Glagov, S., Guyton, J. R., Insull, W., Rosenfeld, M. E., Schaffer, S. A., Schwartz, C. J., Wagner, W. D. and Wissler, R. W. (1994) 'A definition of initial, fatty streak, and intermediate lesions of atherosclerosis - A report from the committee on vascular lesions of the council of arteriosclerosis, American Heart Association', *Circulation*, 89(5), 2462-2478.

Streitberger, K. J., Wiener, E., Hoffmann, J., Freimann, F. B., Klatt, D., Braun, J., Lin, K., McLaughlin, J., Sprung, C., Klingebiel, R. and Sack, I. (2011) 'In vivo viscoelastic properties of the brain in normal pressure hydrocephalus', *NMR in biomedicine*, 24(4), 385-392.

Suetens, P. (2009) *Fundamentals of Medical Imaging*, Cambridge, UK: Cambridge University Press.

Sumpio, B. E. (1993) *Hemodynamic forces and vascular cell biology*, Austin, Texas: R.G. Landes.

Surry, K. J. M., Austin, H. J. B., Fenster, A. and Peters, T. M. (2004) 'Poly(vinyl alcohol) cryogel phantoms for use in ultrasound and MR imaging', *Physics in Medicine and Biology*, 49(24), 5529-5546.

Takaya, N., Yuan, C., Chu, B. C., Saam, T., Underhill, H., Cai, J. M., Tran, N., Polissar, N. L., Isaac, C., Ferguson, M. S., Garden, G. A., Cramer, S. C., Maravilla, K. R., Hashimoto, B. and Hatsukami, T. S. (2006) 'Association between carotid plaque characteristics and subsequent ischemic cerebrovascular events - A prospective assessment with MRI - Initial results', *Stroke*, 37(3), 818-823.

Tang, D. L., Yang, C., Kobayashi, S. and Ku, D. N. (2004a) 'Effect of a lipid pool on stress/strain distributions in stenotic arteries: 3-D fluid-structure interactions (FSI) models', *Journal of Biomechanical Engineering - Transactions of the ASME*, 126(3), 363-370.

Tang, D. L., Yang, C., Zheng, J., Woodard, P. K., Sicard, G. A., Saffitz, J. E. and Yuan, C. (2004b) '3D MRI-based multicomponent FSI models for atherosclerotic plaques', *Annals of Biomedical Engineering*, 32(7), 947-960.

Tang, T. Y., Howarth, S. P. S., Li, Z. Y., Miller, S. R., Graves, M. J., U-King-Im, J. M., Trivedi, R. A., Walsh, S. R., Brown, A. P., Kirkpatriek, P. J., Gaunt, M. E. and Gillard, J. H. (2008) 'Correlation of carotid atheromatous plaque inflammation with biomechanical stress: Utility of USPIO enhanced MR imaging and finite element analysis', *Atherosclerosis*, 196(2), 879-887.

Thomas-Seale, L., Klatt, D., Hollis, L., Sack, I., Roberts, N., Pankaj, P. and Hoskins, P. (2015) 'Simulating magnetic resonance elastography: A computational parameter evaluation', *International Journal of Numerical Methods in Biomedical Engineering*, (Submitted).

Thomas-Seale, L. E. J., Kennedy, P., Klatt, D., Anderson, T., Hammer, S., Semple, S., Mirsadraee, S., Sack, I., Pankaj, P., Roberts, N. and Hoskins, P. R. (2013) 'Magnetic resonance elastography through atherosclerosis: The progression from computational simulations to experimental feasibility', *Proceedings of the 12th International Tissue Elasticity Conference,* 1st-4th October, Lingfield, UK, 45.

Thomas-Seale, L. E. J., Klatt, D., Pankaj, P., Roberts, N., Sack, I. and Hoskins, P. R. (2011a) 'A simulation of the magnetic resonance elastography steady state wave response through idealised atherosclerotic plaques', *IAENG International Journal of Computer Science,* 38(4), 394-400.

Thomas-Seale, L. E. J., Pankaj, P., Roberts, N. and Hoskins, P. R. (2011b) ‘Computational modelling of magnetic resonance elastography shear wave behaviour through atherosclerotic plaque with disease development’, *Lecture Notes in Engineering and Computer Science: Proceedings of the World Congress on Engineering,* 6th-8th July, London, UK, 2636-2639.

Toole, J. F., Baker, W. H., Castaldo, J. E., Chambless, L. E., Moore, W. S., Robertson, J. T., Young, B. and Howard, V. J. (1995) 'Endarterectomy for asymptomatic carotid artery stenosis', *Journal of the American Medical Association,* 273(18), 1421-1428.

Torr, G. R. (1984) 'The acoustic radiation force', *American Journal of Physics,* 52(5), 402-408.

Townsend, N., Wickramasinghe, K., Bhatnagar, P., Smolina, K., Nichols, M., Leal, J., Luengo-Fernandez, R. and Rayner, M. (2012) *Coronary heart disease statistics 2012 edition,* London, UK: British Heart Foundation.

Trahey, G. E., Dahl, J. J., McAleavey, S. A., Gallippi, C. M. and Nightingale, K. R. (2003) 'Arterial stiffness measurements with acoustic radiation force impulse imaging', *Proceedings of Medical Imaging 2003: Ultrasonic Imaging and Signal Processing,* 17th-20th Feb, San Diego, California, 235-241.

Trivedi, R. A., U-King-Im, J., Graves, M. J., Horsley, J., Goddard, M., Kirkpatrick, P. J. and Gillard, J. H. (2004) 'Multi-sequence in vivo MRI can quantify fibrous cap and lipid core components in human carotid atherosclerotic plaques', *European Journal of Vascular and Endovascular Surgery,* 28(2), 207-213.

U-King-Im, J. M., Trivedi, R., Cross, J., Higgins, N., Graves, M., Kirkpatrick, P., Antoun, N. and Gillard, J. H. (2004) 'Conventional digital subtraction x-ray angiography versus magnetic resonance angiography in the evaluation of carotid disease: patient satisfaction and preferences', *Clinical Radiology,* 59(4), 358-363.

Uffmann, K., Abicht, C., Grote, W., Quick, H. H. and Ladd, M. E. (2002) 'Design of an MR-compatible piezoelectric actuator for MR elastography', *Concepts in Magnetic Resonance,* 15(4), 239-254.

Valdez-Jasso, D., Bia, D., Zocalo, Y., Armentano, R. L., Haider, M. A. and Olufsen, M. S. (2011) 'Linear and nonlinear viscoelastic modeling of aorta and carotid pressure-area dynamics under in Vivo and ex vivo conditions', *Annals of Biomedical Engineering,* 39(5), 1438-1456.

Valdez-Jasso, D., Haider, M. A., Banks, H. T., Santana, D. B., German, Y. Z., Armentano, R. L. and Olufsen, M. S. (2009) 'Analysis of viscoelastic wall properties in ovine arteries', *IEEE Transactions on Biomedical Engineering,* 56(2), 210-219.

Van Houten, E. E. W., Doyley, M. M., Kennedy, F. E., Weaver, J. B. and Paulsen, K. D. (2003) 'Initial in vivo experience with steady-state subzone-based MR elastography of the human breast', *Journal of Magnetic Resonance Imaging,* 17(1), 72-85.

Van Houten, E. E. W., Miga, M. I., Weaver, J. B., Kennedy, F. E. and Paulsen, K. D. (2001) 'Three-dimensional subzone-based reconstruction algorithm for MR elastography', *Magnetic Resonance in Medicine,* 45(5), 827-837.

Van Houten, E. E. W., Paulsen, K. D., Miga, M. I., Kennedy, F. E. and Weaver, J. B. (1999) 'An overlapping subzone technique for MR-based elastic property reconstruction', *Magnetic Resonance in Medicine,* 42(4), 779-786.

VanEpps, J. S. and Vorp, D. A. (2007) 'Mechanopathobiology of atherogenesis: A review', *Journal of Surgical Research,* 142(1), 202-217.

Versluis, A., Bank, A. J. and Douglas, W. H. (2006) 'Fatigue and plaque rupture in myocardial infarction', *Journal of Biomechanics,* 39(2), 339-347.

Vito, R. P. and Dixon, S. A. (2003) 'Blood vessel constitutive models-1995-2002', *Annual Review of Biomedical Engineering,* 5, 413-439.

Vonesh, M. J., Cho, C. H., Pinto, J. V., Kane, B. J., Lee, D. S., Roth, S. I., Chandran, K. B. and McPherson, D. D. (1997) 'Regional vascular mechanical properties by 3-D intravascular ultrasound with finite-element analysis', *American Journal of Physiology-Heart and Circulatory Physiology,* 272(1), H425-H437.

Waite, L. and Fine, J. M. (2007) *Applied biofluid mechanics,* New York: McGraw-Hill.

Wan, W. K., Campbell, G., Zhang, Z. F., Hui, A. J. and Boughner, D. R. (2002) 'Optimizing the tensile properties of polyvinyl alcohol hydrogel for the construction of a bioprosthetic heart valve stent', *Journal of Biomedical Materials Research,* 63(6), 854-861.

Wang, H., Weaver, J. B., Perreard, I. I., Doyley, M. M. and Paulsen, K. D. (2011) 'A three-dimensional quality-guided phase unwrapping method for MR elastography', *Physics in Medicine and Biology,* 56(13), 3935-3952.

Wang, X., Keith, J. C., Jr., Struthers, A. D. and Feuerstein, G. Z. (2008) 'Assessment of arterial stiffness, a translational medicine biomarker system for evaluation of vascular risk', *Cardiovascular Therapeutics,* 26(3), 214-223.

Webb, S. (1988) *The Physics of Medical Imaging,* Abingdon, UK: Taylor and Francis Group.

Wedding, K. L., Draney, M. T., Herfkens, R. J., Zarins, C. K., Taylor, C. A. and Pelc, N. J. (2002) 'Measurement of vessel wall strain using cine phase contrast MRI', *Journal of Magnetic Resonance Imaging,* 15(4), 418-428.

Woodrum, D. A., Herrmann, J., Lerman, A., Romano, A. J., Lerman, L. O. and Ehman, R. L. (2009) 'Phase-contrast MRI-based elastography technique detects early hypertensive changes in ex vivo porcine aortic wall', *Journal of Magnetic Resonance Imaging,* 29(3), 583-587.

Woodrum, D. A., Romano, A. J., Lerman, A., Pandya, U. H., Brosh, D., Rossman, P. J., Lerman, L. O. and Ehman, R. L. (2006) 'Vascular wall elasticity measurement by magnetic resonance imaging', *Magnetic Resonance in Medicine,* 56(3), 593-600.

Xu, L., Chen, J., Glaser, K. J., Yin, M., Rossman, P. J. and Ehman, R. L. (2013) 'MR elastography of the human abdominal aorta: A preliminary study', *Journal of Magnetic Resonance Imaging,* 38(6), 1549-1553.

Xu, L., Chen, J., Yin, M., Glaser, K. J., Chen, Q. S., Woodrum, D. A. and Ehman, R. L. (2012) 'Assessment of stiffness changes in the ex vivo porcine aortic wall using magnetic resonance elastography', *Magnetic Resonance Imaging,* 30(1), 122-127.

Yabushita, H., Bourna, B. E., Houser, S. L., Aretz, T., Jang, I. K., Schlendorf, K. H., Kauffman, C. R., Shishkov, M., Kang, D. H., Halpern, E. F. and Tearney, G. J. (2002) 'Characterization of human atherosclerosis by optical coherence tomography', *Circulation*, 106(13), 1640-1645.

Yasar, T. K., Royston, T. J. and Magin, R. L. (2013) 'Wideband MR elastography for viscoelasticity model identification', *Magnetic Resonance in Medicine*, 70(2), 479-489.

Yuan, C., Zhang, S. X., Polissar, N. L., Echelard, D., Ortiz, G., Davis, J. W., Ellington, E., Ferguson, M. S. and Hatsukami, T. S. (2002) 'Identification of fibrous cap rupture with magnetic resonance imaging is highly associated with recent transient ischemic attack or stroke', *Circulation*, 105(2), 181-185.

Zhao, S. Z., Ariff, B., Long, Q., Hughes, A. D., Thom, S. A., Stanton, A. V. and Xu, X. Y. (2002) 'Inter-individual variations in wall shear stress and mechanical stress distributions at the carotid artery bifurcation of healthy humans', *Journal of Biomechanics*, 35(10), 1367-1377.

Zheng, Y., Chan, Q. C. C., Li, G., Lam, E. Y. and Yang, E. S. (2007) 'A study of femoral artery by twin drivers in magnetic resonance interference elastography', *Proceedings of the 29th Annual International Conference of the IEEE Engineering in Medicine and Biology Society*, 23rd-26th August, Lyon, France, 2034-2037.